A DEEPER UNDERSTANDING OF THE INPUTS FOR REACTION THEORY THROUGH UNCERTAINTY QUANTIFICATION

By

Amy Elizabeth Lovell

A DISSERTATION

Submitted to
Michigan State University
in partial fulfillment of the requirements
for the degree of

Physics — Doctor of Philosophy

2018

ABSTRACT

A DEEPER UNDERSTANDING OF THE INPUTS FOR REACTION THEORY THROUGH UNCERTAINTY QUANTIFICATION

By

Amy Elizabeth Lovell

Nuclear reactions are important for studying the properties of nuclei across the nuclear chart and in answering the biggest questions in nuclear science, ranging from the formation of the elements in the universe to societal applications. The exact description of nuclei in terms of a few degrees of freedom is not known, so models are developed to mimic the resulting phenomena. Because these prescriptions are, by definition, approximations, it is crucial to quantify the uncertainties that result from these approximations. These uncertainties arise not only from the simplifications that are made to the solutions of the scattering problem and degrees of freedom removed from the model space, but also from the parameterization of the effective potentials. Although it is important to rigorously quantify each uncertainty, we take the first step by systematically studying the effect of parametric uncertainties arising from fitting optical model parameters to elastic-scattering data. To do this, we use simple reaction models, the distorted-wave Born approximation (DWBA) and the adiabatic wave approximation (ADWA), for computationally inexpensive calculations. Two methods of parametric uncertainty quantification were explored in this work, a frequentist approach and a Bayesian approach.

In the frequentist study, χ^2 minimization was used to constrain optical model parameters in the incoming scattering channel, using neutron and deuteron elastic-scattering data. Then 95% confidence bands were constructed around the best-fit calculation for elastic scattering and were propagated in order to compute 95% confidence bands for predicted (d,p) and (n,n$'$)

cross sections using DWBA. A correlated χ^2 fitting function was introduced to take into account the angular correlations within the elastic-scattering model. Using this correlated χ^2 function led to broader confidence bands and more physical descriptions of the angular distributions.

For the Bayesian study, a wide Gaussian prior was used in conjunction with neutron, proton, and deuteron elastic-scattering data to construct posterior distributions through a Markov Chain Monte Carlo. From the posterior distributions, 95% confidence intervals were constructed for the elastic-scattering cross sections and then propagated to predict 95% confidence intervals for (d,p) and (d,n) reactions using either ADWA or DWBA. In this way, the parametric uncertainties from ADWA and DWBA could be directly compared, and ADWA was found to have smaller uncertainties. The effect of artificially reducing the experimental errors on elastic-scattering data was studied, and it was found that the uncertainties in the transfer cross section decreased but not by the same percent that the experimental errors were reduced.

Overall, the uncertainties on the predicted cross sections due to fitting optical model parameters to elastic-scattering data ranged from $20 - 120\%$, significantly larger than the $10 - 30\%$ uncertainties that are assumed to be introduced by these fits. Uncertainties beyond those introduced by fitting to data must also be included, such as those introduced by the few-body approximations. In addition, the propagation of uncertainties has to be reliable. A full description of theoretical uncertainties is vital for predictions, especially as we move toward the edge of the nuclear landscape.

ACKNOWLEDGMENTS

I would first like to thank my adviser, Filomena Nunes for all of her support and guidance, for telling me that I "don't look like an experimentalist" (the only reason this work was even possible), and for helping me remember that there is a light at the end of the tunnel and a clearing in the woods. I would especially like to thank her, not just for her support academically and scientifically, but personally as well. She led by example of how to be a productive scientist and have a healthy work-life balance and encouraged me to do the same. However, I cannot thank her enough for helping me me to become more independent in my research and trusting me to work away from the lab for weeks over the course of the year so that my relationship remained healthy.

I would also like to thank my guidance committee members, Morten Hjorth-Jensen, Witek Nazarewicz, Brian O'Shea, and Artemis Spyrou for their suggestions and motivation throughout the course of my studies. This work would also have not been possible without many collaborators and advisors, including Ian Thompson, Stefan Wild, Jason Sarich, Pierre Capel, and Scott Pratt who have spent countless hours helping me learn their codes, implementing new methods, deepening my understanding of nuclear physics and statistical methods, and ultimately boosting my confidence with their feedback. I wold also like to thank Gowri Srinivasan for mentoring me at Los Alamos and unhesitatingly taking on a would-be nuclear physicist for a geophysics uncertainty quantification project. That, just as much as anything else, has boosted my confidence about having skills that are applicable in a wide range of fields.

Thank you to my fellow group-mates, both past and present, Luke Titus, Terri Poxon-Pearson, Alaina Ross, Michael Quinonez, Paul Wright, Garrett King, Neelam Upadaya,

Gregory Potel, Jimmy Routaeu, Wichuan Li, and Linda H'lophe. It has been great traveling with you, learning from you, and helping you learn. I would not have been able to complete my time at MSU if it had not been for the graduate students in the physics department, but especially Wei Jia Ong, Josh Bradt, Becky Lewis, and Chris Izzo. You guys kept me sane, and I cannot wait for more road trips, football-watching, dinner-cooking, cookie-baking, and great conversations.

I would not have made it this far without the love and support of my parents, Carol and John, who have continuously driven me to do my best, even though I did not study engineering, or without my brother, Matt, who from the minute he was born helped me to learn to share, to play nice with others, and that sometimes hair-pulling is a part of life. Thank you to my future in-laws, Mary and Andy, who have so readily welcomed me into their family and never fail to be excited to see me regardless of how often I visit. Last but certainly not least, I want to thank my fiancè, Tony Cao, for listening to my ups and downs (and reminding me why I chose to do this in the first place), diving whole-heartedly into this exhaustive adventure that we call long-distance, supporting my dreams even though his own are delayed, and being patient as I stumble along this journey that is graduate school.

TABLE OF CONTENTS

LIST OF TABLES

LIST OF FIGURES

Chapter 1

Introduction

The nuclear physics community has identified several overarching goals [12]. These goals include answering:

1. How did visible matter come into being and how does it evolve?

2. How does subatomic matter organize itself and what phenomena emerge from this organization?

3. To what extent are the fundamental interactions that are critical to the structure of matter understood?

4. How can the knowledge and technical progress provided by nuclear physics best be used to benefit society?

Reactions can be used to study each of these points. Because these questions span the full scope of nuclear physics, a wide range of experimental techniques is required. Reliable reaction theory is crucial for extracting information using these various probes.

The study of big bang nucleosynthesis aims at answering the question as to how the elements were formed throughout the history of the universe. For models to correctly reproduce the observed isotopic abundances, many properties of nuclei have to be measured, including reaction rates, lifetimes, and masses, often of resonance states in the continuum. Many of the reactions of interest are neutron or proton capture reactions which take place far

from stability. Since targets for short-lived radioactive isotopes cannot be made, reactions are instead often studied in inverse kinematics [13, 14, 15, 16] where a radioactive beam is impinged upon a stable target. However, neutron capture reactions cannot be performed in this manner, so surrogate reactions are used instead. For example, a (d,p) transfer reaction can be used to populate the same states that a neutron capture reaction would populate [17, 18]. Understanding the reaction mechanisms in both cases is crucial in extracting the same information from both of these studies.

Many novel phenomena emerge across the nuclear chart, especially at the limits of stability - the neutron and proton driplines, beyond which a nucleus can no longer form bound states. Neutron and proton halo nuclei have a single nucleon (or multiple nucleons) that is spatially separated from the remaining nucleons in the core, giving rise to interesting features such as a ^{11}Be radius that is as large as that of ^{208}Pb (when the radius usually scales with $A^{1/3}$, and it is only the valence neutron orbital that is the size of ^{208}Pb). This was first noticed through the extraction of radii from reaction cross sections [19]. Borromean nuclei, which can be thought of as a core and two valence protons or neutrons, are bound but do not support any two-body bound states. ^{11}Li, for example, is well-described as $n + n + ^9$Li but neither the nn or $n-^{10}$Li subsystems are bound [20]. These systems have unusually large reaction cross sections compared to neighboring nuclei, and they can often only occur for specific configurations (the valence nucleons have to have low values of angular momentum). The evolution of these shells can be probed using transfer and knockout reactions [21, 22, 23]. In certain cases, measurements from Penning traps, which can precisely measure properties of nuclei, are able to provide detailed information into the structure of matter [24], as do β- and γ-decays (e.g. [25, 26]), but much information is still obtained from reactions.

Finally, two of the most prominent societal applications from nuclear physics are to

energy and medicine. Reactions involving neutrons, deuteron, and tritium play a key role in development and design of nuclear reactors [27, 28]. Exotic isotopes far from stability can be harvested during experimental runs at basic science laboratories. These nuclei occur as by-products of proposed experiments and are used as radiotracers for imaging and therapy [29, 30]. Whether or not enough of these isotopes can be produced for collection directly relates to the reaction mechanism that is used to produce them.

A concrete understanding of reaction theory is crucial for extracting information from the experimental studies used to answer these questions. Extracted quantities are often model-dependent due to the simplifications or effective interactions that have been developed and the theoretical methods that are applied. Each model uses different degrees of freedom and takes into account different reaction mechanisms which can be more or less important depending on the reaction being studied. The important degrees of freedom change based on the energy range, mass and charge of the system, and the structure of the projectile and target. The implementation of many reaction theories relies on phenomenological potentials, which introduce further ambiguities into the observables. Parameters within the potential can vary significantly but still give rise to the same elastic angular distributions (which are typically used to constrain these parameters). A thorough understanding of the limitations of these reaction models, as well as their inputs, is crucial to accurately interpret reaction data and make predictions.

1.1 Uncertainty Quantification

It is important not only to have robust input for our theories but also to study the degree to which these inputs are uniquely constrained and well determined. This has been recognized

for decades in several math and science communities. Mathematical overviews, such as [31], have been the starting point for analyzing parametric uncertainties and implementing procedures that correct for model inadequacies. The analysis of high energy experiments routinely uses advanced statistical techniques for the resulting large data sets, for example [32, 33]. Astronomy and astrophysics communities have been using Bayesian approaches to interpret observed quantities such as neutron star radii [34] and luminosities [35]. They have also studied and understood the importance of explicitly encoding assumptions into their interpretations of observations. The many examples of [36] show that observations can be misleading when prior information is not taken into account (e.g. overestimation of the mass of a distant galaxy because of an incorrect assumption of the shape of the mass function, which describes the distribution of mass of a group of stars). Climate science has relied on uncertainty quantification in connecting observations such as solar irradiance, greenhouse gas concentration, volcanism, tree rings, sediment records, and ice cores to the temperature [37]. Model and parametric uncertainties have been also been studied in geophysics (e.g. [38]). Over the past several years, there has been a push in the atomic physics community to include uncertainties on theoretical calculations whenever possible [39].

Within the past few years, the nuclear theory community has also recognized the importance of rigorously including uncertainties in calculations. Most of the recent work to systematically quantify uncertainties in nuclear theory has been within the nuclear structure community [40, 41, 42, 43, 44, 45, 46, 47, 48]. For example, effective field theory (EFT) methods rely on an order-by-order expansion to calculate observables (such as cross sections) that are based on potentials (also constructed through an order-by-order expansion) constrained by nucleon-nucleon interactions (e.g. [49]). Interactions derived from EFT are written in such a way that two-nucleon forces dominate the interaction and are followed by

three-nucleon interactions, four-nucleon interactions, and so on. This hierarchy introduces free parameters (low energy constants, LECs) that are constrained by data. The expansion for observables is controlled by a dimensionless quantity which, as the nucleon-nucleon interaction itself, decreases with every successive term in the expansion.

This type of formulation provides a myriad of opportunities for systematic uncertainty quantification. Parametric uncertainties can be addressed in the fitting of the LECs. Assumptions can be directly tested, such as the expansion coefficients for observable calculations should be of order one. In addition, because the theory is constructed on a systematic expansion where each successive order becomes smaller than the previous, there is a straightforward way of quantifying the uncertainty on a given order based on the next order's calculation. All in all, this theory provides a diverse playground for investigating various types of uncertainties.

Because of this, much progress has been made in recent years to quantify uncertainties in EFT. Theoretical uncertainties of phase shifts and observables, based on the construction of the EFT interaction at various orders, was investigated in [50] where this error was shown to decrease order-by-order. Statistical uncertainties from the constraints on the LECs were propagated to observables using covariance matrices [40, 41]. Bayesian methods have been used to calculate uncertainties on the expansion parameters of observables [42, 51] where the naturalness (order unity) of these parameters can be included as prior knowledge. The framework is very flexible, allowing for these assumptions to be explicitly included, tested, and then modified if necessary [43, 52, 44].

Uncertainties are also being systematically quantified in density function theory (DFT). Density function theory is a microscopic theory that is able to reproduce observables across the entire nuclear chart. It is commonly used to predict masses and fission properties [53].

Many DFTs are generated from known symmetries, and because the model is not built upon an underlying theory - like EFT is - parameters must be constrained by experimental data [45, 54, 46]. Constraining the parameters and computing the associated uncertainties has been accomplished through covariance analysis as well as using Bayesian techniques [55]. Ambiguities in model parameters arise when various sets of data are used to constrain these parameters. The information content of these data sets can be evaluated by calculating the uncertainty associated with each parameterization [47] (and references therein).

Understanding the information content of experimental data with regard to a given model has also been investigated in heavy ion collisions, where models can have hundreds of parameters and are computationally expensive. Techniques, such as principle component analysis (PCA) and those discussed in [48], are used to understand the correlations between model parameters, as well as to determine which parameters can be constrained based on the observables that are calculated [56, 57]. Principle component analysis also aids in the creation of emulators which replicate the trends and correlations of the theory of interest in order to decrease computation time but still mirror the results of the full calculation.

This, of course, is not a complete history of uncertainty quantification, but it is representative of the depth of studies that can be performed. While significant effort has gone into quantifying uncertainties in nuclear structure and heavy ion collisions, the same cannot be said of direct nuclear reaction theory. Many of the sources of uncertainties in reaction theory are similar to those in EFT and DFT. However, the formulation of the models in reaction theory makes it such that, while we can use similar techniques to quantify our uncertainties, these techniques have to be re-explored for scattering models.

1.2 Motivation

There are four main sources of uncertainty in few-body reaction theory [58]: 1) the degrees of freedom left out of the model space, 2) the effective interactions used, 3) structure functions (such as overlap functions), and 4) approximations made to the few-body problem. Many of these sources of uncertainty have been investigated through comparative methods (as will be discussed in this section), but until recently in reaction theory, there have been no systematic studies aimed at rigorously quantifying these uncertainties. This is important not only for moving the field forward and keeping up with new implementations in other fields - as discussed in Section 1.1 - but also for reliably interpreting information from experimental data.

The first source of uncertainty in reaction theory is the simplification made to cast the many-body problem into the framework of a more tractable few-body problem. The full three-body problem for three nucleons can be solved exactly, with and without the Coulomb potential (which can present a significant challenge) [59, 60]. However, many more complicated reactions are also cast as three-body problems - such as single nucleon transfer, in the context of A(d,p)B (e.g. [61]) which is often treated within a $n+p+A$ model. This removal of degrees of freedom from the model space can have a noticeable affect on calculated observables. For instance, excited states in the target can influence the reaction mechanism, as has been shown for ^{11}Be [62, 63]. Including the first excited 2^+ state in ^{10}Be has a significant effect on the transfer cross section for ^{10}Be(d,p)^{11}Be(g.s.) [64]. Being able to take these effects into account is particularly important for transition nuclei for which a simple vibrational model, rotational model, or single-particle excitation is not enough to describe the complex excitations. The ultimate goal in this sector is to *a priori* understand the un-

certainty associated with each of these simplifications of the model space without having to compare with the full calculation for each reaction (many of which are out of reach of present-day reaction theories).

The second source of uncertainty comes from the effective nucleon-target interactions which are usually taken to be optical potentials. These are constructed to mimic the interaction between the projectile and target in a simple, parameterized form. In principle, these potentials can be built up from nucleon-nucleon interactions, but recent work has shown a lack of absorption in the potentials constructed this way [65]. Instead, the parameters within these effective interactions are usually constrained by fitting elastic-scattering data, introducing ambiguities in the resulting reaction observables. (The same elastic cross sections can arise from different parameterizations of the potentials.) These ambiguities are not typically taken into account when experimental results are being interpreted (e.g. [14]); if they are, this is done by direct comparison between two parameterizations (e.g. [13]), which does not describe the full extent of the uncertainties introduced in this manner. Global parameterizations are constructed by fitting mass- and energy-dependent parameters to a large range of nucleon elastic scattering on nuclei across the nuclear chart, and although these forms tend to interpolate well to other energies and nuclei within the fitted region, extrapolations away from stability can be uncontrolled. An analysis of covariance matrices can give an idea of the uncertainty associated with a given fitted parameterization, but these uncertainties will vary based on the minimum. It is therefore important to be able to calculate uncertainties for a single parameterization and understand how these uncertainties propagate to predictions.

The structure functions included in the reaction model provide the third source of uncertainty. For example, in a single-nucleon transfer reaction, information is needed about the bound state of the nucleon that is transferred from the projectile onto the target. These

bound states are often described as a single-particle state in a mean field generated by a Woods-Saxon potential. The geometry of this potential is rather arbitrary and only the depth is constrained to reproduce the binding energy of that state. This geometry, however, can greatly influence the magnitude of the transfer cross section which then affects extracted quantities, such as the spectroscopic factor (e.g. [58]). Asymptotic properties of the bound-state wave function are known to also be sensitive to the geometry of the mean field, so constraining these properties directly can reduce the uncertainty in quantities extracted from the transfer cross section. Understanding how changes in the mean field affect the magnitude of the transfer cross section will probe the uncertainties introduced from this source.

For the final source of uncertainty, there are the approximations that are made to the solution of the few-body problem itself. While the exact three-body problem has been solved for three nucleons with techniques such as the Faddeev equations for coordinate space [66] and corresponding Alt-Grassberger-Sandhas (AGS) equations in momentum space [67], applying these techniques to heavier systems becomes challenging due to the long-distance nature of the Coulomb interaction between charged bodies. Simpler solutions have been developed where approximations are made to the exact few-body scattering wave function. One such approximation is the distorted-wave Born approximation (DWBA) which replaces the exact three-body wave function by the elastic channel (a distorted wave that describes the scattering between the projectile and target multiplied by a corresponding bound-state wave function). However, for reactions involving loosely bound systems, this approximation falls short and is often replaced by methods that include effects of the continuum, such as the continuum discretized coupled channel (CDCC) [68] and adiabatic wave approximation (ADWA) [69] methods. Although these methods compare favorably to the exact three-body

methods for deuteron-induced reactions on targets with mass $A \leq 50$ (for example [70]), this direct comparison is not possible for heavier systems because of the difficulties associated with the Coulomb force. In addition, these methods may be difficult to converge and are computationally expensive. For this reason, theories such as DWBA are still widely used. Similarly to the first point, the goal for this sector is to *a priori* understand the uncertainties arising from simplifications to the full three-body wave function.

Although systematic uncertainty quantification has been studied mainly within the nuclear structure community discussed in Section 1.1, informal methods of uncertainty evaluation have been used in reaction theory for decades. Several different potential parameterizations can give rise to identical - or nearly identical - elastic-scattering cross sections while producing significantly different transfer cross sections [58]. Uncertainties are evaluated by calculating the percent difference between observables produced from the two parameterizations. Model uncertainties have been historically explored by directly comparing observables calculated from two reaction models with identical interactions. However, these comparisons do not provide a systematic path for quantifying uncertainties in general.

Systematically studying all of these sources of uncertainty is imperative. However, the magnitude of that task is far and beyond the work that could be done here and will continue in a later stage of this project. In this work, we begin by investigating the uncertainties related to the effective interactions, specifically those that arise from fitting optical model parameters to elastic-scattering data. To that end, we need to develop and implement tools for uncertainty quantification to reaction theory models. We also want to test the validity of these methods across the range of reaction probes and models of interest. Because the models that most accurately describe the physics of reactions in all of these areas are in themselves computationally expensive - and even the simplest forms of uncertainty quantification add

several orders of magnitude to the computation time - for this work, we restrict ourselves to simple reaction formalisms. Although these do not take into account the complexity of most of the reactions that we studied, they are ideal for developing and exploring techniques for parametric uncertainty quantification. Eventually, these uncertainty quantification techniques will be applied to more state-of-the-art reaction models, but that is beyond the scope of this thesis.

1.3   Outline

This thesis is organized in the following way. In Chapter 2, the necessary reaction theory is presented. Chapter 3 formulates the implementation of uncertainty quantification in the theories previously mentioned, focusing on the uncertainties coming from the parameterizations of the optical model - and not from the choice of the reaction model. Two separate methods are discussed here, first a frequentist model and then a Bayesian method. Chapter 4 provides selected results from the frequentist study, including the comparison of the two χ^2 fittings that were performed. Next, the Bayesian results are presented in Chapter 5, which includes the various prior choices that were investigated, the dependence of results on the size of the experimental errors, and the results of the elastics scattering and transfer calculations. Finally, the conclusions will be drawn in Chapter 6 followed by the future directions that this work can take.

This thesis also contains several appendices that hold important work that does not necessarily fit into the main body of this text. Appendix A contains the test of the Monte Carlo code that was developed to calculate posterior distributions for the Bayesian calculations. It also contains the extensive tests that were performed on the various prior distribution

shapes. For both the frequentist and Bayesian projects, more reactions were studied than could be included in the main text; the details of these remaining reactions are provided in Appendices B and C.

There are also two projects that, although important to the field, do not necessarily fit under the heading of uncertainty quantification; these are detailed in Appendices D and E. In the first, the introduction of energy-dependence into non-local potentials is described [5]. This work connects to Luke Titus' PhD thesis work [71] and the master thesis work of Pierre-Loic Bacq [2] and serves as a motivation to reexamine phenomenological non-locality. Finally, Appendix E presents results from a three-body calculation for ^{16}Be in response to an experiment run at the National Superconducting Cyclotron Laboratory (NSCL) in 2012 [72] that observed the two-neutron decay of this nucleus. This work is the first three-body calculation performed for ^{16}Be [3] and involves n-^{14}Be interactions which are very poorly constrained due to a lack of data.

Chapter 2

Reaction Theory

Different reaction probes can be used to extract a variety of nuclear properties. Elastic scattering provides information about the interaction between the projectile and target nuclei, including the size of the nuclear potential and its strength. The diffraction-like patterns that are seen in the elastic-scattering cross sections are related to the size of the target nucleus. Inelastic scattering observables contain information about the shape of a nucleus.

A deuteron impinged upon a target can transfer a proton or neutron in a single-particle transfer reaction. Because the shape of the angular distributions are determined by the angular momentum transfer of the reaction, these reactions can be used to probe specific states within the final nucleus that are populated by the transfer. Within the scope of a given model, the calculated cross section can be decomposed into its partial wave components and compared to data, for example [73]. Transfer reactions also provide a connection between structure and reaction, by connecting observables (e.g. cross sections) to theoretically calculated quantities, such as spectroscopic factors.

Robust reaction theory, as well as a sound understanding of the approximations and limitations of the different frameworks, is crucial to interpreting experimental results. The main goal of this work is to study the theoretical uncertainties that are introduced by fitting parameters in optical model potentials to experimental elastic scattering data. Here, the fitted potentials include those that describe the scattering of projectiles and targets.

Bound state interactions (such as that between the neutron and proton in the deuteron) are also constrained by data, but the uncertainties from these potentials are not considered in this work. There is also uncertainty introduced in the theory from the simplification from a many-body problem to a few-body problem and in the approximations that are made within the reaction models (first order expansions, etc.). Even though we do not directly include uncertainties coming from the approximations within the models, it is important to understand the applicability of each framework so that our interpretation of the uncertainties coming from the potential parameterizations are not skewed by the limitations of the model. The following chapter will provide information about the potentials that are used to describe target-projectile interactions and then discuss the reaction models used within the remainder of this thesis.

2.1   Optical Model

Throughout this work, the potentials that describe the interactions between the target and projectile are defined by the optical model. Phenomenological optical potentials consist of real and imaginary parts; they are local and strongly energy- and mass-dependent. Because these potentials effectively describe the complexity of the many-body A-N system by two-body interactions instead, these dependences are intended to take into account effects such as anti-symmetrization, non-locality, and couplings from the elastic channel to all other channels not explicitly included in the model space [74, 75, 76, 77].

Even though they are simple, phenomenological potentials still play an important role in few-body reaction theory. Global parameterizations, which are fit to a wide range of data across the nuclear chart to constrain mass- and energy-dependences, are particularly

useful for interpolating between available data sets to make predictions for reactions that have not yet been measured. There are several commonly used global optical potentials [1, 78, 79, 80, 81, 82] which were developed between the 1970's and early 2000's. In this work, these are used as is or as the starting point for a local optical potential that is further constrained by a single set of two-body scattering data.

The optical model describes the interaction between the target and projectile with real and imaginary components,

$$U(R) = V(R) + i(W(R) + W_s(R)) + V_{SO}(R) + V_C(R). \tag{2.1}$$

The imaginary component takes into account the absorption of flux that occurs at higher energies when other reaction channels become accessible. The potentials considered in this work have three parts, a volume term, a surface term, and a spin-orbit term (each of which can consist of a real and imaginary potential) and are generally parameterized as Woods-Saxons shapes or their derivatives. The volume term is given as

$$V(R) = -\frac{V}{1 + e^{(R-R_R)/a_R}}, \tag{2.2}$$

for the real part, and

$$W(R) = -\frac{W}{1 + e^{(R-R_w)/a_w}}, \tag{2.3}$$

for the imaginary part, both of which are parameterized by a depth V_i, radius $R_i = r_i A^{1/3}$ (where A is the mass number of the target), and diffuseness a_i. The geometries of these two terms tend to be similar, $r_i \sim 1.2$ fm and $a_i \sim 0.6$ fm. The real depths are typically around $40 - 50$ MeV, and the imaginary depths are closer to $10 - 20$ MeV for $E \sim 10 - 20$ MeV

(these are strongly energy dependent).

The surface potential is typically entirely imaginary and is parameterized as the derivative of a Woods-Saxon,

$$W_s(R) = -4a_s \frac{d}{dR} \frac{W_s}{1 + e^{(R-R_s)/a_s}}.$$
(2.4)

As the energy changes, there is an interplay between the two imaginary terms. In the energy range of $10 - 50$ MeV, as energy increases, the imaginary volume term becomes more important (and the surface absorption becomes less important).

Like the surface terms, the spin-orbit potential is generally parameterized as the derivative of a Woods-Saxon shape and typically only consists of a real part of the form

$$V_{so} = \left(\frac{\hbar}{m_\pi c} \right)^2 \frac{2\boldsymbol{L} \cdot \boldsymbol{s}}{R} \frac{d}{dR} \frac{V_{so}}{1 + e^{(R-R_{so})/a_{so}}},$$
(2.5)

where m_π is the pion mass. In this definition, the depth of V_{so} is between 5 and 8 MeV for nucleons.

For the scattering of two charged particles, a Coulomb term is included as well. Outside of the Coulomb radius $(R_C = r_C A^{1/3})$, the potential is defined as the simple point-Coulomb potential,

$$V_C(R) = \frac{Z_p Z_t e^2}{R}.$$
(2.6)

However, within the Coulomb radius, this term has to take into account the non-zero mean charge radius of the target. This is parameterized as

$$V_C(R) = \frac{Z_p Z_t e^2}{R_C} \left(\frac{3}{2} - \frac{R^2}{2R_C^2} \right).$$
(2.7)

In both equations, $Z_p e$ and $Z_t e$ are the charges of the projectile and target, respectively.

The phenomenological potentials of Eq. (2.1) are typically fit to elastic-scattering data to determine the parameters, either globally or locally. Global potentials, as discussed previously, are fit to a large variety of elastic-scattering data (spanning a few to a few hundred data sets across a range of masses and energies). These potentials tend to capture trends across the nuclear chart or within a broad mass and energy range. Optical potentials can also be constructed for a specific projectile-target combination. In our work, a global potential is used as the starting point for a fit to data of a given target-projectile combination at a specific energy, and the parameters are adjusted (through χ^2 minimization) such that the theoretical predictions for the cross sections better reproduce the experimental ones.

2.2 Two-body Scattering

We continue by considering two-body elastic and inelastic scattering. For the cases that are studied in this work, these two-body interactions describe a neutron, proton, or deuteron (treated as a single particle) impinged upon a heavier target. The target is treated as a single body with a total spin and parity, J^π, instead of as A individual nucleons. This simple case is instrumental to not only build upon when considering the three-body theories used in this work, but also to illustrate the complexity of passing information from the potential itself to the observable cross sections that can be compared directly to experiment.

2.2.1 Elastic Scattering

For the simplest case of elastic scattering, we begin with the projectile of mass m_p, charge Z_p, and mass number A_p impinging on a target of mass m_t, charge Z_t, and mass number
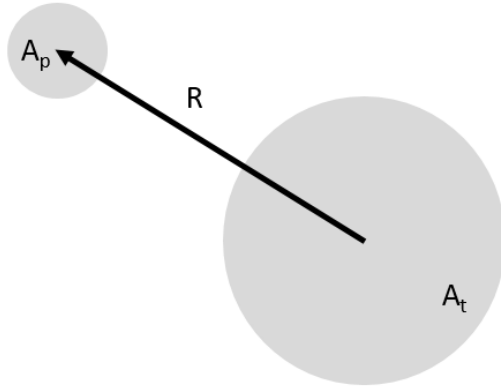
Figure 2.1: Two-body coordinate system.

A_t. The interaction between the pair is described by a spherical potential, as in the previous section, which only depends on the distance between the projectile and center of mass of the target, R, as shown in Figure 2.1. Fixing the projectile's momentum, $\vec{k}$, along the z-axis, the corresponding wave function should be cylindrically symmetric. After interacting with the potential, $U(R)$, the wave function of the system should have the asymptotic form,

$$\psi^{\text{asym}}(R,\theta) = e^{i[kz+\eta\ln k(R-z)]} + f(\theta)\frac{e^{i[kR-\eta\ln k2R]}}{R}, \tag{2.8}$$

where η is the dimensionless Sommerfeld parameter,

$$\eta = \frac{Z_p Z_t e^2}{\hbar}\left(\frac{\mu}{2E}\right)^{1/2}. \tag{2.9}$$

The asymptotic wave function of Eq. (2.8) is composed of the incoming plane wave plus an outgoing spherical wave that is modified by the interaction with the potential. The scope of this modification is captured in $f(\theta)$, the scattering amplitude, and is used to directly calculate the elastic-scattering cross section.

When both nuclear and Coulomb potentials are included, the scattering amplitude is com-

18

posed of a point-Coulomb amplitude and a Coulomb-distorted nuclear amplitude, $f(\theta) = f_c(\theta) + f_n^c(\theta)$ [83] (akin to the two potential formulation for the T-matrix). Because the Coulomb potential has infinite range, the point-Coulomb amplitude, $f_c(\theta)$, must be calculated explicitly. The Coulomb-distorted nuclear amplitude, $f_n(\theta)$, can be calculated through a partial-wave expansion.

The point-Coulomb scattering amplitude [83] (chapter 3) is

$$f_c(\theta) = -\frac{\eta}{2k\sin^2(\theta/2)}\exp[-i\eta\ln(\sin^2(\theta/2)) + 2i\sigma_0(\eta)], \qquad (2.10)$$

where $\sigma_0(\eta)$ is the Coulomb phase shift,

$$\sigma_L(\eta) = \arg\Gamma(1 + L + i\eta) \qquad (2.11)$$

for $L = 0$. The point-Coulomb cross section resulting from this is identical to the classical Rutherford cross section,

$$\left(\frac{d\sigma}{d\Omega}\right)_{\text{Ruth}} = \frac{\eta^2}{4k^2\sin^4(\theta/2)}. \qquad (2.12)$$

To then calculate $f_n(\theta)$, the asymptotic solution of Eq. (2.8) is matched with the solution of the time-independent Schrödinger equation (with center of mass motion removed),

$$[T + U(R) + V_C(R) - E]\psi(R, \theta) = 0 \qquad (2.13)$$

where the kinetic energy operator is defined in the typical way (for example [83]).

To solve, $\psi(R, \theta)$ is written using a partial-wave expansion with Legendre Polynomials,

$P_L(\cos\theta)$,

$$\psi(R, \theta) = \sum_{L=0}^{\infty} (2L + 1) i^L P_L(\cos\theta) \frac{1}{kR} \chi_L(R). \tag{2.14}$$

The Legendre Polynomials are eigenfunctions of $\vec{L}^2$ each with an eigenvalue of $L(L + 1)$. Thus, the radial equation for each L value,

$$\left[-\frac{\hbar^2}{2\mu} \left(\frac{d^2}{dR^2} - \frac{L(L + 1)}{R^2} \right) + V(R) + V_C(R) - E \right] \chi_L(R) = 0, \tag{2.15}$$

can be solved independently.

In practice, each of these equations can be solved through numerical integration by taking $\chi_L(R) = B_L u_L(R)$, and solving Eq. (2.15) for $u_L(R)$. This numerical solution then gets matched to the wave function outside of the range of the nuclear interaction,

$$\chi_L(R > R_{\text{int}}) \rightarrow A_L \left[H_L^-(\eta, kR) - S_L H_L^+(\eta, kR) \right], \tag{2.16}$$

where S_L is the S-matrix element for each L value, and $H_L^{\pm}(\eta, kR)$ are Hankel functions [84] which include the Coulomb effects through η. The S-matrix element can be calculated numerically through the R-matrix which equates the logarithmic derivatives of the interior and asymptotic wave functions at some point beyond the range of the nuclear interaction, a,

$$R_L = \frac{1}{a} \frac{\chi_L(a)}{\chi_L'(a)} = \frac{1}{a} \frac{u_L(a)}{u_L'(a)}. \tag{2.17}$$

The scattering amplitude can be written in terms of S_L by making use of the partial-wave expansion for e^{ikz} and e^{ikR} and matching these with the wave function of Eq. (2.8).

The Coulomb-distorted nuclear amplitude is then

$$f_n(\theta) = \frac{1}{2ik} \sum_{L=0}^{\infty} (2L+1) P_L(\cos\theta) \exp(2i\sigma_L(\eta))(S_L^n - 1), \tag{2.18}$$

and the resulting differential cross section is

$$\frac{d\sigma}{d\Omega} = |f_c(\theta) + f_n(\theta)|^2, \tag{2.19}$$

which is often calculated as a ratio to the Rutherford cross section of Eq. (2.12) since Eq. (2.19) goes to infinity at small angles for the scattering of two charged particles.

Equation (2.19) illustrates several difficulties in performing uncertainty quantification using these formulations. First, there is a clear but not trivial connection between the parameterization of the potential and the cross section, due to the non-linearity of the model. All of the information from the potential is contained in S_L, and it is not easy to write the potential or cross section as a polynomial expansion. Although we understand how individual parameters change the cross sections, it is not straightforward to know *a priori* the effect that combinations of parameters will have or if they will interfere with one another to negate changes. This has to be explored numerically. Second, the construction of the cross section using partial-wave decomposition, where all of the angular dependence is contained in the Legendre Polynomials, causes the fitting of the cross section at one angle to influence its value at all other angles. This introduces correlations within the model that are not necessarily taken into account when using a typical χ^2-based fitting method. (This will be discussed in more detail in Section 3.1.2.)

2.2.2 Inelastic Scattering

Not all excited states of a nucleus will have the same spin and parity as the ground state, and the central nuclear and Coulomb potentials that have been discussed so far are not able to change either the spin or parity. The simplest model that will cause an inelastic excitation of the target nucleus is a rotational model that deforms the surface of the target nucleus. In this work, we only consider coupling to the first excited state of the target nucleus which is taken to be caused by quadrupole or octupole deformations. The potentials described here are specific to those couplings.

To couple to a 2^+ excited state to a 0^+ ground state, for example, the potential can be expanded in spherical harmonics as

$$U(R, \hat{\xi}, \hat{\mathbf{R}}) = U_0(R) Y_0^0(\hat{\mathbf{R}}) + \beta_2 U_2(R) Y_2^0(\hat{\mathbf{R}}) Y_2^0(\hat{\xi}), \qquad (2.20)$$

where $\hat{\xi}$ is the internal coordinate of the target, $\hat{\mathbf{R}}$ are the angular coordinates of $\mathbf{R}$, and β_2 is the quadrupole deformation of the target. This inclusion of the spherical harmonics can change the state of the deformed nucleus. A similar expansion can be made using the octupole deformation, β_3 instead of the quadrupole deformation. For many cases, it is a reasonable approximation to only include the first excited state. For the sake of exploring techniques of uncertainty quantification in inelastic reactions, we want to keep the models simple and therefore will constrain our applications to the inclusion of only the first excited state. We understand, however, that the differences in theoretical and experimental cross sections can be due to neglecting these higher-lying states. Although interesting and important, here, we take a one-step approach for consistency with the other reaction formalisms presented. The analysis of the importance of including higher-lying states is beyond the scope of this work.

22

2.2.3 Coupled-Channel Equations

Let us consider the target's ground state to be 0^+ and it's first excited state to be 2^+. Because we are now coupling two channels together, the wave function can be written as a linear combination of the ground state and first excited state

$$\psi(R, \hat{\xi}) = \chi_0(R)\phi_0(\hat{\xi}) + \chi_2(R)\phi_2(\hat{\xi}), \tag{2.21}$$

where χ_i is the scattering wave function and ϕ_i is the wave function for the internal state of the system. The internal wave functions satisfy the eigenvalue equation

$$H_i(\xi)\phi_i(\xi) = \epsilon_i\phi_i(\xi), \tag{2.22}$$

with eigenenergies ϵ_i. In general, an arbitrary number of coupled channels can be solved through

$$[T_L(R) + U_{\alpha\alpha}(R) - E_{pt}]\chi_\alpha(R) + \sum_{\alpha' \neq \alpha} U_{\alpha\alpha'}\chi_{\alpha'}(R) = 0, \tag{2.23}$$

where E_{pt} is the reaction energy minus the excitation energies of the internal states, and the coupling potentials for the rotational bands are defined as

$$U_{ij}(R) = \langle Y_{L_i}^{M_i}(\hat{\mathbf{R}})\phi_i(\hat{\xi})|U(R, \hat{\xi}, \hat{\mathbf{R}})|Y_{L_j}^{M_j}(\hat{\mathbf{R}})\phi_j(\hat{\xi})\rangle. \tag{2.24}$$

The simplest method to solve Eq. (2.23) is through direct numerical integration. However, for many cases, especially when the centrifugal barrier is large, this can lead to significant numerical instabilities, so alternative methods - often using basis expansions - have been developed to provide greater stability. A discussion of each of these methods is outside

of the scope of this work, but details can be found in [85, 86, 87, 88, 89, 90, 91, 92].

Because we only couple to the first excited state, we have two coupled equations from Eq. (2.23):

$$[T_L(R)U_{00}(R) - E_{pt}]\chi_0(R) + U_{02}(R)\chi_2(R) = 0, \tag{2.25}$$

and

$$[T_L(R) + U_{22}(R) - E_{pt}]\chi_2(R) + U_{20}(R)\chi_0(R) = 0. \tag{2.26}$$

Together, these include full couplings between the elastic and inelastic channels. Often, an approximation is made where the inelastic channel includes couplings from the elastic but the elastic channel does not include couplings from the inelastic channel; this is the one-step distorted-wave Born approximation. This amounts to first removing the coupling potential from Eq. (2.25) to solve

$$[T_L(R) + U_{00}(R) - E]\chi_0(R) = 0, \tag{2.27}$$

and then using this wave function to calculate $\chi_2(R)$ from Eq. (2.26).

2.3 Three-body Scattering

Often, reactions have other degrees of freedom that are not well described in a simple two-body approach. This is especially true if the mass partitions are rearranged, as in transfer reactions. For example, in a transfer reaction $A(d,p)B$, a valence neutron, n, is transferred from d ($d = n + p$) onto A forming B ($B = A + n$) as shown in the Figure 2.2. Here, it is useful to calculate the cross section in terms of the T-matrix. For a three-body system such as this, the T-matrix can be written exactly, using either the coordinates of the initial system (prior form) or the coordinates of the final system (post form). In the post form, the
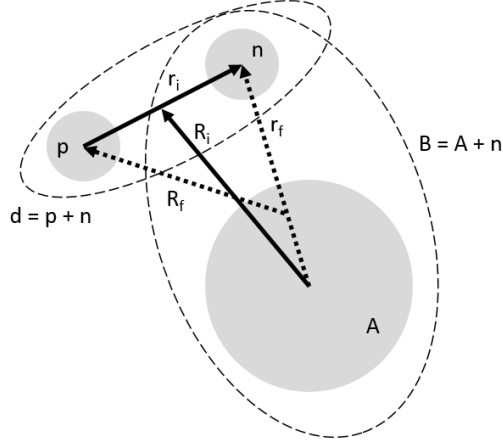
Figure 2.2: Coordinate system for a three-body problem. The solid lines show incoming coordinates, and the dashed lines show the outgoing coordinates.

T-matrix is written as

$$\boldsymbol{T}_{\text{post}}^{\text{exact}} = \langle \Phi_{I_A I_B}(\vec{r}_f) \chi_f^-(\vec{R}_f) | V_{np} + V_{nA} - U_f | \Psi^{\text{exact}} \rangle. \tag{2.28}$$

Here, Ψ^{exact} is the exact three-body wave function, each V_{jk} is the interaction between bodies j and k, and U_f is the optical potential between B and the scattered proton that gives rise to the corresponding distorted wave, χ_f. Typically the post form is used because, in this coordinate system, the remnant term, $V_{nA} - U_f$, is small due to the scaling of the optical potentials. For a single nucleon transfer reaction, the two potentials in the remnant differ by one nucleon. In such cases V_{NA} is roughly $A/(A+1)U_{N(A+1)}$, so for all but light targets, the remnant term can be neglected.

The exact three-body wave function is defined by the solution of

$$[T_R + H_{\text{int}}(\vec{r}) + V_{pA} + V_{nA} - E]\Psi^{\text{exact}}(\vec{r}, \vec{R}) = 0, \tag{2.29}$$

where the internal Hamiltonian is defined for the projectile as $H_{\mathrm{int}} = T_r + V_{np}(r)$. Beyond

the range of the nuclear interaction, the radial part of Ψ^{exact} for each partial wave behaves

like

$$\psi(R) \to \delta_{\alpha\alpha_i} F_{L_i}(\eta_L, kR) + \mathbf{T}_{\alpha\alpha_i} H_L^+(\eta_L, kR), \tag{2.30}$$

where α denotes a set of quantum numbers (with α_i for the incoming channel) and F_L is

the regular Coulomb function [84]. Often, Ψ^{exact} is obtained by making approximations

to the exact three-body problem in order to formulate a more tractable problem, one that

is significantly less computationally expensive than solving for the full three-body wave

function. Having a simplified model is particularly important for our initial investigation into

parametric uncertainties. As will be discussed in Chapter 3, the uncertainty quantification

methods that we use rely on running hundreds or thousands of calculations for a single

reaction, adding another three orders of magnitude to the computation time. Therefore, it

is essential that the reaction models we implement are efficient. Two of these three-body

approximations are discussed below.

2.3.1 Distorted-Wave Born Approximation

The distorted-wave Born approximation (DWBA) simplifies the exact three-body wave func-

tion to the elastic channel, namely a distorted wave, $\chi_i(\vec{R}_i)$, multiplied by the corresponding

bound state, $\Phi_d(\vec{r}_i)$. Neglecting the remnant, as we will do for the rest of this work, the

T-matrix then becomes

$$T_{fi}^{DWBA} = \langle \Phi_{I_A I_B}(\vec{r}_f) \chi_f^-(\vec{R}_f) | V_{np} | \Phi_d(\vec{r}_i) \chi_i(\vec{R}_i) \rangle. \tag{2.31}$$

However, the projectile can break-up within the field of the target before the valence nucleon is transfered to the target. Because of the deuteron's small binding energy, this is particularly important for deuteron-induced reactions. Several studies have shown (e.g. [93]) that taking into account the break-up of the deuteron is critical for reproducing experimental results. Using the adiabatic wave approximation (ADWA), we can make an approximation for the three-body scattering wave function that takes into account break-up of the incoming deuteron.

2.3.2   Adiabatic Wave Approximation

Adiabatic approximations rely on the separation of fast and slow variables, where the slow variable can be assumed to not change over the course of the reaction. One such separation is in the sudden approximation where the internal motion of the projectile is considered slow compared to the motion of the center of mass of the projectile-target system. The internal energy spectrum associated with the projectile should be much lower than the beam energy, and because of this, the excitations of the projectile can be taken to be (practically) degenerate with its ground state.

Considering the post form of the T-matrix from Eq. (2.28), V_{np} is the dominating interaction (since, again, the remnant term is small), and therefore, the three-body wave function is only needed in the region of V_{np} [69]. The wave function can then be expanded in terms of Weinberg states, $\phi_i(\vec{r})$ which describe the relative motion within the projectile, and χ_i, the relative motion between the projectile and target,

$$\Psi^{\text{exact}} \approx \Psi^{\text{ad}} = \sum_{i=0}^{\infty} \phi_i(\vec{r})\chi_i(\vec{R}).$$

(2.32)

Weinberg states [94] are defined by

$$(T + \lambda_i V_{np} - \epsilon_d)\phi_i = 0, \tag{2.33}$$

and are only complete within the range of the deuteron interaction. These states are normalized as

$$\int \phi_i V_{np}\phi_j dr = \delta_{ij}. \tag{2.34}$$

In ADWA [69], we retain only the first Weinberg state so that

$$\Psi^{ad} \approx \phi_0(\vec{r})\chi_0(\vec{R}), \tag{2.35}$$

which has been shown to be a good approximation [95]. Here, the first Weinberg state, ϕ_0, is an eigenfunction of the internal Hamiltonian for the deuteron with eigenenergy, $-\epsilon_d$, the deuteron binding energy.

The three-body problem of Eq. (2.29) then becomes

$$[T_R - (E + \epsilon_d)]\phi_0(\vec{r})\chi_0(\vec{R}) = -(U_{pA} + U_{nA})\phi_0(\vec{r})\chi_0(\vec{R}), \tag{2.36}$$

and can be solved through direct integration methods, as

$$[T_R - (E + \epsilon_d)]\chi_0(\vec{R}) = -\langle\phi_0|V_{np}(U_{pA} + U_{nA})|\phi_0\rangle\chi_0(\vec{R}). \tag{2.37}$$

Because the Weinberg states are only complete in the range of V_{np}, the asymptotics of the resulting χ_0 no longer describe the projectile-target elastic scattering. At short distances, this method produces a distorted wave that takes into account the breakup of the projectile

to all orders. The resulting T-matrix is then

$$T_{\mathrm{fi}}^{\mathrm{ADWA}} = \langle \Phi_{I_A I_B}(\vec{r}_f) \chi_f^-(\vec{R}_f) | V_{np} | \Psi^{ad} \rangle. \tag{2.38}$$

2.3.3 Transfer Observables

Once the three-body T-matrix has been calculated under either approximation (DWBA or ADWA), the differential cross section for the transfer reaction can be computed

$$\frac{d\sigma}{d\Omega} = \frac{1}{(2I_{p_i}+1)(2I_{t_i}+1)} \sum_{\mu_p \mu_t \mu_{p_i} \mu_{t_i}} \left| f_{\mu_p \mu_t \mu_{p_i} \mu_{t_i}}^{xpt}(\theta) \right|^2 \tag{2.39}$$

where $f_{\mu_p \mu_t \mu_{p_i} \mu_{t_i}}^{xpt}(\theta)$ is proportional to the three-body T-matrix and I_i is the internal spin of the target or projectile (with $I_{p_i} = I_d = 1$). By using the appropriate nucleon-target interactions for the distorted waves, this process can be followed for either single-neutron or single-proton transfer reactions - (d,p) and (d,n) - which are the cases that we are interested in for this work.

A spectroscopic factor, S, can then be extracted from the transfer angular distributions. This quantity, which is the probability that a composite nucleus in B behaves like a valence nucleon sitting on top of a core, A, in a certain configuration, can be extracted experimentally and calculated theoretically. Under the single-particle approximation, the experimental spectroscopic factor is extracted by comparing the measured and calculated cross sections at the first peak,

$$\left(\frac{d\sigma}{d\Omega} \right)_{\mathrm{exp}} = S^{\mathrm{exp}} \left(\frac{d\sigma}{d\Omega} \right)_{\mathrm{th}}. \tag{2.40}$$

The value of $(d\sigma/d\Omega)_{\mathrm{th}}$ depends on the reaction formalism used to calculate the theoretical

cross section (such as DWBA and ADWA as just discussed), and is therefore model depen-

dent. The theoretical spectroscopic factor is the norm the overlap of the wave function of

the core (A) and core plus valence nucleon $(B = A + 1)$,

$$S^{\text{th}} = |\langle \Psi_B(r_1, ..., r_A, r_B) | \Psi_A(r_1, ..., r_A) \rangle|^2 \,, \tag{2.41}$$

and is also model dependent. Because S^{exp} and S^{th} are model dependent, it is important

that the theory going into the calculation of the cross section is consistent with the Sth of

Eq. (2.41) to be able to make meaningful comparisons.

Chapter 3

Implementation of Uncertainty Quantification

As an initial exploration into uncertainty quantification for reaction theory, we begin with simple reaction models (as described in Chapter 2) and only study the effect that changing the optical model parameters has on the resulting cross sections. Typically, to constrain optical model parameters, elastic-scattering data are fit, and then this best-fit parameterization is used to calculate elastic, inelastic, and transfer cross sections. However, the potentials constrained in this manner are not unique, and slight changes in the optical model parameters can lead to significant changes in the predicted (inelastic or transfer) cross sections, as well as in other observables.

3.1 Non-linear Regression Methods

The purpose of the frequentist method used here is to identify a minimum in the parameter space and characterize the region around it. Unless we were to systematically search the entire multi-dimensional parameter space (given a set of physically defined boundaries), it is impossible to know whether this minimum is the global minimum or merely one of many local minima. Therefore, we can only discuss properties of a single minimum then compare various minima for the same reaction to ensure that any conclusions that we draw hold

regardless of the parameterization. This is described in the following sections, using both uncorrelated and correlated χ^2 minimization procedures.

3.1.1 Uncorrelated χ^2 Fitting

The goal of χ^2 fitting is to describe a true function, $\sigma(\theta)$, with a known model, $\sigma^{\text{th}}(\mathbf{x}, \theta)$. The true function describes nature, and the model is our representation of these resulting phenomena. Throughout the course of this work, this model predicts the differential cross section as a function of angle, θ, and is parameterized by M free parameters, $\mathbf{x} = (x_1, ..., x_M)$, which are the parameters of the optical model. The model aims to describe N pairs of data, $\{(\theta_1, \sigma_1^{\text{exp}}), ..., (\theta_N, \sigma_N^{\text{exp}})\}$, where each pair has an associated experimental error, $\Delta\sigma_i$. We assume that the measurements and associated errors are independent of one another such that each data point can be described as,

$$\sigma_i^{\text{exp}} = \sigma(\theta_i) + \epsilon_i, \tag{3.1}$$

with

$$\epsilon_i \sim \mathcal{N}(0, (\Delta\sigma_i)^2). \tag{3.2}$$

Here $\mathcal{N}$ is the normal distribution with mean 0 and stand deviation $\Delta\sigma_i$. To describe all of the experimental data simultaneously, Eq. (3.1) can be written in matrix form,

$$\sigma^{\text{exp}} \sim \mathcal{N}(\sigma, \Sigma), \tag{3.3}$$

where Σ is an $N \times N$ diagonal matrix with $(\Delta\sigma_i)^2$ on the diagonals. The experimental cross sections are ideally described by the true function while allowing for a normally distributed

offset for each data point.

Because the theory model, $\sigma^{\text{th}}(\boldsymbol{x}, \theta)$, is our description of the true function, we assume that the residuals, the difference between the experimental data and the model evaluation at a given angle, are also normally distributed,

$$[\sigma_1^{\text{exp}} - \sigma^{\text{th}}(\theta_1, \mathbf{x}), ..., \sigma_N^{\text{exp}} - \sigma^{\text{th}}(\theta_N, \mathbf{x})] \sim \mathcal{N}(0, \Sigma). \tag{3.4}$$

To find the set of parameters that allows the model to best describe the data, we maximize the associated likelihood of $\mathbf{x}$, where the likelihood, $l(\mathbf{x}, \theta, \sigma^{\text{exp}})$ is proportional to the exponentiated χ^2. Maximizing the likelihood corresponds to minimizing the uncorrelated χ^2 function,

$$\chi^2_{UC} = \sum_{i=1}^{N} \left(\frac{\sigma_i^{\text{exp}} - \sigma^{\text{th}}(\theta_i, \mathbf{x})}{\Delta \sigma_i} \right)^2. \tag{3.5}$$

This function is proportional to the standard definition of χ^2, and minimizing it gives us the best-fit parameter set, $\hat{\mathbf{x}}$. The process of minimizing the residuals ensures that equal numbers of experimental cross sections are distributed above and below the theoretical calculation, with most of the data lying closest to the calculation and fewer data farther away.

To construct confidence bands around the differential cross sections, we define a parameter-space distribution around $\hat{\mathbf{x}}$ that describes the local minimum. Although $\hat{\mathbf{x}}$ contains the best-fit parameters for this system, these are not the parameters of the true function that exactly reproduce the data. The true parameters should be distributed around the best-fit parameters. A Gaussian distribution assumes the least amount of information about the parameter distribution. We therefore assume that the true parameter values are normally distributed

around the best-fit parameters, described by the multivariate Gaussian distribution,

$$\mathcal{N}(\hat{\mathbf{x}}, \mathbb{C}_p) \sim \exp[-\frac{1}{2}(\mathbf{x} - \hat{\mathbf{x}})^T \mathbb{C}_p^{-1}(\mathbf{x} - \hat{\mathbf{x}})]. \tag{3.6}$$

$\mathbb{C}_p$ is the $M \times M$ parameter covariance matrix (see Section 3.1.3), which gives a non-normalized description of the correlations between the various parameters within the model. Two-dimensional slices of parameter space, as a function of χ^2_{UC}, can be used to justify the assumption of a normally distributed parameter space [96]. (Non-normal distributions are discussed in Section 3.1.4.) To include the goodness-of-fit in the parameter distribution Eq. (3.6), the parameter covariance matrix is scaled by

$$s^2 = \frac{\chi^2_{UC}}{N - M}, \tag{3.7}$$

such that $\mathbb{C}_p \to s^2 \mathbb{C}_p$. As the χ^2 value increases, the covariance matrix will be stretched and a wider range of parameters will be drawn, increasing the size of the confidence bands; the confidence bands should scale with χ^2. From this scaled distribution, 200 sets of parameters are sampled and then run through the model, $\sigma^{\text{th}}(\mathbf{x}, \theta)$. This leads to 200 differential cross section calculations around the best-fit calculation. At each angle where the model was evaluated, the highest 2.5% and lowest 2.5% of the calculations are removed. The remaining calculations form 95% confidence bands around the result of the best-fit parameterization.

To have a quantity with which to compare confidence bands for different systems, we define the average width of the band,

$$\overline{W}_{UC} = \frac{1}{K_\theta} \sum_{i=1}^{K_\theta} (\sigma_i^{\text{max}} - \sigma_i^{\text{min}}), \tag{3.8}$$

where $\sigma_i^{\max}$ ($\sigma_i^{\min}$) is the maximum (minimum) theoretically calculated cross-section value of the 95% confidence band at a given angle, θ_i, and K_θ is the number of angles at which cross sections were calculated.

3.1.2 Correlated χ^2 Fitting

Correlations within the theoretical model can have an effect on the parameterizations found through χ^2 minimization, but they are not taken into account in χ^2_{UC} as defined in Eq. (3.5). These correlations can be observed through the ϵ_i values which are not independent of one another. Recall, also, single-channel elastic scattering (e.g. Eq. (2.18)): due to the addition of the Legendre polynomials, fitting to data at a single angle is enough to constrain the remaining angles which gives rise to strong correlations between angles. This can be taken into account in the formulation of the χ^2 function.

These model correlations can be taken into account by defining a model covariance matrix, $\mathbb{C}_m$, which describes the correlations between pairs of angles within the model. This is discussed in more detail in Section 3.1.3.

To then modify the χ^2 function, we make the assumption that the model is normally distributed around the true function, σ,

$$[\sigma^{\text{th}}(\mathbf{x}, \theta_1), ..., \sigma^{\text{th}}(\mathbf{x}, \theta_N)] \sim \mathcal{N}(\sigma, \mathbb{C}_m). \tag{3.9}$$

Calculating the residuals with this new distribution, they become distributed as,

$$[\sigma_1^{\text{exp}} - \sigma^{\text{th}}(\theta_1, \mathbf{x}), ..., \sigma_N^{\text{exp}} - \sigma^{\text{th}}(\theta_N, \mathbf{x})] \sim \mathcal{N}(0, \Sigma + \mathbb{C}_m), \tag{3.10}$$

where now the residuals are distributed normally around zero, with a covariance matrix that is the sum of the errors on the data and the model covariance matrix. The resulting correlated χ^2 minimization objective function becomes

$$\chi^2_C = \sum_{i=1}^{N}\sum_{j=1}^{N} \mathbb{W}_{ij}(\sigma_i^{\text{exp}} - \sigma^{\text{th}}(\mathbf{x}, \theta_i))(\sigma_j^{\text{exp}} - \sigma^{\text{th}}(\mathbf{x}, \theta_j)), \tag{3.11}$$

where $\mathbb{W}_{ij}$ is the $(ij)^{\text{th}}$ elements of the matrix $\mathbb{W} = (\Sigma + \mathbb{C}_m)^{-1}$. This takes into account correlations between the residuals at different angles through the model covariance matrix. Eq. (3.11) reduces to Eq. (3.5) when $\mathbb{C}_m = 0$ as $\mathbb{W} = \Sigma^{-1}$, with diagonal elements of $\frac{1}{(\Delta\sigma_i)^2}$.

Typically, $\chi^2_{UC}/N \approx 1$ is the definition of a statistically good fit, however, that is not necessarily true for the correlated case. The model covariance matrix is not normalized, and its elements are often larger than the errors on the experimental cross sections. This leads to χ^2_C generally being smaller than χ^2_{UC}, even when the same reactions are studied from identical starting optical model potentials.

Ninety-five percent confidence bands for the correlated fitting function are defined in the same way as for the uncorrelated case, substituting χ^2_{UC} by χ^2_C. We can also again define the average width of the confidence band as

$$\overline{W}_C = \frac{1}{K_\theta}\sum_{i=1}^{K_\theta}(\sigma_i^{\text{max}} - \sigma_i^{\text{min}}). \tag{3.12}$$

Again, K_θ is the number of angles at which the cross section calculations were performed, and σ_i^{max} (σ_i^{min}) are the maximum (minimum) cross section values for the correlated 95% confidence bands at θ_i.

3.1.3 Covariance and Correlation Matrices

There are several matrices that need to be defined, either for the χ^2 analysis of the previous section or for the analysis of the results from this minimization process. First, the parameter covariance matrix is defined as

$$\mathbb{C}_p = \left(\mathbb{J}^T \mathbb{J} \right)^{-1},$$
(3.13)

where, $\mathbb{J}$, the Jacobian, is calculated through its matrix elements as

$$\mathbb{J}_{ij} = \left. \frac{\partial \sigma^{\text{th}}(\mathbf{x}, \theta_i)}{\partial x_j} \right|_{\mathbf{x} = \hat{\mathbf{x}}}.$$
(3.14)

In practice, this derivative is taken numerically using a three-point formula (the symmetric difference quotient), since it would be impossible to analytically take the derivative of the cross section with respect to the optical potential parameters.

The parameter correlation matrix, $\mathbb{C}_{\text{corr}}$, is defined by a transformation of the parameter covariance matrix,

$$\mathbb{C}_{\text{corr}} = \mathbb{A}^T \mathbb{C}_p \mathbb{A}.$$
(3.15)

The matrix elements of $\mathbb{A}$ are given as

$$\mathbb{A}_{ij} = \begin{cases} \dfrac{1}{\sqrt{(\mathbb{C}_p)_{ij}}}, & \text{if } i = j \\[2ex] 0, & \text{if } i \neq j \end{cases}$$
(3.16)

by definition. $\mathbb{A}$ is a diagonal matrix that transforms the covariance matrix into one which has $(\mathbb{C}_{\text{corr}})_{ii} = 1$ (for the diagonal elements) and $(\mathbb{C}_{\text{corr}})_{ij} \in [-1, 1]$ (on the off-diagonal). A matrix element of zero for $(\mathbb{C}_{\text{corr}})_{ij}$ indicates that parameters x_i and x_j are not at all

correlated, where an element of one (negative one) indicates that the two parameters are fully correlated (anti-correlated) [96]. The ones along the diagonal show that, as expected, every parameter is fully correlated with itself.

The model covariance matrix, $\mathbb{C}_m$, is defined slightly differently. Because we are interested in the correlations within the model, not dependent on a specific minimum, we instead sample the parameter space, constrained by the physical bounds on the parameters, and define the elements of the covariance matrix as

$$(\mathbb{C}_m)_{ij} = \frac{1}{K_M} \sum_{k=1}^{K_M} (\sigma_i^k - \bar{\sigma}_i)(\sigma_j^k - \bar{\sigma}_j), \qquad (3.17)$$

where K_M is the total number of parameter sets sampled and $\bar{\sigma}_i$ is the average value of the differential cross section at θ_i. These cross section values are calculated for each of the angles at which the experimental data was taken so that the resulting model covariance matrix has dimensions $N \times N$.

3.1.4 Non-Gaussian Parameter Space

The assumption that the parameter space is described by a Gaussian distribution as in Eq. (3.6) does not have to hold in each case. Instead, parameter sets around the best fit can be sampled from the exact χ^2 distribution. In this case, $\chi^2(\mathbf{x})$ for each parameter set is tested against the inequality,

$$\chi^2(\mathbf{x}) - \chi^2(\hat{\mathbf{x}}) \leq 9N. \qquad (3.18)$$

The parameter sets that fulfill this inequality are within three standard deviations of the minimum.

To understand this, we consider that around a minimum, the χ^2/N distribution can be expanded as in a Taylor series

$$\chi^2(\mathbf{x})/N \approx \chi^2(\hat{\mathbf{x}})/N + \mathbb{J}(\mathbf{x} - \hat{\mathbf{x}})/N + \frac{1}{2N}(\mathbf{x} - \hat{\mathbf{x}})^T\mathbb{H}(\mathbf{x} - \hat{\mathbf{x}}), \qquad (3.19)$$

where $\mathbb{J}$ is the Jacobian - the matrix of first derivatives of the χ^2 function with respect to each of the parameters - and $\mathbb{H}$ is the Hessian - the matrix of second derivatives of the χ^2 function with respect to the parameters. Since this expansion is around a minimum, the Jacobian is zero, leaving only the χ^2 value at the best fit set of parameters and the Hessian term. The Hessian can be approximated as $2(\mathbb{J}^T\mathbb{J})$ which we can identify as $2(\mathbb{C}_p)^{-1}$ from Eq. (3.13).

Under the assumption that the best fit parameters are described by a Gaussian, as in Eq. (3.6), the parameters are within three standard deviations of the best fit parameter values when

$$(\mathbf{x} - \hat{\mathbf{x}})^T\mathbb{C}_p(\mathbf{x} - \hat{\mathbf{x}}) = 9. \qquad (3.20)$$

(The factor of 9 is easily seen if we consider a one-dimensional Gaussian distribution $\sim \exp[-(x - \hat{x})^2/(2\Delta^2)]$ and take $x = \hat{x} \pm 3\Delta$. This leaves us with a Gaussian distribution $\sim \exp[-9/2]$, hence the factor of 9.) Substituting the Hessian for the parameter correlation matrix from Eq. (3.19), we find

$$\chi^2(\mathbf{x})/N \approx \chi^2(\hat{\mathbf{x}})/N + 9. \qquad (3.21)$$

Thus, for a parameter set to fall within three standard deviations of the best-fit parameter set, we are back at the condition of Eq. (3.18).

Once 200 parameter sets are drawn that fulfill this inequality, they are run through the reaction model. The area within three standard deviations of the center of a Gaussian distribution contains 99.7% of the area of the Gaussian. Therefore, to define a 95% confidence band, instead of removing the highest 2.5% and lowest 2.5% of the cross section calculations, we remove the highest 2.35% and lowest 2.35%. This trims each 99.7% band to a 95% confidence band.

3.2 Bayesian Methods

The analysis described in Section 3.1 is one method to explore the properties of a specific minimum in parameter space. Oftentimes though, we would like to know properties of the model space constrained by physical limits or other prior knowledge. Bayesian statistics can be used to this purpose and provide an alternate interpretation of the uncertainties. Frequentist statistics treat the model's free parameters as fixed and the resulting observations as having an uncertainty associated with them (given the parameters, what should the data tell us - i.e. a 95% confidence band tells us that 95% of the measurements, were the experiment to be repeated over and over, will fall within that band). On the other hand, Bayesian statistics takes the opposite approach (given the data, what is known about the parameter space). Using Bayesian statistics, as probability is defined as the degree of belief about a given hypothesis which allows probabilities to be defined, not only, for infinitely repeatable events but also for situations that only occur once. The formulation allows for physical insight and prior information to be explicitly included in the uncertainty model; the results can then be explored given this information. It also allows us to ask the question: how dependent are our results on the assumptions that are incorporated into our

model? Further, there is a straightforward way to directly compare different models within a rigorous framework, and although that topic is beyond the scope of this work, this type of formulation will be important to quantify the more complex uncertainties introduced by model simplification (or the formulation of the model) [97].

3.2.1   Bayes' Theorem

Ultimately, Bayes' Theorem is a result of basic rules of probability, specifically that if one were to pull two items from a bag - without replacing them - the probability of drawing a given pair of items does not depend on which item was drawn first (see box below).

Take the example of a bag with six green marbles and four white marbles. The probability that (i) a green marble is drawn first then a white marble is drawn is the same as if (ii) a white marble is drawn first then a green marble. This is because for (i)

$$p(green, white) = p(green) \times p(white|green) = \frac{6}{10} \times \frac{4}{10}, \tag{3.22}$$

and for (ii)

$$p(white, green) = p(white) \times p(green|white) = \frac{4}{10} \times \frac{6}{10}. \tag{3.23}$$

Therefore,

$$p(green) \times p(white|green) = p(white) \times p(green|white). \tag{3.24}$$

Clearly, the two probabilities are identical. This works both with and without replacing the first marble before drawing the second.

Independent drawing probabilities.

Bayes' Theorem is given by

$$p(H|D) = \frac{p(H)p(D|H)}{p(D)}, \tag{3.25}$$

which corresponds to making the substitutions $green \rightarrow D$ and $white \rightarrow H$. In Eq. (3.25), $p(H|D)$ is the posterior - the quantity of interest - which gives the distribution of the parameter space (H, hypothesis) updated by the data - D, $p(H)$ is the prior which summarizes

what is predicted for (or known about) the parameter space without knowledge of the data, $p(D|H)$ is the likelihood which contains information about how well the given parameter set describes the data (typically containing some sort of χ^2 factor), and $p(D)$ is the Bayesian evidence (or marginal likelihood) [98].

The prior reflects the knowledge that one has about the system before seeing the data; this can be motivated by previous experimental results, intuition, or physical constraints. Since the priors reflect probability, they should be "proper" - normalizable [99]. Contrary to some thought (as discussed in [99]), this does allow for flat or constant priors over a given variable, as long as the prior is defined over a fixed range. Other common distributions are multi-dimensional Gaussian distributions, log-normal distributions, and Jeffreys' prior (which is a constant distribution over the logarithm of a variable) [99].

The resulting posterior can either be driven by the prior or by the likelihood. As one would imagine, for results to be independent of the prior, the posterior must be likelihood-driven. This is true when the likelihood function is more sharply peaked than the prior - which is a result of having well-determined data. For example, consider the case of a Gaussian prior with mean μ and variance Σ^2,

$$p(H) = H_o e^{-(\theta-\mu)^2/2\Sigma^2}, \tag{3.26}$$

and a Gaussian likelihood with mean m and variance σ^2,

$$p(H|D) = L_o e^{-(\theta-m)^2/2\sigma^2}. \tag{3.27}$$

The posterior distribution is found to be proportional to

$$p(D|H) \propto e^{-(\theta-m)^2/2\sigma^2} e^{-(\theta-\mu)^2/2\Sigma^2}, \tag{3.28}$$

which is just a third Gaussian with mean

$$\bar{\mu} = \frac{m + (\sigma/\Sigma)^2 \mu}{1 + (\sigma/\Sigma)^2}, \tag{3.29}$$

and variance

$$\tau^2 = \frac{\sigma^2}{1 + (\sigma/\Sigma)^2}. \tag{3.30}$$

The ratio σ/Σ can be used to gain information as to whether the resulting posterior is data-driven or prior-driven. When $\sigma/\Sigma \ll 1$, the likelihood mean is smaller than that of the prior and the posterior is essentially the likelihood - the posterior results are driven by the data. For cases where this inequality is not as strongly satisfied, it could indicate that the collection of more data would better constrain the model. Therefore, there is a limit in the precision of the posterior based on the precision of the data and the assumptions made in the prior. In principle, the effect of the prior can be entirely removed, either by having well-constrained data (small σ) or a large variety of data. Although these results were obtained from a simplified example, they hold generally for more complicated prior and likelihood distributions.

Even if the effect of the prior choice cannot be completely removed, this can also give information about the constraining power of the data at hand. If different priors lead to different posteriors, the data is not able to discriminate between the priors, which is a result within itself. In this case, either the various assumptions that have been made are equally

valid (or do not matter), or the available data does not have enough resolving power (it should be measured with better precision or different data is needed to draw a conclusion).

The likelihood contains information about how well the model reproduces the data. Often, this is encoded in an exponentiated χ^2 function, such as

$$p(D|H) \propto e^{-\chi^2/2}, \tag{3.31}$$

where the χ^2 function can be defined in several different ways (two examples are given in Equations (3.5) and (3.11)). When performing parameter estimations, the χ^2 function is the direct comparison between the experimental data and the theoretical calculations that are performed with a given set of parameters. Minimizing the χ^2 is equivalent to maximizing the likelihood, and in Bayesian statistics, it is the combination of likelihood and prior distributions that matters. Again, if the likelihood is sharply peaked, the data are informative enough to render the specific choice of prior inconsequential.

Finally, the evidence is defined as

$$p(D) = \sum_H p(D|H)p(H), \tag{3.32}$$

which is the likelihood given a certain hypothesis (model or parameter set) weighted by a prior for that hypothesis. Because the evidence requires a sum over all possible hypotheses, there are very few cases where $p(D)$ is known or can be expressed in closed form. Therefore, the posterior becomes a function that is extremely difficult (or impossible) to calculate explicitly. Monte Carlo methods are then the techniques that are often used to estimate the shape of the posterior when exploring uncertainties due to the parameterization of the model.

For an infinitely long - and computationally impractical - Monte Carlo chain, the shape of the posterior would be identical to the exact function $p(H|D)$; for practical purposes, it is enough to collect sufficient statistics.

3.2.2   Markov Chain Monte Carlo

Markov Chain Monte Carlo (MCMC) methods are a general class of statistical methods that can be used for sampling distributions, such as the Bayesian posterior distribution, for numerically computing integrals and for optimization problems [100]. Although discussing the full theory behind these methods is beyond the scope of this work, we give a brief outline here. Each MCMC is defined by a Markov chain, a sequence of random variables $\{Y^1, Y^2, Y^3...\}$, where successive quantities are defined probabilistically based on the value of the previous set (Y^i depends on the value of Y^{i-1}, typically through a probability distribution centered on the ith value). The important property of these chains is that they tend toward and converge to an equilibrium state (which is the solution of interest). That is, this limiting distribution does not change as successive quantities are added, which means that the quantity Y^{i+1} will be sampled from the desired distribution [101] (Chapter 4).

These methods are useful for the Bayesian approach as the joint distribution of the prior and likelihood can often be numerically computed, but the normalization of the posterior is not known. This normalization depends heavily on the Bayesian evidence, which is often challenging or impossible to compute. However, unless model comparisons are being performed, this is just a normalization factor which does not change the shape of the posterior distribution. Thus, Monte Carlo methods allow for the sampling of the shape of the posterior distribution without bothering with the overall normalization.

The Bayesian evidence is not needed in these computations due to the nature of the

Monte Carlo algorithms. Since each new iteration of the chain is dependent on the previous one and the evidence is a constant for all occurrences, the ratio that compares the ith and $(i+1)^{th}$ draws will be independent of its value - this leads to drawing from a distribution proportional to the true posterior. There are several different algorithms to construct a Markov chain, including Gibbs sampling, the Metropolis-Hastings algorithm, and the slice sampler. This work uses the Metropolis-Hastings algorithm which will be discussed below, but more details about all of these methods can be found in [100].

Nicholas Metropolis and collaborators proposed a prescription to compute properties of interacting molecules using a Markov chain [102]. They proposed new configurations for the group of molecules by allowing each one to randomly move within a predefined square with periodic boundary conditions, and then accepted the proposed move if either the new configuration had a lower energy or with probability $\exp(-\Delta E/kT)$ if the energy increased. Wilfred Keith Hastings added a new element to this sampling by proposing that the jump would be accepted with a probability given by a random number in the interval zero to one for each new iteration of the chain [103]. It is this version of the algorithm, now called the Metropolis-Hastings algorithm, that is implemented in this work.

For the Bayesian methods, specifically considering the case of sampling model parameters, the algorithm works in the following way. An initial parameter set, $\mathbf{x}_i$, is chosen and the prior and likelihood are evaluated for that set, $p(H_i)p(D|H_i)$. A second parameter set is chosen based on the first, $\mathbf{x}_f = \mathbf{x}_i + \mathbf{x}'$, where $\mathbf{x}'$ is a vector of numbers sampled from a Gaussian distribution $\mathcal{N}(0, \epsilon\mathbf{x}_0)$, with x_0 the starting optical potential parameter for each variable. The prior and likelihood are again calculated for that set, $p(H_f)p(D|H_f)$. The two

are compared, and if the new parameter set fulfills the condition

$$R < \frac{p(H_f)p(D|H_f)}{p(H_i)p(D|H_i)}, \tag{3.33}$$

where $R \in [0, 1]$ is a uniformly sampled random number, then the new parameter set becomes the initial parameter set. Otherwise, the set is rejected, the initial set remains the same, and a new parameter set is chosen, in the same way as $\mathbf{x}_f$. This process is repeated until a predefined number of parameter sets have been accepted. The dependence on the random number, R, is important for sampling the distribution. If we were instead interested in using the MCMC to find a minimum in parameter space, we would want $p(H_f)p(D|H_f) > p(H_i)p(D|H_i)$, in order to maximize the likelihood under the constraint of the prior. Allowing the new parameter set to do slightly worse in describing the data or to fall slightly farther outside of the maximal value for the prior distribution allows for the sampling of the posterior distribution.

Initially, the Markov chain does not sample the distribution of interest because there is no guarantee that the starting parameter set is within the posterior distribution. Therefore, some initial portion of the Markov chain, called the burn-in, should be discarded before any conclusions are drawn (black circles in Figure 3.1). Once the burn-in has concluded and the equilibrium distribution is being sampled, the likelihood function should no longer strictly increase. Also, each of the parameters within the model should not be systematically changing but should oscillate around a mean value. Depending on the initial parameterization and the step taken between the initial and new parameter sets, the burn-in portion of the chain might be shorter or longer. It is therefore necessary to have a conditional cut-off for the burn-in.
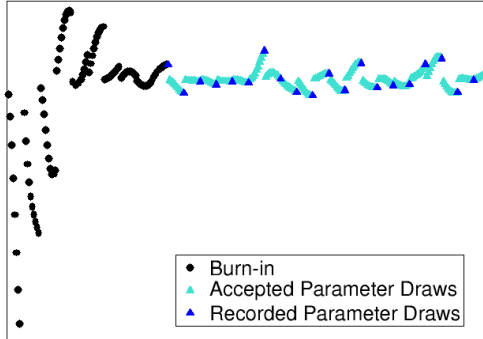
Figure 3.1: Fictitious MCMC run showing a burn-in period (black circles) followed by the region of accepted parameter draws (teal triangles). Blue triangles show the parameter draws that would be recorded (here, one out of every ten).

Independent parameter draws from the distribution are often desired, but the fundamental base of the Markov chain is that each new chain step depends on the previous instance. One way to decouple the sequential draws is to use an averaging over the chain where it is broken down into lengths of 10-50 instances which are then averaged over in order to compute one step in the Monte Carlo [101]. Another way to do this is to only record one out of every several accepted chain steps (blue in Figure 3.1). By thinning the accepted values, independence in the draws is enforced due to the gaps between recorded values.

3.2.3 Diagnostic Tools

After sampling from the posterior distribution, there are several quantities of interest that can be calculated. One such quantity is the marginal posterior distribution for a given parameter, say x_1, within the model (denoted as $H(x_1) \equiv H_1$). To calculate this, for a continuous variable

$$p(H_1|D) = \int p(H|D)dx_2 dx_3...dx_M, \tag{3.34}$$

for M parameters in the model. This corresponds to integrating the posterior distribution over all parameters except x_1. However, doing this is almost trivial when the posterior distribution is sampled using a Markov chain. One can simply take all of the samples for a given variable from the chain, create a sequence of bins over the range of the parameter, and distribute the elements according to which bin they fall within - creating a histogram of the sampled values. This density then reflects the shape of the full marginal posterior.

The mean of each parameter can be calculated by averaging over the values of that parameter within the chain,

$$\langle x_i \rangle = \frac{1}{K} \sum_{t=1}^{K} x_i^{(t)}, \tag{3.35}$$

where K is the number of parameter draws that were recorded. The mean can also be calculated for a function of the parameters,

$$\langle f(x) \rangle = \frac{1}{K} \sum_{t=1}^{K} f(x^{(t)}). \tag{3.36}$$

Likewise, the variances can be computed as

$$\langle x_i^2 \rangle = \frac{1}{K} \sum_{t=1}^{K} (x_i^{(t)} - \langle x_i \rangle)^2, \tag{3.37}$$

for each parameter and

$$\langle f(x)^2 \rangle = \frac{1}{K} \sum_{t=1}^{K} (f(x^{(t)}) - \langle f(x) \rangle)^2, \tag{3.38}$$

for any function (generally the observables of interest). The standard deviation for any of these quantities is then defined as the square root of the corresponding variance. We can

again define a covariance matrix between the parameters, similar to the model covariance matrix of Eq. (3.17),

$$C(x_i, x_j) = \frac{1}{K} \sum_{t=1}^{K} (x_i^{(t)} - \langle x_i \rangle)(x_j^{(t)} - \langle x_j \rangle). \tag{3.39}$$

In the same way as in Section 3.1.3 for the parameter covariance matrix, a correlation matrix can be defined. Again, every diagonal element in the correlation matrix is one, and the off-diagonal elements range from zero to (negative) one, where zero indicates the two parameters are not correlated and (negative) one indicates that the two parameters are fully (anti-)correlated.

Within the Bayesian model, $(1 - \alpha)100\%$ confidence intervals can be constructed for either the parameters of the model or the resulting observables. To do this, the interval needs to be determined where $(1 - \alpha)100\%$ of the calculations are concentrated. While there are several regions where this is the case (e.g. remove the high $\alpha100\%$ of the calculations or remove the lowest $\alpha100\%$ of the calculations), the calculations that are removed should be the most extreme outliers - that is the greatest density of calculations should be retained within the interval. Therefore, the calculations remaining within the $(1 - \alpha)100\%$ interval should span the smallest range, whether this is the smallest parameter range or smallest range of cross section values. Clearly, using the 95% interval for the parameters to calculate the 95% interval for the cross section values will not give the same results as calculating the 95% interval for a function as just discussed. However, defining the observable confidence intervals from the parametric confidence intervals would give a skewed picture of the results, especially since the parameters considered in this work are highly correlated and are not linearly related to the calculated observables. Calculating confidence intervals on the observables separately

from the parameters folds in these complex correlations and non-linearities.

An interval, C, defines a $(1 - \alpha)100\%$ confidence interval if

$$1 - \alpha = \int_C p(H|D)d\mathbf{x}. \tag{3.40}$$

Confidence intervals can likewise be defined for numerically sampled posteriors by ordering the draws, then determine the shortest interval that contains $(1 - \alpha)K$ (the nearest integer) of the draws. These intervals summarize the degree of belief that we have in our calculations. For example, if $\alpha = 0.05$, the 95% confidence interval for parameter i gives the range of values that we would expect for x_i with a 95% confidence.

Chapter 4

Regression Results

In this chapter, we will present results from the frequentist interpretation of uncertainties, Section 3.1, which were published in [4]. Six projectile-target pairs were studied, chosen for their range of target masses and the availability of elastic and inelastic or transfer differential cross section data over a wide angular range with small errors. For each pair, elastic-scattering data were fit, and then inelastic-scattering or transfer cross sections were predicted and compared to experimental data. Table 4.1 lists the reactions that were studied and gives the reference of the initial optical model potential and the experimental data set for each reaction. Here, we describe in detail the results of two of these calculations - one transfer and one inelastic scattering reaction. The remaining results are then summarized (details in Appendix B). The reactions that we discuss here are not necessarily well-described by the single-step approximations that have been presented. However, the goal was to include uncertainties in a consistent framework, so we use methods where the incoming elastic channel can be directly fit to elastic-scattering data and the predicted cross sections use this same elastic potential for the incoming channel.

Therefore, the transfer calculations were performed using the distorted-wave Born approximation (DWBA, Section 2.3.1), and the inelastic calculations were performed using the DWBA approximation to the full coupled-channel solution (Section 2.2.3). For the two transfer reactions, the optical potential in the outgoing channel was defined as in [106] for

Reaction	Energy (MeV)	Data	Potential
^{12}C(d,d)^{12}C	11.8	[104]	[105]
^{12}C(d,p)^{13}C(g.s.)	11.8	[106]	—
^{90}Zr(d,d)^{90}Zr	12.0	[107]	[78]
^{90}Zr(d,p)^{91}Zr(g.s.)	12.0	[108]	—
^{12}C(n,n)^{12}C	17.29	[109]	[110]
^{12}C(n,n′)^{12}C(2_1^+)	17.29	[109]	—
^{48}Ca(n,n)^{48}Ca	7.79	[111]	[112]
^{48}Ca(n,n′)^{48}Ca(2_1^+)	7.79	[111]	—
^{54}Fe(n,n)^{54}Fe	16.93	[113]	[1]
^{54}Fe(n,n′)^{54}Fe(2_1^+)	16.93	[113]	—
^{208}Pb(n,n)^{208}Pb	26.0	[114]	[1]
^{208}Pb(n,n′)^{208}Pb(3_1^-)	26.0	[115]	—

Table 4.1: List of studied reactions. The third column references the experimental data set, and the fourth column references the optical potential initialization in the fitting.

^{12}C(d,p) and as in [108] for ^{90}Zr(d,p). The binding potential between the target and the transfered neutron was described by a Woods-Saxon shape with a radius of $1.2A^{1/3}$ fm and diffuseness of 0.60 fm; the depth of the potential was adjusted to reproduce the experimental binding energy of the $A+1$ system. A spin-orbit potential was also included in the neutron-target binding potential, with standard depth, radius, and diffuseness of 7.0 MeV, $1.2A^{1/3}$ fm, and 0.60 fm, respectively. The np interaction for the deuteron was defined as in [116]. Throughout, A is the mass number of the target. For the inelastic scattering calculations, all δ_2 and δ_3 values were adjusted from [117] to better reproduce the magnitude of the inelastic cross sections (note that δ_2 and δ_3 were not included as fitted parameters). For ^{12}C, ^{48}Ca, and ^{54}Fe, the δ_2 values were 1.0852 fm, 0.85 fm, and 0.967 fm, respectively, and the δ_3 values for ^{208}Pb were 0.296 fm for the uncorrelated fit and 0.230 fm for the correlated fit.

Each of the following results (and those in Appendix B) was obtained through the statistical methods of Section 3.1 which makes use of the reaction codes FRESCO and SFRESCO [118]. The minimization procedure in SFRESCO employs routines from MINUIT [119].

4.1 Uncorrelated χ^2 Fitting

Initially, each of the the six sets of elastic-scattering data was fit using the uncorrelated χ^2 formula, Eq. (3.5). After the best-fit parameterization was calculated, the shape of the χ^2 contours were examined, and 95% confidence bands were constructed for both the fitted elastic-scattering angular distribution and the predicted inelastic or transfer distribution. Then, the parameter correlation matrix was constructed as in Eq. (3.15).

Potential	E	V_R	r_R	a_R	W_I	r_I	a_I
^{12}C(d,d)^{12}C	11.8						
Volume		*111.505*	**1.002**	**0.731**	0.000	0.000	0.000
Surface		0.000	0.000	0.000	**27.582**	**1.235**	**0.284**
^{90}Zr(d,d)^{90}Zr	12.0						
Volume		**166.319**	**0.948**	**0.655**	0.000	0.000	0.000
Surface		0.000	0.000	0.000	**18.589**	**0.934**	*0.771*
^{12}C(n,n)^{12}C	17.29						
Volume		**61.925**	**1.252**	**0.480**	0.000	0.000	0.000
Surface		0.000	0.000	0.000	*3.287*	**1.171**	**0.755**
^{48}Ca(n,n)^{48}Ca	7.79						
Volume		**46.685**	**0.956**	**0.694**	0.000	0.000	0.000
Surface		0.000	0.000	0.000	**7.172**	**1.119**	*0.189*
^{54}Fe(n,n)^{54}Fe	16.93						
Volume		**29.597**	*1.690*	**0.450**	**7.564**	*1.078*	*0.560*
Surface		0.000	0.000	0.000	**21.494**	**1.504**	*0.125*
^{208}Pb(n,n)^{208}Pb	26.0						
Volume		**42.932**	**1.031**	**0.767**	**1.196**	**1.289**	*0.580*
Surface		0.000	0.000	0.000	**8.772**	**1.050**	**0.419**

Table 4.2: Best fit parameter values for each of the reactions listed in Table 4.1 using the uncorrelated χ^2 fitting function. Column 1 gives the part of the potential (either volume or surface - the spin-orbit potential was fixed to its original parameterization), column 2 gives the reaction energy (MeV), columns 3, 4, and 5 (6, 7, and 8) give the values for the real (imaginary) depth (MeV), radius (fm), and diffuseness (fm) of each potential part. Values in italics were initially varied but held constant during the final fitting; bold values were included in the final fitting.

The first uncorrelated example we show is fitting ^{12}C(d,d)^{12}C at 11.8 MeV to predict

^{12}C(d,p)^{13}C(g.s.). The resulting best-fit parameterization is listed in Table 4.2, giving $\chi^2/N = 4.513$. (Note that some of the initially varied parameters were held constant at during the final fitting process. This was to keep them within physical bounds.) Before parameter sets could be drawn to construct the confidence bands, the χ^2 contour plots for each pair of variable was examined to see whether draws could come from a multivariate Gaussian of the form of Eq. (3.6) or if pulls had to be made from the exact χ^2 distribution, as in Section 3.1.4. To calculate the contours, a grid of χ^2 values was computed for each pair of parameters within plus and minus one standard deviation of the best-fit parameters; the remaining parameters were kept fixed at the best-fit value. Contours of constant χ^2 were then plotted. Elliptical contours indicate that the Gaussian distribution of Eq. (3.6) is a good description of the parameter space around the minimum. The slope of the resulting elliptical contour shows how correlated the two parameters are; circular, horizontal, or vertical contours indicate uncorrelated parameters while sloped ellipses indicate highly correlated parameters. The χ^2 contours for the ^{12}C(d,d) minimum are shown in Figure 4.1. Since all of these contours are elliptical, we can directly pull from the multivariate Gaussian.
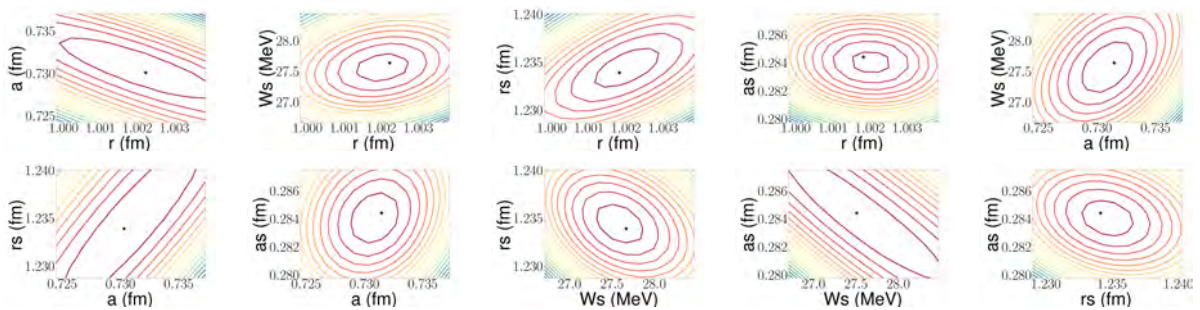
Figure 4.1: Contours of constant χ^2 for the fitted parameters of ^{12}C(d,d) elastic scattering at 11.8 MeV, using the uncorrelated χ^2 function. Black stars indicate the best-fit parameters. Figure from [4].

The resulting 95% confidence bands for the differential cross sections are shown in Figure 4.2 for (a) the fitted elastic scattering and (b) the predicted transfer reaction. The calculation

from the best fit parameterization reproduces the data very well for the elastic scattering except for $\theta > 150°$, where the best fit no longer passes through the data (this is reflected overall in the χ^2 value). The shape of the peak for the transfer reaction is reproduced, however, the extracted spectroscopic factor, $S^{\text{exp}} = 0.435^{+0.019}_{-0.017}$, is significantly lower than literature values ([120] and references therein).
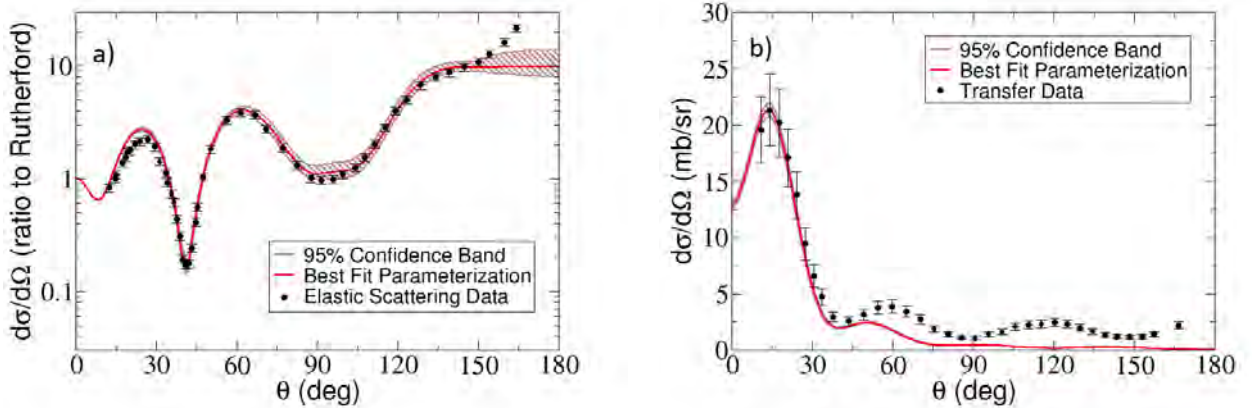
Figure 4.2: 95% confidence bands constructed from the uncorrelated fitting of $d+^{12}$C elastic-scattering data for (a) the elastic-scattering angular distribution and (b) the predicted ^{12}C(d,p)^{12}C(g.s.) transfer angular distribution, both at an incoming deuteron energy of 11.8 MeV. The calculations from the best-fit parameterization are shown in red (solid), the 95% confidence bands are shown in brown (hatched), and the data is given as the (black) circles. Figure from [4].

For both calculations, the 95% confidence bands are significantly narrower than is typically expected from the uncertainty in the parameterization $(10 - 30\%)$. This, among other results, suggests that we may need to consider a correlated χ^2 calculation which will be discussed in Section 4.2.

Last, we calculate the parameter correlation matrix for the five fitted parameters,

$$
\mathbb{C}_{\text{corr}} = \begin{bmatrix}
 & r & a & W_s & r_s & a_s \\
r & 1.000 & -0.765 & 0.380 & -0.479 & -0.535 \\
a & -0.765 & 1.000 & 0.070 & 0.879 & 0.102 \\
W_s & 0.380 & 0.070 & 1.000 & 0.154 & -0.941 \\
r_s & -0.479 & 0.870 & 0.154 & 1.000 & -0.050 \\
a_s & -0.535 & 0.102 & -0.941 & -0.050 & 1.000
\end{bmatrix}, \tag{4.1}
$$

(the notation here is such that -0.765 gives the correlation between r and a, etc.). Most of the parameters are highly correlated - only a few of the correlations are closer to zero than ± 0.5. Those parameters with correlations in this range are $r - a$, $r - a_s$, $r_s - a$, and $W_s - a_s$.

The neutron-scattering example that we consider is fitting ^{54}Fe(n,n)^{54}Fe at 16.929 MeV to predict the inelastic scattering to the first excited 2^+ state. The best-fit parameterization is also listed in Table 4.2 with $\chi^2/N = 151.889$. This χ^2 value is significantly larger than that of ^{12}C(d,d)^{12}C (and the ideal condition of $\chi^2/N \approx 1$); this is produced, in part, by small experimental errors, which can artificially inflate the χ^2 and over-constrain the fit parameters. The starting point for this potential [1] has an imaginary volume term in addition to a surface term, unlike the previous potential (and most of the other starting potentials in Table 4.1). In principle, adding three more parameters should allow for a better fit to the experimental data (more flexibility), but here, nearly half of the total parameters had to be held constant while the remaining were allowed to vary in order to find a well-behaved minimum.

The χ^2 contour plots for this minimum are shown in Figure 4.3, and again the multivariate Gaussian distribution is used to make parameter draws since the contours are elliptical. The resulting confidence bands for the elastic and inelastic cross sections are shown in Figure
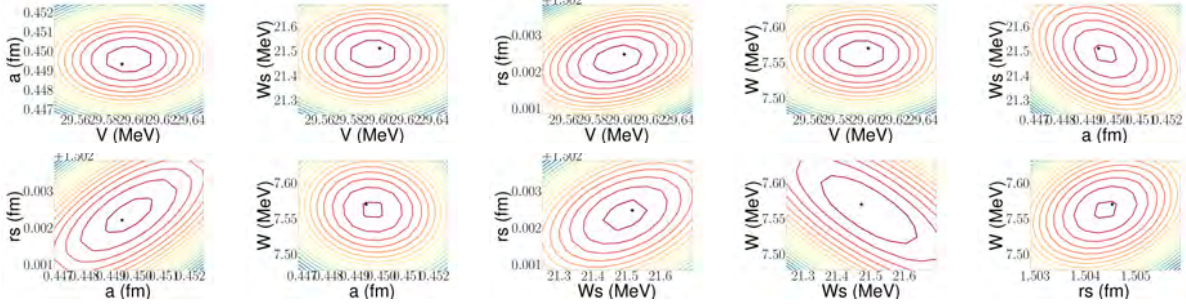
Figure 4.3: Same as Figure 4.1 for ^{54}Fe(n,n) elastic scattering at 16.929 MeV.

4.4 (a) and (b). The elastic-scattering best fit better reproduces the data than the χ^2 value indicates (the best fit goes through most of the data points), and despite the large χ^2 value, the 95% confidence bands are still narrow. Moreover, the inelastic-scattering prediction does not reproduce the data, and the 95% confidence band is not wide enough to encapsulate it. Typically, the deformation parameter (which influences the magnitude of the calculation) is extracted from the inelastic scattering prediction; however, in this case, changing the deformation parameter and refitting the elastic scattering does not improve the description of the magnitude or shape of the experimental inelastic angular distribution.

There are two processes by which to calculate the elastic and inelastic scattering. Often, both elastic- and inelastic-scattering data are fit simultaneously to extract the deformation parameter (which is included as one of the free parameters). Using both sets of data to determine the interaction should provide more stringent constraints on the optical model parameters. However, the philosophy here was to construct the predicted (d,p) and (n,n$'$) cross sections on the same footing - by just fitting the incoming elastic channel to make predictions for a separate channel. The ultimate goal of systematic uncertainty studies is not only to be able to extract information that includes theoretical uncertainties but to include uncertainties on predictions. Understanding the reduction in uncertainty when multiple types of data are fitted is important but beyond the scope of this work.

58
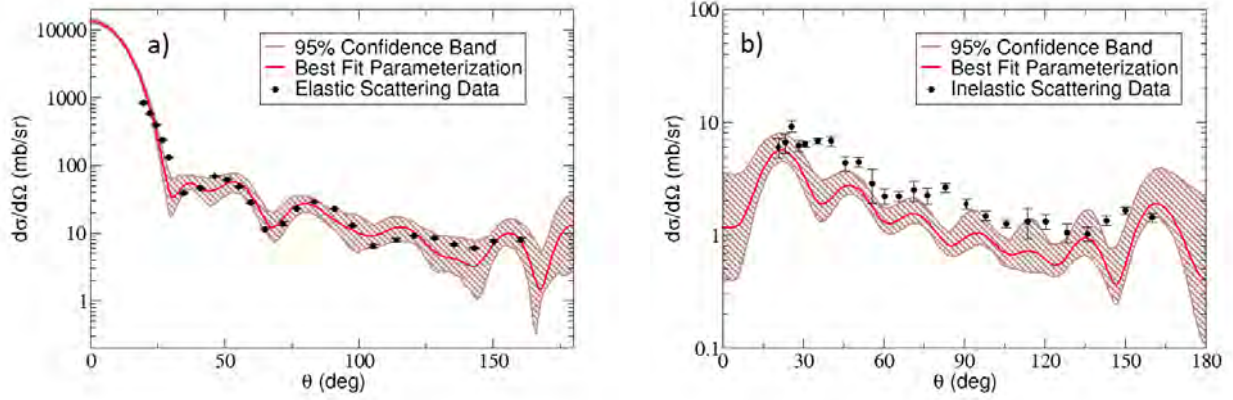
Figure 4.4: Same as Figure 4.2 for (a) ^{54}Fe(n,n)^{54}Fe and (b) ^{54}Fe(n,n)^{54}Fe(2_1^+) at 16.929 MeV.

The parameter correlation matrix is given by

$$
\mathbb{C}_{\text{corr}} = \begin{bmatrix}
 & V & a & W_s & r_s & W \\
V & 1.000 & 0.210 & 0.019 & 0.284 & 0.029 \\
a & 0.210 & 1.000 & -0.228 & 0.629 & 0.239 \\
W_s & 0.019 & -0.228 & 1.000 & 0.065 & -0.674 \\
r_s & 0.284 & 0.629 & 0.065 & 1.000 & 0.168 \\
W & 0.029 & 0.239 & -0.674 & 0.168 & 1.000
\end{bmatrix}.
\tag{4.2}
$$

These are a small subset of the nine free parameters defined in this potential. If we compare to the correlations calculated among the parameters for ^{12}C(d,d) in Eq. (4.1), the only pairs of parameters that are fit in between both cases are $a - W_s$, $a - r_s$, and $W_s - r_s$. For ^{54}Fe, the parameters are almost all uncorrelated, except for a and r_s, which were also strongly coupled in the ^{12}C fit. The pairs shown here are typically less correlated to one another (more in Section 4.3) so there is no contradiction between the two $\mathbb{C}_{\text{corr}}$ results discussed in this section.

4.2 Correlated χ^2 Fitting

As discussed in Section 3.1.2, correlations are present in the elastic-scattering model which are not taken into account in the uncorrelated χ^2 minimization function. Although we know that these angular correlations should be present, we can also visualize them. To do this, we randomly draw two hundred optical model parameter sets from a flat distribution in parameter space, and calculate the elastic cross sections for each set. Figure 4.5 then shows the correlations between these cross section values at selected angles for the two elastic-scattering reactions discussed in Section 4.1 (a) ^{12}C(d,d)^{12}C at 11.8 MeV and (b) ^{54}Fe(n,n)^{54}Fe at 16.93 MeV. We see strong correlations across the entire angular range for both reactions, especially at backwards angles.
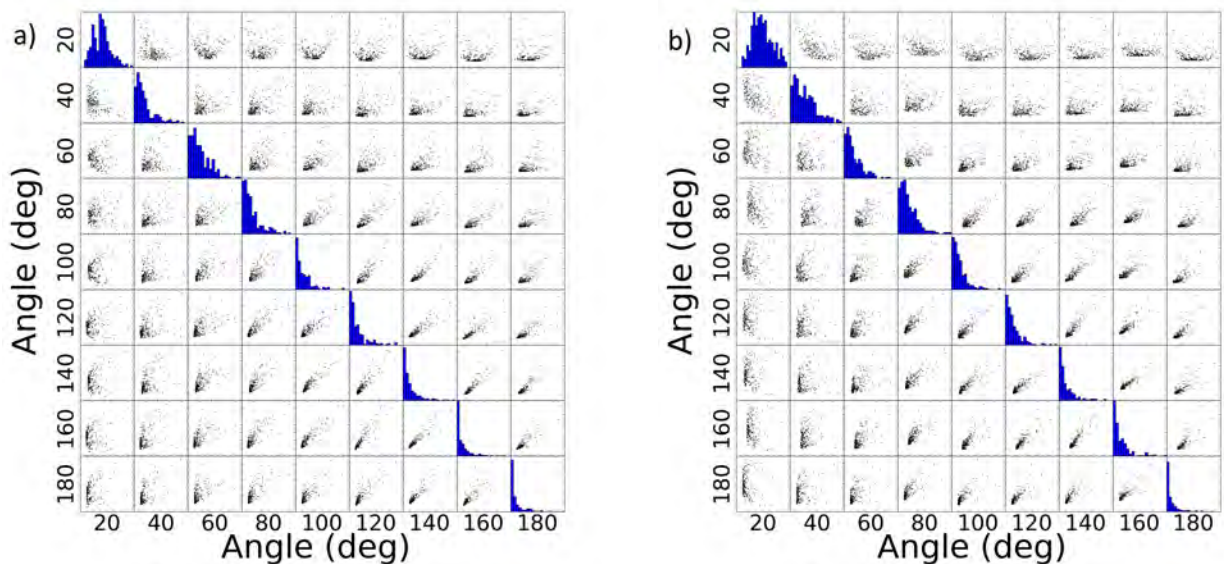
Figure 4.5: Selected angular correlations for (a) ^{12}C(d,d)^{12}C at 11.8 MeV and (b) ^{54}Fe(n,n)^{54}Fe at 16.93 MeV. Each scatter plot shows the values of the differential cross section at the angle listed on the x-axis compared to the differential cross section at the angle listed on the y-axis for two hundred calculations with randomly drawn optical model parameter sets. The histograms along the diagonal show the spread of cross section values at the given angle.

Because of this, the six reactions of Table 4.1 were fit using the correlated χ^2 function of Eq. (3.11). The starting points for these fits were the corresponding uncorrelated χ^2 minima. In the following section, we show the correlated fit for the two examples of Section 4.1. The details of the remaining reactions can be found in Appendix B along with a brief discussion of each one.

Potential	E	V_R	r_R	a_R	W_I	r_I	a_I
^{12}C(d,d)^{12}C	11.8						
Volume		**55.126**	**1.121**	**0.670**	0.000	0.000	0.000
Surface		0.000	0.000	0.000	*40.931*	**1.193**	*0.196*
^{90}Zr(d,d)^{90}Zr	12.0						
Volume		**106.868**	**1.069**	**0.575**	0.000	0.000	0.000
Surface		0.000	0.000	0.000	**31.516**	**1.118**	*0.368*
^{12}C(n,n)^{12}C	17.29						
Volume		**66.817**	**1.299**	**0.370**	0.000	0.000	0.000
Surface		0.000	0.000	0.000	**17.922**	**1.070**	*0.247*
^{48}Ca(n,n)^{48}Ca	7.79						
Volume		**36.813**	**1.201**	*0.456*	0.030	1.460	0.490
Surface		0.000	0.000	0.000	**13.318**	*1.015*	*0.241*
^{54}Fe(n,n)^{54}Fe	16.93						
Volume		**47.371**	*0.932*	**0.600**	**2.292**	*1.161*	*0.112*
Surface		0.000	0.000	0.000	**5.433**	**1.104**	*0.585*
^{208}Pb(n,n)^{208}Pb	26.0						
Volume		**42.403**	**1.040**	**0.696**	**1.680**	*1.456*	**0.580**
Surface		0.000	0.000	0.000	**11.224**	**1.052**	**0.225**

Table 4.3: Same as Table 4.2 using the correlated χ^2 fitting function.

We again start by fitting (using χ^2_C) ^{12}C(d,d)^{12}C at 11.8 MeV to predict the transfer cross section for ^{12}C(d,p)^{13}C(g.s.). The best-fit parameterization for the elastic scattering is found in Table 4.3, with $\chi^2/N = 0.283$. (This χ^2 is an order of magnitude smaller than χ^2_{UC}.) The real volume depth for this fit is about half the size of the uncorrelated depth (~ 100 MeV, consistent with many global deuteron parameterizations), while the imaginary surface depth has increased by about a third. However, if the real volume depth is fixed at the

uncorrelated depth, 111.505 MeV - which is more physical - and the remaining parameters are included in the minimization, the imaginary surface depth increases even more dramatically to compensate.

The χ^2 contours for the fit in Table 4.3 are shown in Figure 4.6. While several of these pairwise contours are approximately elliptical close to the minimum, far from the minimum, they are not. In this case, we find it necessary to pull from the exact χ^2 distribution instead of a multivariate Gaussian.
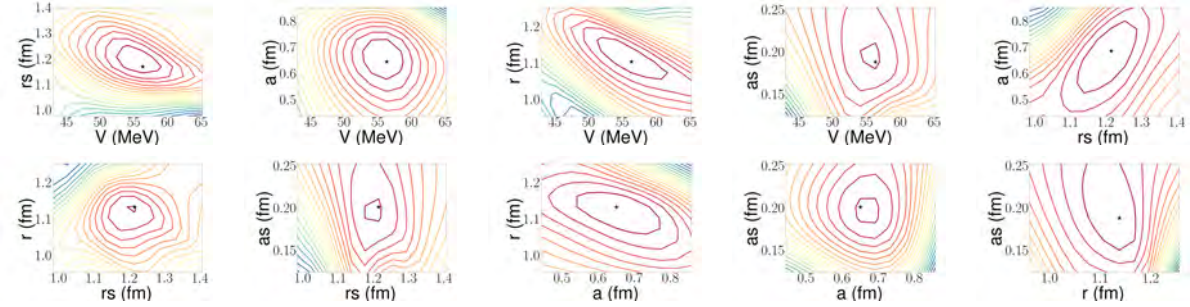
Figure 4.6: Contours of constant χ^2 for the fitted parameters of ^{12}C(d,d) elastic scattering at 11.8 MeV, using the correlated χ^2 function.

The resulting 95% confidence bands are shown in Figure 4.7 for the fitted elastic scattering (a) and the predicted transfer cross section (b). Although the best-fit elastic scattering does not pass through all of the data points, it reproduces the data up to $\sim 60°$, and where the magnitude of the data is not reproduced, the angular dependence is. For the predicted transfer cross section, the experimental angular distribution around the peak of the cross section is again well reproduced. As in Section 4.1, the extracted spectroscopic factor ($S^{\mathrm{exp}} = 0.352^{+0.223}_{-0.050}$) is significantly smaller than what is found in literature.
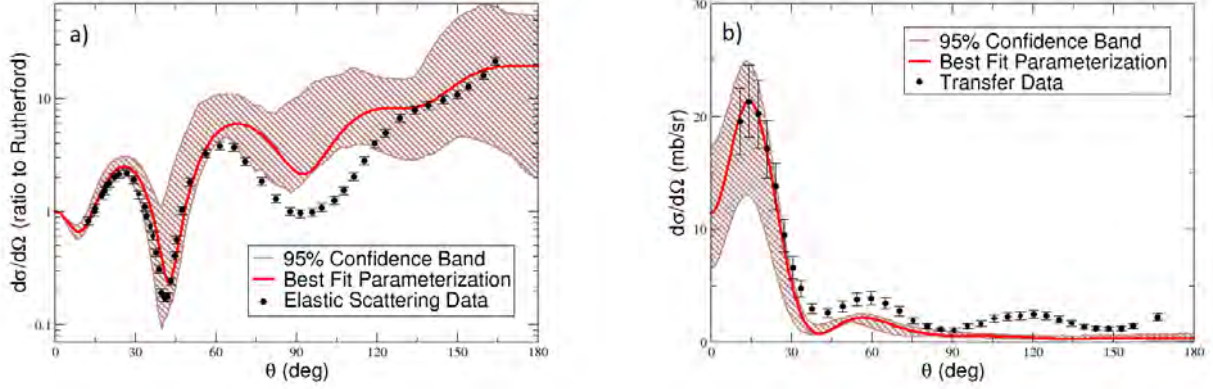
Figure 4.7: Same as Figure 4.2 using the correlated χ^2 function for (a) ^{12}C(d,d)^{12}C and (b) ^{12}C(d,p)^{13}C(g.s.). Figure from [4].

Here, the parameter correlation matrix is

$$
\mathbb{C}_{\text{corr}} = \begin{pmatrix}
1.000 & -0.568 & 0.013 & -0.910 & 0.486 \\
-0.568 & 1.000 & 0.720 & 0.307 & 0.248 \\
0.013 & 0.720 & 1.000 & -0.322 & 0.620 \\
-0.910 & 0.307 & -0.322 & 1.000 & -0.704 \\
0.486 & 0.248 & 0.620 & -0.704 & 1.000
\end{pmatrix},
\tag{4.3}
$$

and the order of the parameters is V, r_s, a, r, a_s. Because different parameters were used in the correlated fit compared to the uncorrelated fit, it is difficult to directly compare individual correlations. We still see that many of the parameters are highly correlated, especially V and r (-0.910). Typically, these are two of the most correlated parameters.

We then use the correlated χ^2 function to fit ^{54}Fe(n,n)^{54}Fe at 16.929 MeV to predict the inelastic scattering to the first 2^+ excited state. The best-fit parameterization is found in the fifth section of Table 4.3 ($\chi^2/N = 1.080$). This χ^2 value is significantly lower than the uncorrelated value. A decrease in χ^2 is typical for the correlated fitting function, but here

we see a larger decrease than for any of the other reactions.

The χ^2 contour plots are shown in Figure 4.8. The contours of constant χ^2 are mostly elliptical, and although we pull from the exact χ^2 distribution, the same 95% confidence bands result if the multivariate Gaussian is used to describe the parameter space.
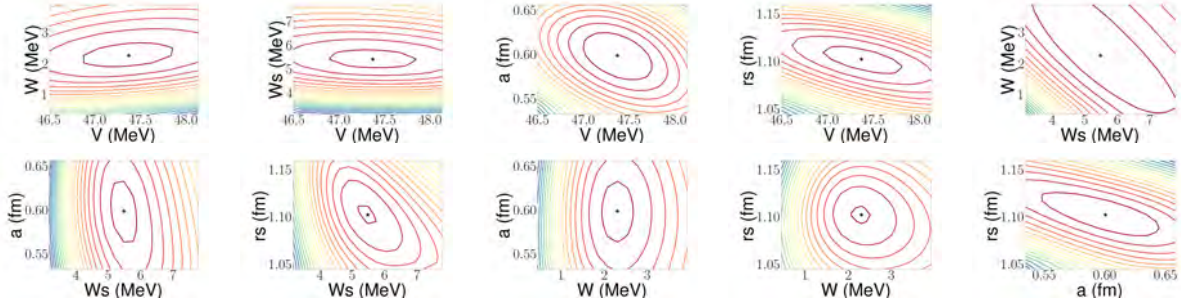
Figure 4.8: Same as Figure 4.3 for ^{54}Fe(n,n)^{54}Fe using the correlated χ^2 function.

These 95% confidence bands are shown in Figure 4.9 (a) and (b) for the elastic and inelastic scattering. The best-fit elastic scattering exactly passes through the data at forward angles, and even at larger angles, the overall shape of the experimental angular distribution is reproduced. It is also important to note that once the calculation falls below the data, it stays below the data, instead of the parameterization changing such that half of the data are above the best fit and half are below (as a typical χ^2 calculation is ensures). This change, due to the inclusion of the model covariance matrix, leads to a more physical description of the data. The inelastic-scattering prediction also provides a more physical description of the data (in comparison to Figure 4.4 (b)). The overall magnitude of the inelastic cross section has decreased (without changing the deformation parameter), and the diffraction pattern for the correlated fit better describes the experimental angular distribution.
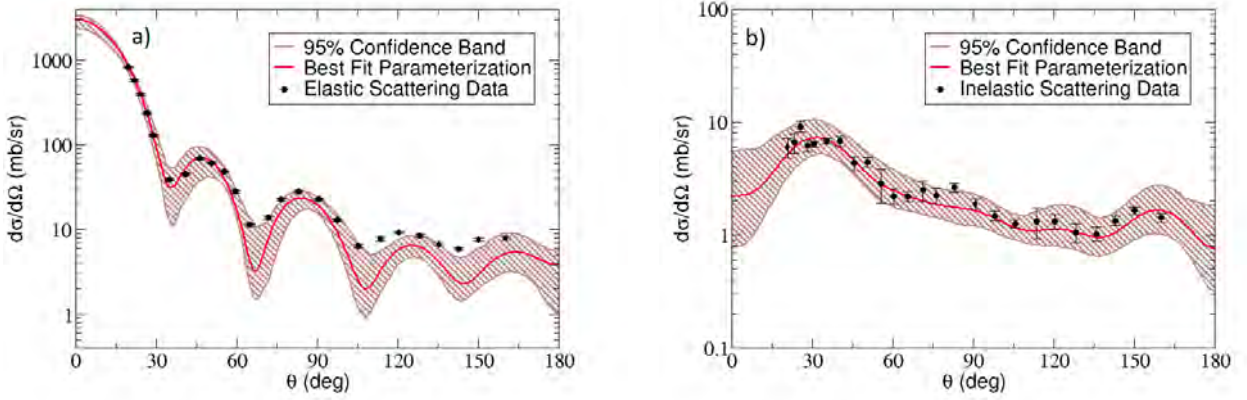
Figure 4.9: Same as Figure 4.4 using the correlated χ^2 fitting function, for fitting (a) ^{54}Fe(n,n)^{54}Fe and predicting (b) ^{54}Fe(n,n$'$)^{54}Fe at 16.93 MeV.

The parameter correlation matrix is

$$
\mathbb{C}_p = \begin{bmatrix}
 & V & W_s & W & a & r_s \\
V & 1.000 & -0.458 & 0.551 & 0.027 & 0.058 \\
W_s & -0.458 & 1.000 & -0.965 & 0.249 & -0.801 \\
W & 0.551 & -0.965 & 1.000 & -0.191 & 0.713 \\
a & 0.027 & 0.249 & -0.191 & 1.000 & -0.615 \\
r_s & 0.058 & -0.801 & 0.713 & -0.615 & 1.000
\end{bmatrix}.
\tag{4.4}
$$

Two of the most correlated parameters are W_s and r_s. In fact, we often find that the depths

and radii have the largest correlations.

4.3 Discussion

Before discussing the general conclusions that we can draw from all of the reactions that

were studied, we comment on the two examples that were shown in this chapter. First,
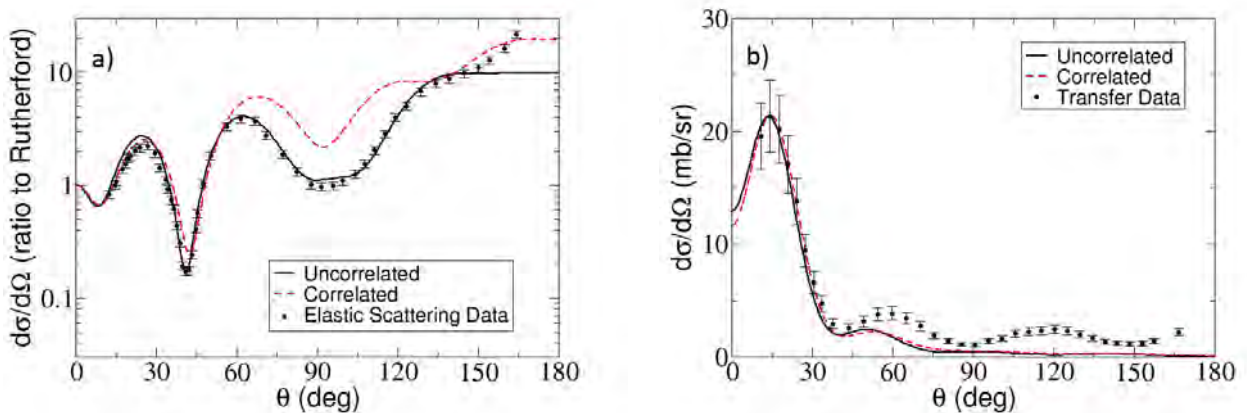
Figure 4.10: Comparison between the uncorrelated (black solid) and the correlated (red dashed) calculations for (a) ^{12}C(d,d)^{12}C and (b) ^{12}C(d,p)^{13}C(g.s.) at 11.8 MeV.

we comment on the comparison between the uncorrelated and correlated calculations for ^{12}C(d,d) and ^{12}C(d,p) which are shown in Figure 4.10. For the elastic scattering in (a), although the uncorrelated calculation fits the data at all but angles greater than 150°, the best fit from the correlated formulation provides a more consistent description of the experimental cross section. At grazing angles, around 30°, the correlated calculation is fitted better to the data, and at backward angles the upward turn of the data is reproduced by the correlated calculation, instead of flattening off as in the uncorrelated fit. Even at angles around 90° where the correlated calculation does not reproduce the magnitude of the data (as the uncorrelated calculation does), the shape of the experimental angular distribution is reproduced.

The differences are much less apparent for the predicted transfer calculations, once they have been normalized to the data. The uncorrelated spectroscopic factor is larger than the correlated one, but its value falls within the confidence bands of the correlated value. It is well-understood that DWBA does not provide an accurate description of this reaction (e.g. [121]) because the effective deuteron optical potential does not explicitly account for
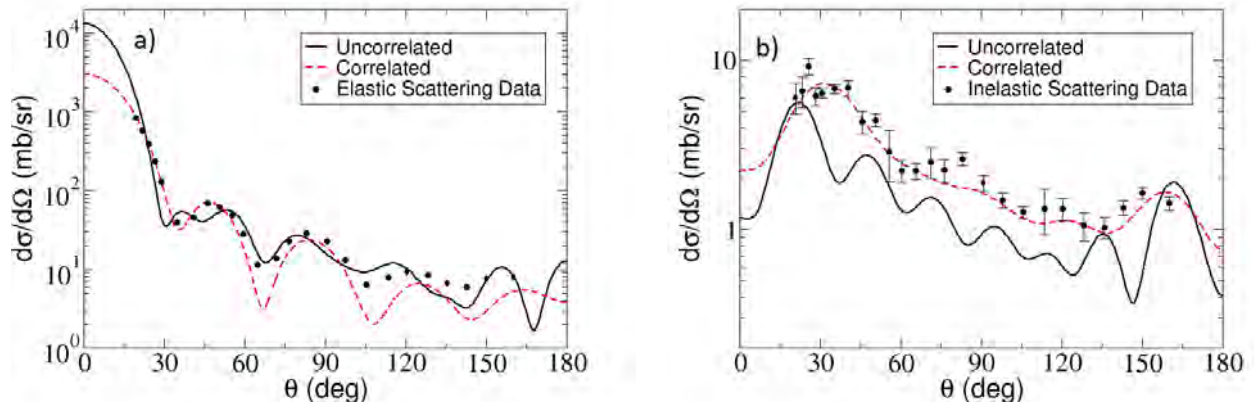
Figure 4.11: Same as Figure 4.10 for (a) ^{54}Fe(n,n)^{54}Fe and (b) ^{54}Fe(n,n$'$)^{54}Fe(2_1^+) at 16.93 MeV. Figure from [4].

np breakup - and is therefore unreliable [70].

We also directly compare the correlated and uncorrelated calculations for ^{54}Fe, Figure 4.11. For both the fitted and predicted cross sections, it is clear that the correlated fitting provides a much better description of the data. Although the magnitude of the uncorrelated elastic-scattering fit (a) remains consistent with the data across the entire angular range, it is clear that the standard χ^2 function causes half of the data to fall above the calculation and half to fall below which does not necessarily reproduce the shape of the angular distribution. When this condition is removed by the inclusion of model correlations, the shape of the cross section is much better reproduced. This addition then produces an inelastic-scattering prediction (b) that agrees with the shape and magnitude of the experimental angular distribution, even though only the elastic-scattering properties were modified.

In both of these comparisons, χ^2_C is smaller than χ^2_{UC} by an order of magnitude or more. The confidence bands for the correlated calculations are wider than those resulting from the uncorrelated calculation. (^{54}Fe is the exception: the average width for the fitted elastic-scattering confidence band is narrower for the correlated case, but the correlated confidence

67

band is wider for the predicted inelastic scattering. However, this is mainly due to the difference in magnitude of the elastic-scattering cross sections at forward angles.) Overall, the fitted parameters are also less strongly correlated when model correlations are taken into account.

We now turn to the broad conclusions that can be drawn from the fits shown in this chapter and Appendix B. Table 4.4 gives an overview of some properties of the reactions that were studied, including the fitted χ^2 for the elastic cross sections and the average width ($\overline{W}$) and uncertainty ($\overline{\varepsilon}$) of the 95% confidence bands, for the uncorrelated and correlated fits. These are defined as

$$\overline{W} = \frac{1}{N_\theta} \sum_{i=1}^{N_\theta} (\sigma_i^{\max} - \sigma_i^{\min}), \tag{4.5}$$

and

$$\overline{\varepsilon} = \frac{1}{N_\theta} \sum_{i=1}^{N_\theta} \frac{\sigma_i^{\max} - \sigma_i^{\min}}{\overline{\sigma}_i} \times 100\%, \tag{4.6}$$

the average of the width of the 95% confidence band divided by the best-fit cross section value, $\overline{\sigma}_i$.

From Table 4.4, we see that the correlated χ^2 values are an order of magnitude (or more) smaller than the uncorrelated χ^2 values. Partially, this is due to the difference in normalization between the model covariance matrix and experimental errors. Since $(\mathbb{C}_m)_{ij}$ is larger than $\Delta\sigma_i$, $\mathbb{W}$ is overweighted by $\mathbb{C}_m$ instead of the two contributing equally. To rigorously compare the χ^2 values between the uncorrelated and correlated fits, this difference in normalization would have to be accounted for. Still, the correlated χ^2 values are much more consistent among the six elastic-scattering reactions, instead of spanning three orders of magnitude as in the uncorrelated case.

The confidence bands for the correlated calculations are, on average, wider than the

Reaction	χ^2_{UC}/M	$\overline{W}_{UC}$	$\overline{\varepsilon}_{UC}$	χ^2_C/M	$\overline{W}_C$	$\overline{\varepsilon}_C$	$\overline{\varepsilon}_{exp}$
^{12}C(d,d)^{12}C	4.513	1.3577	25.336	0.283	18.181	223.01	8.0
^{12}C(d,p)^{13}C(g.s.)	—	0.77888	21.939	—	7.9226	103.58	15.0
^{90}Zr(d,d)^{90}Zr	1.421	0.086926	57.052	0.142	0.22664	92.208	5.0
^{90}Zr(d,p)^{91}Zr(g.s)	—	1.5235	51.087	—	2.2567	63.194	10.0
^{12}C(n,n)^{12}C	68.321	204.35	398.10	0.808	85.972	122.89	3.6
^{12}C(n,n')^{12}C(2^+_1)	—	17.212	205.51	—	12.681	150.40	5.1
^{48}Ca(n,n)^{48}Ca	22.344	134.21	59.823	2.142	380.91	373.91	4.0
^{48}Ca(n,n')^{48}Ca(2^+_1)	—	7.1640	91.135	—	35.586	978.15	8.9
^{54}Fe(n,n)^{54}Fe	158.098	151.89	116.44	1.080	92.191	97.617	3.4
^{54}Fe(n,n')^{54}Fe(2^+_1)	—	1.4722	112.46	—	2.2338	95.707	14.0
^{208}Pb(n,n)^{208}Pb	3.678	86.105	42.497	1.401	613.57	540.20	6.5
^{208}Pb(n,n')^{208}Pb(3^-_1)	—	0.42104	76.874	—	0.76070	231.34	14.0

Table 4.4: Summary of properties of the reactions studied for this chapter. The first column lists the reaction, while χ^2/M values for the uncorrelated (correlated) fits are given in column two (five), the average width (over all angles) of the uncorrelated (correlated) 95% confidence bands is given in the third (sixth) column, and the average percent uncertainty (over all angles) of the uncorrelated (correlated) calculations is given in the fourth (seventh) column. The eighth column gives the average experimental error (percent).

uncorrelated confidence bands, despite smaller χ^2 values being used to scale the parameter covariance matrix. This indicates that the minimum in parameter space is broader when the correlated fitting function is used, and the decrease in χ^2 is not large enough to make up for this difference. Typically, it is assumed that the optical model parameterization contributes between 10% and 30% uncertainty to the differential cross sections. However, we find that our average percent uncertainties, $\overline{\varepsilon}$, are significantly larger. These are listed in Table 4.4 for the fitted and predicted cross sections. Just as the confidence bands are wider for the correlated fits, the corresponding uncertainties are larger as well.

We also examine the change in parameter correlations between the uncorrelated and correlated fits. This is difficult to quantify for each individual reaction due to the low number of fitted parameters. Because many variables were fixed before the final minimization and these fixed variables were changed between each reaction, there are several pairs that do not have

correlation matrix elements for both the uncorrelated and correlated fits. Still, there were several pairs of variables where this comparison could be made, and two trends were noticed. First, the correlation between a potential depth and its corresponding radius decreased by $10 - 15\%$ from the uncorrelated to correlated fits. The depths and radii were the two most correlated parameter pairs overall, both for uncorrelated and correlated fitting functions. We expect this because elastic scattering is sensitive to the volume of the interaction, and it it likely that the depth and radius cannot be separately constrained. Second, the depths of the potentials became more correlated by $30 - 40\%$ for the correlated fit compared to the uncorrelated fit.

One drawback of this fitting method became increasingly obvious throughout the project. In many instances, it was not possible to keep the parameters within their physical limits which forced us to fix their values during the minimization procedure and only fit the remaining parameters. This made it very difficult to draw conclusions about how the parameter correlations change between fitting with the uncorrelated and correlated χ^2 functions. Rarely are the same set of parameters used in both minimizations. Thus, a method that can *a priori* introduce our physics knowledge and provide a hands-off fitting procedure (such as in Bayesian) would be greatly beneficial. In addition, we have more knowledge of the parameter space and correlations than is introduced in the χ^2 minimization. Finally, $\bar{\varepsilon}$ in Table 4.4 provides parametric uncertainties within a model, but this prescription does not allow us to quantify model uncertainties. A more sophisticated method to quantifying uncertainties is necessary.

Chapter 5

Bayesian Results

Here, we continue the work of the previous chapter, focusing on the uncertainties coming from constraining optical model parameters by fitting elastic scattering but now using a Bayesian approach, as described in Section 3.2. We also focus on two models, the adiabatic wave approximation (ADWA) and the distorted-wave Born approximation (DWBA), which differ in the approximations made to the three-body wave function to describe deuteron-target scattering. In doing this, we can directly compare the uncertainties that arise from these two theories based on the optical potentials in the incoming channel. Further, instead of just constraining the parametric uncertainties from the incoming deuteron channel, we also include uncertainties in the optical model of the outgoing $(A+1)$-nucleon potential. Because of the nature of the Bayesian method - and the possibility of dependence on the choice of the prior - we first investigate the dependence of the prior on the posterior distributions.

There are several potentials that must be constrained in order to run the full adiabatic calculation. The binding potential between the neutron and the proton in the deuteron, the $(A+1)$ bound state, neutron-target and proton-target optical potentials at half the deuteron energy, and proton-target (or proton-$(A+1)$) optical potential at the energy of the outgoing channel. To compare to DWBA, we also need deuteron elastic-scattering data. Further, it is useful to have (d,p) data at the incoming deuteron energy to compare to our predictions. Finding this combination of data, at the correct energies, limits the targets that we can use

for this study, especially if we want to use a range of targets across the nuclear chart.

We use stable targets with 0^+ ground states for which there is nucleon-target and deuteron-target data across a wide angular range (greater than $100°$ and in most cases, greater than $150°$). All of the nucleon-target reactions fall within the suggested range of mass and energy of the Becchetti and Greenlees potential [1]. We choose reactions that have a good chance of being reasonably described within the scope of the single-channel approach. At this point, because we are focusing on the implementation of uncertainty quantification, we do not need state-of-the-art models, only a reasonable description.

5.1 Prior Comparison

Depending on the quality of the data that is being used to constrain parameters, the prior can play a more or less significant role in the posterior distributions that are calculated using Bayes' Theorem. Before we blindly apply the Monte Carlo process for the reactions of interest, we investigate the role of the shape of the prior on data-constrained elastic cross sections and predicted transfer cross sections. We consider a Gaussian prior and a flat prior, each with two different widths. As a test case, we consider ^{90}Zr(n,n)^{90}Zr elastic scattering at 24.0 MeV [122]. The two priors are defined independently for each parameter in the volume and surface terms of the ^{90}Zr-n optical potential. The narrower of the two priors (M) covers a range of physical values for each parameter while not overly constraining them; the wider prior puts almost no constraint on the parameters. Table 5.1 lists the means and widths of these four priors.

Figure 5.1 shows the posterior distributions (histograms) and initial prior distributions (solid lines) for the priors listed in Table 5.1. For the real volume parameters (V, r, and
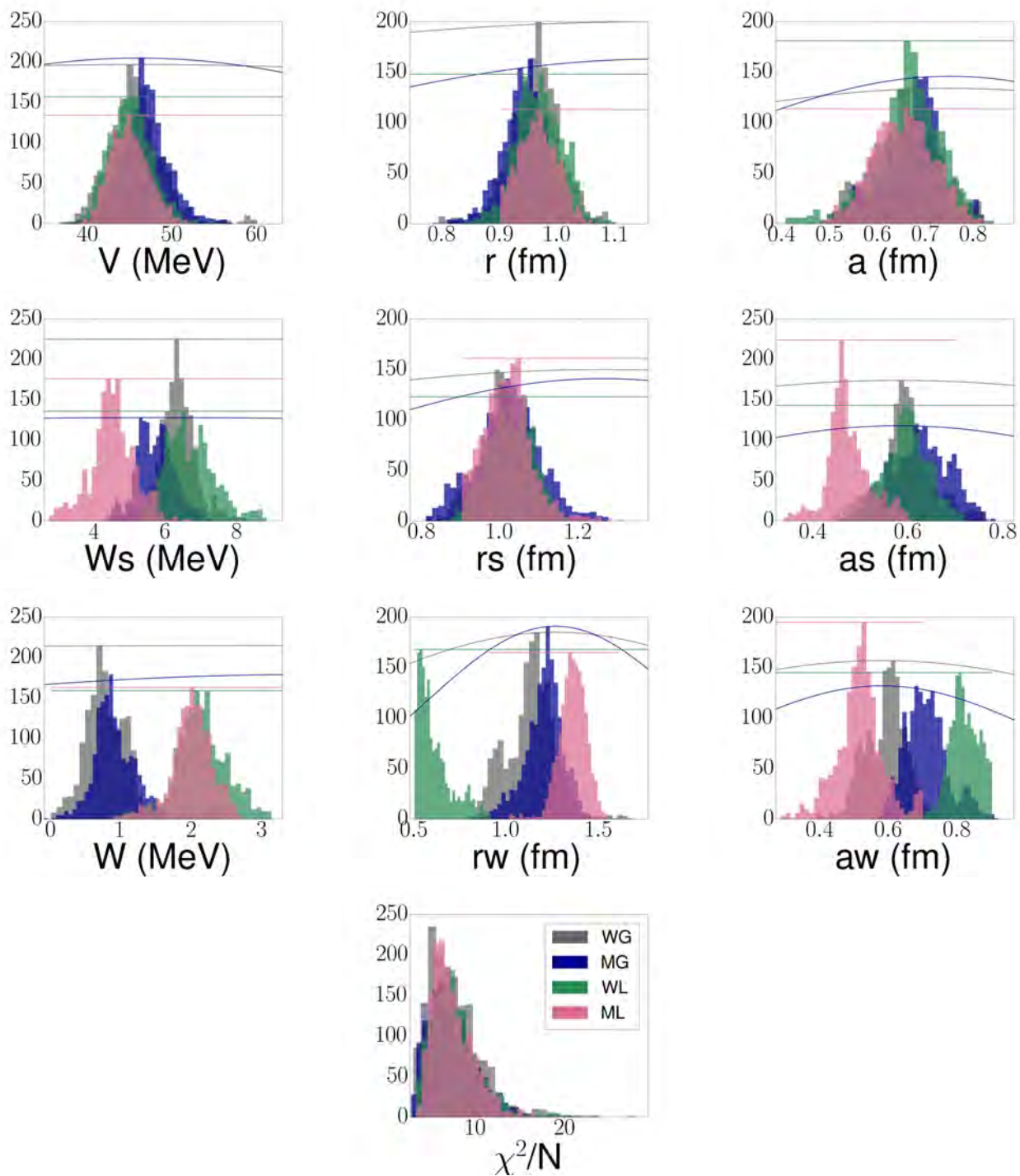
Figure 5.1: Comparison of prior shapes (with $\epsilon = 0.005$) for the optical model parameters constrained by ^{90}Zr(n,n)^{90}Zr elastic scattering at 24.0 MeV, for the wide Gaussian (gray histogram), medium Gaussian (blue histogram), wide linear (green histogram), and medium linear (pink histogram) posterior distributions, all shown with respect to their associated prior distribution (lines of the same color).

x	x_{oML}	x_{oMG}	Δx_M	x_{oWL}	x_{oWG}	Δx_W
V	50.0	46.0	40.0	60.0	46.0	100.0
r	1.25	1.17	0.7	1.15	1.17	01.3
a	0.65	0.75	0.5	0.60	0.75	0.8
W_s	15.0	5.7	30.0	40.0	5.7	80.0
r_s	1.25	1.26	0.7	1.15	1.26	1.3
a_s	0.45	0.58	0.5	0.45	0.58	0.9
W	5.0	3.7	10.0	20.0	3.7	40.0
r_w	1.25	1.26	0.7	1.15	1.26	1.3
a_w	0.45	0.58	0.5	0.45	0.58	0.9

Table 5.1: Summary of centers (x_o) and widths (Δx_i) for the medium linear (ML) prior, medium Gaussian (MG) prior, wide linear (WL) prior, and wide Gaussian (WG) prior. Columns four and seven give the widths of the medium and wide priors, respectively. These are given for ^{90}Zr(n,n)^{90}Zr at 24.0 MeV. For all other reactions, the widths of the priors and the center of the linear priors remained the same; the center of the Gaussian priors were defined to be the optical potential values for each parameter, taken from [1]. Depths are given in MeV, and radii and diffusenesses are given in fm.

a), regardless of the choice of prior, the means and widths are essentially identical. This is not true for the imaginary volume and surface parameters which are peaked at significantly different values (except for r_s). We also see that for several of the parameters, there is a sharp cut-off for the posterior distributions using the medium linear prior because of the fixed limits that are imposed by this prior shape. However, the χ^2 distributions for the four priors are nearly identical indicating that the correlations between parameters are more important than the parameter values themselves.

We know that different parameterizations for the optical potentials can lead to identical elastic-scattering angular distributions, and it is ultimately the differences in the observables that illustrate the effect of the prior distribution. Figure 5.2 (a) shows the 95% confidence intervals for each of the posterior distributions from Figure 5.1. The four confidence intervals are also nearly identical, which is perhaps not surprising since the χ^2 distributions are so similar. It also indicates that the correlations between the parameters are more significant
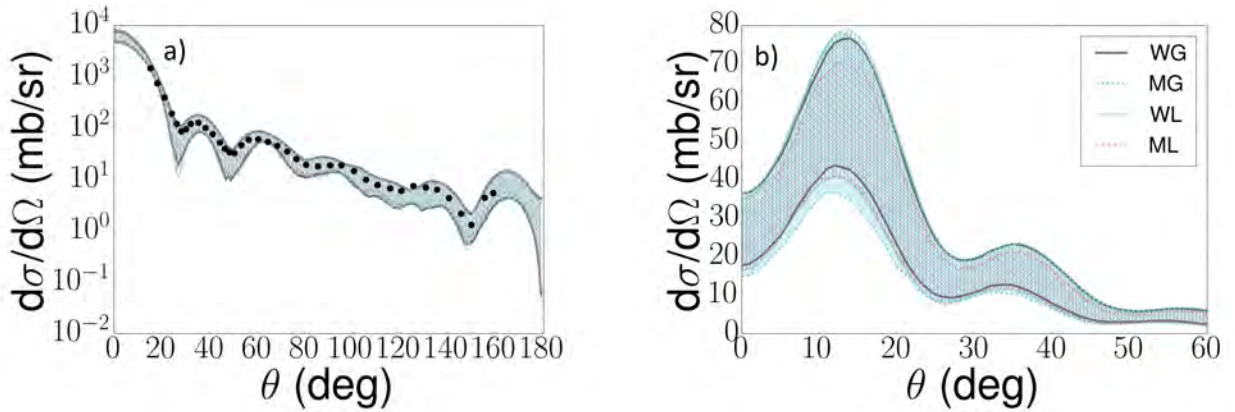
Figure 5.2: Comparison of cross sections for the four prior distributions listed in Table 5.1 (with $\epsilon = 0.005$) for (a) ^{90}Zr(n,n)^{90}Zr and (b) ^{90}Zr(d,p)^{91}Zr(g.s.) at 24.0 MeV for the wide Gaussian (gray), medium Gaussian (blue), wide linear (green), and medium linear (pink).

(when calculating observables) than the parameter values themselves.

However, it is also known that different parameterizations that give rise to the same elastic-scattering cross sections do not necessarily lead to similarities in other observables, such as the transfer cross section. Because we have only constrained neutron-target elastic scattering, we have to make some approximations in order to calculate a transfer cross section. For simplicity, we approximate the deuteron-target potential as being twice the neutron-target potential (which is a reasonable assumption considering that the neutron and proton potentials are nearly identical except for Coulomb effects); then we use the distorted-wave Born approximation (DWBA) to calculate the (d,p) transfer cross section. The results for the 95% confidence intervals for each of the four priors are shown in Figure 5.2 (b). Here, there are some differences between the four priors. The two medium priors have thinner confidence intervals; the linear prior, in particular, produces a distinct confidence interval, most likely due to the fixed boundaries of the prior which lead to abrupt cut-offs for some of the posterior distributions.

We also see that the two wide priors lead to more similar posterior distributions than the two smaller priors, so we prefer the wide priors which allow all the parameters to be fully constrained by the data. In principle, both the Gaussian and linear priors would work (since they lead to the same observables), however, the flat prior has the chance of sharply cutting off the parameter space and forcing the parameters into a false minimum because of this restriction. In that sense, we prefer the Gaussian because it encourages the parameters to stay within a physical range without this abrupt cut-off. Plus, we do have more prior knowledge of the parameter space than just the physical ranges for these parameters. The global optical models parameters that we start with have been fit to large amounts of data across the nuclear chart, so the initial parameters should already provide a reasonable description of the data that only needs slight adjustments. For the rest of this work, we consider a Gaussian prior.

Next, we take the wide Gaussian prior, and consider changing the scaling factor, ϵ (which controls the step size for each parameter). If too small of a step is taken, not enough of the parameter space will be sampled because the parameterization will not escape from the starting local minimum. If too large of a step is taken, the parameters will not be well-constrained. Also, as the step size becomes larger, more parameter samples do not meet the condition of Eq. (3.33), the Monte Carlo will take longer to converge (and therefore more parameter sets will be rejected before the appropriate number are accepted). Ideally, around 50% of the sampled parameter sets should be accepted [101]. Figure 5.3 shows the comparison of the ϵ values that were considered. We see that the posterior distributions for $\epsilon = 0.001$ and $\epsilon = 0.002$ do not peak at the same parameter values as the other three scaling factors. These are too small and do not explore enough of the parameter space. On the other hand, $\epsilon = 0.05$ is too large to constrain each parameter. Therefore, using a scaling

factor in the range of 0.005 or 0.01 is ideal. This also causes $\sim 50\%$ of the parameter draws to be accepted, as desired.

For the rest of this work, we consider a Gaussian prior with $\epsilon = 0.005$. This same study was performed for three other elastic scattering reactions to ensure that the conclusions drawn from the ^{90}Zr(n,n) scattering were consistent in other mass and energy regions. These studies are all shown in Appendix A, and the results are identical to those shown for the ^{90}Zr case.

Finally, we can more systematically study the effect that changing the width of the Gaussian prior distribution has on the mean value and width of the resulting posterior distribution. Figure 5.4 shows the mean value of the posterior distributions (blue circles) as a percentage of the mean of the prior distribution for each variable, from [1], plotted as a function of the width of the prior distribution (as a percentage of the mean of each prior distribution for each variable). We first see that the mean values of the posterior distributions remain constant as the width of the prior distributions increase. The error bars on each of the posterior means give the width of the posterior distribution as a percentage of the width of the prior distribution. The shrinking error bars show that the widths of the posterior distributions are becoming a smaller fraction of the widths of the prior distributions; since the widths of the prior distributions are increasing, this indicates that the widths of the posterior distributions are staying constant. Taken together, this indicates that the posterior distributions are driven by the data and not by the prior distribution.
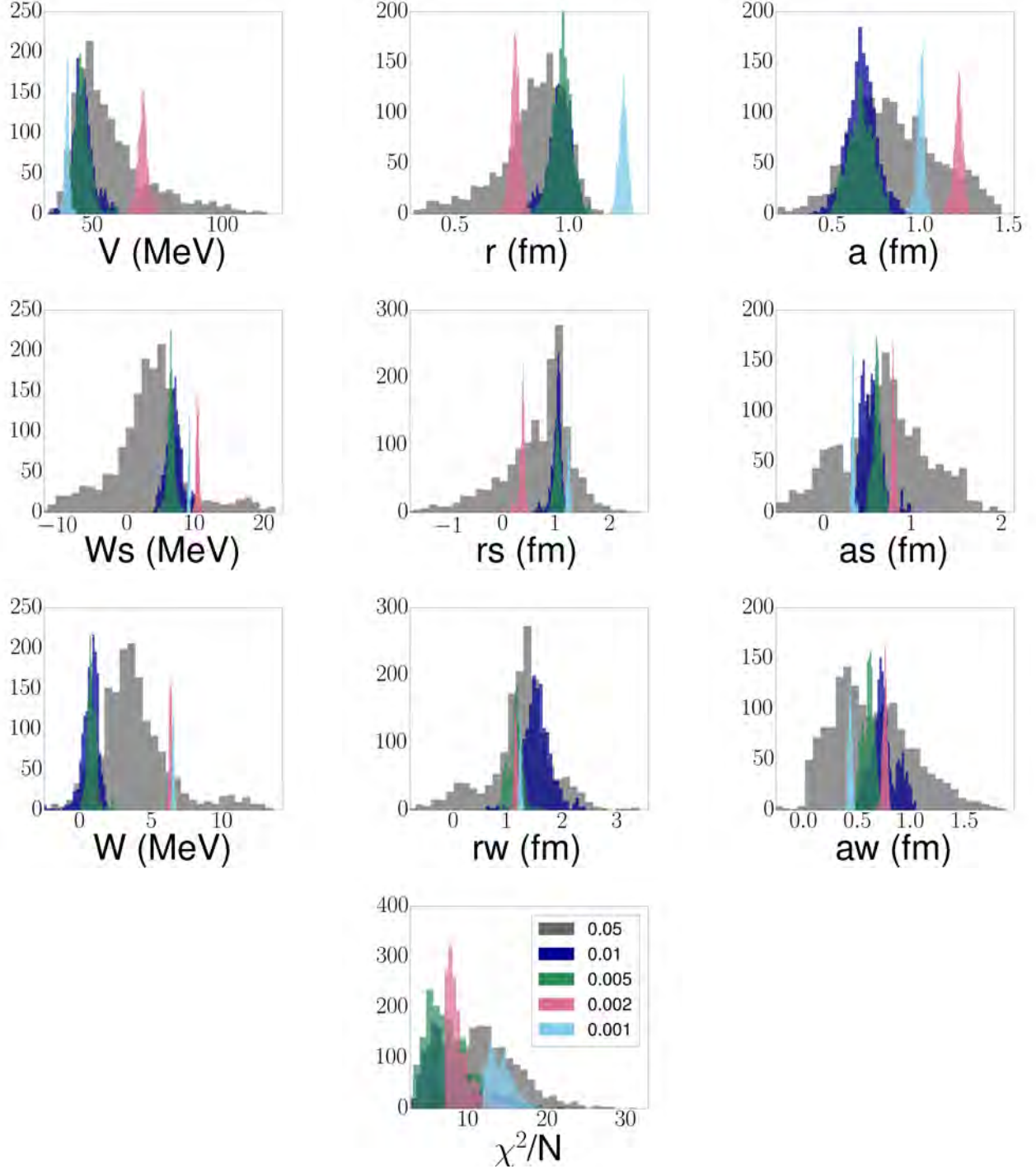
Figure 5.3: Comparison of the scaling factors for the optical model parameters constrained by ^{90}Zr(n,n)^{90}Zr elastic scattering at 24.0 MeV, for $\epsilon = 0.001$ (blue), $\epsilon = 0.002$ (pink), $\epsilon = 0.005$ (green), $\epsilon = 0.01$ (dark blue), and $\epsilon = 0.05$ (gray). The prior distribution was taken to be the wide Gaussian, as defined in Table 5.1.
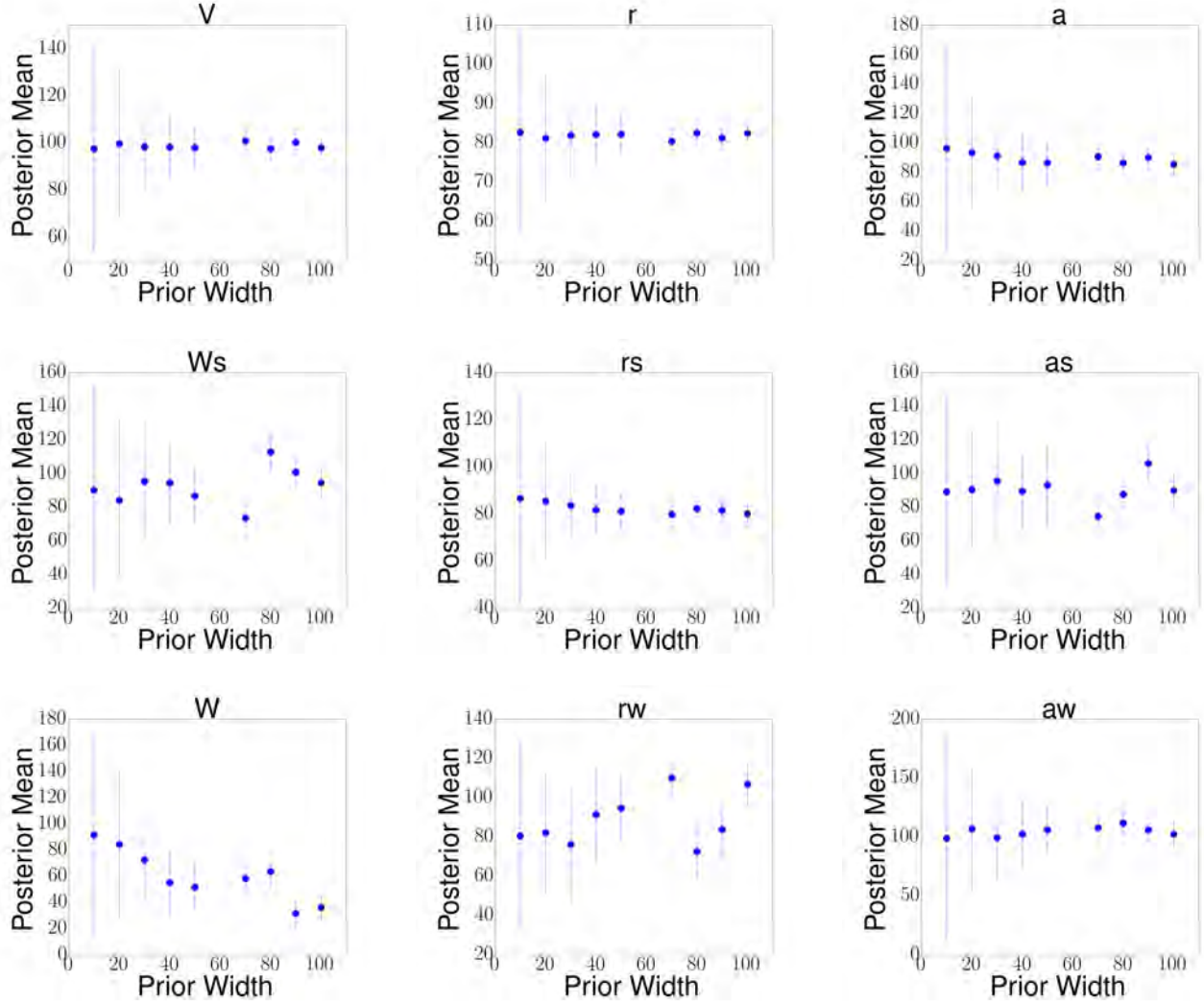
Figure 5.4: A systematic study of the mean and width of the posterior distribution for each optical model parameter as a function of the width of the prior distribution. The x-axis gives the width of the Gaussian prior distribution as a percentage of the original optical model value for each parameter. Blue circles show the means of each of the posterior distributions, as a percentage of the original prior mean. The error bars give the width of the posterior distributions as a percentage of the prior widths.

Reaction	Energy (MeV)	Data
$^{48}Ca(p,p)^{48}Ca$	21.0	[123]
$^{90}Zr(p,p)^{90}Zr$	40.0	[124]
$^{120}Sn(n,n)^{120}Sn$	13.9	[125]
$^{90}Zr(n,n)^{90}Zr$	24.0	[122]

Table 5.2: Reactions used to test the various prior shapes of Table 5.1. All data for the elastic-scattering reactions come from the references in column three.

5.2 Numerical Details

Now that we have an understanding of the Bayesian method, we can focus on the physics. Recall from Eq. (2.28) that there are three wave functions that need to be constrained to calculate the transfer cross section. The bound state between the target and the transferred nucleon, the outgoing $(A+1)$-proton (or $(A+1)$-neutron) distorted wave, and the exact wave function for the initial three-body system. In the two three-body approximations discussed in Section 2.3, the exact wave function is approximated, either by the deuteron bound state multiplied by a distorted wave for the deuteron-target system in DWBA or in ADWA as an adiabatic wave function. In ADWA, the wave function is constrained through neutron-target and proton-target elastic scattering data at half of the incident deuteron energy. In (DWBA), the constraint is deuteron-target elastic scattering at the incident deuteron energy. The outgoing $(A+1)$-proton (or neutron) wave function is constrained by A-proton (or neutron) elastic scattering data - as this data is more readily available, and the difference in the optical potential between the A-nucleon and $(A+1)$-nucleon are on the order of 1%.

Continuing from Chapter 4, we explore the parametric uncertainties remain when constraining optical model parameters with elastic-scattering data. This includes the uncertainties that enter through the scattering wave function in the incoming and outgoing channels, but does not include uncertainties associated with the bound states. The bound state of the deuteron is defined by a Gaussian that reproduces the binding energy of the deuteron (as in [126]). The bound state of the target plus transferred nucleon is parameterized by a central potential (Woods-Saxon shape) and spin-orbit term, with standard radius and diffuseness parameters of 1.2 fm and 0.65 fm. The depth of the Woods-Saxon is fixed to reproduce the binding energy of this two-body system in the appropriate ℓ_j state. The depth of the

Target	Projectile	E (MeV)	Data
^{48}Ca	p	14.03	[127]
^{48}Ca	n	12.0	[128]
^{48}Ca	p	24.0	[129]
^{48}Ca	d	23.3	[130]
^{90}Zr	p	12.7	[131]
^{90}Zr	n	10.0	[122]
^{90}Zr	p	22.5	[132]
^{90}Zr	n	24.0	[122]
^{90}Zr	d	23.2	[130]
^{116}Sn	p	22.0	[133]
^{116}Sn	n	24.0	[134]
^{116}Sn	p	49.35	[135]
^{208}Pb	p	16.9	[136]
^{208}Pb	n	16.0	[137]
^{208}Pb	p	35.0	[138]
^{208}Pb	d	28.8	[139]

Table 5.3: Summary of elastic scattering pairs used in this work. Column four gives the corresponding reference for the experimental data.

spin-orbit potential is the standard value of 6.0 MeV.

Ultimately, there were five single-nucleon transfer reactions that we studied, given in Table 5.4. In the next sections, we show the results of constraining the nucleon-target optical model parameters for obtaining the ADWA transfer cross sections and then including the deuteron-target elastic scattering to construct the transfer cross sections under DWBA for one of these reactions, ^{48}Ca(d,p)^{49}Ca(g.s.). Table 5.3 also lists all of the reactions that were used to constrain optical model parameters within this work. Table 5.4 lists the references to any data that were used to compare the magnitude and shape of the transfer cross sections, in addition to the transfer reactions that were studied.

Within these two reaction frameworks, we also study the impact of the reduction in experimental error: if the experimental error is reduced by 50%, is there a corresponding reduction in the widths of the confidence intervals for the elastic scattering and transfer cross

System	E (MeV)	Data
^{48}Ca(d,p)^{49}Ca	24.0	[140]
^{90}Zr(d,p)^{91}Zr	22.0	[141]
^{90}Zr(d,n)^{91}Nb	20.0	—
^{116}Sn(d,p)^{117}Sn	44.0	—
^{208}Pb(d,p)^{209}Pb	32.0	—

Table 5.4: Transfer reactions that were calculated using either ADWA or DWBA, the energy at which the calculation was performed (column two), and a reference to experimental data, if any (column three).

sections? For this purpose, we first take the error on the experimental data to be 10% of the cross section value at each angle, and then reduce it to 5% at each angle.

5.3   Transfer Reactions with ADWA

We first begin by constraining the optical model parameters for ^{48}Ca-nucleon interactions to construct the ^{48}Ca(d,p)^{49}Ca transfer cross section to the ground state (g.s.) using ADWA. In this framework, the incoming neutron- and proton-target potentials have to be calculated at half of the incoming deuteron energy. For each of the scattering cases, the prior distributions are centered at the starting parameter values from the Becchetti and Greenlees global optical potential [1] with a width equal to the initial parameter value.

Figure 5.5 shows the posterior distributions (histograms) compared to the prior distributions (solid lines) for the potential parameters of ^{48}Ca(n,n)^{48}Ca at 12.0 MeV, using both 10% errors on the experimental cross section values (gray) and 5% errors (blue). The means and widths for each parameter in the posterior distribution are listed in Table 5.5, columns two and three. We see that the posterior distributions are all centered around physical values, and even though the prior distributions are wide, the posterior distributions are well-constrained. Using 5% errors, compared to the 10% errors, has little effect on the peak value

82

ε_{exp}	x	$\bar{x}_\mathrm{n}^\mathrm{in}$	$\Delta x_\mathrm{n}^\mathrm{in}$	$\bar{x}_\mathrm{p}^\mathrm{in}$	$\Delta x_\mathrm{p}^\mathrm{in}$	$\bar{x}_\mathrm{p}^\mathrm{out}$	$\Delta x_\mathrm{p}^\mathrm{out}$
	V	45.510	2.735	51.147	4.043	53.490	4.192
	r	1.222	0.054	1.242	0.053	1.141	0.049
	a	0.682	0.055	0.560	0.050	0.726	0.055
	Ws	7.376	0.538	11.749	0.922	6.825	0.549
10%	rs	1.255	0.076	1.308	0.057	1.335	0.067
	as	0.292	0.041	0.520	0.040	0.589	0.047
	W	0.950	0.086	0.430	0.043	2.249	0.330
	rw	1.210	0.123	1.313	0.151	1.278	0.127
	aw	0.601	0.062	—	—	0.606	0.074
ε_{exp}	x	$\bar{x}_\mathrm{n}^\mathrm{in}$	$\Delta x_\mathrm{n}^\mathrm{in}$	$\bar{x}_\mathrm{p}^\mathrm{in}$	$\Delta x_\mathrm{p}^\mathrm{in}$	$\bar{x}_\mathrm{p}^\mathrm{out}$	$\Delta x_\mathrm{p}^\mathrm{out}$
	V	45.346	1.468	51.339	2.246	52.173	2.598
	r	1.226	0.028	1.240	0.038	1.154	0.030
	a	0.683	0.034	0.579	0.037	0.717	0.038
	Ws	6.796	0.594	11.780	0.858	7.125	0.670
5%	rs	1.260	0.037	1.312	0.046	1.351	0.036
	as	0.314	0.031	0.522	0.023	0.563	0.046
	W	1.008	0.114	0.359	0.040	2.469	0.258
	rw	1.133	0.148	1.262	0.166	1.173	0.136
	aw	0.616	0.054	—	—	0.664	0.065

Table 5.5: Means ($\bar{x}_i$) and widths (Δx_i) for the posterior distributions shown in Figure 5.5 (columns two and three), Figure 5.7 (columns four and five), and Figure 5.8 (columns six seven) using the 10% experimental errors (top) and 5% errors (bottom).

of the posterior distribution for each parameter, but the widths of the posterior distributions are much narrower for several of the parameters. In some cases, there is a 50% decrease in the width of the parameters, but in other cases there is an increase instead (such as for W_s and W - which speaks to the ambiguity between the two imaginary terms which is discussed more in Appendix D).

Figure 5.6 shows the comparison of the 95% confidence intervals (defined as in Eq. (3.40) with $\alpha = 0.05$) that are constructed from the posterior distributions in Figure 5.5. The data is well-bounded by the 95% confidence intervals, and again, there is a reduction in the width of the confidence intervals when a smaller error is used - however, this width does not decrease by 50% as the experimental errors do.
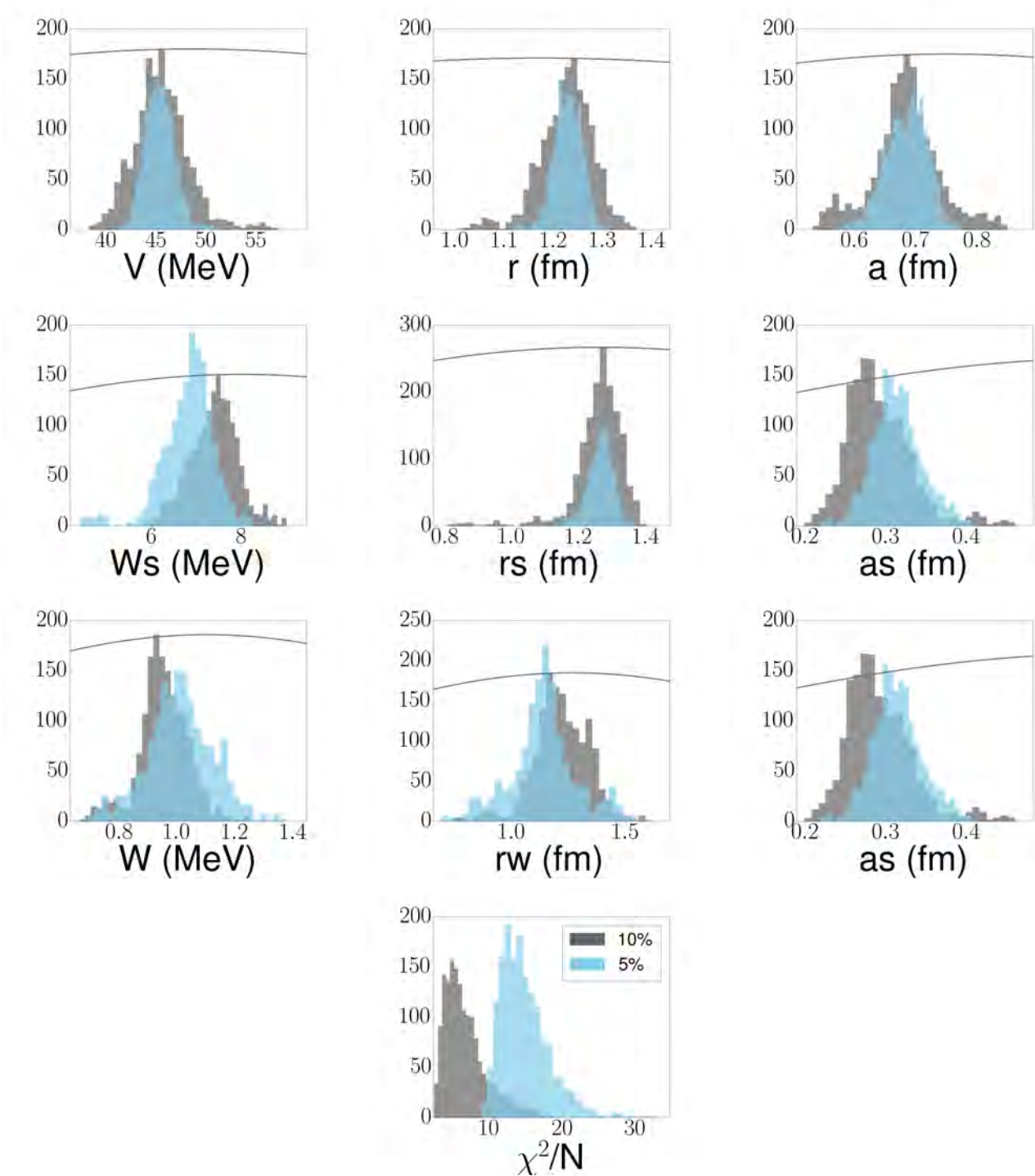
Figure 5.5: Posterior distributions (histograms) constraining the optical potential parameters using ^{48}Ca(n,n)^{48}Ca elastic scattering data at 12.0 MeV, comparing 10% errors on the experimental cross sections (gray) and 5% errors (blue). Original prior distributions are shown as gray solid lines.
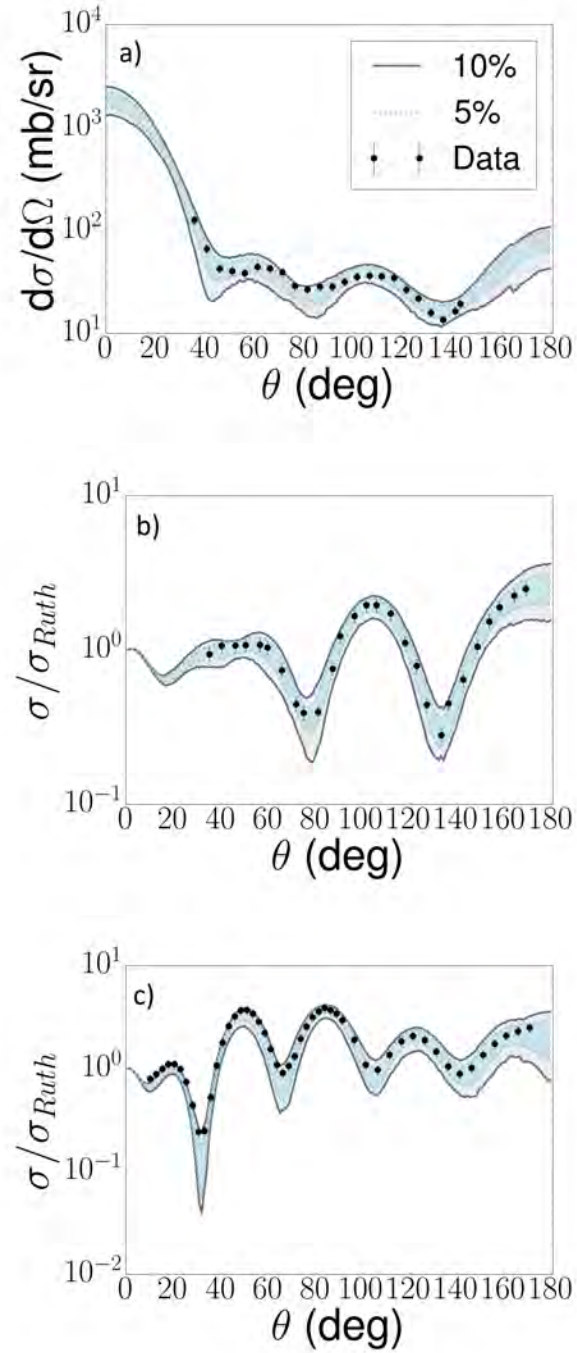
Figure 5.6: The 95% confidence interval for (a) ^{48}Ca(n,n)^{48}Ca at 12.0 MeV, (b) ^{48}Ca(p,p)^{48}Ca at 14.03 MeV, and (c) ^{48}Ca(p,p)^{48}Ca at 25.0 MeV, from the posterior distributions of Figures 5.5, 5.7, and 5.8, using 10% errors (gray) and 5% errors (blue).

Next, we do the same for the ^{48}Ca(p,p)^{48}Ca elastic-scattering optical-model parameters at 14.03 MeV (still used to constrain the incoming deuteron-target scattering). The posterior distributions (gray histograms for 10% experimental errors and blue histograms for 5%) are compared to the initial prior distributions (gray solid) in Figure 5.7. The means and widths are listed in Table 5.5, columns four and five. Again, there is mostly a reduction in the width of the posterior distributions when the smaller errors are used, but this is not always the case. For this reaction, note that a posterior distribution is not shown for a_w; this parameter was not included as a free parameter in the Monte Carlo because it could not be constrained by the elastic-scattering data (for an example of this lack of constraint, see Figure A.4 for the posterior distributions and Figure A.5 (c) for the resulting elastic angular distribution). Figure 5.6 (b) shows the resulting 95% confidence intervals for the elastic-scattering cross sections from these two prior distributions.

Finally, we also constrain the outgoing ^{49}Ca-p channel with ^{48}Ca(p,p)^{48}Ca elastic scattering data at 25.0 MeV (which, converting to the center of mass, is close to the incident deuteron energy minus the Q-value for the (d,p) reaction). The posterior distributions using 10% (5%) experimental errors are shown as gray (blue) histograms compared to the prior distribution (gray solid) in Figure 5.8. The resulting 95% confidence intervals for the elastic cross sections are shown in Figure 5.6 (c), where we again see a reduction in the width of these intervals when reducing the experimental errors from 10% (gray) to 5% (blue), though not to the same extent as the reduction in the error.

We can now use the posterior distributions from the three nucleon-target elastic-scattering reactions to construct the transfer cross sections under ADWA by randomly drawing a parameter distribution for each potential for a single calculation. It is important to remember once more that we are constraining the two scattering distorted waves with the nucleon-
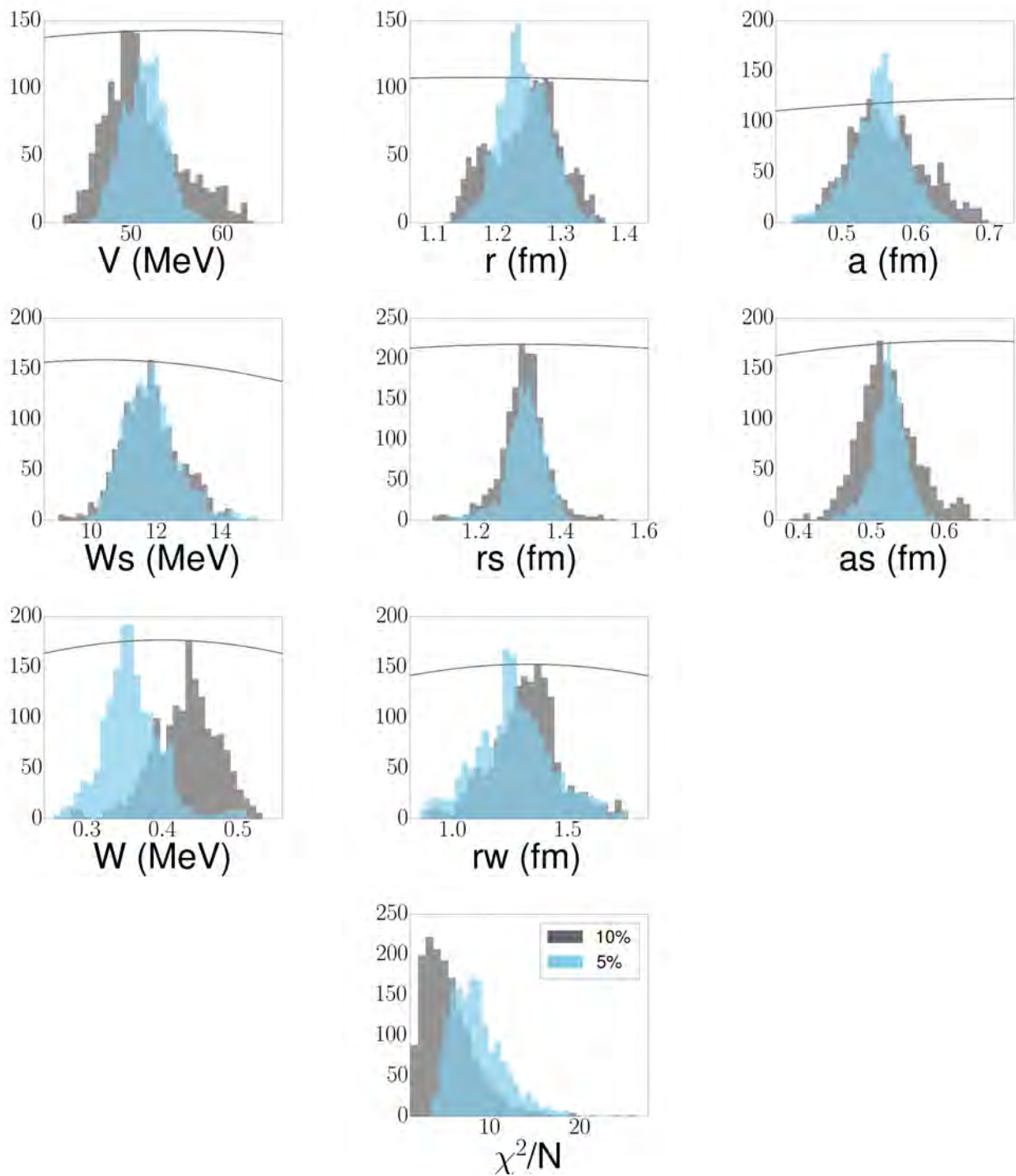
Figure 5.7: Same as Figure 5.5 for ^{48}Ca(p,p)^{48}Ca elastic scattering at 14.03 MeV where a_w was not included as a free parameter.
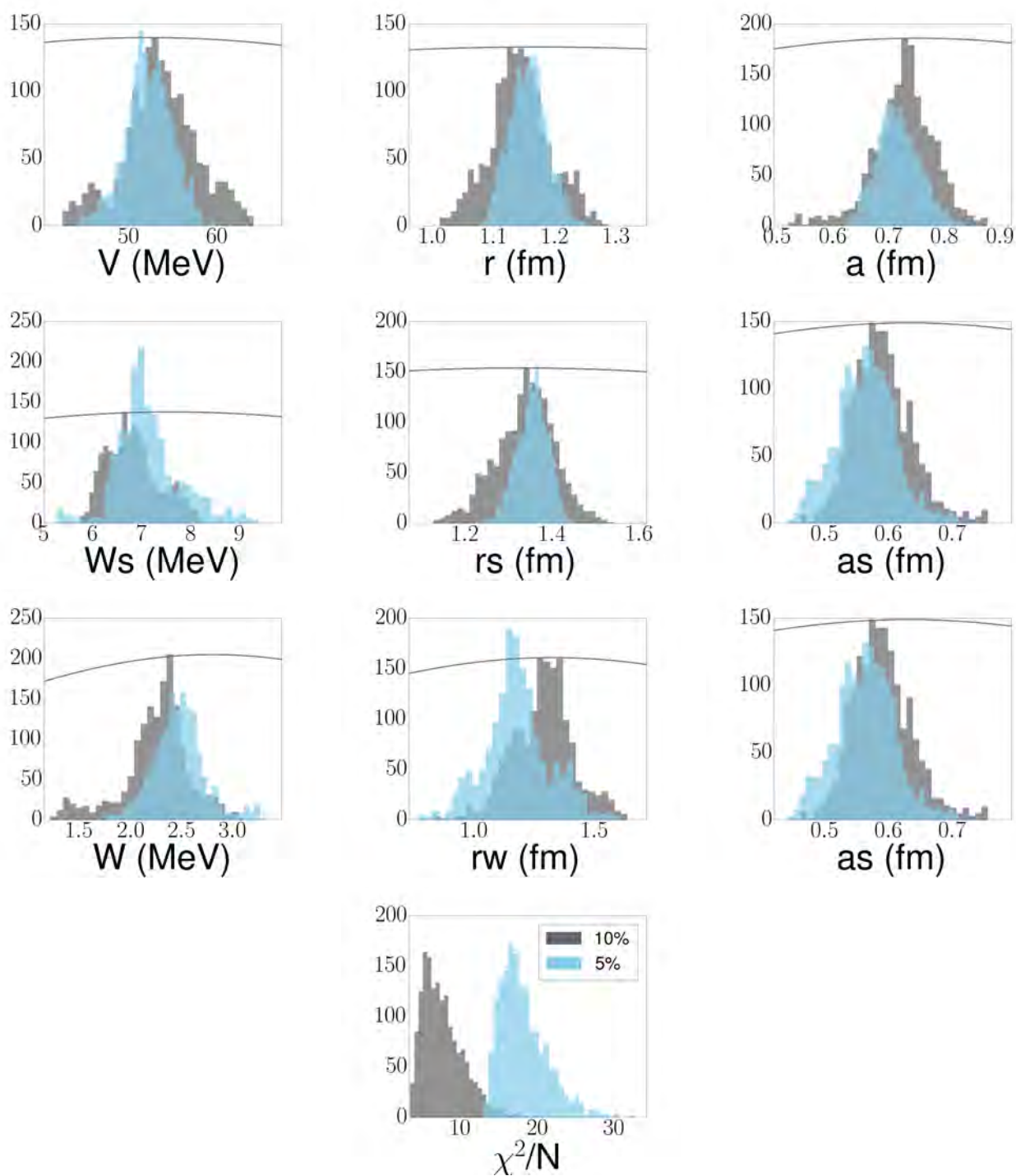
Figure 5.8: Same as Figure 5.5 for ^{48}Ca(p,p)^{48}Ca elastic scattering at 25.0 MeV.
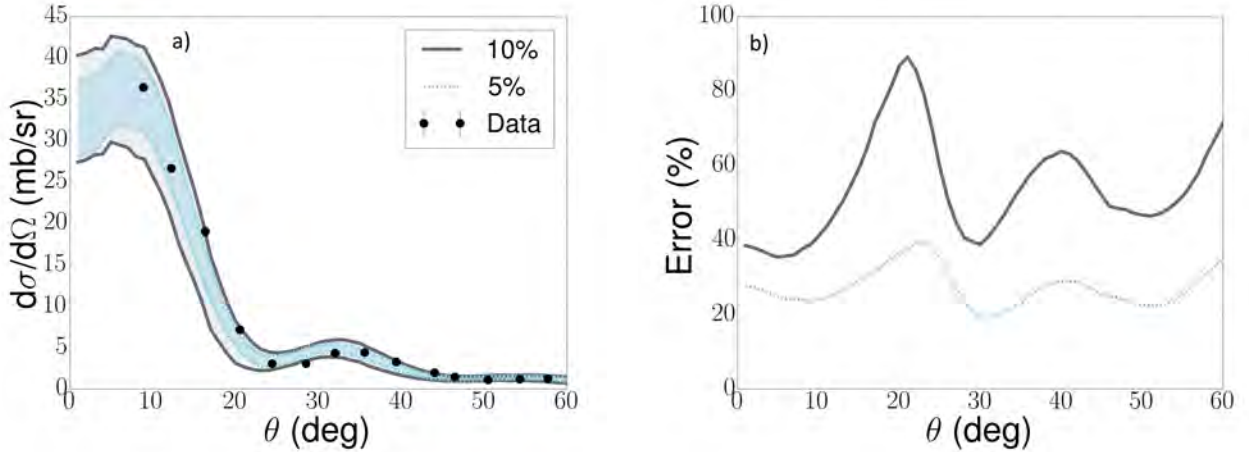
Figure 5.9: 95% confidence intervals for ^{48}Ca(d,p)^{49}Ca(g.s.) at 24.0 MeV (a), using 10% (gray) and 5% (blue) error bars on the experimental data for the elastic scattering of the incoming and outgoing channels and percentage uncertainties (b) using ADWA.

target scattering discussed in the previous section and fixing the properties of the bound states.

First, we construct the ^{48}Ca(d,p)^{49}Ca(g.s.) cross section at 24.0 MeV using the posterior distributions shown in Figures 5.5, 5.7, and 5.8. The 95% confidence intervals for this reaction are shown in Figure 5.9 when the nucleon elastic scattering distributions were constrained using 10% experimental errors (gray) and 5% experimental errors (blue). To have a quantifiable way to compare the two distributions, we define percentage uncertainty

$$\varepsilon = \frac{\sigma_{\text{max}}^{95} - \sigma_{\text{min}}^{95}}{\bar{\sigma}} \times 100\%, \tag{5.1}$$

which is the width of the confidence intervals divided by the mean value; this is defined at each angle. Although it is clear that the 95% confidence intervals are narrower when the 5% errors were used, this provides an indication of how much narrower (and is especially useful when comparing between the resulting intervals for different reaction models that might not

89

have the same shape). The comparison between the two percentage uncertainties is shown in Figure 5.9 (b).

In many of the proton scattering reactions (such as ^{48}Ca(p,p) at 14.03 MeV), we were not able to constrain a_w with the other parameters. This seemed to be true especially at higher scattering energies. The fact that removing this parameter had very little effect on the remaining posterior distributions and resulting elastic scattering cross sections shows the importance of correlations among the parameters and the constraining power of the elastic-scattering data. In principle, we could have constrained some combination of the optical model parameters (which could be found from a diagonalization of the covariance matrix), but significant study would have to go into determining the correct combination of these parameters across the range of elastic-scattering reactions. In addition, we would lose the evaluation power we have in knowing whether or not the parameters are reasonable. We know the range of physical values for the optical potential parameters, but this would be lost in fitting a combined set of parameters.

5.4   Transfer Reactions with DWBA

To construct transfer cross sections using DWBA instead of ADWA, the incoming channel has to be constrained with deuteron-target elastic-scattering data rather than nucleon-target scattering data. In this section, we go through the deuteron-target constraints for ^{48}Ca(d,p)^{49}Ca(g.s.) and construct the resulting transfer cross section using DWBA. The other three DWBA transfer reactions can be found in Appendix C. (Because deuteron scattering data was not available, this calculation was not performed for ^{116}Sn(d,p)^{117}Sn.)

We constrain the incoming channel for ^{48}Ca(d,p)^{49}Ca(g.s.) using elastic-scattering data

ε_{exp}	x	$\bar{x}_{^{48}\text{Ca}}$	$\Delta x_{^{48}\text{Ca}}$	$\bar{x}_{^{90}\text{Zr}}$	$\Delta x_{^{90}\text{Zr}}$	$\bar{x}_{^{208}\text{Pb}}$	$\Delta x_{^{208}\text{Pb}}$
	V	106.133	7.341	89.696	6.890	99.610	6.631
	r	1.027	0.050	1.198	0.051	1.146	0.042
	a	0.782	0.042	0.676	0.050	0.802	0.068
	Ws	8.579	0.630	9.262	0.788	8.159	1.052
10%	rs	1.337	0.051	1.285	0.064	1.401	0.080
	as	0.814	0.064	0.873	0.057	0.868	0.048
	W	2.695	0.294	2.407	0.229	2.855	0.263
	rw	1.128	0.132	1.357	0.125	1.356	0.086
	aw	—	—	—	—	—	—
ε_{exp}	x	$\bar{x}_{^{48}\text{Ca}}$	$\Delta x_{^{48}\text{Ca}}$	$\bar{x}_{^{90}\text{Zr}}$	$\Delta x_{^{90}\text{Zr}}$	$\bar{x}_{^{208}\text{Pb}}$	$\Delta x_{^{208}\text{Pb}}$
	V	105.488	7.660	90.209	5.208	97.665	5.243
	r	1.035	0.057	1.191	0.045	1.167	0.043
	a	0.774	0.046	0.687	0.043	0.759	0.064
	Ws	8.708	0.546	8.822	0.803	8.220	0.900
5%	rs	1.326	0.044	1.308	0.058	1.354	0.082
	as	0.818	0.056	0.861	0.048	0.894	0.060
	W	2.526	0.298	2.501	0.269	2.842	0.355
	rw	1.113	0.122	1.373	0.110	1.325	0.086
	aw	—	—	—	—	—	—

Table 5.6: Means (x) and widths (Δx) for deuteron elastic scattering posterior distributions shown in Figure 5.10 (columns two and three), Figure C.18 (columns four and five), and Figure C.22 (columns six and seven).

for ^{48}Ca(d,d)^{48}Ca at 23.2 MeV. The resulting posterior distributions are shown in Figure 5.10, again comparing the results using 10% experimental errors (gray histograms) and 5% experimental errors (blue histograms) as well as the initial prior distributions (gray solid). There is less of a reduction in the width of the posterior distributions here than there was for the nucleon-target scattering cases (Figures 5.5, 5.7, and 5.8); this is also seen in the 95% confidence intervals for the elastic-scattering cross sections, Figure 5.11. It is interesting to note that there is much less angular coverage for this deuteron elastic-scattering data than there had been for the corresponding nucleon scattering data.

To construct the transfer cross sections using DWBA, we use the deuteron-target elastic scattering posterior distributions from Figure 5.10 combined with the outgoing $(A + 1)$-
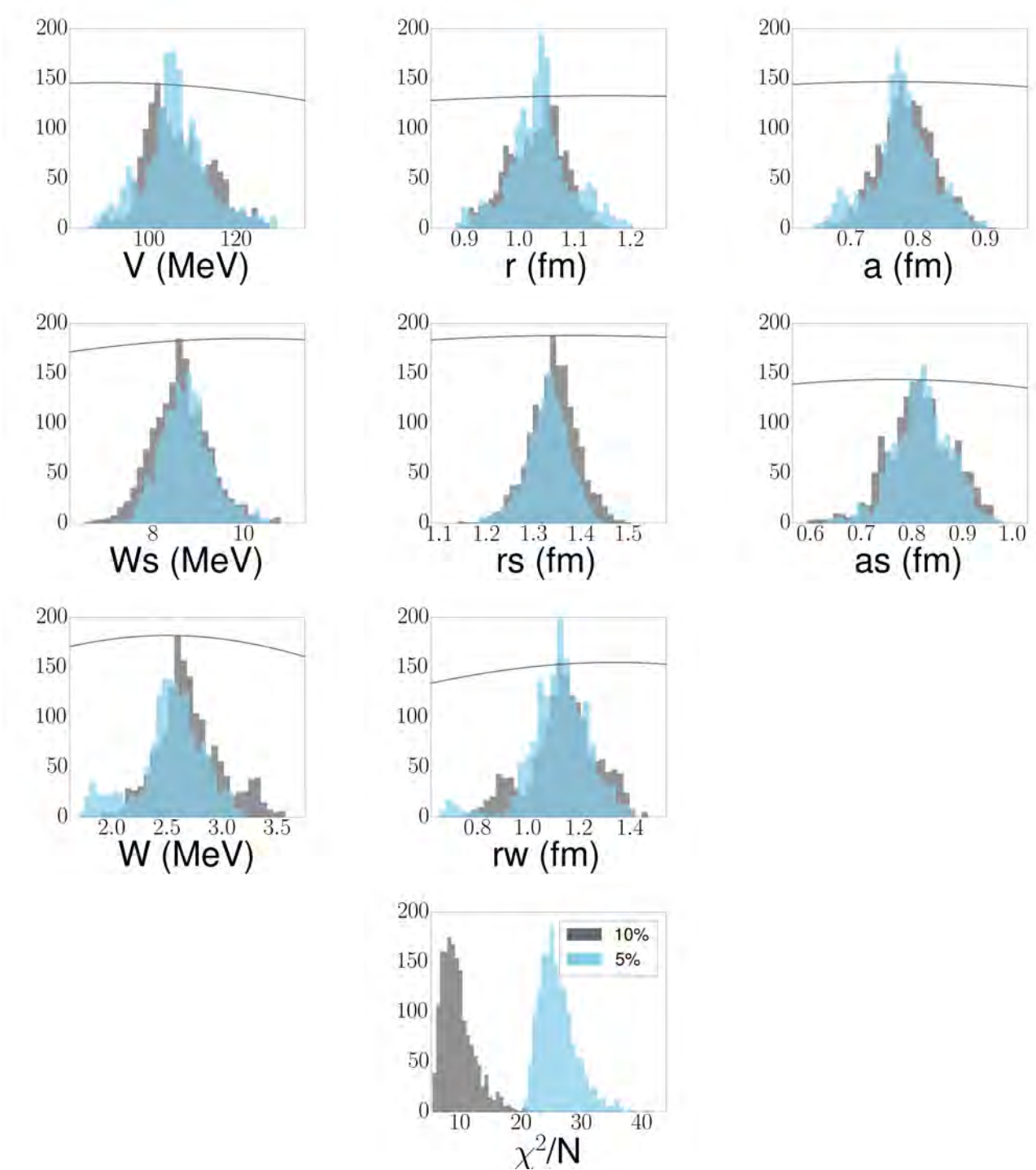
Figure 5.10: Posterior distributions (histograms) constraining the optical potential parameters using ^{48}Ca(d,d)^{48}Ca elastic scattering data at 23.2 MeV, comparing 10% errors on the experimental cross sections (gray) and 5% errors (blue). Original prior distributions are shown as gray solid lines.
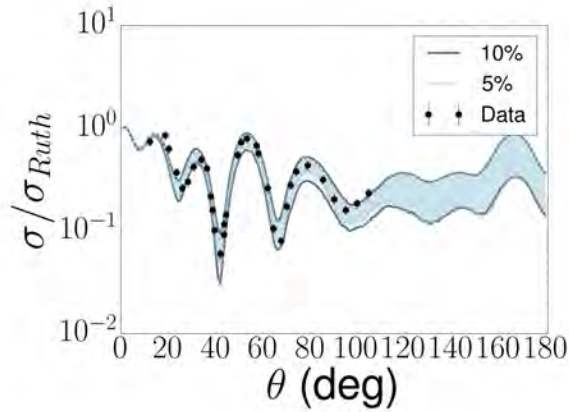
Figure 5.11: 95% confidence interval for the ^{48}Ca(d,d)^{48}Ca elastic scattering cross sections at 23.2 MeV from the posterior distributions of Figure 5.10 using 10% errors (gray) and 5% errors (blue).

nucleon elastic scattering posteriors from Section 5.3. (The outgoing channel is the same within these two reaction frameworks.) The bound state properties of the deuteron and transferred nucleon are defined as in Section 5.2. The 95% confidence intervals for the transfer cross sections are shown in Figure 5.12 using the 10% experimental errors (gray) and 5% errors (blue). These intervals are also compared to data, at 19.3 MeV. There is a slight mismatch between the energy at which the data was taken and the calculations performed here, but the comparison is to show that the computed cross sections are reasonable, rather than to make a statement about the validity of any extracted quantities.

5.5 Discussion

Once all five transfer reactions were calculated (see Appendix C for details of the four reactions not shown here), we could look for common trends among them. There are three themes to investigate: uncertainties from the optical potentials, the effect of reducing the experimental error, and the comparison between DWBA and ADWA. Before discussing each
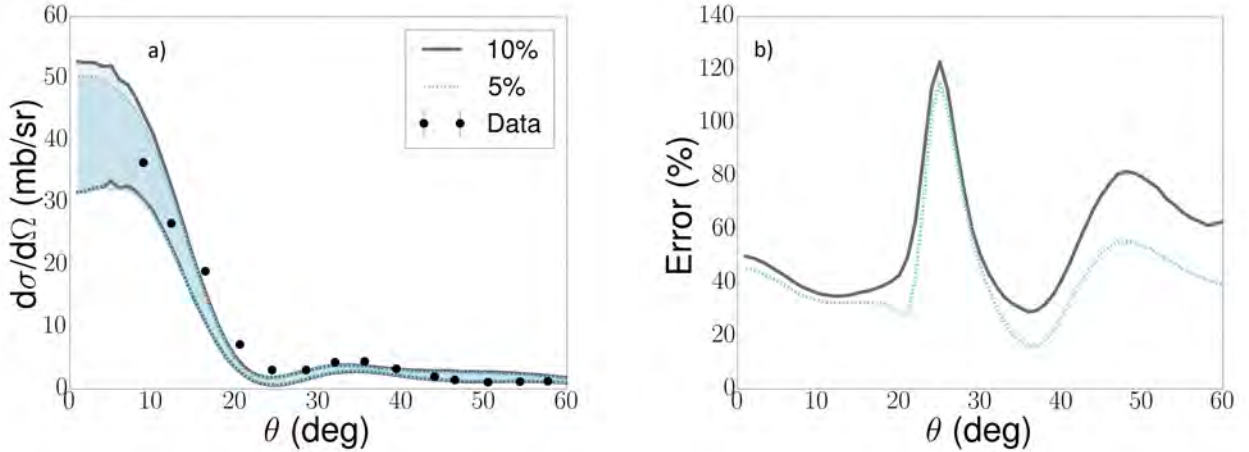
Figure 5.12: Same as Figure 5.9 using DWBA.

of these in detail, summaries of the results are presented. Table 5.7 gives an overview of each of the transfer reactions in terms of the percentage uncertainty (defined as in Eq. (5.1)). The uncertainty is calculated at the peak of the transfer cross section for both the 95% confidence intervals (two standard deviations, column six) and 68% confidence intervals (one standard deviation, column seven); the value at the peak is listed in column four, and the angle corresponding to this peak is given in column three. The extracted spectroscopic factors are listed in column five (where data was available). The theory used to calculate the transfer cross section (column two) is listed in terms of either ADWA or DWBA and the 10 or 5 indicates the experimental errors used in the calculation, corresponding to 10% or 5% of the experimental cross section value. Note that the DWBA calculations were not performed for ^{116}Sn(d,p)^{117}Sn because of a lack of (d,d) elastic scattering data near 44.0 MeV.

From Table 5.7, we can calculate two reduction factors, Δ_{exp} and Δ_{th}, both shown in Table 5.8. The first, columns three and four (for the 95% and 68% confidence intervals, respectively) shows the reduction in the uncertainty at the peak of the transfer cross section for the reaction model (column one) between the 10% and 5% experimental errors and is

Reaction	Theory	θ (deg)	Peak* (mb/sr)	SF	ε_{95} (%)	ε_{68} (%)
^{48}Ca(d,p)	ADWA10	6	34.09	1.07	35.76	16.47
^{48}Ca(d,p)	ADWA5	6	33.38	1.09	24.24	11.53
^{48}Ca(d,p)	DWBA10	3	41.56	1.02	47.93	22.57
^{48}Ca(d,p)	DWBA5	4	40.73	1.02	42.03	22.36
^{90}Zr(d,n)	ADWA10	31	2.16	—	44.44	17.59
^{90}Zr(d,n)	ADWA5	31	2.13	—	20.19	9.91
^{90}Zr(d,n)	DWBA10	31	3.04	—	38.82	21.52
^{90}Zr(d,n)	DWBA5	30	3.15	—	26.35	13.29
^{90}Zr(d,p)	ADWA10	14	16.63	0.74	47.62	21.95
^{90}Zr(d,p)	ADWA5	14	17.94	0.69	30.88	14.99
^{90}Zr(d,p)	DWBA10	16	17.09	0.72	58.86	29.02
^{90}Zr(d,p)	DWBA5	16	17.41	0.71	30.61	14.26
^{116}Sn(d,p)	ADWA10	1	4.64	—	121.77	48.31
^{116}Sn(d,p)	ADWA5	1	5.93	—	101.52	55.12
^{208}Pb(d,p)	ADWA10	11	13.32	—	37.84	18.95
^{208}Pb(d,p)	ADWA5	14	13.97	—	25.48	11.42
^{208}Pb(d,p)	DWBA10	9	7.44	—	72.72	43.84
^{208}Pb(d,p)	DWBA5	7	8.38	—	63.01	30.08

Table 5.7: Overview of the errors for each transfer calculation. Column one lists the transfer reaction, and column two lists the reaction theory used (ADWA or DWBA) with 5 or 10 indicating the percentage experimental errors used. The angle (in degrees) at which the cross section peaks is listed in column three, and the value of the cross section at the peak (in mb/sr) is listed in column four. The spectroscopic factors are given in column five (for the reactions that have been measured experimentally). Column six (seven) lists the percentage error (width of the confidence interval divided by the mean multiplied by 100%) at the peak assuming a 95% (68%) confidence interval. *Peak values are given in terms of the 95% confidence intervals. These values change by 5-10% at most when 68% confidence intervals are calculated (and fall within the 95% intervals).

Reaction	Theory	$(\Delta_{exp})_{95}$	$(\Delta_{exp})_{68}$	Error	$(\Delta_{th})_{95}$	$(\Delta_{th})_{68}$
^{48}Ca(d,p)	ADWA	32.22	30.03	10%	25.39	27.03
^{48}Ca(d,p)	DWBA	12.30	0.91	5%	42.33	48.43
^{90}Zr(d,n)	ADWA	54.58	43.69	10%	-14.48	18.26
^{90}Zr(d,n)	DWBA	32.12	38.24	5%	23.38	25.43
^{90}Zr(d,p)	ADWA	35.15	31.68	10%	19.10	24.36
^{90}Zr(d,p)	DWBA	47.99	50.87	5%	-0.88	-5.12
^{116}Sn(d,p)	ADWA	16.63	-14.10	—	—	—
^{208}Pb(d,p)	ADWA	32.65	39.71	10%	47.96	56.77
^{208}Pb(d,p)	DWBA	13.35	31.39	5%	147.29	62.03

Table 5.8: Overview of the reduction (or increase) factor between calculations using the 10% and 5% experimental errors for the reaction model listed in column two as well as the reduction (or increase) factor between the DWBA and ADWA calculations for the 10% and 5% experimental error calculations (column five). This is done for both the 95% and 68% confidence intervals. Details in text.

defined as

$$\Delta_{exp} = \frac{\varepsilon_i(\text{ADWA10}) - \varepsilon_i(\text{ADWA5})}{\varepsilon_i(\text{ADWA10})} \times 100\%. \tag{5.2}$$

All of the calculations show a reduction in uncertainty when the experimental error bars are decreased, except for ^{116}Sn(d,p)^{117}Sn but only for the 68% confidence interval. (This will be discussed in greater detail in Section 5.5.1.) Columns six and seven show the reduction factor between the DWBA and ADWA calculations for the experimental error listed in column five,

$$\Delta_{th} = \frac{\varepsilon_i(\text{DWBA}) - \varepsilon_i(\text{ADWA})}{\varepsilon_i(\text{DWBA})} \times 100\%. \tag{5.3}$$

A negative value indicates that the uncertainty from Table 5.7 was smaller for the DWBA calculation than for the ADWA calculation. Here, there were a few outliers (negative values), but these cases will also be discussed in more detail in Section 5.5.1. This factor could not be calculated for ^{116}Sn(d,p)^{117}Sn because the DWBA calculation was not performed for this reaction.

5.5.1 Outlying Cases

As mentioned previously, there were a few reactions in Table 5.8 that do not match the trends of the others from this table. These cases will be discussed briefly in this section.

The first case that we discuss is that of ^{116}Sn(d,p)^{117}Sn. Here, the theoretical uncertainties increased in the 68% confidence interval when smaller experimental error bars were used to constrain the posterior distributions. This is due to the distribution of cross section values in the posterior distribution. For the 68% confidence intervals, there is no strong peak in the distribution of values at each angle in the transfer cross section which results in the mean value being arbitrarily defined.

The next case we discuss is the single nucleon transfer onto ^{90}Zr. From Table 5.8, there are three cases where the DWBA calculation had a smaller theoretical uncertainty at the peak than the ADWA calculation. In principle, we would expect the ADWA calculation to have smaller uncertainties because the nucleon scattering data that is used to constrain the optical potentials that are included in the calculation are generally of better quality than deuteron elastic scattering data of DWBA - covering both a larger angular range and being measured more precisely. In addition, because ADWA explicitly takes into account the breakup of the deuteron in the field of the target, it should provide a more physical description of the reaction process compared to DWBA - which could be reflected in the theoretical uncertainty. Since this reduction of uncertainty between DWBA and ADWA is seen in every other reaction, it is worthwhile to investigate why these are different than the rest. One reason for this could be the quality of the deuteron-target optical potential [142] which seems to be particularly well-defined for ^{90}Zr-d scattering. Over the range of energies investigated in [142], the authors quote an overall χ^2 of 4.03 for ^{90}Zr; on the other hand,

97

$\chi^2 = 123.58$ for ^{48}Ca and $\chi^2 = 17.42$ for ^{208}Pb.

5.5.2 Uncertainties from the Optical Potential

We first focus on the uncertainties being introduced by the optical model parameters. Taking the 95% confidence intervals for the ADWA calculations from Table 5.7, the theoretical uncertainties range from 20% to 120% which are larger than the 10% to 30% that is naïvely assumed to come from the parameterization of the optical model. The uncertainties for the 95% confidence intervals for the DWBA calculations are, on average, larger, but this will be discussed in Section 5.5.4.

These uncertainties can be decomposed into the uncertainty that comes from each nucleon-target potential. This is shown in Table 5.9. For each reaction, we use only the posterior from one of the nucleon-target potential and fix the other two at the original potential values from [1]. (The only exception to this is for the entries marked d_{in} where the incoming neutron-target and proton-target posteriors are both varied and the outgoing nucleon-target potential is kept fixed. This mimics changing the incoming deuteron potential.) For each reaction, the largest uncertainties are introduced by the outgoing channel. For the ^{116}Sn(d,p)^{117}Sn reaction the most notable difference in the outgoing channel is that there is only data up to 88° (column five); however, this is the only case where there is such a drastic difference in the angular coverage of the data between the incoming channels and the outgoing one. For each of the other reactions, the angular coverage in the outgoing channel is as good as or better than in the incoming channels.

Table 5.9 also lists the quadrature uncertainty, for the 95% confidence intervals, calculated as

$$AD_{\text{quad}} = \sqrt{\varepsilon_{p_{in}}^2 + \varepsilon_{n_{in}}^2 + \varepsilon_{N_{out}}^2} \tag{5.4}$$

Reaction	Projectile	ε_{10}	ε_5	θ_{max} (deg)
^{48}Ca(d,p)	p_{in}	22.90	11.82	158
^{48}Ca(d,p)	n_{in}	15.82	7.96	143
^{48}Ca(d,p)	p_{out}	26.70	17.37	170
^{48}Ca(d,p)	d_{in}	26.08	15.61	—
^{48}Ca(d,p)	AD_{quad}	38.57	22.47	—
^{90}Zr(d,n)	p_{in}	18.44	15.28	165
^{90}Zr(d,n)	n_{in}	16.96	9.17	150
^{90}Zr(d,n)	n_{out}	26.04	12.08	159
^{90}Zr(d,n)	d_{in}	28.72	17.17	—
^{90}Zr(d,n)	AD_{quad}	36.14	21.53	—
^{90}Zr(d,p)	p_{in}	17.53	12.81	165
^{90}Zr(d,p)	n_{in}	13.78	8.92	150
^{90}Zr(d,p)	p_{out}	38.24	19.96	154
^{90}Zr(d,p)	d_{in}	23.77	19.18	—
^{90}Zr(d,p)	AD_{quad}	44.27	25.34	—
^{116}Sn(d,p)	p_{in}	80.50	64.60	169
^{116}Sn(d,p)	n_{in}	35.26	18.43	155
^{116}Sn(d,p)	p_{out}	87.05	79.64	88
^{116}Sn(d,p)	d_{in}	88.65	64.16	—
^{116}Sn(d,p)	AD_{quad}	123.70	104.19	—
^{208}Pb(d,p)	p_{in}	16.42	7.76	165
^{208}Pb(d,p)	n_{in}	22.35	12.92	154
^{208}Pb(d,p)	p_{out}	33.00	21.41	168
^{208}Pb(d,p)	d_{in}	30.98	19.62	—
^{208}Pb(d,p)	AD_{quad}	43.11	26.69	—

Table 5.9: For the reaction given in column one, percent errors, using 10% (5%) experimental errors, extracted at the peak of the cross section, column three (four). The projectile in column two indicates which part of the potential was varied (while the remaining nucleon-target potentials were fixed at their original parameterizations from [1]). (Here, the error on the deuteron channel comes from varying the incoming neutron and proton potentials simultaneously, and AD_{quad} are calculated as in Eq. (5.4).) Column five shows the maximum angle for which there is experimental data.

where ε_i gives the uncertainty coming from only varying either the incoming proton, incoming neutron, or outgoing proton/neutron potential while fixing the other two. All but three of these quadrature uncertainties are within 10% of the total uncertainty when all three potentials are varied simultaneously (as in Table 5.7), and all are within 20%. The quadrature uncertainties in DWBA show the same result when compared to the total uncertainties. This is a somewhat surprising result, as one might expect the total uncertainty to be less than the quadrature uncertainty, just considering the non-linearity of the models being studied.

There does not appear to be a strong correlation between the widths of the parameter posteriors and the uncertainties in the transfer cross sections. Over all, the potentials with wider posterior distributions (and larger uncertainties, not shown) do not contribute larger uncertainties on the associated transfer cross sections. Generally, the real volume depth, radius, and diffuseness have smaller uncertainties (defined as the width compared to the mean value of the distribution) than the imaginary terms. The imaginary volume depth, radius, and diffuseness have larger uncertainties ($\sim 10\%$ instead of a few percent). Ideally, we would like a quantifiable measurement of how the uncertainties between the parameters and the cross sections are correlated, but further study is needed to investigate this due to the nonlinearity of the models.

We also studied the effect of the angular range of the elastic-scattering data. To do this, we compared the posterior distributions of elastic and transfer cross sections when the entire range of data was used to constrain the optical model parameters and when only data up to $100°$ was used to constrain the parameters. Although the parameter posterior distributions are not shown, the resulting elastic scattering cross sections and transfer cross section are shown in Figure 5.13 and Figure 5.14. Especially for the proton scattering (Figure 5.13 (b) and (c)), the confidence intervals broaden significantly at backwards angles when only data

up to 100° is included. The resulting transfer distribution only shows noticeable differences at angles less than 10°. There is ~ 20% reduction in the theoretical uncertainty when the whole angular range of data is used to constrain the parameters, which is less of a reduction than in the comparison of experimental error sizes and model approximations.
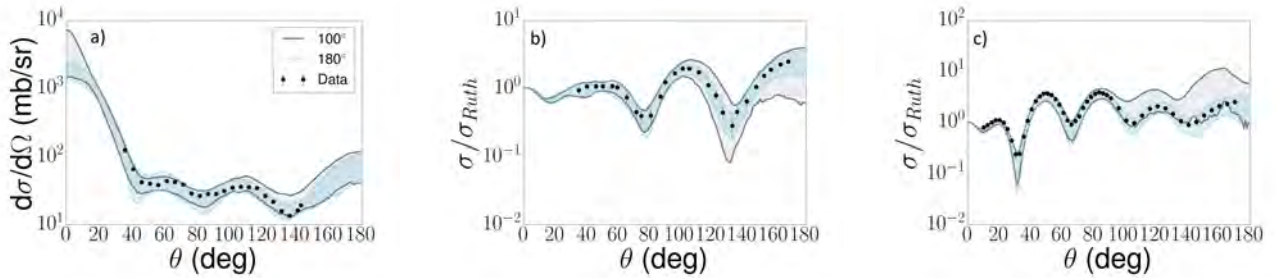
Figure 5.13: 95% confidence intervals when scattering data up to 100° (gray) and 180° (blue) was used to constrain the optical model parameters for (a) ^{48}Ca(n,n) at 12.0 MeV, ^{48}Ca(p,p) at 14.03 MeV, and ^{48}Ca(p,p) at 25.0 MeV.
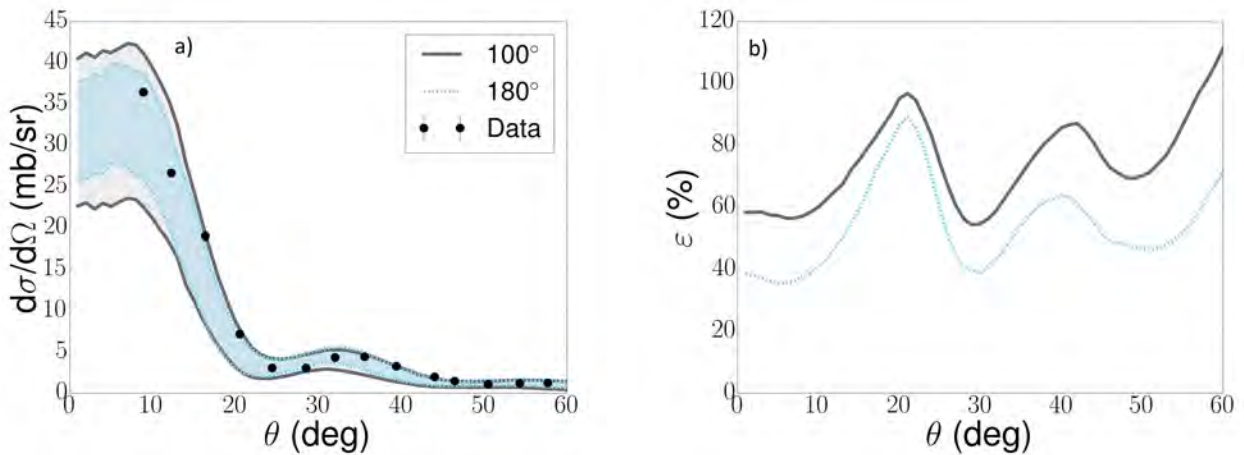
Figure 5.14: Same as Figure 5.9 when elastic-scattering data up to 100° (gray) and 180° (blue) were used to constrain the optical model parameters using ADWA.

5.5.3 Reduction of the Experimental Errors

We next study the effect that reducing the experimental error bars has on the resulting parameter distributions and the uncertainties of the cross sections. Although the experimental error bars are reduced by 50%, this reduction does not propagate to the uncertainties of the parameters or cross sections. We explore this in detail in Table 5.5 which lists the means and widths (standard deviation) for each of the parameter posterior distributions for ^{48}Ca-nucleon elastic scattering. The means are similar when the errors are reduced, and the widths decrease for many of the parameter distributions considered, although they are not all by $\sim 50\%$. The real depths, radii, and diffusenesses scale closer to 50% when the experimental error is reduced by that much, but this is not as notable for the imaginary parameters. In particular, we see several cases where the parameter widths actually increase when the experimental errors decrease, such as for r_w.

When we consider the 95% confidence intervals for the transfer cross sections, the theoretical uncertainties are smaller when 5% error bars are included on the data than when 10% error bars are used, for every case that was studied. However, it is clear from Table 5.8 (columns three and four) that the reduction of theoretical uncertainty at the peak of the calculation is not equal to the reduction in experimental uncertainty. While the reduction in experimental uncertainty was 50%, the only cases where the theoretical uncertainty was reduced this much were for two of the ^{90}Zr reactions. For most of the reactions, we find an $\sim 30\%$ reduction in the theoretical uncertainty.

Naïvely, since we have an exponentiated χ^2 as our likelihood, it appears that the only effect of reducing the experimental errors should be a factor in the likelihood, which would then simply scale the posterior distributions. However, we do not see a constant scaling

in the widths of the posterior distributions when the errors are reduced, nor do we see a constant reduction in the uncertainty in the transfer cross sections. In fact, for the ^{48}Ca(d,d) scattering, reducing the experimental errors reduces the widths of only half of the parameters causing only a slight reduction in the width of the confidence interval for the elastic cross section (Figure 5.11), and an $\sim 10\%$ reduction in the uncertainty in the DWBA calculation. This reduction (or lack thereof) is not consistent between models or among the targets studied.

5.5.4 Comparison between DWBA and ADWA

Finally, we directly compare the parametric uncertainties of the two reaction models. While this is not a substitution for rigorous model comparison and a more thorough evaluation of model uncertainties, comparing these two frameworks within the same parametric uncertainty quantification allows us to begin to form a picture of which model gives a more accurate description of the data. Table 5.8 shows the reduction factor between the theoretical uncertainty in ADWA and DWBA. In all cases (except the ^{90}Zr-d cases discussed previously), the ADWA calculations had a smaller uncertainty than the DWBA calculations. For ^{48}Ca(d,p)^{49}Ca and ^{90}Zr(d,p)^{91}Zr (which are the only two reactions where data has been taken at corresponding energies), the ADWA calculations better reproduce the shape of the experimental angular distributions. However, because of the width of the parametric uncertainty intervals, we cannot fully rule out one model or the other.

In each calculation, the reduction in the theoretical uncertainty from DWBA to ADWA is between 20% and 50% (with the exception of ^{208}Pb(d,p) which has an even larger reduction). The adiabatic calculations should better describe the physics of each reaction since they explicitly take into account the breakup of the deuteron in the field of the target which

103

has been shown to be important in many reactions [70]. Here, we provide another piece of evidence for this assumption. However, if we consider the spectroscopic factors extracted for ^{48}Ca(d,p) and ^{90}Zr(d,p) (see Table 5.7), there are differences between the two models of only a few percent. This is significantly smaller than the uncertainty introduced by the parameterization. To more rigorously compare between models, model selection methods must be introduced and consistent angular ranges for the data should be used - so that the models are being compared one-to-one with no external influence.

Chapter 6

Conclusion and Outlook

6.1 Conclusion

There are many sources of uncertainties within reaction theory, each of which should be investigated in a systematic way. In this work, we take the first step toward that ultimate goal by calculating the parametric uncertainties that arise from fitting the optical model parameters to elastic-scattering data. The two methods of uncertainty quantification discussed here create a path forward for further uncertainty studies.

First, we implemented a frequentist method based on using χ^2 minimization to construct 95% confidence bands. These bands were calculated from best-fit elastic-scattering angular distributions and then propagate to predicted transfer and inelastic cross sections. We fit six sets of elastic-scattering data for deuteron and neutron projectiles on targets with $A = 12 - 208$ and $E = 5 - 25$ MeV/u. Deuteron elastic-scattering data was fit to constrain the incoming scattering channel for constructing (d,p) transfer cross sections, and neutron elastic-scattering data was fit to predict inelastic cross sections. Because of the strong correlations in the elastic-scattering model, a correlated χ^2 function was introduced. These correlations were shown to be important for fitting elastic-scattering data: the fits produced were more physical and better reproduced the shape of the experimental angular distributions, the 95% confidence bands became wider, and the χ^2 values were lower than those

obtained when using the uncorrelated χ^2 function.

However, frequentist approaches are limited when taking non-parametric uncertainties into account. There is no clear path forward for calculating uncertainties arising from model simplifications which are particularly important considering the few-body approximations that are commonly used in reaction theory. Also, correlations in the model must be built in by hand, as was done for the angular correlations in χ^2_C. Because of this, the second uncertainty quantification method implemented was a Bayesian approach. This served to further quantify parametric uncertainties and opened the door for computing uncertainties from other sources.

Within the Bayesian framework, we used nucleon elastic-scattering data to constrain optical model parameters in order to construct (d,N) transfer cross sections using ADWA. We first investigated the effect of a variety of prior shapes on the posterior distributions for optical model parameters and found that a wide Gaussian prior allowed the experimental data to completely determine the resulting parameters. The widths of these parameter posterior distributions were significantly narrower than the original prior distributions. With this wide prior, elastic-scattering data was used to constrain parameters for nucleon-target interactions to predict (d,N) transfer cross sections with uncertainties defined by 95% confidence intervals. This study was also performed using deuteron elastic-scattering data to constrain the deuteron-target scattering wave function. Then, transfer cross sections were constructed with uncertainties using DWBA.

These studies were performed for five different transfer reactions for $A = 48 - 208$ and $E = 10 - 25$ MeV/u, assuming errors of 10% and 5% on the experimental elastic-scattering cross sections. Although the 95% confidence intervals for the elastic-scattering cross sections were well-constrained, this was not the case for the 95% intervals of the resulting transfer

cross sections, regardless of the reaction model. Uncertainties at the peak of the transfer cross section range from 20% to 120%, depending on the target, although the uncertainties under ADWA are smaller than those from DWBA for nearly all cases. Still, these uncertainties are large enough that transfer data cannot distinguish between the two reaction frameworks. Decreasing the experimental errors by a factor of two decreases the resulting uncertainties in the transfer cross sections but by less than 50%.

There are many differences between these two uncertainty quantification methods. Computationally, the fitting process requires more time for the Monte Carlo than the standard frequentist χ^2 minimization, but the MCMC is significantly more autonomous. Once sufficient input parameters (step size, prior shape, etc.) have been identified, the MCMC requires no human interaction, unlike the χ^2 minimization in which a multi-step process is often required to find a minimum within the physical parameter space. As long as the data drive the minimization in both methods, the "best-fit" parameter sets should be similar. There are also philosophical differences between the two methods. Frequentist methods rely on the standard construction of probability, which gives the likelihood of an outcome relative to other possibilities. In this case, confidence bands define regions that the data should fall within given the values of parameters that we have defined as the best fit. Instead, Bayesian methods define the probability for a single event without direct comparison to others. In this interpretation, posterior distributions denote the likelihood of the parameterization being reality based on the data.

Ultimately, the Bayesian philosophy provides a more consistent interpretation of the uncertainties. It also makes explicit the assumptions that go into this interpretation, something that is hidden in frequentist methods. Furthermore, there is a more natural framework on top of which to build future uncertainty quantification studies, especially those related to

107

the simplifications of the model. Although these two methods of uncertainty quantification have philosophical and practical differences in their implementations, one message is absolutely clear: the 10-30% uncertainties that have been assumed in association with the choice of optical model parameters have been greatly underestimated, at least when only elastic scattering is used to constrain the parameters of the optical potentials. This calls for both a better understanding of the range of data that is necessary to fully constrain these parameters and the impact of the data on the level of correlations between parameters.

6.2 Outlook

The parametric uncertainties that we have investigated here are just the beginning. Beyond the uncertainties associated with the parameters in the scattering states, there are also uncertainties associated with the bound state of the deuteron and the transferred nucleon to the target. The deuteron bound state is well-described in so much as the transfer reactions discussed here are insensitive to the differences in the various nucleon-nucleon potentials that have been developed [143]. The mean-field parameters of the nucleon-target bound states are not as well-defined. The type of data that is used to constrain this interaction could greatly change the shape of the mean field producing this bound state (binding energies contain different information than a quantity that probes the external region of the reaction).

In addition to parametric uncertainties, systematic uncertainties coming from the choice of the model must be taken into account. These uncertainties will add to the already large parametric uncertainties, and in order for the model uncertainties to be meaningful, the parametric uncertainties must be under control (since these caused the models studied in this work to be indistinguishable). The reaction models implemented here represent significant

simplifications to the full three-body solution on top of simplifications that were already made to the many-body solution. Several studies have shown that the physics that is incorporated within these more exact models is important to describe experimental results (such as the necessity of including deuteron break-up [70]), but it is possible that incorporating this extra physics within the model still makes the sophisticated model identical to the simplified model, within uncertainties. If two calculations are identical within the full theoretical uncertainties, there is no longer a reason to prefer one over the other (outside of physical arguments) until the uncertainties are reduced. This, in principle, makes a powerful (and perhaps somewhat unsatisfactory) argument as to when an approximate calculation can replace an exact one.

However, model uncertainties can provide a better understanding as to where model improvements can be most impactful. From the Bayesian results presented in this thesis, it was found that the largest parametric uncertainty in the transfer cross sections comes from the elastic-scattering potential in the outgoing channel. This could indicate that the description of this channel is insufficient. Model uncertainties could provide similar insight, allowing us to pin-point specific areas of the theory that can be improved instead of overhauling entire frameworks.

The methods that we have developed here should be integrated into more complex reaction frameworks. These frameworks become increasingly important as more complex reactions are described (multi-step, breakup, halo nuclei, etc.). At this point, interpolations and extrapolations are often made beyond the region of validity of a given parameterization or reaction formalism, and uncertainties will also have to be propagated. Having a reliable way to do this is another important path to pursue, as uncertainty quantification gains wider acceptability and use.

As it becomes increasingly important to always include theoretical uncertainties, the

codes for performing these uncertainty quantification calculations should be integrated into the current available reaction theory framework. New codes should then be developed with this goal in mind. This includes optimizing any numerical algorithms and parallelizing codes. This also calls for the development of uncertainty quantification methods that do not rely on fitting to experimental data since it is likely that data will not be available for many cases far from stability.

Finally, it is becoming increasingly important to understand the information content of experimental data as it pertains to constraining model parameters. In this work, we only used elastic-scattering data to fit the optical model parameters, but it has been shown [144] that additional data, such as total cross sections, provide further constraints. As we look ahead to constructing new global optical potentials (with uncertainties), it is crucial to identify the data sets that will be best for this purpose (whether that includes a range of beam energies, targets, asymmetries, or observables). A principle component analysis (PCA) which identifies unique degrees of freedom should be particularly useful. We have performed preliminary studies demonstrating that elastic, inelastic, and transfer angular distributions do not provide independent constraints on the optical model parameters. However, this type of correlation study should also be performed for other observables such as total and reaction cross sections, cross sections of higher-lying inelastic states, and nuclear radii. Including a greater variety of observables in a fit could reduce the theoretical parametric uncertainties to a greater extent than was seen by reducing the experimental error bars on the elastic scattering data alone. The PCA would also identify the number of independent parameters within the models and identify if there is any chance of fully constraining each individually.

Overall, the future of uncertainty quantification and reaction theory is bright. There are new and exciting projects which will significantly increase the knowledge in the field and

provide opportunities for students as well as experts. The work that has been done here only skims the surface of what is available and hopefully opens the door for many future studies as described above.

APPENDICES

Appendix A

Tests of MCMC Code

Before using the Monte Carlo technique described in Section 3.2.2 to compute posterior distributions for the reactions of interest, the code that was written as a wrapper for FRESCO [118] had to be tested in order to make sure that we understood the way it worked, its limitations, and how the inputs affected the resulting posterior distributions. This testing is described here. This appendix also provides the remaining prior shape tests referenced in Section 5.1.

Numerical Tests

A crucial part of the Monte Carlo process is the burn-in stage, which contains the accepted parameter draws before the posterior distribution is being sampled. The length of the burn-in, $N_{burn-in}$, varies based on the step size in parameter space as well as how close the initial parameter set is to the maximum likelihood. It is hard to determine a fixed number of steps after which the burn-in will always be completed. For this reason, the burn-in within this code is implemented in a variable manner. Once 500 parameter sets have been rejected in a row (without another parameter set being accepted by the MCMC criteria of Eq. (3.33)), the burn-in finishes and parameter sets are recorded. This condition of five hundred parameter sets was found to be a sufficient indication that the Monte Carlo had found a relative minimum and was not still exploring the parameter space.

The burn-in also uses a step size that is five times larger than the step size defined in the input file. This not only causes the burn-in to run more quickly but allows more of the parameter space to be sampled; also, the minimum that is ultimately found during the burn-in will be sampled more finely than the initial search. During the burn-in, parameter sets are accepted such that the likelihood weighted by the prior distribution is strictly maximized, instead of being subject to the criteria of Eq. (3.33) which samples around the currently accepted parameter set.

Once the burn-in is completed, the χ^2 values no longer steadily decrease but remain bounded within a certain region (depending on the minimum value and the shape of the parameter space). Therefore, a successful burn-in can be evaluated based on the χ^2 values that result from the Monte Carlo draws. An example of this is shown in Figure A.1, for ^{90}Zr(n,n) elastic scattering at 24.0 MeV. It can be seen that the χ^2 values (bottom) are not decreasing but rather jump randomly across all of the runs that were performed.

Because the code was parallelized, the independence of the processors also had to be tested. In addition, this verifies the independence of the random number generator for each processor - so parameter sets are not being pulled in the same order across all of the processors. In Figure A.1, the recorded values of each parameter are shown as a function of run number, where each color indicates a draw using a different processor for the same reaction. In every case, the first draw of all processors has the same value, due to the design of the code. Each processor performs a separate burn-in, after which the likelihoods from each processor are compared. The largest likelihood - and corresponding parameter set - is then given as the starting point of the Monte Carlo sampling for each of the processors, hence the identical starting points for each variable.

However, after this initial parameter set, each of the processors follows an independent
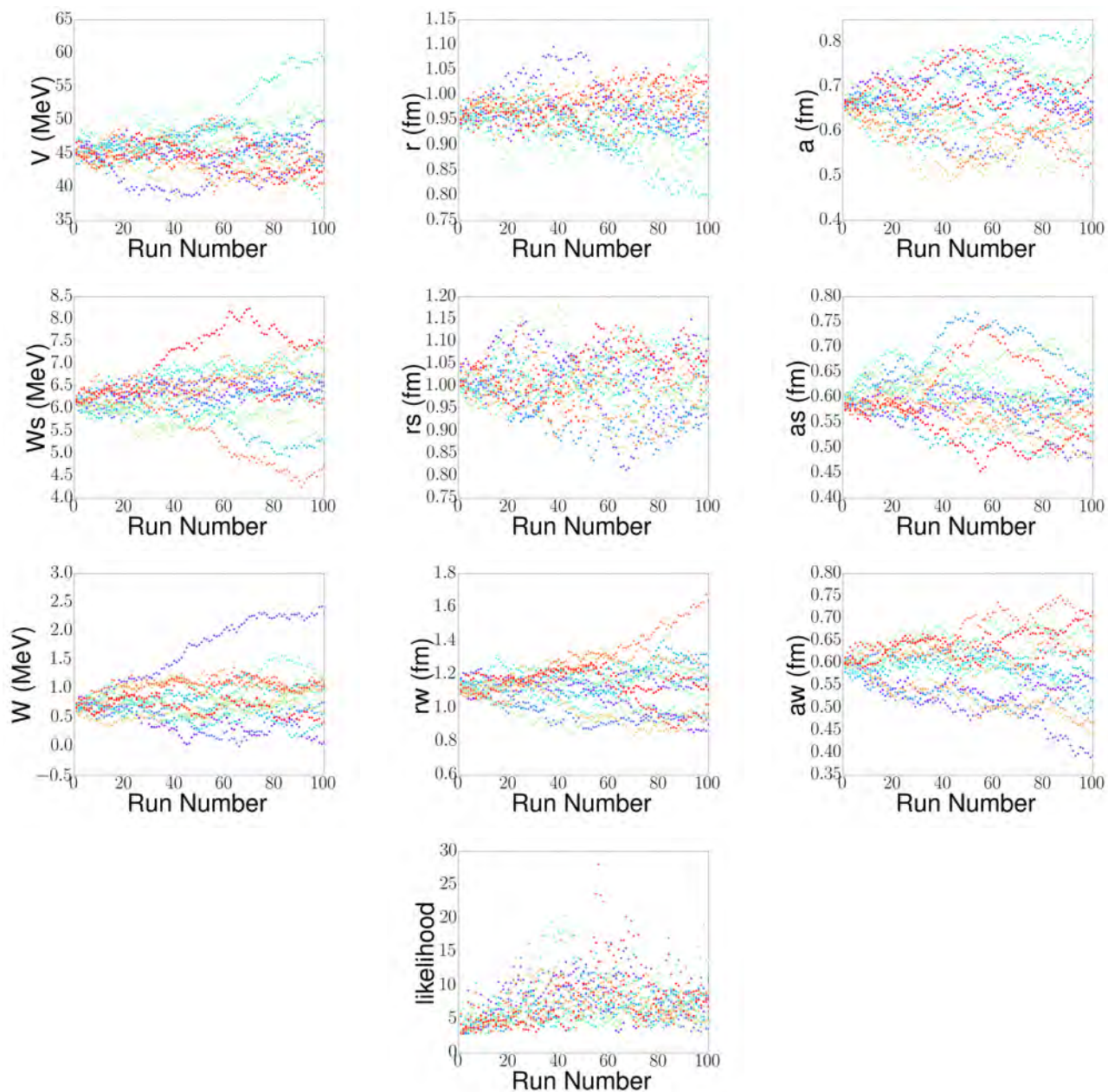
Figure A.1: Recorded parameter values as a function of run number from the Monte Carlo process, constrained by elastic scattering data for ^{90}Zr(n,n)^{90}Zr at 24.0 MeV. Each color denotes the processor that was used to make the parameter draws.

115

path through parameter space in the vicinity of the minimum, as seen by the diverging trajectories in Figure A.1. We also see that, although each parameter fluctuates, its value does not change drastically over the course of the calculation - and the parameter values fluctuate around a mean, instead of all drifting toward a different value (which would be an indication that the burn-in is not complete). This fluctuation also indicates that the sampling is coarse enough. Finally, when parameter sets are written, only one out of every ten accepted parameter sets is saved to file as part of a thinning process. This ensures that the parameter draws within the posterior are independent of one another (since parameter draws from Monte Carlo methods are by definition not independent). As can be seen in Figure A.1, for a given processor, the parameter values do not follow a smoothly varying curve but instead fluctuate around some mean value.

It is clear that some of the parameters, for a single processor, tend to deviate from the rest of the runs (for example, the purple points in the draws for W). However, in the corresponding χ^2/N plot, these values are not following any sort of distinctive trend. This indicates that the minimum is being sampled instead of a path being followed through parameter space.

Step Size Comparison

In Section 5.1, we showed one example of the effect of the step size on the posterior distribution and resulting cross-section confidence intervals. (Again, recall that the step size is defined based on the original parameterization for each system. Quoted here are the scaling factors, ϵ, used to compute each step size, where the new parameter set is drawn from a Gaussian distribution centered around the previous parameter set, $\mathbf{x}_f \sim \mathcal{N}(\mathbf{x}_i, \epsilon \mathbf{x}_0)$.) Three

more examples, neutron and proton scattering on a range of target masses at several energies, are examined in this section, to insure that the conclusions that were drawn from the ^{90}Zr-n scattering cases are robust.

Parameter	V	r	a	Ws	rs	as	W	rw	aw
Width (L)	100.0	1.3	0.8	80.0	1.3	0.9	40.0	1.3	0.9
Width (M)	40.0	0.7	0.5	30.0	0.7	0.5	10.0	0.7	0.5

Table A.1: Row two (three) shows the widths for the wide (medium) Gaussian prior for each of the listed parameters. The mean for each of the prior distributions was the original parameter value for each target-projectile system, defined by Becchetti and Greenlees [1]. Depths are given in MeV and radii and diffusenesses are given in fm.

Figure A.2 shows the values of ϵ tested for fitting ^{120}Sn(n,n) elastic scattering at 13.9 MeV, using the wide Gaussian prior defined in Table A.1. This assumption was also used to compare scaling factors for ^{48}Ca(p,p) elastic scattering at 21.0 MeV (Figure A.3) and ^{90}Zr(p,p) elastic scattering at 40.0 MeV (Figure A.4). For nearly all examples, $\epsilon = 0.001$ was too small; the minimum here is significantly different than those for the other values of ϵ. It is also clear that $\epsilon = 0.05$ is to large - the χ^2 values have a large spread and the parameters are not constrained. With this value, many of the parameters extend far beyond their physical ranges. The parameter distributions for $\epsilon = 0.002, 0.005, 0.01$ have nearly the same behavior as one another (which we expect to happen once the step size for each parameter becomes large enough), and the decision comes down to the percentage of parameters accepted. Ideally, 50% of the parameter sets should be accepted by the Monte Carlo criteria of Eq. (3.33) and 50% should be rejected [101]. The value of ϵ for which this happens is between 0.005 and 0.01.

Also for ^{90}Zr(p,p) elastic scattering shown in Figure A.4, the a_w values range anywhere from 0 to 12 fm when the Gaussian priors were used. This is significantly outside of a physically allowable range, and the relatively flat distribution suggests that this parameter

is not well constrained by this data. This was also observed for several of the fits shown in Chapter 5 with little to no effect on the cross section confidence intervals. Thus, even though these parameters are unrealistic, it should not affect the conclusions that we draw from the tests presented here. (For the physics cases we study, a_w is kept constant.)

Figure A.5 shows the elastic-scattering cross sections using the five ϵ values for each of these reactions. It is again clear that $\epsilon = 0.05$ is much too large. In all cases, except for ^{120}Sn(n,n) elastic scattering, the angular distribution for this factor is completely different than the others. In only one case (^{90}Zr(p,p), Figures A.5 c)), $\epsilon = 0.001$ is radically different: the confidence bands formed from this set of parameter draws is much narrower than the others. This is consistent with the very narrow parameter distributions for $\epsilon = 0.001$ in Figure A.4. In all three cases, the cross sections resulting from the scaling factors of 0.005 and 0.01 are nearly identical, and as mentioned previously, this is also the range where half of the Monte Carlo draws are accepted.

Comparison of Prior Shapes

The comparison of prior shapes for each ϵ values for ^{90}Zr(n,n)^{90}Zr at 24.0 MeV have been previously shown in 5.1, but the same exercise was repeated for other three scattering reactions. Here, $\epsilon = 0.005$ was chosen to compare the four prior types, two flat priors and two Gaussian priors. The widths of the wide and medium Gaussian priors are given in Table A.1 (the means for each Gaussian were the original parameter values defined in [1]); the parameter limits for the two flat priors are given in Table A.2. The posterior distributions are shown in Figures A.6, A.7, and A.8 for the elastic scattering of ^{120}Sn(n,n) at 13.9 MeV, ^{48}Ca(p,p) at 21.0 MeV, and ^{90}Zr(p,p) at 40.0 MeV, respectively.

Parameter	Min (W)	Max (W)	Min (M)	Max (M)
V	10.0	110.0	30.0	70.0
r	0.5	1.8	0.9	1.6
a	0.2	1.0	0.4	0.9
Ws	0.0	80.0	0.0	30.0
rs	0.5	1.8	0.9	1.6
as	0.0	0.9	0.2	0.7
W	0.0	40.0	0.0	10.0
rw	0.5	1.8	0.9	1.6
as	0.0	0.9	0.2	0.7

Table A.2: Minimum and maximum parameter values for the wide (columns two and three) and medium (columns four and five) flat prior distributions. (Prior distributions were not centered around the original parameterization.) Minima and maxima are given in MeV for the depths and fm for the radii and diffusenesses.

In each case (akin to what was shown in Section 5.1), the posterior distributions for the real depth, radius, and diffuseness are nearly identical, regardless of the prior shape. For the imaginary parts of the potential - both the volume term and surface term - this is not the case. Especially for the imaginary depths, each of the priors can give rise to distinct peaks within a realistic parameter range. These distinct peaks are often seen within the corresponding radius or diffuseness as well for the same potential term. For the two flat priors, one can often see sharp cut-offs in the parameter space of the posterior distribution where the parameter came upon the edge of the prior distribution, although this is more common for the medium than for the wide flat prior.

However, looking at the elastic-scattering cross sections, Figure A.9, each of the angular distributions is nearly identical. The only exception to this is for the flat priors when some parameter ran up against its boundary, as for ^{90}Zr(p,p) (c). In cases such as this, the cross section bands are narrower than the bands formed by taking the Gaussian prior distributions. The similarities in the majority of the cross sections is indicative that it is the correlations between the parameters, more so than the parameter distributions themselves,

that determine the width of the cross-section confidence bands.
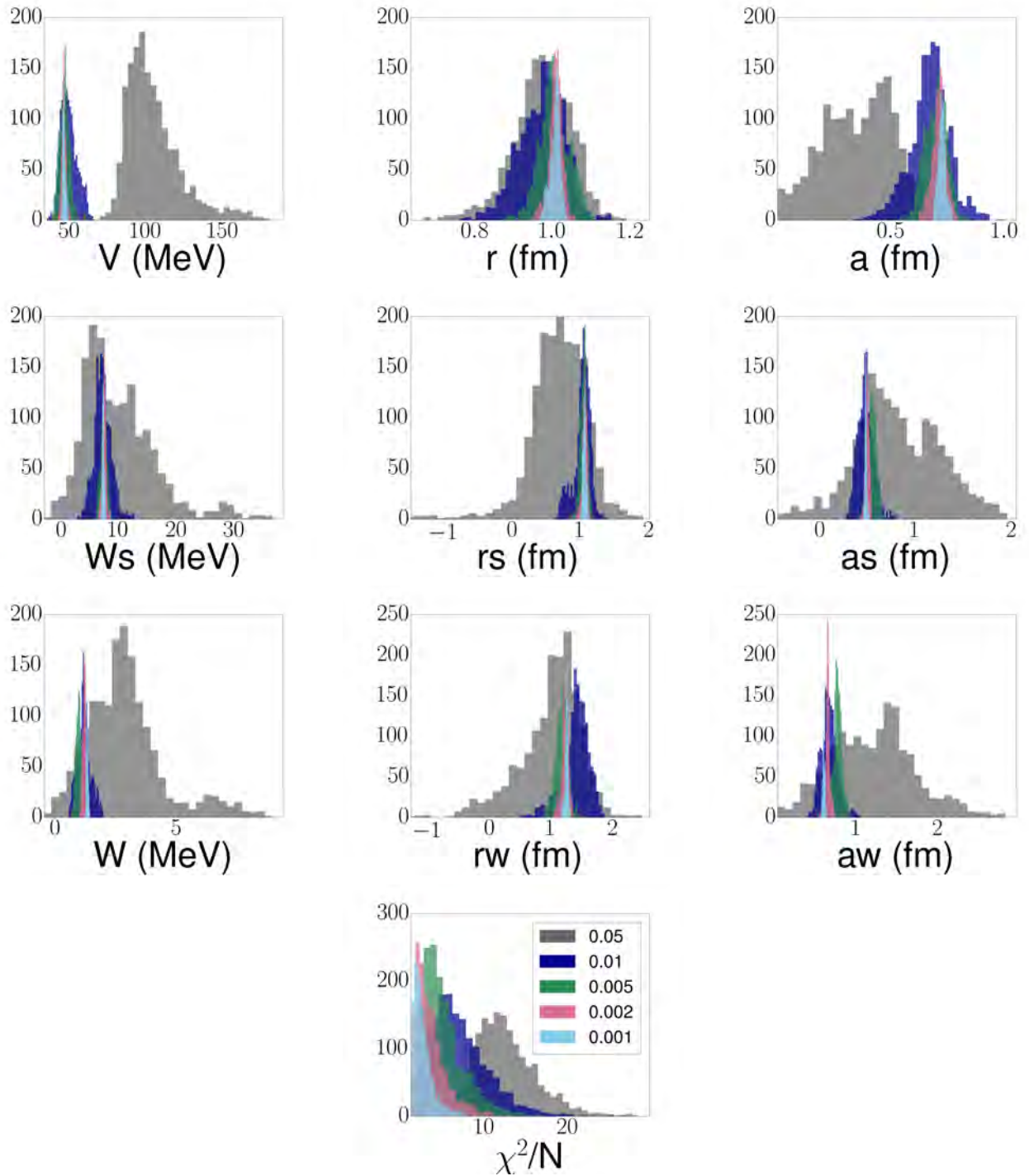
Figure A.2: Comparison between five values of ϵ (given by the legend on the χ^2/N plot) for the wide Gaussian prior using ^{120}Sn(n,n) elastic scattering at 13.9 MeV. The experimental errors on the data used in the Monte Carlo were taken to be 10% of the data values for each angle.
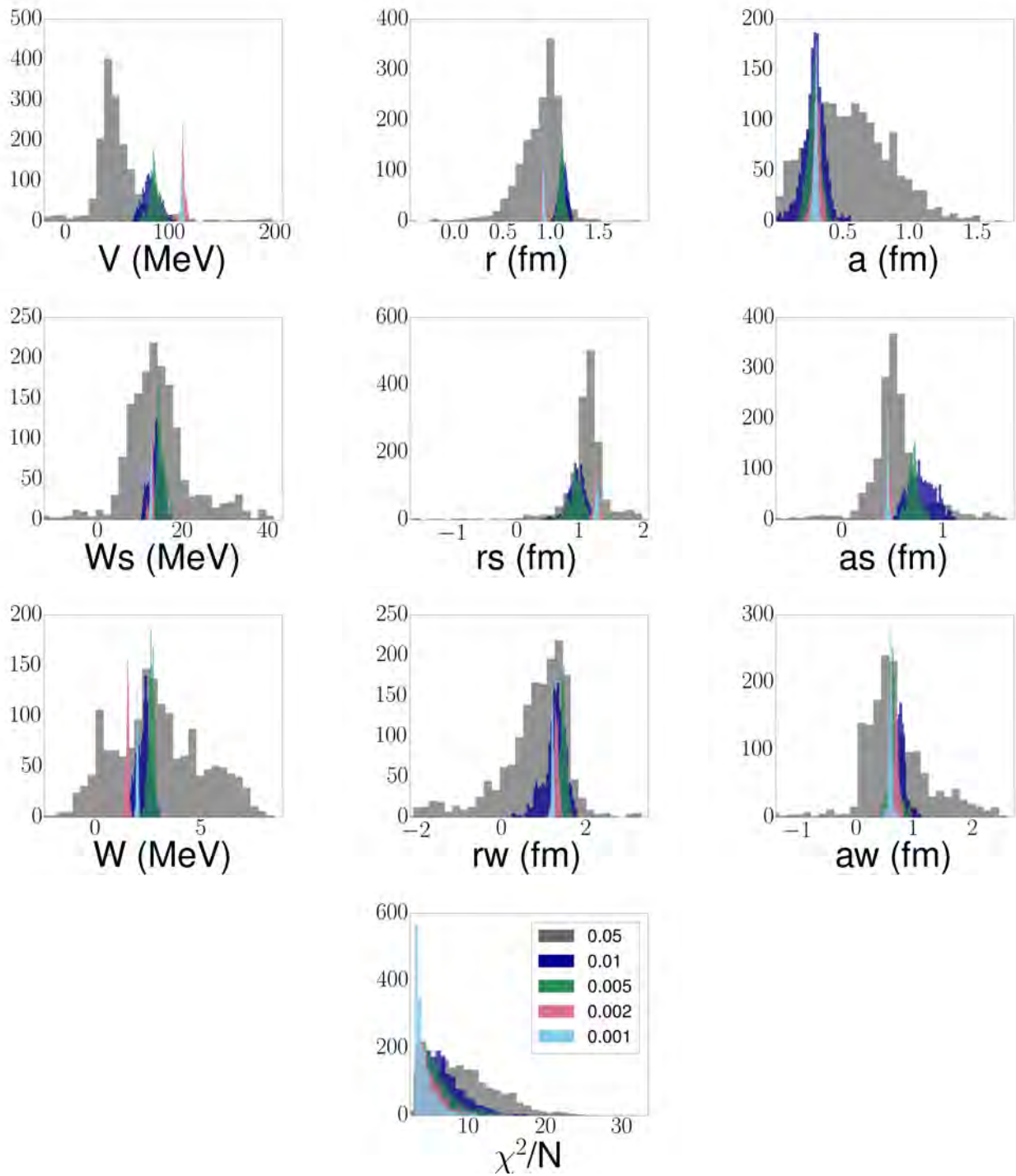
Figure A.3: Same as Figure A.2 for ^{48}Ca(p,p) elastic scattering at 21.0 MeV.
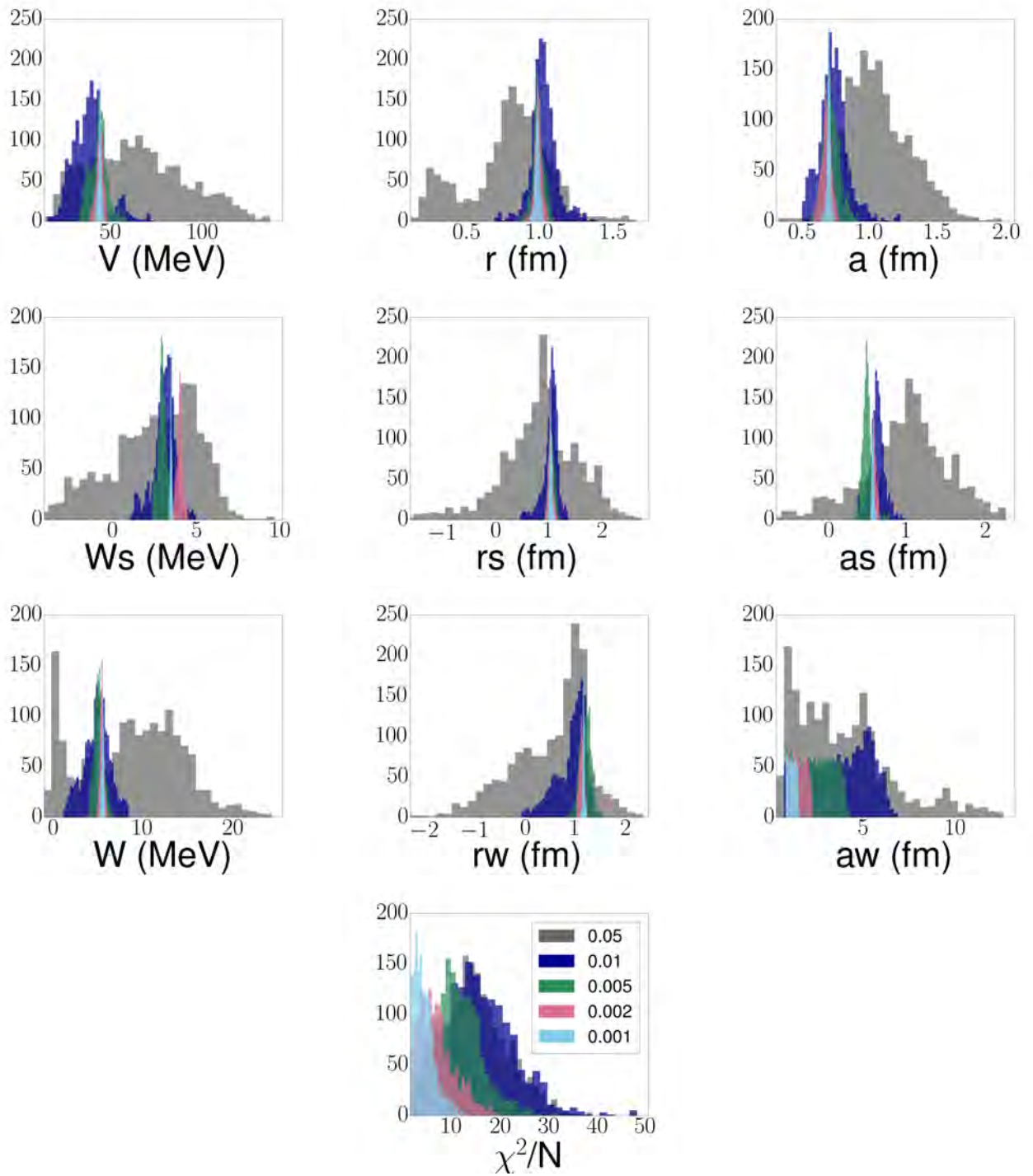
Figure A.4: Same as Figure A.2 for ^{90}Zr(p,p) scattering at 40.0 MeV.
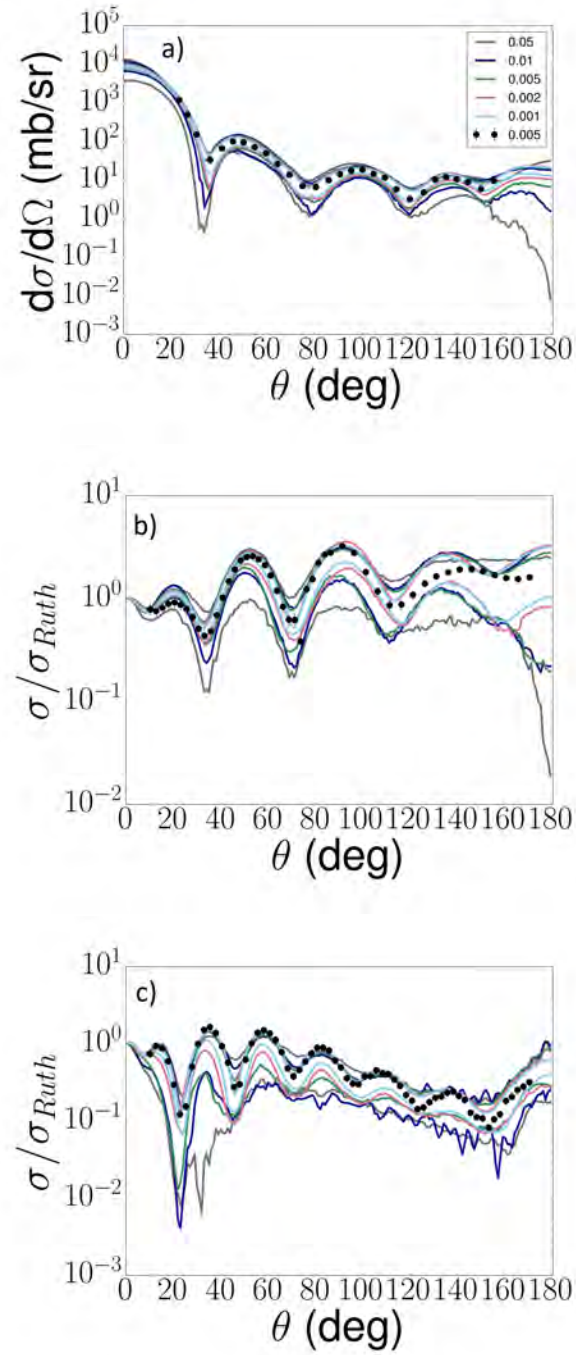
Figure A.5: Comparison of results using different ϵ (with the wide Gaussian prior) for the elastic scattering of (a) ^{120}Sn(n,n) at 13.9 MeV, (b) ^{48}Ca(p,p) at 21.0 MeV, and (c) ^{90}Zr(p,p) at 40.0 MeV.
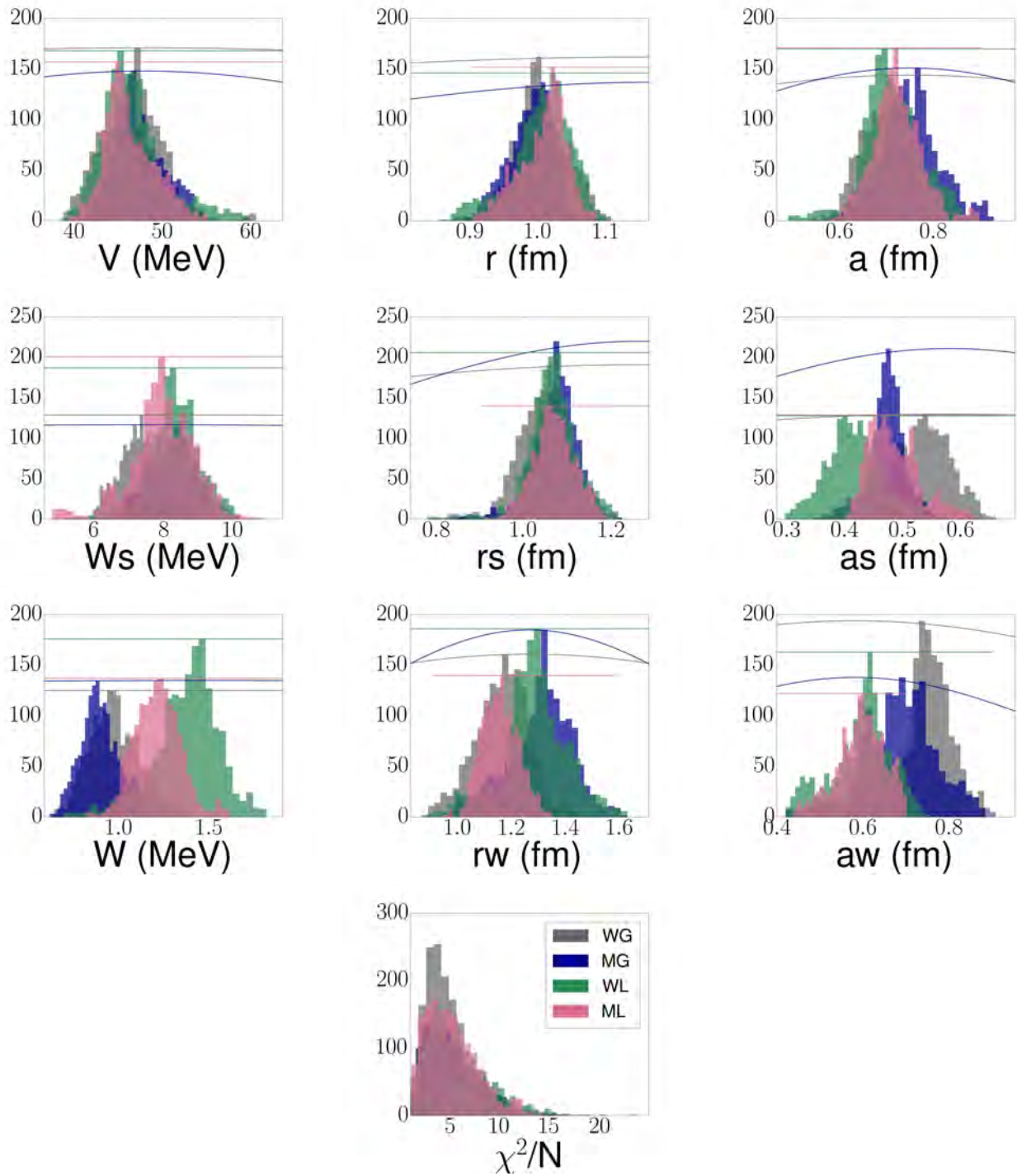
Figure A.6: Comparison between four different prior types (wide Gaussina - WG, medium Gaussian - MG, wide flat - WL, and medium flat - ML) for $\epsilon = 0.005$ using ^{120}Sn(n,n) elastic scattering at 13.9 MeV. The experimental errors on the data used in the Monte Carlo were taken to be 10% of the data values for each angle.
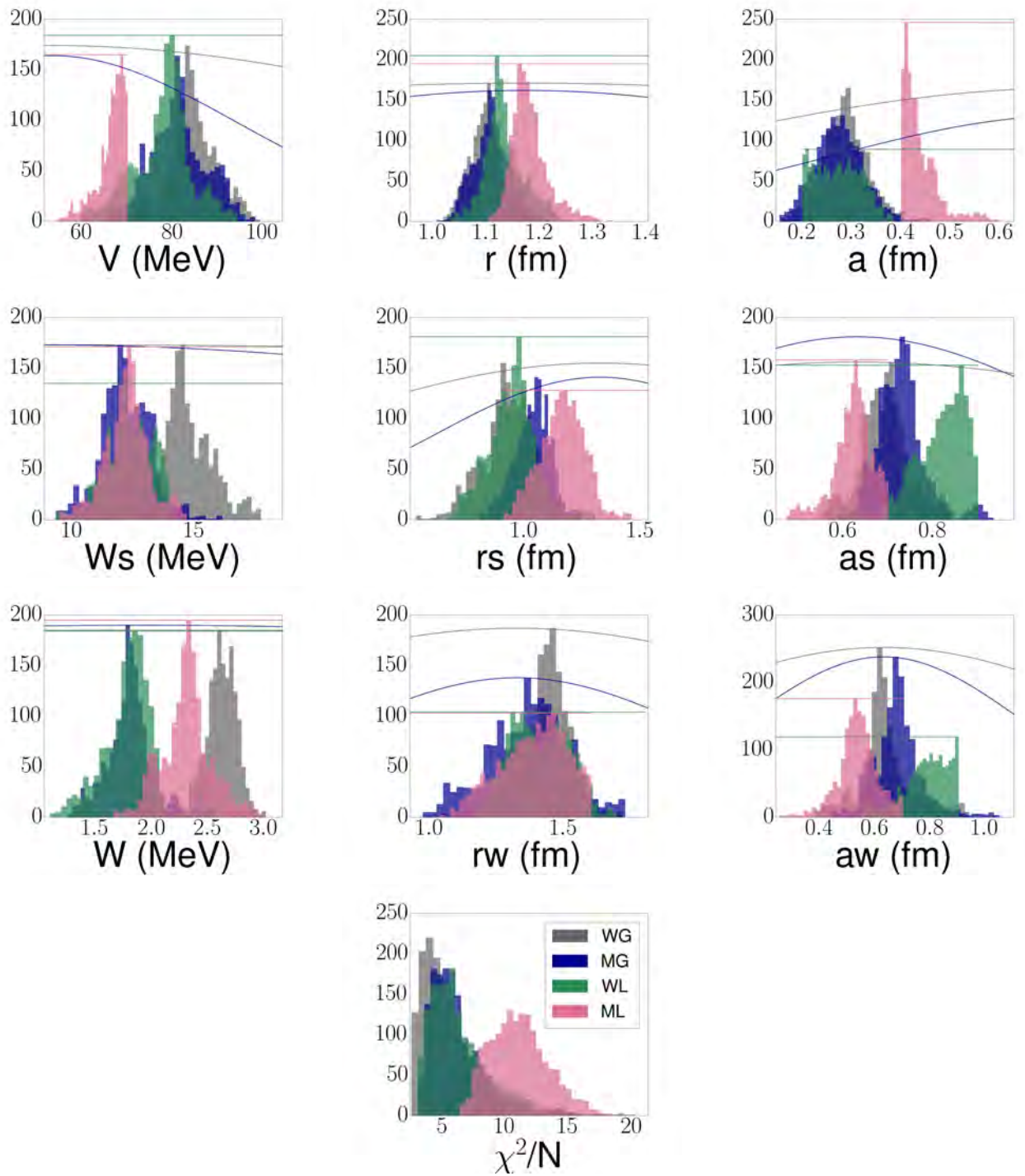
Figure A.7: Same as A.6 for ^{48}Ca(p,p) elastic scattering at 21.0 MeV.
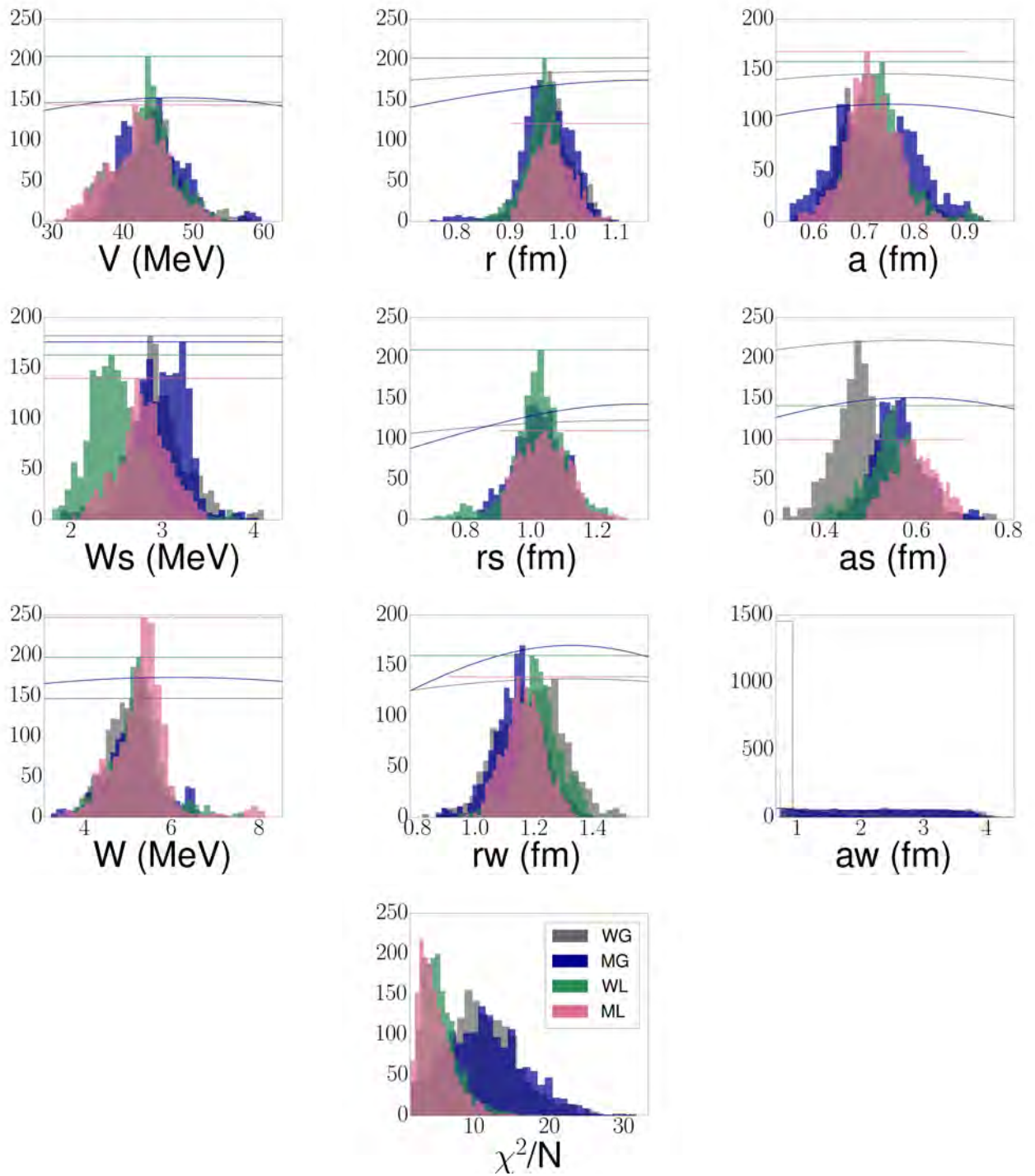
Figure A.8: Same as A.6 for ^{90}Zr(p,p) elastic scattering at 40.0 MeV.
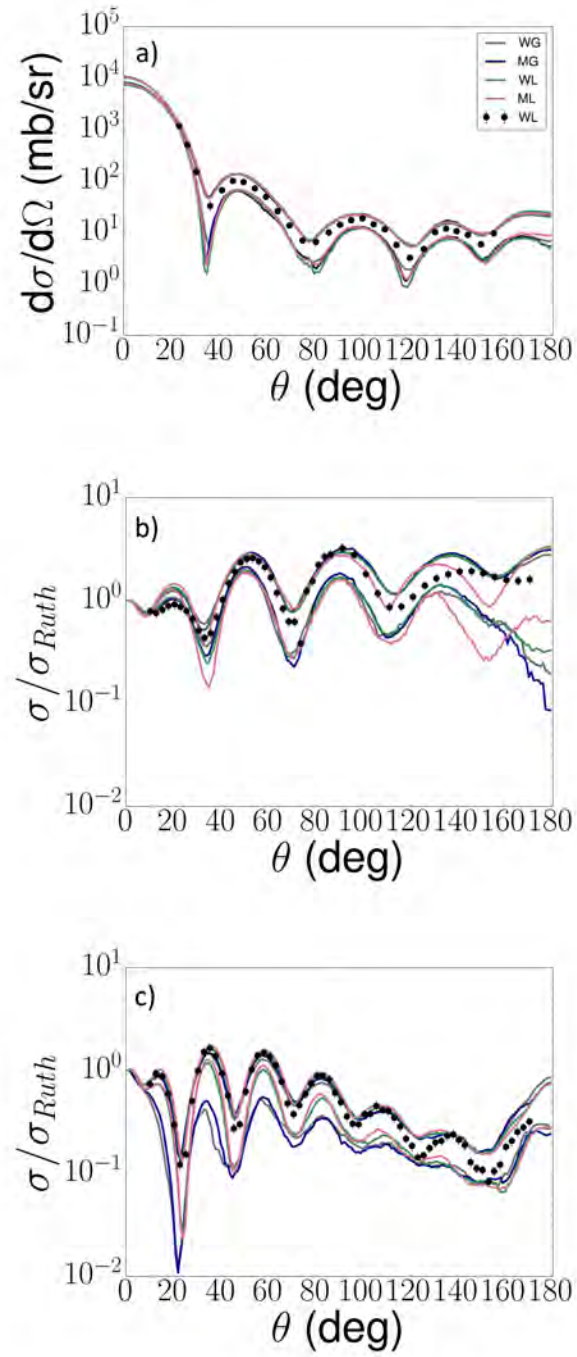
Figure A.9: Comparison of prior types ($\epsilon = 0.005$) for the elastic scattering of (a) ^{120}Sn(n,n) at 13.9 MeV, (b) ^{48}Ca(p,p) at 21.0 MeV, and (c) ^{90}Zr(p,p) at 40.0 MeV.

Appendix B

Details of Regression Results

In this appendix, we show results for the four reactions in Table 4.1 that were not discussed in detail in Chapter 4. First, the uncorrelated χ^2 fitting is presented for the remaining transfer and neutron scattering reactions; then, the same is presented for the correlated χ^2 fitting.

Uncorrelated χ^2 Fitting

We first discuss the second transfer case, fitting ^{90}Zr(d,d)^{90}Zr at 12.0 MeV. The best fit parameterization is listed back in Table 4.2, with $\chi^2/N = 1.421$. The χ^2 contours for the five fitted parameters are shown in Figure B.1, and since they are not elliptical, samples are pulled from the exact χ^2 distribution. (This was the only set of uncorrelated contours that were not elliptical.)
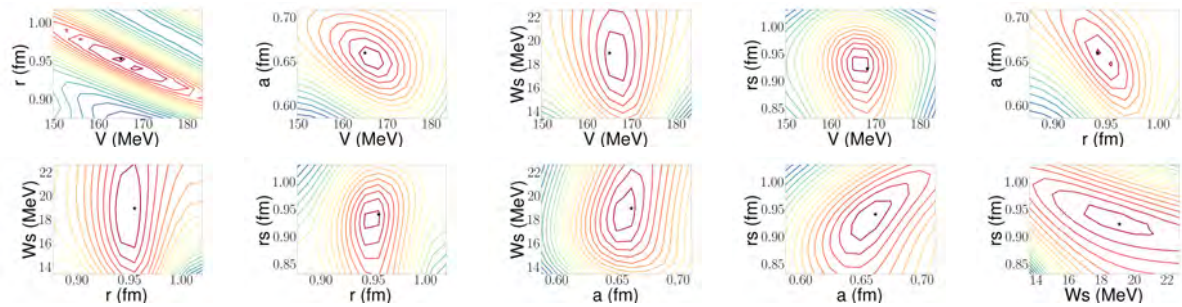
Figure B.1: Contours of constant χ^2 for the fitted parameters of ^{90}Zr(d,d) elastic scattering at 12.0 MeV, using the uncorrelated χ^2 function. Black stars indicate the best-fit parameters.

The 95% confidence bands are shown in Figure B.2 for the (a) elastic scattering fit and (b) transfer cross section prediction. The best-fit parameterization describes the elastic-scattering data well (which is reflected in the χ^2 value), however, the confidence bands are extremely asymmetric. The predicted transfer cross section (b) reproduces the shape of the experimental angular distribution at forward angles, but once past 30°, the calculated cross section is systematically shifted from the data. The predicted spectroscopic factor, $S^{\mathrm{exp}} = 0.720^{+0.097}_{-0.060}$, is smaller than the values extracted from [108], as in the ^{12}C(d,p) case, although the mismatch between this work and the literature values is not as large.
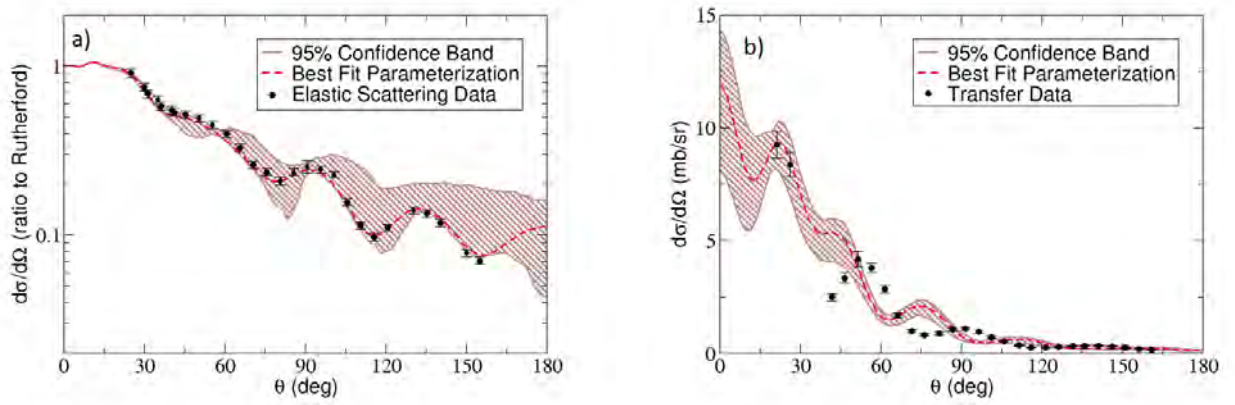
Figure B.2: 95% confidence bands from the uncorrelated fitting of $d+^{90}$Zr elastic-scattering data for (a) ^{90}Zr(d,d)^{90}Zr and (b) ^{90}Zr(d,p)^{91}Zr(g.s.) at 12.0 MeV. The calculations from the best-fit parameterizations are shown in red (dashed), the 95% confidence bands are shown in brown (hatched), and the data is given as (black) circles.

We compute the parameter covariance matrix,

$$
\mathbb{C}_{\mathrm{corr}} =
\begin{bmatrix}
 & V & r & a & W_s & r_s \\
V & 1.000 & -0.997 & 0.972 & -0.949 & 0.926 \\
r & -0.997 & 1.000 & -0.987 & 0.967 & -0.951 \\
a & 0.972 & -0.987 & 1.000 & -0.990 & 0.987 \\
W_s & -0.949 & 0.967 & -0.990 & 1.000 & -0.993 \\
r_s & 0.926 & -0.951 & 0.987 & -0.993 & 1.000
\end{bmatrix},
\tag{B.1}
$$

(remember in this notation, the $V - r$ correlation is -0.997, etc.). In this case, all of the parameters are extremely correlated - there is only one matrix element with absolute value less than 0.950, between V and W_s (-0.949). Although we expect the parameters to be significantly correlated, this is extreme compared to the other cases that were studied.

Next, we focus on fitting neutron elastic-scattering data used to predict inelastic cross sections. The first reaction we show here is the uncorrelated fitting of ^{12}C(n,n)^{12}C at 17.29 MeV to predict the inelastic scattering to the first excited 2^+ state. The best-fit parameterization is found in Table 4.2 with $\chi^2/N = 68.321$. Although this χ^2 value is higher than the ideal value of $\chi^2/N \approx 1$ (like ^{54}Fe), it is a significant reduction from the original χ^2/N value of 473.186, and the χ^2 value is most likely inflated by the small error bars on the data (which are $\sim 3.5\%$ for the elastic scattering).

The χ^2 contour plots are shown in Figure B.3, and since the contours are all elliptical, we draw parameters from the multivariate Gaussian. The 95% confidence bands for (a) the elastic-scattering fit and (b) the inelastic-scattering prediction are shown in Figure B.4. Although the best-fit calculation for the elastic scattering does not pass through all of the data points, the magnitude of the calculation is correct, and about half of the data points are
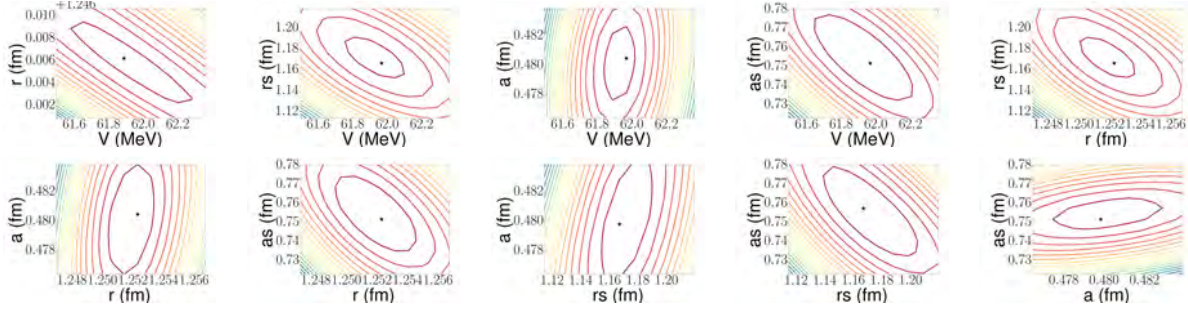
Figure B.3: Same as Figure B.1 for ^{12}C(n,n) elastic scattering at 17.29 MeV.

above and half below the data - as the typical χ^2 calculation should ensure. Still, the 95% confidence band encloses nearly all of the data, with only two or three data points falling outside of the band. The prediction for the inelastic-scattering cross section describes the overall trend of the experimental data, but the forward angles are underestimated; this is unusual considering that these calculations are more accurate at forward angles compared to backwards angles. However, the width of the 95% confidence band is large enough that all of the data fall completely within it.
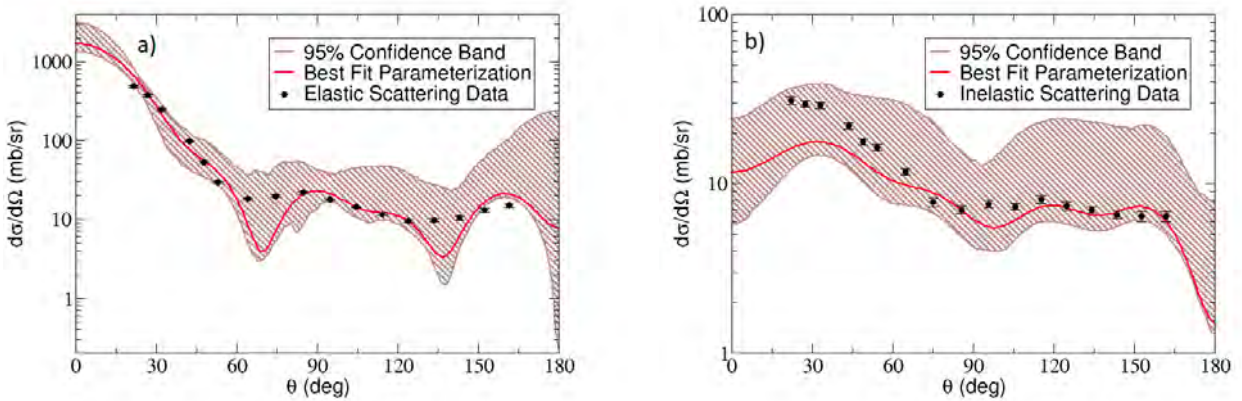
Figure B.4: Same as Figure B.2 for (a) ^{12}C(n,n)^{12}C and (b) ^{12}C(n,n$'$)^{12}C(2_1^+) at 17.29 MeV.

The parameter covariance matrix is

$$
\mathbb{C}_{\text{corr}} =
\begin{bmatrix}
 & V & r & r_s & a & a_s \\
V & 1.000 & -0.918 & 0.488 & -0.161 & -0.650 \\
r & -0.918 & 1.000 & -0.669 & 0.050 & 0.695 \\
r_s & 0.488 & -0.669 & 1.000 & 0.317 & -0.888 \\
a & -0.161 & 0.050 & 0.317 & 1.000 & -0.094 \\
a_s & -0.650 & 0.695 & -0.888 & -0.094 & 1.000
\end{bmatrix}.
\tag{B.2}
$$

All parameters are highly correlated, except for the pairs $a - r$ and $a - a_s$. (In this case, a does not appear to be strongly correlated with any of the other variables.) The most correlated pair of variables is V and r, as seen in most of the other reactions for the depths and corresponding radii.

Next, we fit ^{48}Ca(n,n)^{48}Ca at 7.97 MeV to predict inelastic scattering to the first 2^+ excited state. The best-fit parameterization is found in Table 4.2. Here, the best-fit parameterization has $\chi^2/N = 22.344$. This is again larger than the typical $\chi^2/N \approx 1$ that is ideal for a statistical fit, but this data set also has very small error bars, mostly $\sim 2 - 3\%$. The χ^2 contour plots, which are shown in Figure B.5, are all elliptical, allowing for pulls from the multivariate Gaussian distribution.
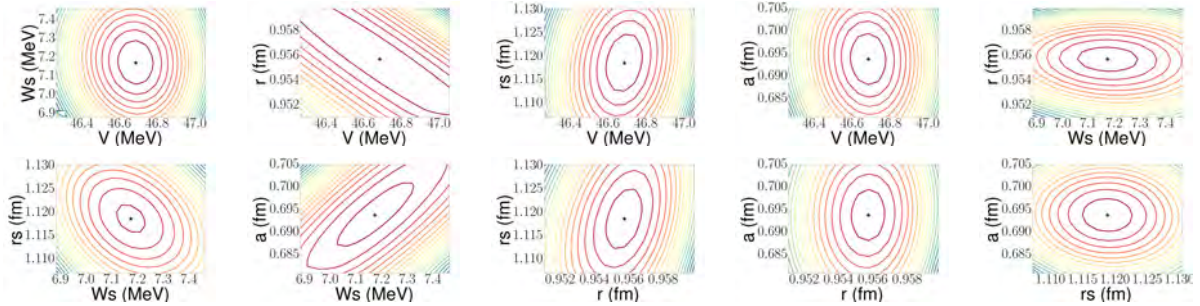
Figure B.5: Same as Figure B.1 for ^{48}Ca(n,n) elastic scattering at 7.97 MeV.

Despite this larger χ^2/N value, the best-fit parameterization reproduces the shape and magnitude of the experimental angular distribution in Figure B.6 (a). The χ^2/N value also does not cause the 95% confidence bands to become broad for the elastic scattering. However, the inelastic scattering prediction Figure B.6 (b) does not show the same well-constrained behavior. The prediction for inelastic scattering does not follow the shape of the experimental angular distribution, and the width of the 95% confidence band allows it to captures all but two data points.
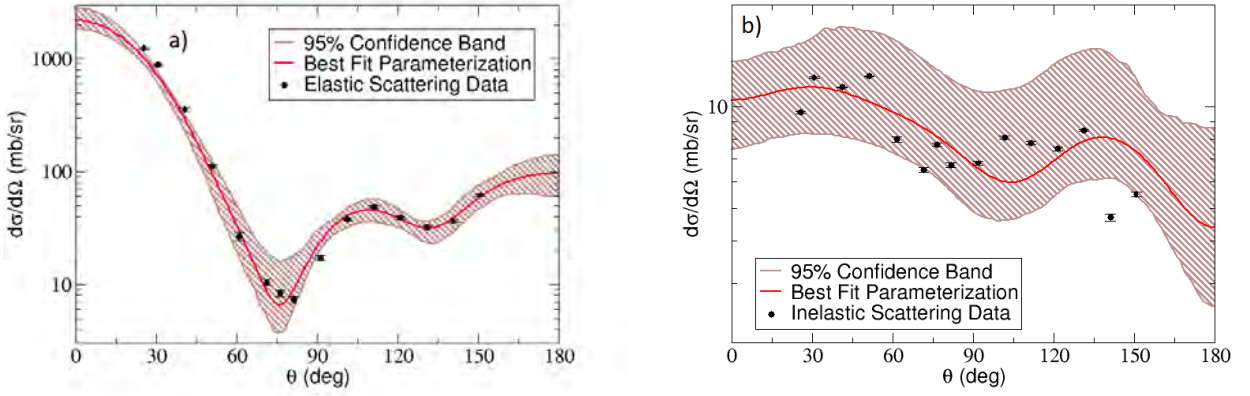
Figure B.6: Same as Figure B.2 for (a) ^{48}Ca(n,n)^{48}Ca and (b) ^{48}Ca(n,n′)^{48}Ca(2_1^+) at 7.97 MeV.

The parameter correlation matrix is

$$
\mathbb{C}_{\text{corr}} =
\begin{bmatrix}
 & V & W_s & r & r_s & a \\
V & 1.000 & -0.173 & -0.952 & 0.279 & -0.322 \\
W_s & -0.173 & 1.000 & 0.008 & -0.617 & 0.884 \\
r & -0.952 & 0.008 & 1.000 & 0.454 & 0.171 \\
r_s & -0.279 & -0.617 & 0.454 & 1.000 & -0.489 \\
a & -0.322 & 0.884 & 0.171 & -0.489 & 1.000
\end{bmatrix}. \tag{B.3}
$$

Because of the parameters that were fit, it is more clear that both $V - r$ and $W_s - r_s$ have significant correlations (although this is slightly higher for the real volume pair than the imaginary surface pair).

Figure B.7: Same as Figure B.1 for ^{208}Pb(n,n) elastic scattering at 26.0 MeV.

The last uncorrelated reaction we investigate is fitting ^{208}Pb(n,n)^{208}Pb at 26.0 MeV to predict the inelastic scattering to the first excited 3^- state. The best-fit parameterization is found in the last section of Table 4.2 with $\chi^2/N = 3.678$. This χ^2 value is particularly interesting because the starting parameterization for this and ^{54}Fe(n,n) from Section 4.1 are the same (nine free parameters at most), and the error on the data points for the ^{208}Pb elastic scattering is a few percent or less - the same as the experimental error for ^{54}Fe. Yet,

for ^{208}Pb, the χ^2 value is orders of magnitude smaller than that of ^{54}Fe.

Parameter sets can again be pulled from the multivariate Gaussian distribution since the pairwise χ^2 contours, Figure B.7, are elliptical. The resulting 95% confidence bands for the elastic and inelastic cross sections are shown in Figure B.8 (a) and (b). As indicated by the small χ^2 value, the elastic-scattering fit almost exactly reproduces the data at all angles. The 95% confidence band is extremely narrow, but because the best fit well-reproduces the data, nearly all of the data is enclosed within this band. The prediction for the inelastic cross section shows a similarly small 95% confidence band, however, the prediction does not describe the data. In this case, varying the quadrapole deformation parameter is not enough to change the shape of the diffraction pattern, and several studies have shown that Coulomb-excitations are important contributions to the inelastic states [145].
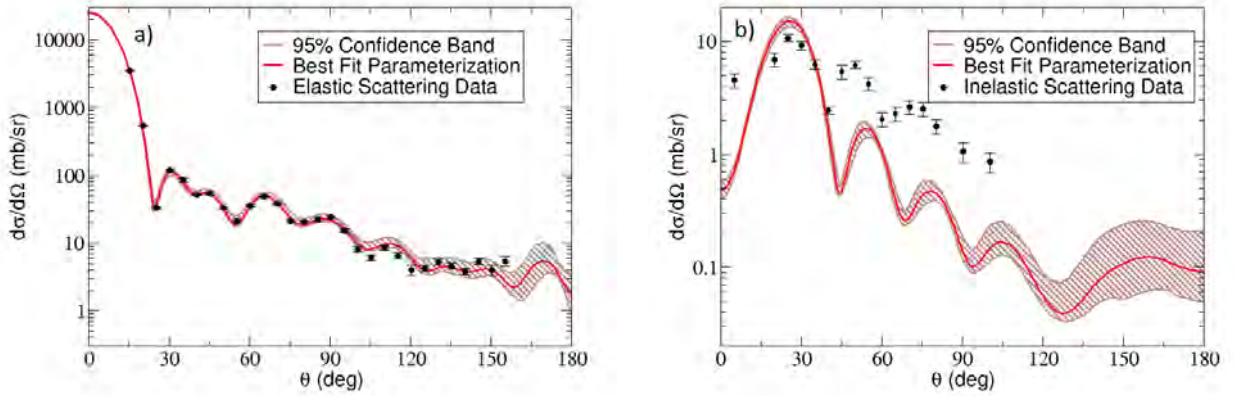
Figure B.8: Same as Figure B.2 for (a) ^{208}Pb(n,n)^{208}Pb and (b) ^{208}Pb(n,n′)^{208}Pb(3_1^-) at 26.0 MeV.

The parameter correlation matrix for the fitted parameters is,

$$
\mathbb{C}_{\mathrm{corr}} =
\begin{bmatrix}
& V & W & W_s & r & a & r_s & a_s & r_w \\
V & 1.000 & -0.441 & -0.530 & -0.994 & 0.701 & -0.521 & 0.450 & 0.577 \\
W & -0.441 & 1.000 & 0.006 & 0.479 & -0.469 & 0.495 & -0.476 & -0.436 \\
W_s & -0.530 & 0.006 & 1.000 & 0.563 & -0.068 & 0.619 & -0.782 & 0.065 \\
r & -0.994 & 0.479 & 0.563 & 1.000 & -0.690 & 0.479 & -0.503 & -0.570 \\
a & 0.701 & -0.469 & -0.068 & -0.690 & 1.000 & 0.016 & 0.228 & 0.395 \\
r_s & -0.521 & 0.495 & 0.619 & 0.579 & 0.016 & 1.000 & -0.612 & -0.362 \\
a_s & 0.450 & -0.476 & -0.782 & -0.503 & 0.228 & -0.612 & 1.000 & -0.196 \\
r_w & 0.577 & -0.436 & 0.065 & -0.570 & 0.395 & -0.362 & -0.196 & 1.000
\end{bmatrix}.
$$

$$(B.4)$$

Here, it is very clear that each radius is highly correlated with the corresponding potential depth, and most of the correlations are around or above 0.5 (either positive or negative).

Correlated χ^2 Fitting

The correlations in the four elastic-scattering reactions discussed in this appendix should be just as strong as those shown in Figure 4.5. This is shown in Figure B.9 for (a) ^{90}Zr(d,d), (b) ^{12}C(n,n), (c) ^{48}Ca(n,n), and (d) ^{208}Pb(n,n). There is again high correlation between the angular pairs, especially at backwards angles. However, this is less obvious in ^{48}Ca(n,n) elastic scattering (c) where many of the angles between $60°$ and $100°$ do not show significant correlation with one another. Still, there is enough evidence of correlation among all of the angles to warrant the study of the correlated χ^2 function for these reactions as well.

Using the correlated χ^2 function, we first fit ^{90}Zr(d,d)^{90}Zr at 12.0 MeV to predict the

transfer reaction ^{90}Zr(d,p)^{91}Zr(g.s.). The best fit parameterization is given in Table 4.3, with $\chi^2/N = 0.142$. The χ^2 contours are shown in Figure B.10 and are not elliptical, so parameter sets are pulled from the exact χ^2 distribution. It is interesting to note that there are hints of another minimum, especially in the V-r contour plot. The parameter space around this minimum appears to be quite complicated.

The resulting 95% confidence bands are shown in Figure B.11 for the elastic scattering fit (a) and the transfer prediction (b). The correlated elastic-scattering fit (a) reproduces the data at forward angles and then remains above the data. Still, at these angles, the shape of the fitted angular distribution mirrors the shape of the experimental angular distribution. Except at backwards angles, the data falls within the 95% confidence band. The resulting predicted transfer cross section (b) reproduces the experimental peak, but the diffraction pattern of the prediction is significantly different from the data past the first peak, both of which were also seen in the uncorrelated case. Here, $S^{\mathrm{exp}} = 0.689^{+0.194}_{-0.079}$, which is again smaller than the values found in the literature but, within errors, consistent with the uncorrelated spectroscopic factor. It is interesting that the correlated and uncorrelated transfer cross sections are so similar, even though the deuteron potentials are significantly different.

The parameter covariance matrix is

$$
\mathbb{C}_{\mathrm{corr}} =
\begin{bmatrix}
 & V & r & a & W_s & r_s \\
V & 1.000 & -0.981 & 0.825 & -0.289 & 0.358 \\
r & -0.981 & 1.000 & -0.904 & 0.375 & -0.495 \\
a & 0.825 & -0.904 & 1.000 & -0.585 & 0.737 \\
W_s & -0.289 & 0.375 & -0.585 & 1.000 & -0.793 \\
r_s & 0.358 & -0.495 & 0.737 & -0.793 & 1.000
\end{bmatrix} . \tag{B.5}
$$

138

This is one of the few cases that was examined where the same parameters are fitted in both the uncorrelated and correlated cases so the changes in correlation can be directly evaluated. The parameters have decoupled compared to the uncorrelated fitting case, besides V and r. It is not necessarily obvious that the parameters should decouple when model correlations are taken into account (since we specifically correlate angles), but it should not be unexpected. Because the formulation of the correlated χ^2 give the model more influence over the fitting, correlations are taken into account there and the parameter space decouples.

Next, we fit neutron elastic scattering to predict the inelastic scattering to the first excited state, beginning by fitting ^{12}C(n,n)^{12}C at 17.29 MeV to predict the inelastic scattering to the first excited 2^+ state. The best-fit parameterization is listed in Table 4.3, and the minimum has $\chi^2/N = 0.483$. Figure B.12 shows the pairwise χ^2 contour plots, which are nearly elliptical so we can draw from the multivariate Gaussian. (There is no difference in the resulting cross sections if draws are made from the exact χ^2 distribution instead of the multivariate Gaussian as has been mentioned for several of these distributions.)

The resulting 95% confidence bands are given in Figure B.13 for the elastic-scattering fit (a) and the inelastic-scattering prediction (b). For the elastic scattering, even though, again, the best-fit calculation does not pass through all of the data, we see that the the calculated cross section follows the shape of the experimental angular distribution, and the 95% confidence bands capture the majority of the data. The same is true for the predicted inelastic cross section. The general trend of the experimental inelastic angular distribution is followed although the details are not reproduced. The data do, however, fall within the 95% confidence band.

The parameter correlation matrix is again calculated,

$$
\mathbb{C}_{\text{corr}} =
\begin{bmatrix}
 & V & r & a & W_s & r_s \\
V & 1.000 & -0.983 & 0.653 & -0.781 & -0.866 \\
r & -0.983 & 1.000 & -0.697 & 0.816 & 0.920 \\
a & 0.653 & -0.697 & 1.000 & -0.580 & -0.539 \\
W_s & -0.781 & 0.816 & -0.580 & 1.000 & 0.768 \\
r_s & -0.866 & 0.920 & -0.539 & 0.768 & 1.000
\end{bmatrix} .
\tag{B.6}
$$

Many of the parameters here are still strongly correlated, and a is more strongly correlated with the other parameters than it was in the uncorrelated case; however, again, because the same pairs of parameters were not fitted in both cases, it is hard to directly compare.

^{48}Ca(n,n)^{48}Ca at 7.97 MeV was then fitted to predict the inelastic scattering to the first excited 2^+ state. The best fit for this reaction is shown in Table 4.3 with $\chi^2/N = 2.142$, which is significantly lower than χ^2_{UC}/N for the same reaction. The χ^2 contours, Figure B.14, are elliptical, although they are all asymmetric (there is a steeper gradient in one direction than the others). Nevertheless, pulling parameter sets from the exact χ^2 distribution and from the multivariate Gaussian give rise to the same 95% confidence bands.

The resulting confidence bands are shown in Figure B.15 (a) and (b) for the fitted elastic scattering and predicted inelastic scattering respectively. The best-fit calculation reproduces the data almost exactly up to $60°$ where we expect this model to be most accurate. At backwards angles, the diffraction pattern of the data is reproduced only shifted forward 10-$20°$. The 95% confidence bands are wide enough that all of the data falls within them. The 95% confidence bands for the inelastic scattering data (b) are very wide as well, and because of this, all of the data falls within this band even though the cross section calculated from

the best-fit parameterization does not reproduce the data. In this case, the uncorrelated fit provides a better description of the data than the correlated fit (the χ^2 is larger for the uncorrelated fit only because of the normalization of $\mathbb{C}_m$). The correlated confidence band for the predicted transfer encloses all of the data because of its large width.

The parameter correlation matrix is

$$
\mathbb{C}_{\mathrm{corr}} =
\begin{bmatrix}
 & V & W_s & r \\
V & 1.000 & 0.655 & -0.979 \\
W_s & 0.655 & 1.000 & -0.659 \\
r & -0.979 & -0.659 & 1.000
\end{bmatrix}.
\tag{B.7}
$$

Again, even though there were 9 free parameters, not all of them could be simultaneously minimized, and the vast majority of the parameters had to be fixed before the final minimization.

The final study is again fitting ^{208}Pb(n,n)^{208}Pb to predict inelastic scattering to the first excited 3^- state. The best-fit parameterization is given in Table 4.3, which has $\chi^2/N = 1.401$. Many of the contours of constant χ^2 are more egg shaped than elliptical so parameter sets are pulled from the exact χ^2 distribution, shown in Figure B.16.

The 95% confidence bands for the fitted elastic scattering and the predicted inelastic scattering are shown in Figure B.17 (a) and (b). The best-fit calculation accurately describes the experimental angular distributions both at forward and backwards angles, as in the uncorrelated fit. (The parameters for the real part of the potential are identical to the uncorrelated best fit, but there are noticeable differences in the imaginary parts, so the similarity in the cross section should not be assumed). Also like the uncorrelated fitting case, the prediction for the inelastic scattering does not reproduce the data, except at the

first peak. The 95% confidence bands are significantly wider for the correlated calculation than they were for the correlated calculation.

The parameter correlation matrix is given below,

$$
\mathbb{C}_{\text{corr}} =
\begin{bmatrix}
 & V & r & a & W_s & r_s & a_s & W \\
V & 1.000 & -0.865 & 0.606 & -0.632 & -0.477 & 0.645 & -0.493 \\
r & -0.865 & 1.000 & -0.651 & 0.701 & 0.124 & -0.674 & 0.385 \\
a & 0.606 & -0.651 & 1.000 & -0.710 & 0.097 & 0.767 & -0.676 \\
W_s & -0.632 & 0.701 & -0.710 & 1.000 & 0.052 & -0.873 & 0.644 \\
r_s & -0.477 & 0.124 & 0.097 & 0.052 & 1.000 & -0.228 & 0.359 \\
a_s & 0.645 & -0.674 & 0.767 & -0.873 & -0.228 & 1.000 & -0.876 \\
W & -0.493 & 0.385 & -0.676 & 0.644 & 0.359 & -0.876 & 1.000
\end{bmatrix} . \quad \text{(B.8)}
$$

where the parameters are given in the order V, r, a, W_s, r_s, a_s, and W. Once more, the real volume depth and radii are two of the most correlated parameters. However, unlike in other cases, there is almost no correlation between the depth and radius of the imaginary surface term. The three depth parameters are also fairly correlated with one another - their correlation parameters are around or above 0.5.
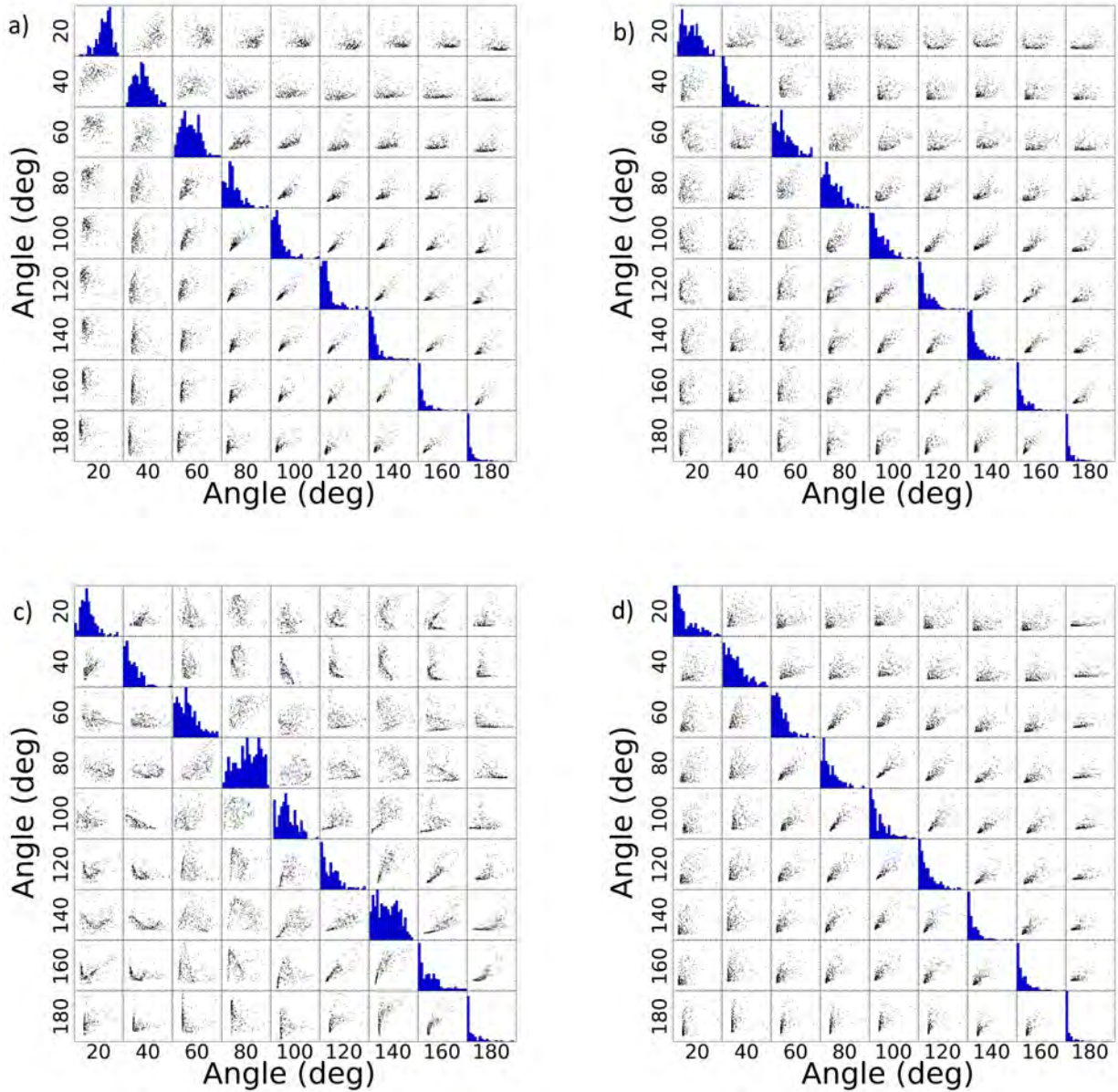
Figure B.9: Selected angular correlations for (a) ^{90}Zr(d,d) at 12.0 MeV, (b) ^{12}C(n,n) at 17.29 MeV, (c) ^{48}Ca(n,n) at 7.79 MeV, and (d) ^{208}Pb(n,n) at 26.0 MeV. Each scatter plot show the values of the differential cross section at the angle listed on the x-axis compared to the differential cross section at the angle listed on the y-axis for two hundred calculations with randomly drawn optical model parameters sets. The histograms along the diagonal show the spread of cross section values at the given angle.
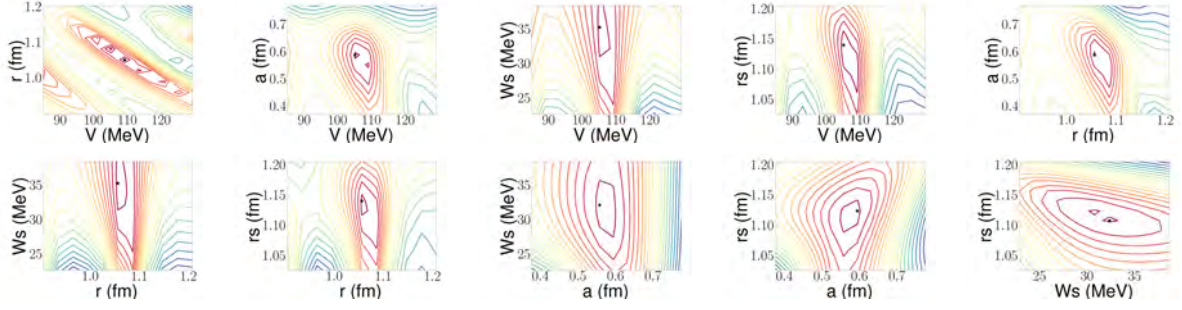
Figure B.10: Same as Figure B.1 for ^{90}Zr(d,d)^{90}Zr now using the correlated χ^2 fitting function.
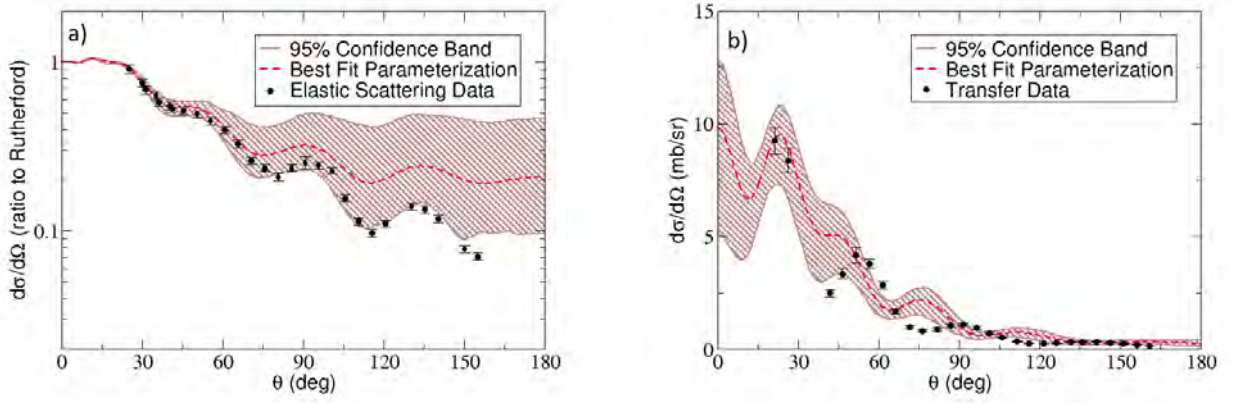
Figure B.11: Same as Figure B.2 for (a) ^{90}Zr(d,d)^{90}Zr and (b) ^{90}Zr(d,p)^{91}Zr(g.s.) at 12.0 MeV using the correlated χ^2 function.
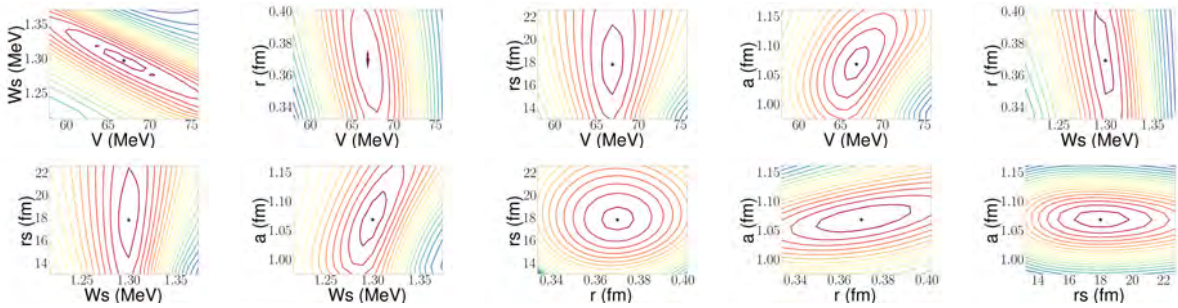
Figure B.12: Same as Figure B.1 for ^{12}C(n,n)^{12}C now using the correlated χ^2 fitting function.
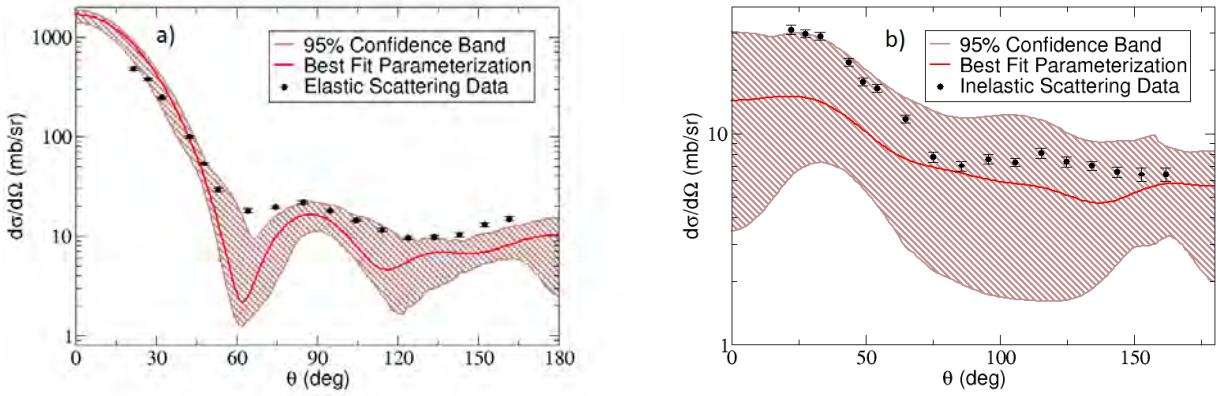
Figure B.13: Same as Figure B.2 for (a) ^{12}C(n,n)^{12}C and (b) ^{12}C(n,n′)^{12}C(2^+_1) at 17.29 MeV using the correlated χ^2 function.
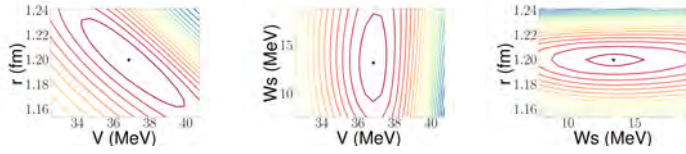
Figure B.14: Same as Figure B.1 for ^{48}Ca(n,n)^{48}Ca now using the correlated χ^2 fitting function.
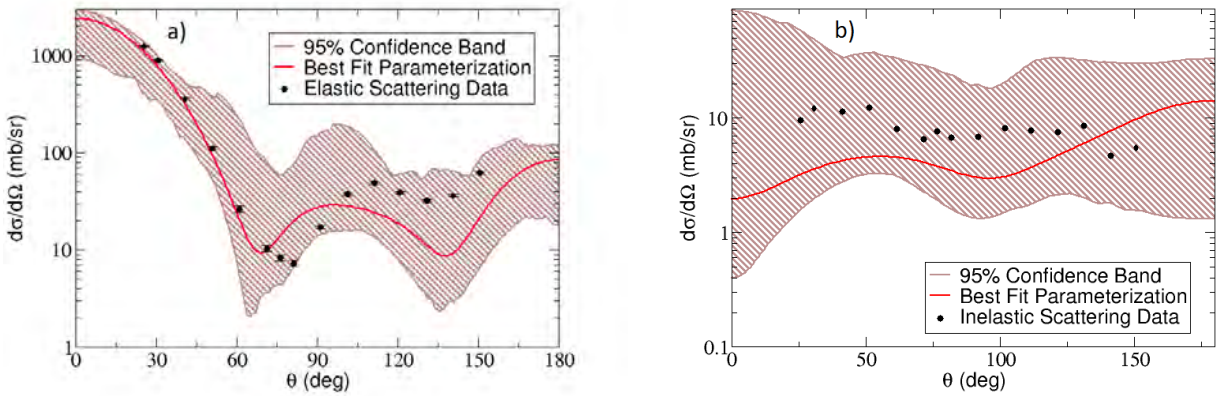
Figure B.15: Same as Figure B.2 for (a) ^{48}Ca(n,n)^{48}Ca and (b) ^{48}Ca(n,n′)^{48}Ca(2^+_1) at 7.79 MeV using the correlated χ^2 function.
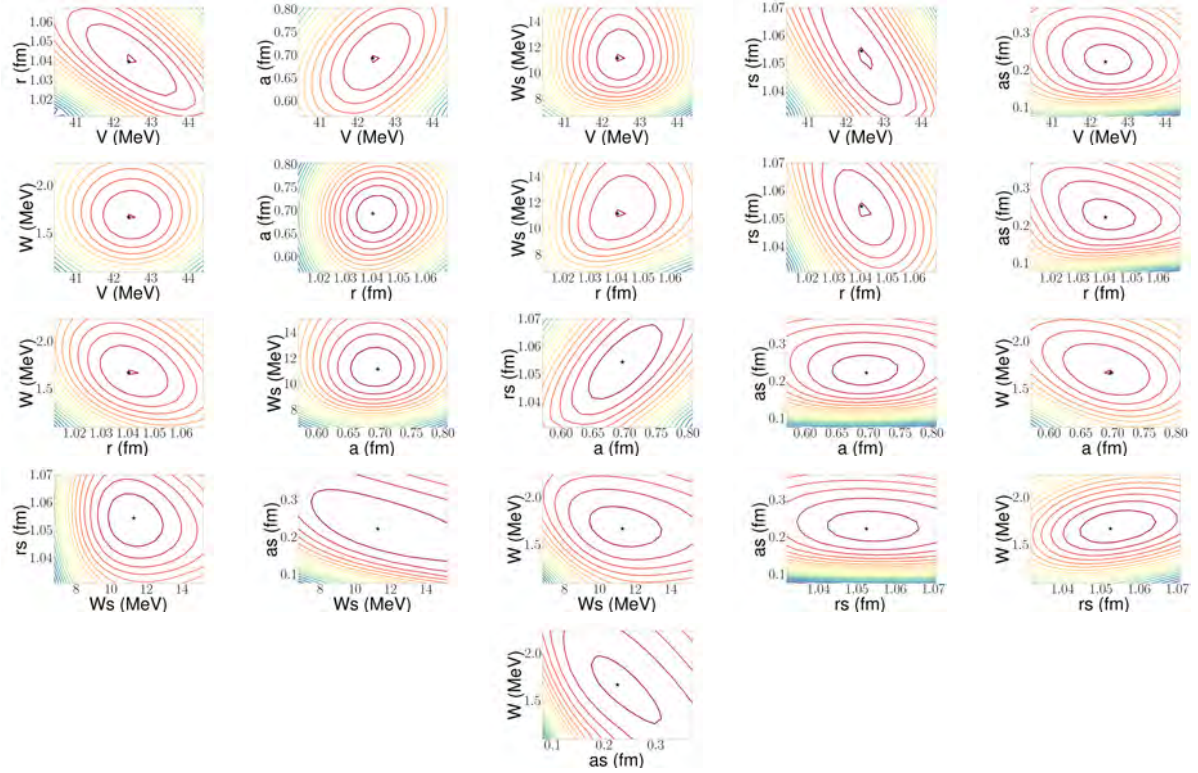
Figure B.16: Same as Figure B.1 for ^{208}Pb(n,n)^{208}Pb now using the correlated χ^2 function.
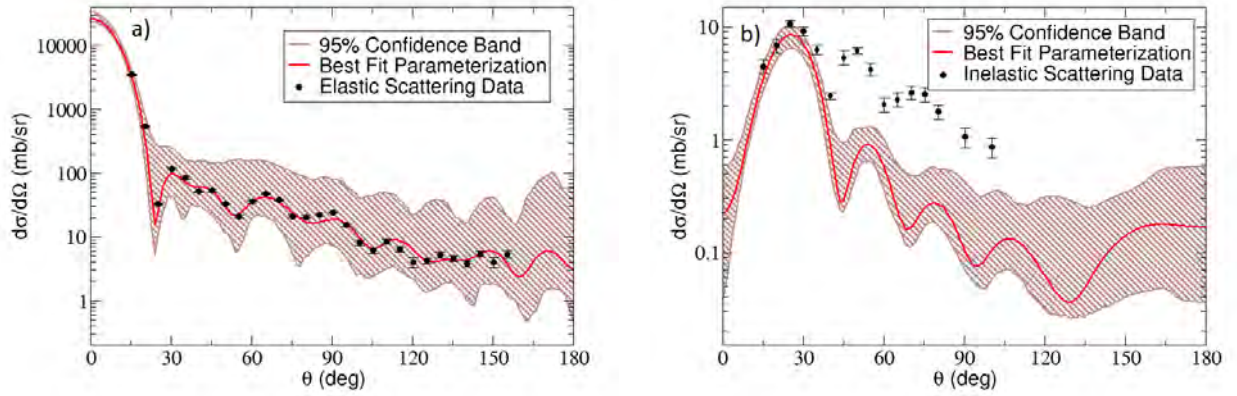
Figure B.17: Same as Figure B.2 for (a) ^{208}Pb(n,n)^{208}Pb and (b) ^{208}Pb(n,n$'$)^{208}Pb(3_1^-) at 26.0 MeV using the correlated χ^2 function.

Appendix C

Details of Bayesian Results

As in Chapter 5, there is a specific set of data we use to predict transfer reactions. For the adiabatic calculations, we need elastic scattering for the incoming neutron-target and proton-target pairs at half of the incoming deuteron energy and outgoing nucleon-target elastic scattering data at center of mass energy of $E_d - Q_{(d,p)}$. Ideally, we would want elastic scattering data for the $(A + 1) + N$ system instead of the $A + N$ system, but typically, this data is much less widely available. There is also only a 1% difference between the optical potentials using nucleus A and $A + 1$ as the target; because this uncertainty is significantly smaller than the uncertainty that is introduced by the parameterization of the potentials, using this substitution is an acceptable alternative.

In addition, we would like to have transfer data near the incident deuteron energy. Besides, ^{48}Ca(d,p) shown in Chapter 5, the only other reaction with available (d,N) data in the correct energy range was ^{90}Zr(d,p). Data is available for ^{116}Sn(d,p) and ^{208}Pb(d,p) [146, 147, 148], but it is either not at the deuteron energy available from the elastic scattering data, or the transfer data were at backwards angles which is not conducive to comparing with these models (as the first peak in the transfer data is the most informative). In addition, most of this data was taken at energies below the Coulomb barrier, at which point the cross section is not sensitive to the nuclear potential.

Last, in order to compare ADWA and DWBA, we need deuteron-target elastic scattering

data at the same deuteron incident energy as the adiabatic calculations. This was available for all but ^{116}Sn(d,d). Although this reduces the number of cases where we can directly compare the two approximations, we decided that being able to compare four out of five reactions was sufficient to understand any trends that might arise. The remaining transfer calculations are described below.

Nucleon Elastic Scattering

First, we consider nucleon scattering on ^{90}Zr to construct both the (d,p) transfer cross section and (d,n) transfer cross section. In the adiabatic framework, these two reactions are constrained by the same incoming channel, and only the outgoing nucleon scattering channel is different. Therefore, there are four potentials for which we have to define priors.

The first in this set is ^{90}Zr(n,n)^{90}Zr elastic scattering at 10.0 MeV, common to both reactions. The prior distributions are shown in Figure C.1 using both the 10% experimental errors (gray histograms) and 5% experimental errors (blue histograms) compared to the prior distributions (gray solid). The means and widths of each posterior distribution are listed in Table C.1, columns two and three. All of the parameters have physical values for their means, and their widths are constrained significantly compared to the width of the prior. The resulting 95% confidence intervals using both 10% and 5% experimental errors are shown in Figure C.2 panel (a) (gray and blue intervals respectively).

Then, we constrain the proton-target elastic scattering using ^{90}Zr(p,p)^{90}Zr at 12.7 MeV. The posterior distributions for each parameter are shown in Figure C.3 again with gray histograms for the 10% experimental errors and blue histograms for the 5% experimental errors, compared to the prior distribution for each parameter, and the values for the means

ε_{exp}	x	$\bar{x}_\text{n}^\text{in}$	$\Delta x_\text{n}^\text{in}$	$\bar{x}_\text{p}^\text{in}$	$\Delta x_\text{p}^\text{in}$	$\bar{x}_\text{n}^\text{out}$	$\Delta x_\text{n}^\text{out}$	$\bar{x}_\text{p}^\text{out}$	$\Delta x_\text{p}^\text{out}$
	V	48.049	2.673	49.253	2.110	45.343	1.934	54.784	2.575
	r	1.217	0.036	1.288	0.053	1.187	0.035	1.138	0.031
	a	0.694	0.050	0.553	0.046	0.603	0.067	0.796	0.056
	Ws	6.217	0.848	8.932	0.990	6.657	0.432	7.322	0.692
10%	rs	1.287	0.070	1.153	0.096	1.232	0.055	1.345	0.075
	as	0.459	0.047	0.609	0.061	0.611	0.041	0.662	0.050
	W	0.621	0.060	0.207	0.023	2.623	0.404	1.759	0.216
	rw	1.288	0.128	1.203	0.128	0.457	0.123	1.416	0.130
	aw	0.539	0.057	0.612	0.071	0.448	0.082	0.588	0.069
ε_{exp}	x	$\bar{x}_\text{n}^\text{in}$	$\Delta x_\text{n}^\text{in}$	$\bar{x}_\text{p}^\text{in}$	$\Delta x_\text{p}^\text{in}$	$\bar{x}_\text{n}^\text{out}$	$\Delta x_\text{n}^\text{out}$	$\bar{x}_\text{p}^\text{out}$	$\Delta x_\text{p}^\text{out}$
	V	49.253	2.110	52.093	2.450	45.319	1.056	54.331	2.204
	r	1.204	0.028	1.288	0.029	1.186	0.018	1.146	0.030
	a	0.694	0.037	0.546	0.043	0.605	0.032	0.778	0.053
	Ws	6.911	0.941	9.141	1.037	5.819	0.388	6.761	0.499
5%	rs	1.267	0.070	1.140	0.091	1.222	0.032	1.341	0.045
	as	0.444	0.052	0.596	0.060	0.702	0.048	0.681	0.039
	W	0.527	0.060	0.195	0.020	2.563	0.423	1.779	0.216
	rw	1.379	0.142	1.319	0.166	0.315	0.124	1.416	0.119
	aw	0.595	0.077	0.586	0.058	0.631	0.049	0.523	0.075

Table C.1: Means ($\bar{x}_i$) and widths (Δx_i) for the posterior distributions shown in Figure C.1 (columns two and three), Figure C.3 (columns four and five), Figure C.4 (columns six and seven), and Figure C.5 (columns eight and nine) using the 10% experimental errors (top) and 5% errors (bottom).
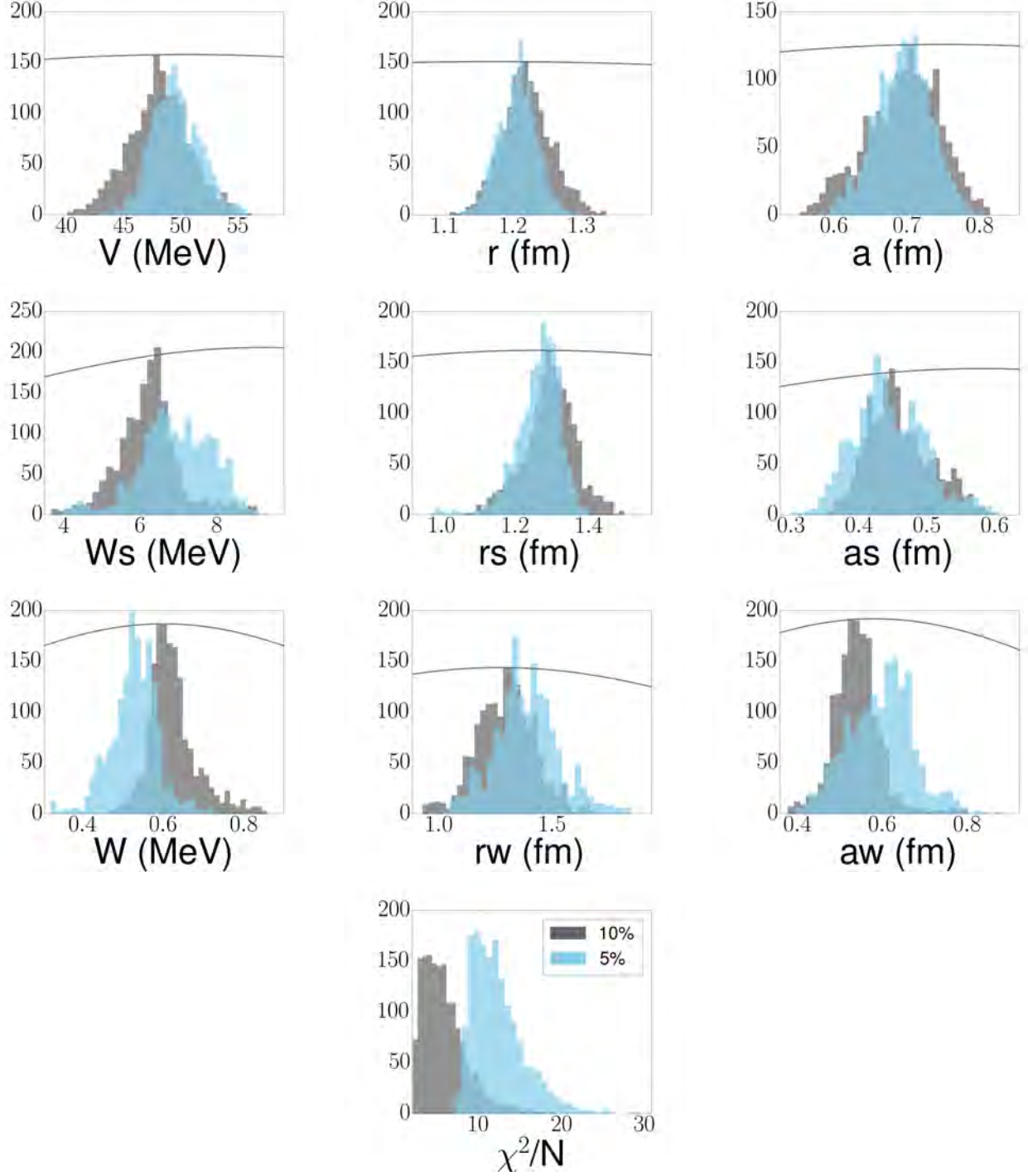
Figure C.1: Posterior distributions (histograms) constraining the optical potential parameters using ^{90}Zr(n,n)^{90}Zr elastic scattering data at 10.0 MeV, comparing 10% errors on the experimental cross sections (gray) and 5% errors (blue). Original prior distributions (a Gaussian with the width equal to the mean) are shown as gray solid lines.
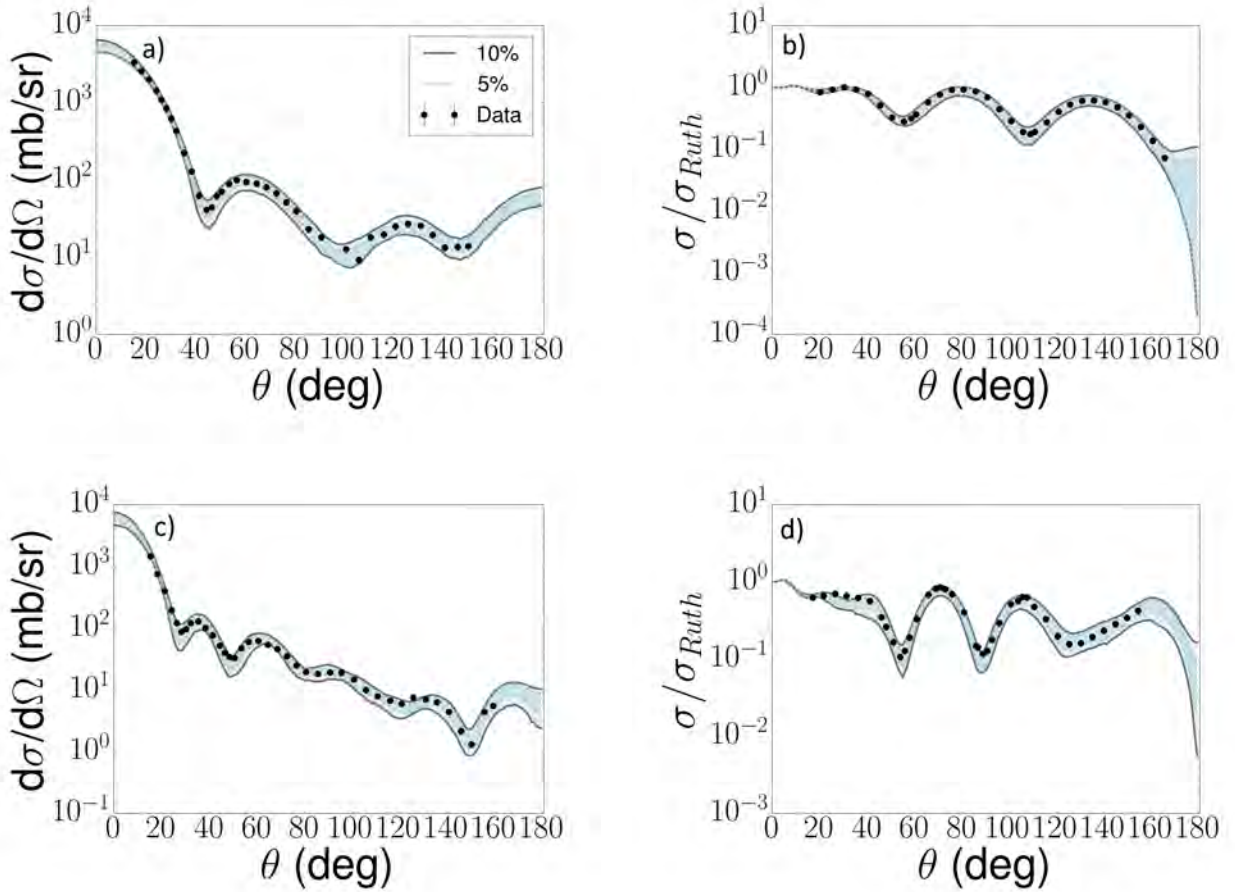
Figure C.2: The 95% confidence intervals for the (a) ^{90}Zr(n,n)^{90}Zr at 10.0 MeV, (b) ^{90}Zr(p,p)^{90}Zr at 12.7 MeV, (c), ^{90}Zr(n,n)^{90}Zr at 24.0 MeV, and (d) ^{90}Zr(p,p)^{90}Zr at 22.5 MeV constructed from the prior distributions of Figures C.1, C.3, C.4, and C.5, using 10% errors (gray), and 5% errors (blue).

and widths of these distributions are shown in Table C.1, columns six and seven. All of the parameters take on physical values. The resulting 95% confidence intervals are shown in Figure C.2 panel (b) using the 10% experimental errors (gray) and 5% experimental errors (blue). These bands provide a good description of the data, and there is only a slight reduction from the 10% error calculation to the 5% error one.

For the (d,n) calculation, we need to constrain the outgoing ^{91}Zr-n channel, which is done using ^{90}Zr(n,n)^{90}Zr elastic-scattering data at 24.0 MeV. The resulting posterior distributions are shown in Figure C.4 using 10% (5%) experimental error bars indicated as gray (blue) histograms. These are compared to the prior distributions for each variable (gray solid). Here, r_w takes on a value that is about a third its normal value; this does not affect the 95% confidence intervals, as in Figure C.2 (c), for elastic scattering, but it could have an affect on the resulting transfer calculations. (This is a case in which we would want to find a fit of similar quality but constrained more by the prior for this parameter instead of the data.)

Finally, for the (d,p) calculation, we need to constrain the outgoing ^{91}Zr-p channel, which is done using ^{90}Zr(p,p)^{90}Zr elastic-scattering data at 22.5 MeV. The resulting posterior distributions are shown in Figure C.5 using 10% experimental errors (gray histograms) and 5% errors (blue histograms) compared to the prior distributions (gray solid). Each parameter distribution is centered on a physically reasonable value with a width that is significantly narrower than the width of the prior distributions. The resulting 95% confidence intervals for the elastic scattering cross sections are shown in Figure C.2 (d).

We can then use these parameter posterior distributions to construct ^{90}Zr(d,p)^{91}Zr(g.s.) and ^{90}Zr(d,n)^{91}Nb(g.s) cross sections. The 95% confidence intervals are given in (a) of Figure C.6 for the (d,n) calculation at 20.0 MeV. The gray band shows the resulting cross section using posterior distributions constrained with 10% experimental errors, and the blue band
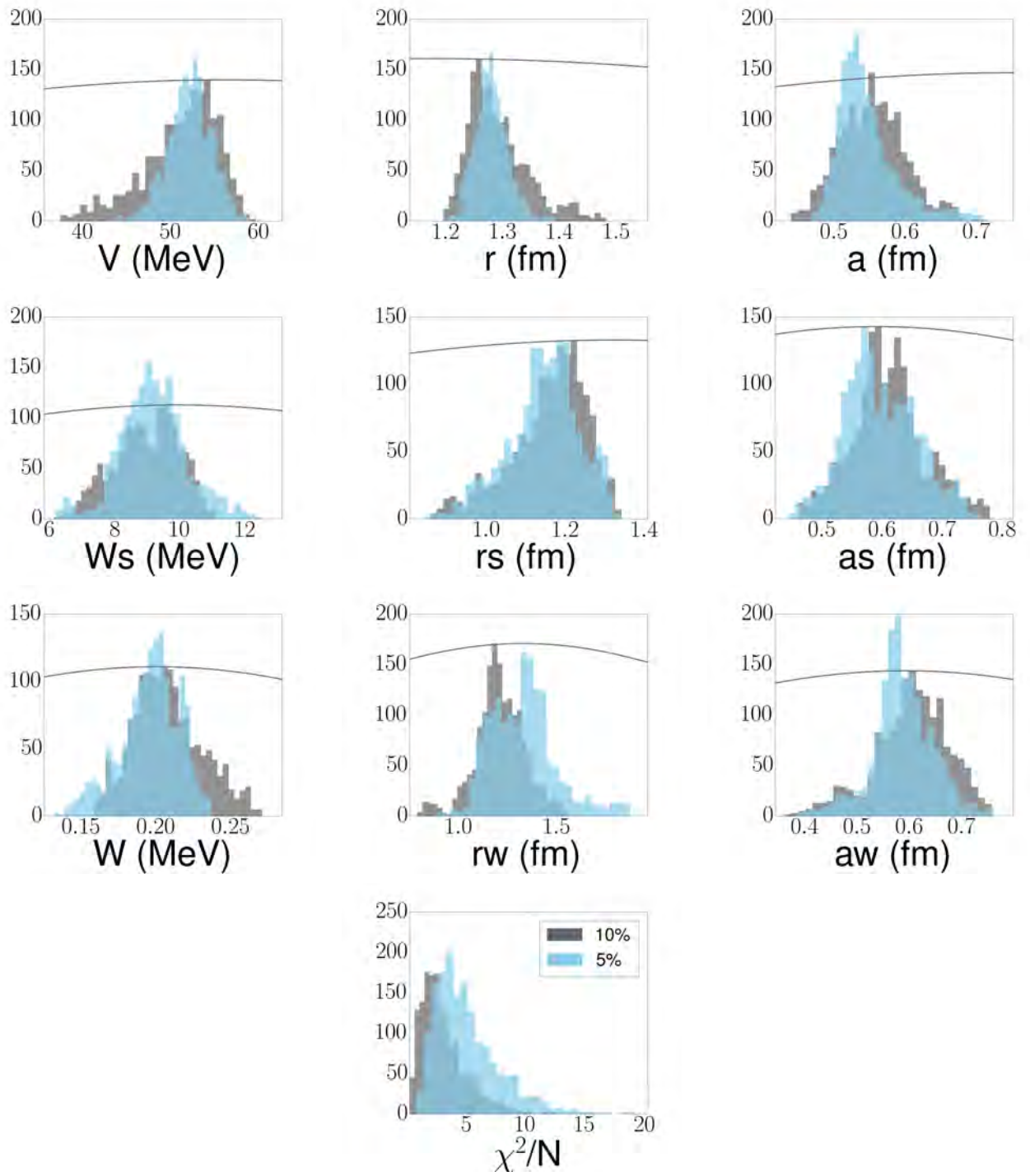
Figure C.3: Same as Figure C.1 for ^{90}Zr(p,p)^{90}Zr elastic scattering at 12.7 MeV.
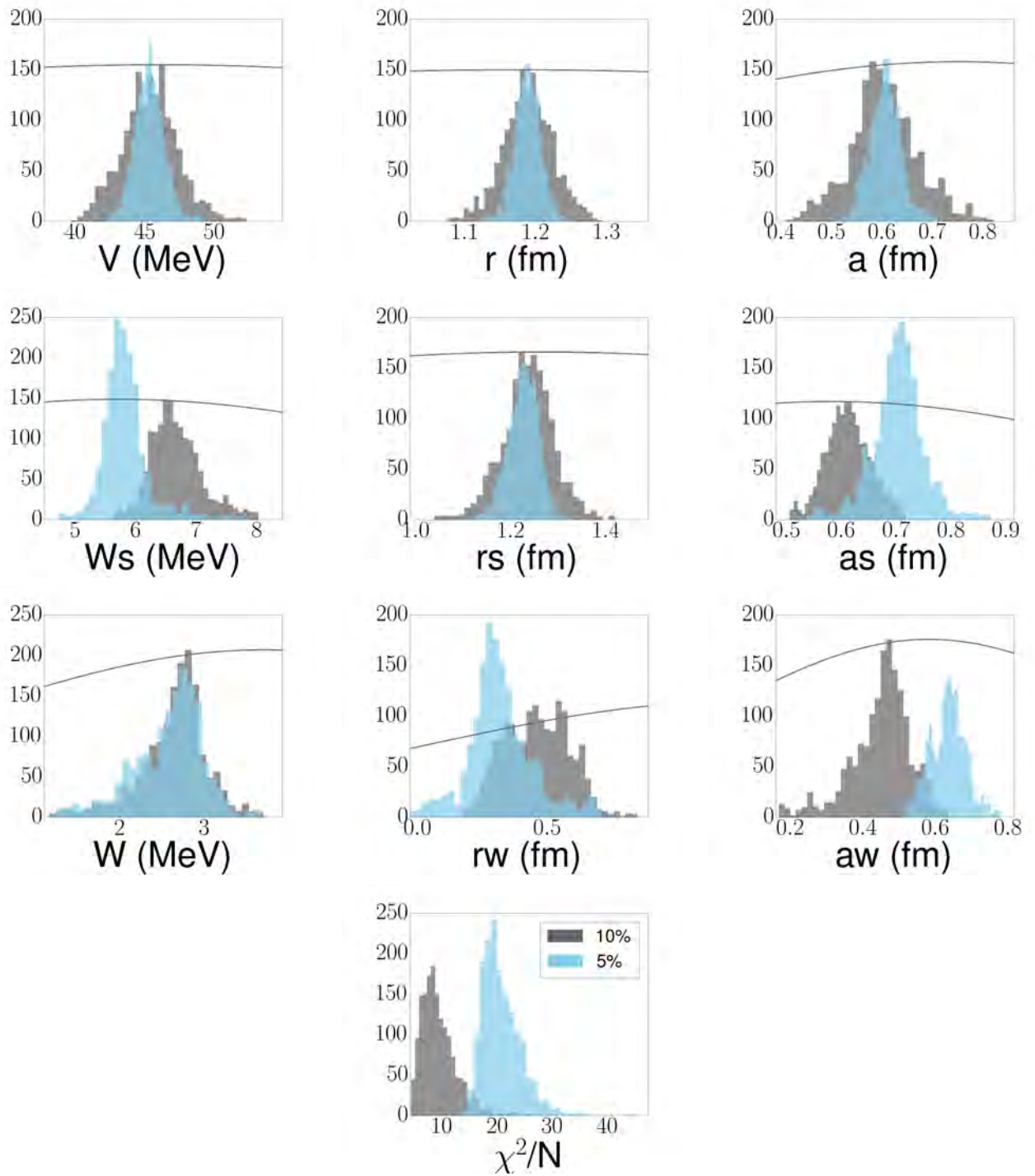
Figure C.4: Same as Figure C.1 for ^{90}Zr(n,n)^{90}Zr elastic scattering at 24.0 MeV.
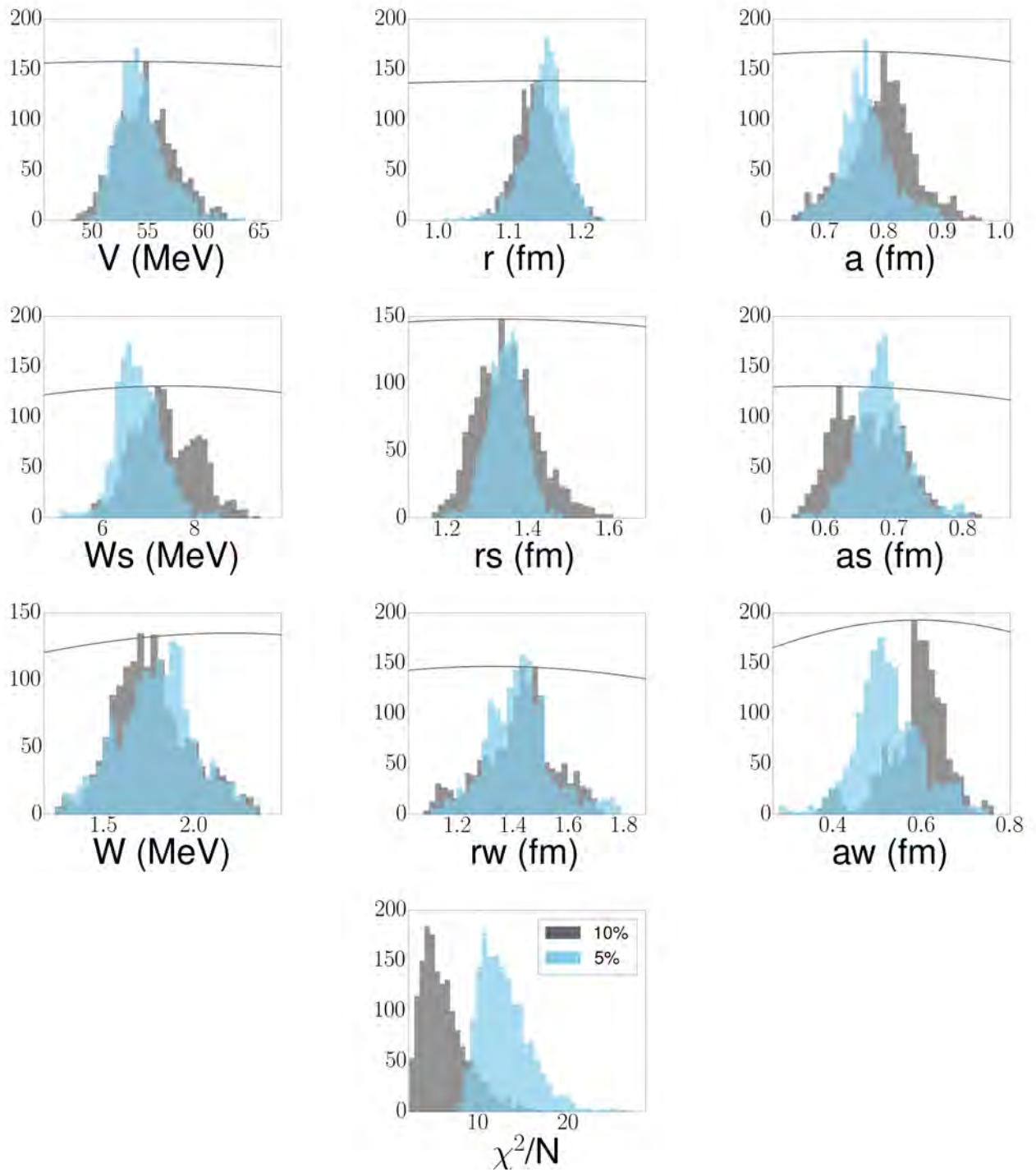
Figure C.5: Same as Figure C.1 for ^{90}Zr(p,p)^{90}Zr elastic scattering at 22.5 MeV.
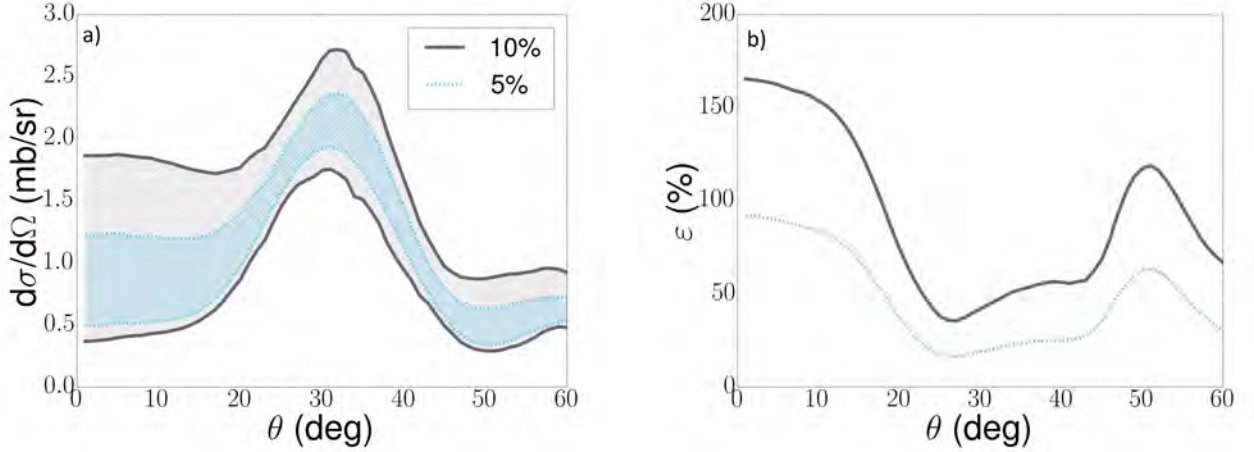
Figure C.6: (a) 95% confidence intervals for ^{90}Zr(d,n)^{91}Nb(g.s.) at 20.0 MeV with 10% (gray) and 5% (blue) error bars on the experimental data for the elastic scattering of the incoming and outgoing channels and (b) percentage uncertainties, using ADWA.

are the same only using 5% experimental errors. The panel (b) of the same figure then shows the corresponding percentage uncertainty calculated for each of the cross sections, defined by Eq. (5.1).

By switching out the outgoing ^{90}Zr-n potential with the ^{90}Zr-p potential at 22.5 MeV, the transfer cross section for the ^{90}Zr(d,p)^{91}Zr(g.s.) can be calculated; this is done at 22.0 MeV. The comparison between this cross section using 10% experimental errors on the nucleon scattering potentials (gray) and 5% errors (blue) are shown in Figure C.7 (a). The corresponding percentage errors as defined in Eq. (5.1) are shown in the same figure in panel (b). As we saw for ^{48}Ca, there is a reduction in the width of the confidence intervals and percentage uncertainty when the experimental errors are reduced for both ^{90}Zr(d,N) calculations.

The next case we consider is the (d,p) transfer on ^{116}Sn. This case will only appear in the adiabatic framework because of the lack of deuteron-target elastic-scattering data at the required incident energy. For the nucleon-target potentials needed to constrain the elastic

156
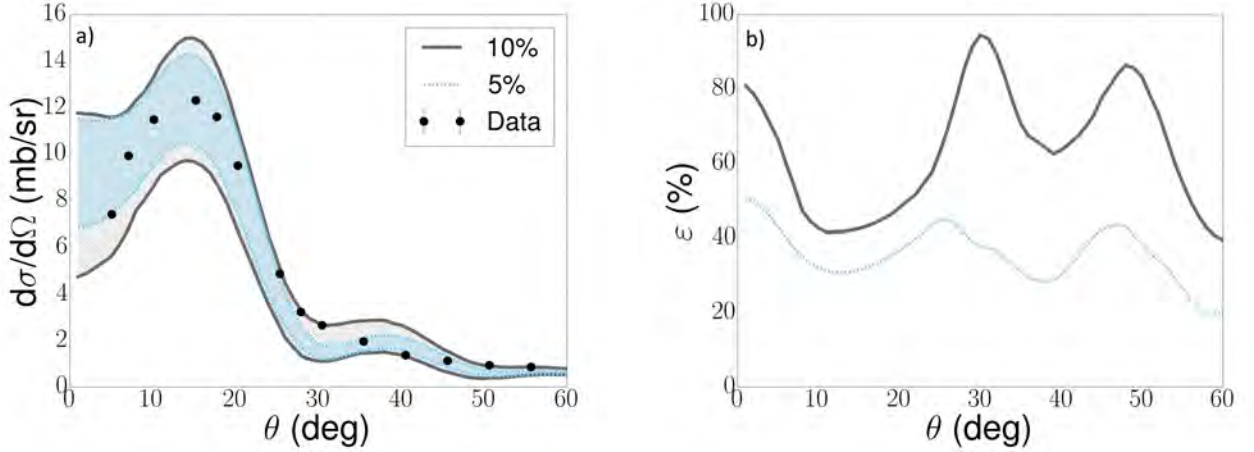
Figure C.7: Same as Figure C.6 for ^{90}Zr(d,p)^{91}Zr(g.s.) at 22.0 MeV.

scattering channels, we begin with ^{116}Sn(n,n)^{116}Sn at 24.0 MeV. The posterior distributions for each of the variables in the potential are shown in Figure C.8 using both 10% and 5% errors on the experimental cross section values as the gray and blue histograms, respectively. These are compared to the prior distributions for each variable which are shown as the gray solid lines. From here, the 95% confidence intervals for each of the resulting elastic scattering cross sections can be calculated. These can be found in Figure C.9 panel (a) as the gray and blue intervals showing the results of constraining with the 10% and 5% errors respectively.

To further constrain the incoming deuteron channel, we use ^{116}Sn(p,p)^{116}Sn elastic scattering at 22.0 MeV. The posterior distributions for the optical model parameters are shown in Figure C.10 where the distributions resulting from the use of 10% (5%) errors on the experimental cross sections are given as gray (blue) histograms. These are compared to the prior distributions which are the gray solid lines in each subplot. These posterior distributions can then be used to construct 95% confidence intervals for each set of parameters, shown in Figure C.9 panel (b), for the 10% and 5% experimental errors in gray and blue, respectively.
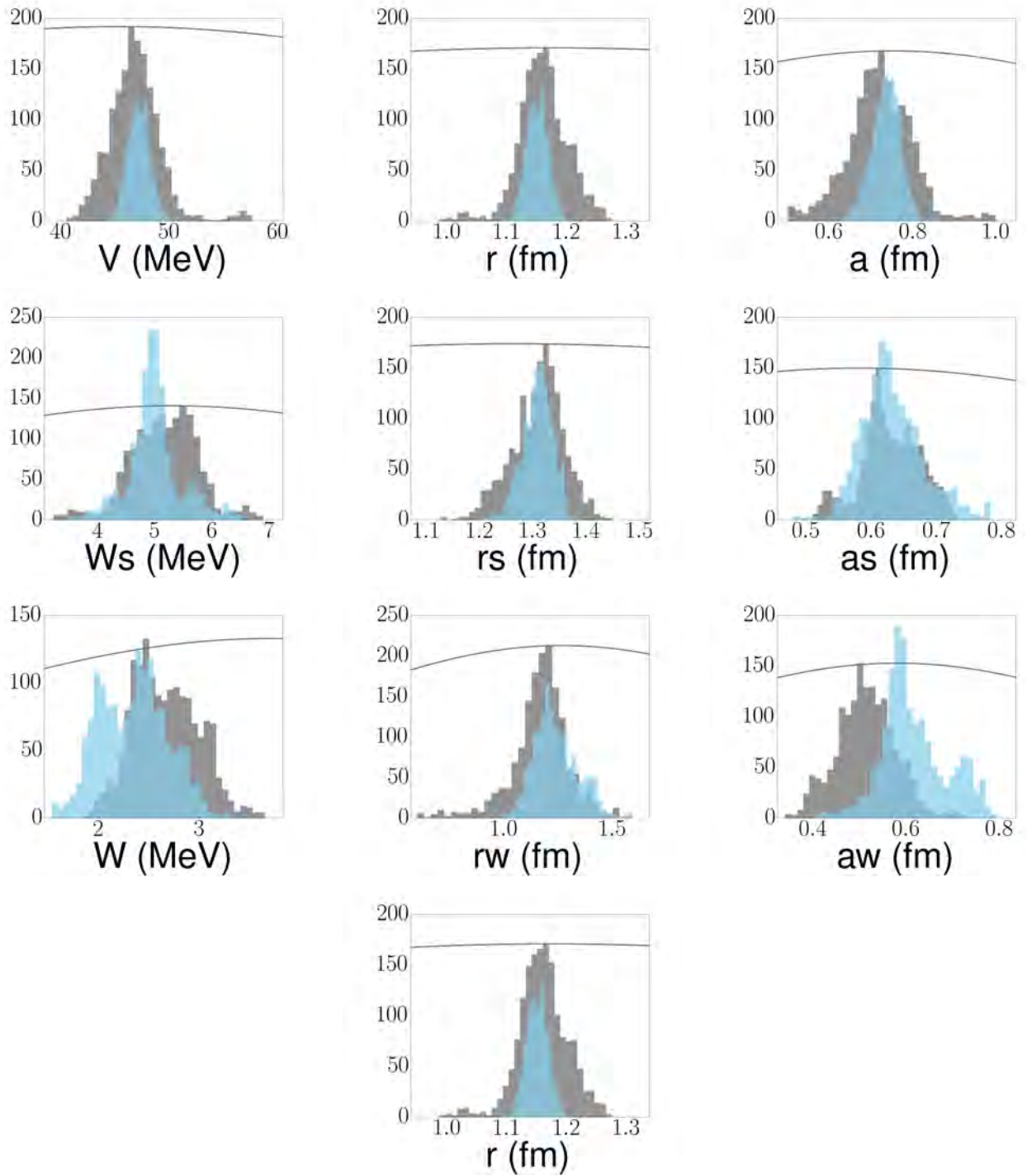
Figure C.8: Posterior distributions (histograms) constraining the optical potential parameters using ^{116}Sn(n,n)^{116}Sn elastic scattering data at 24.0 MeV, comparing 10% errors on the experimental cross sections (gray) and 5% errors (blue). Original prior distributions are shown as gray solid lines.

ε_{exp}	x	$\bar{x}_{\text{n}}^{\text{in}}$	$\Delta x_{\text{n}}^{\text{in}}$	$\bar{x}_{\text{p}}^{\text{in}}$	$\Delta x_{\text{p}}^{\text{in}}$	$\bar{x}_{\text{p}}^{\text{out}}$	$\Delta x_{\text{p}}^{\text{out}}$
	V	46.819	2.411	62.786	3.956	36.968	3.111
	r	1.158	0.041	1.108	0.046	1.227	0.035
	a	0.719	0.077	0.799	0.067	0.680	0.056
	Ws	5.155	0.592	6.992	0.748	1.059	0.110
10%	rs	1.306	0.049	1.479	0.085	1.405	0.092
	as	0.628	0.046	0.761	0.036	0.600	0.073
	W	2.661	0.324	1.655	0.242	3.791	0.637
	rw	1.161	0.134	1.233	0.164	1.553	0.078
	aw	0.513	0.063	—	—	—	—
ε_{exp}	x	$\bar{x}_{\text{n}}^{\text{in}}$	$\Delta x_{\text{n}}^{\text{in}}$	$\bar{x}_{\text{p}}^{\text{in}}$	$\Delta x_{\text{p}}^{\text{in}}$	$\bar{x}_{\text{p}}^{\text{out}}$	$\Delta x_{\text{p}}^{\text{out}}$
	V	47.162	0.891	59.110	2.715	35.666	2.132
	r	1.148	0.018	1.162	0.040	1.255	0.023
	a	0.734	0.034	0.751	0.055	0.620	0.069
	Ws	4.981	0.464	6.903	0.586	1.054	0.105
5%	rs	1.306	0.028	1.408	0.081	1.358	0.103
	as	0.632	0.048	0.764	0.029	0.539	0.079
	W	2.338	0.334	1.554	0.279	3.194	0.400
	rw	1.233	0.012	1.254	0.147	1.643	0.072
	aw	0.615	0.071	—	—	—	—

Table C.2: Same as Table C.1 for the posterior distributions of Figure C.8 (columns two and three), Figure C.10 (columns four and five), and Figure C.11 (columns six and seven).
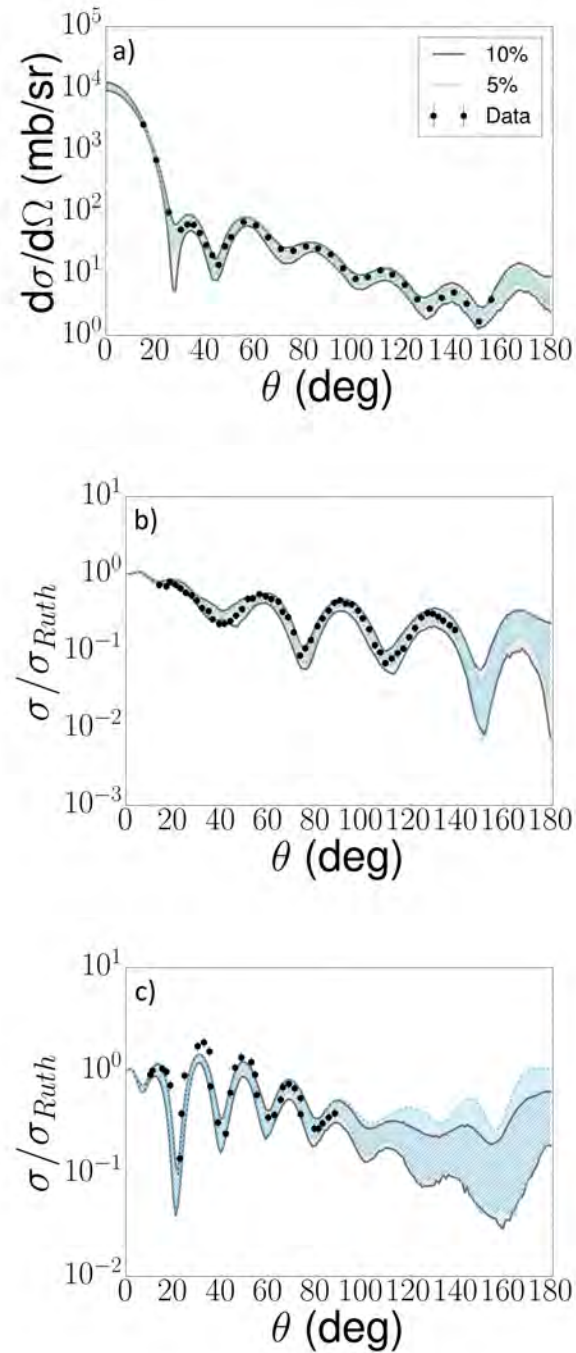
Figure C.9: The 95% confidence interval for the (a) ^{116}Sn(n,n)^{116}Sn elastic scattering cross sections at 24.0 MeV, (b) ^{116}Sn(p,p)^{116}Sn at 22.0 MeV, and (c) ^{116}Sn(p,p)^{116}Sn at 49.35 MeV, from the posterior distributions of Figures C.8, C.10, and C.11, using 10% errors (gray) and 5% errors (blue).
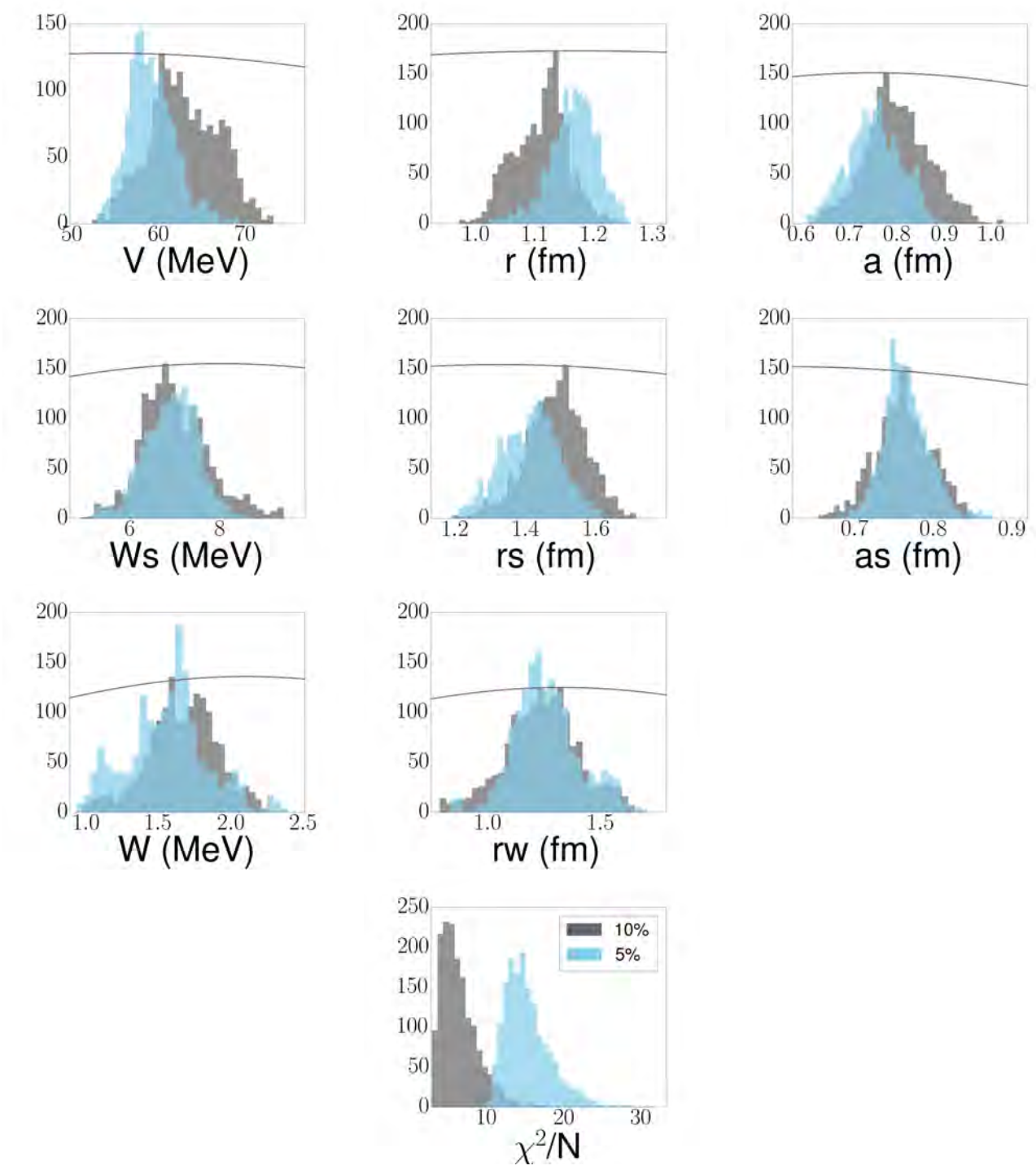
Figure C.10: Same as Figure C.8 for ^{116}Sn(p,p)^{116}Sn elastic scattering at 22.0 MeV.

To complete this transfer calculation, we constrain the outgoing ^{117}Sn-p channel using ^{116}Sn(p,p)^{116}Sn elastic scattering data at 49.35 MeV. The posterior distributions using 10% (5%) experimental errors are shown as the gray (blue) histograms in Figure C.11 compared to the prior distributions for each of the parameters (solid gray). These posterior distributions can then be used to construct 95% confidence intervals, shown in Figure C.9 (c). The gray (blue) regions are the 95% confidence intervals resulting from the 10% (5%) experimental errors. For all three ^{116}Sn-nucleon scattering reactions, the parameters are centered around physical values (although r_w for the outgoing proton channel is larger than normal values of ~ 1.2) with widths that are significantly narrower than the original prior widths. The cross section confidence intervals for the outgoing proton channel also seem to not be able to describe the data at forward angles - though this could be due to the fixed Coulomb radius and not the nuclear potential.

We can then construct the ^{116}Sn(d,p)^{117}Sn(g.s.) transfer cross section with the posterior distributions from Figures C.8, C.10, and C.11. The 95% confidence intervals for the transfer cross section, considering 10% experimental errors on the nucleon-target data shown in gray (5% errors shown in blue) is given in Figure C.12 (a). The corresponding percentage uncertainties are shown in panel (b) of the same figure. As listed in Table 5.8, the width of the 68% confidence interval was larger using 5% experimental errors than for 10% experimental errors. This is discussed in more detail in Section 5.5.1 but is due to the asymmetry of the confidence intervals around the mean cross section value. We also see that the 5% errors cause a wider confidence band in ^{116}Sn(p,p) elastic scattering than the 10% errors which could cause this broadening in the transfer cross section (since the outgoing channel introduces the most uncertainty). In Table 5.9, the uncertainty is reduced when using 5% errors compared to 10% errors when the uncertainty is only considered from the two incoming channels (d_{in}).

162
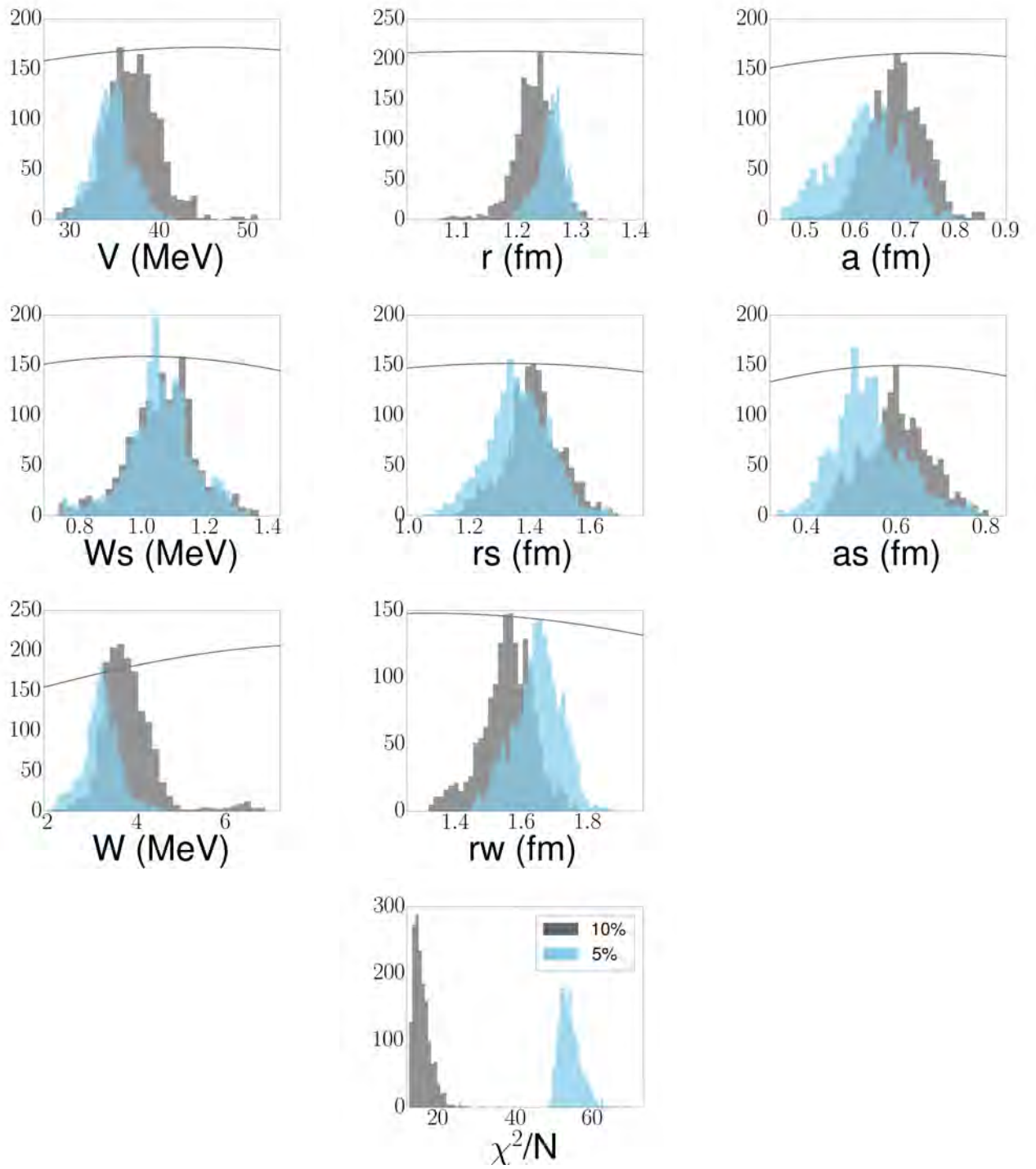
Figure C.11: Same as Figure C.8 for ^{116}Sn(p,p)^{116}Sn elastic scattering at 49.35 MeV.
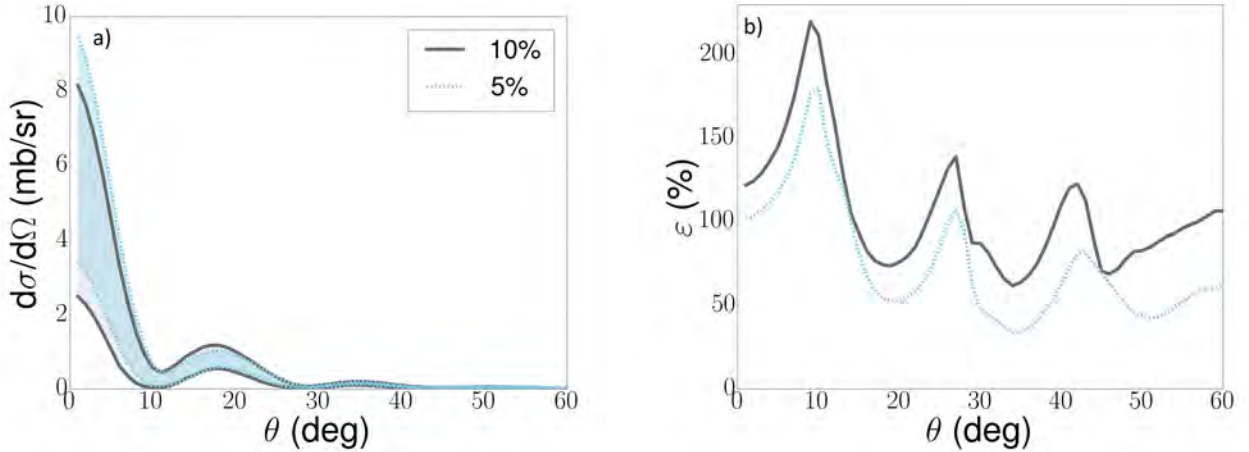
Figure C.12: Same as Figure C.6 for the ^{116}Sn(d,p)^{117}Sn(g.s) transfer reaction at 44.0 MeV.

Finally, we are interested in calculating the ^{208}Pb(d,p)^{209}Pb(g.s.) transfer cross section under the adiabatic approximation. To do this, we use ^{208}Pb(n,n)^{208}Pb scattering at 16.0 MeV to constrain the posterior distributions for each of the optical model parameters. These posteriors are shown in Figure C.13, comparing the distributions using 10% and 5% experimental errors (gray and blue histograms respectively) as well as the initial prior distribution (gray solid). The 95% confidence intervals for the elastic-scattering cross section that result from these posterior distributions are shown in Figure C.14 (a) as the gray (blue) regions for the 10% (5%) experimental errors.

The incident ^{208}Pb-p interaction is constrained with ^{208}Pb(p,p)^{208}Pb elastic scattering data at 16.9 MeV. The posterior distributions for each of the optical model parameters are shown in Figure C.15 as gray (blue) histograms when the 10% (5%) experimental errors were used. These are compared to the prior distributions for each parameter (gray solid lines). These posterior distributions can then be used to construct 95% confidence intervals that result from using the 10% (5%) experimental errors, given as gray (blue) regions shown in Figure C.14 (b).
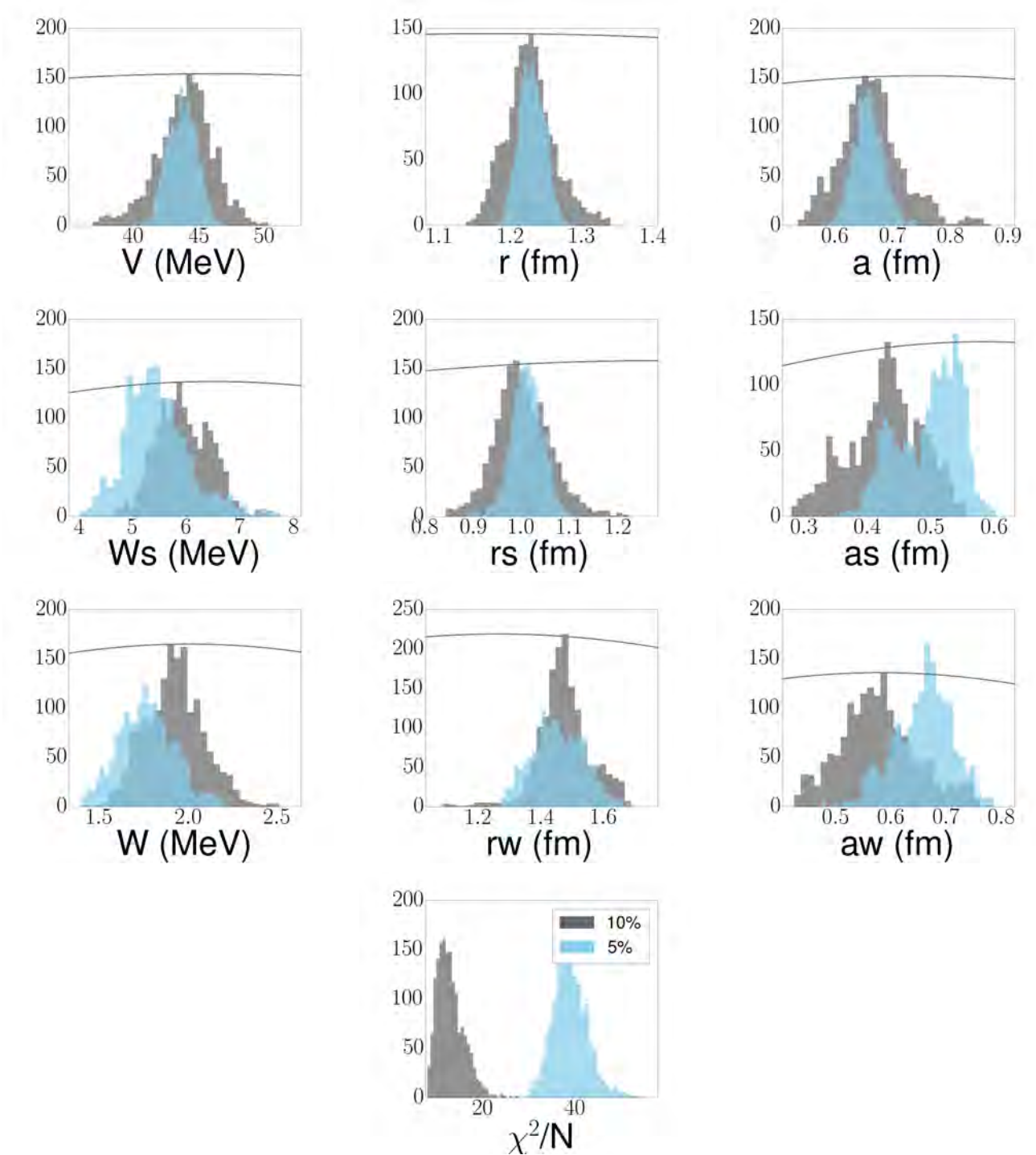
Figure C.13: Posterior distributions (histograms) constraining the optical potential parameters using ^{208}Pb(n,n)^{208}Pb elastic scattering data at 16.0 MeV, comparing 10% errors on the experimental cross sections (gray) and 5% errors (blue). Original prior distributions are shown as gray solid lines.

ε_{exp}	$\mathbf{x}$	$\bar{x}_\text{n}^\text{in}$	$\Delta x_\text{n}^\text{in}$	$\bar{x}_\text{p}^\text{in}$	$\Delta x_\text{p}^\text{in}$	$\bar{x}_\text{p}^\text{out}$	$\Delta x_\text{p}^\text{out}$
	V	43.893	2.134	62.500	5.126	51.089	3.161
	r	1.226	0.035	1.195	0.057	1.189	0.029
	a	0.662	0.055	0.591	0.078	0.690	0.060
	Ws	5.933	0.506	11.913	0.867	5.361	0.657
10%	rs	1.001	0.057	1.100	0.111	1.295	0.054
	as	0.427	0.058	0.516	0.067	0.763	0.050
	W	1.915	0.165	1.028	0.108	4.736	0.312
	rw	1.470	0.084	1.216	0.117	1.295	0.085
	aw	0.577	0.070	0.633	0.069	—	—
ε_{exp}	$\mathbf{x}$	$\bar{x}_\text{n}^\text{in}$	$\Delta x_\text{n}^\text{in}$	$\bar{x}_\text{p}^\text{in}$	$\Delta x_\text{p}^\text{in}$	$\bar{x}_\text{p}^\text{out}$	$\Delta x_\text{p}^\text{out}$
	V	43.685	1.115	66.836	3.304	50.891	2.424
	r	1.228	0.018	1.153	0.031	1.196	0.024
	a	0.657	0.025	0.608	0.044	0.669	0.051
	Ws	5.455	0.614	11.598	0.959	4.860	0.493
5%	rs	1.009	0.032	1.061	0.073	1.273	0.036
	as	0.496	0.050	0.598	0.051	0.772	0.062
	W	1.760	0.157	1.016	0.094	4.394	0.458
	rw	1.449	0.082	1.190	0.123	1.374	0.086
	aw	0.657	0.052	0.600	0.056	—	—

Table C.3: Same as Table C.1 for the posterior distributions of Figure C.13 (columns two and three), Figure C.15 (columns four and five), and Figure C.16 (columns six and seven).
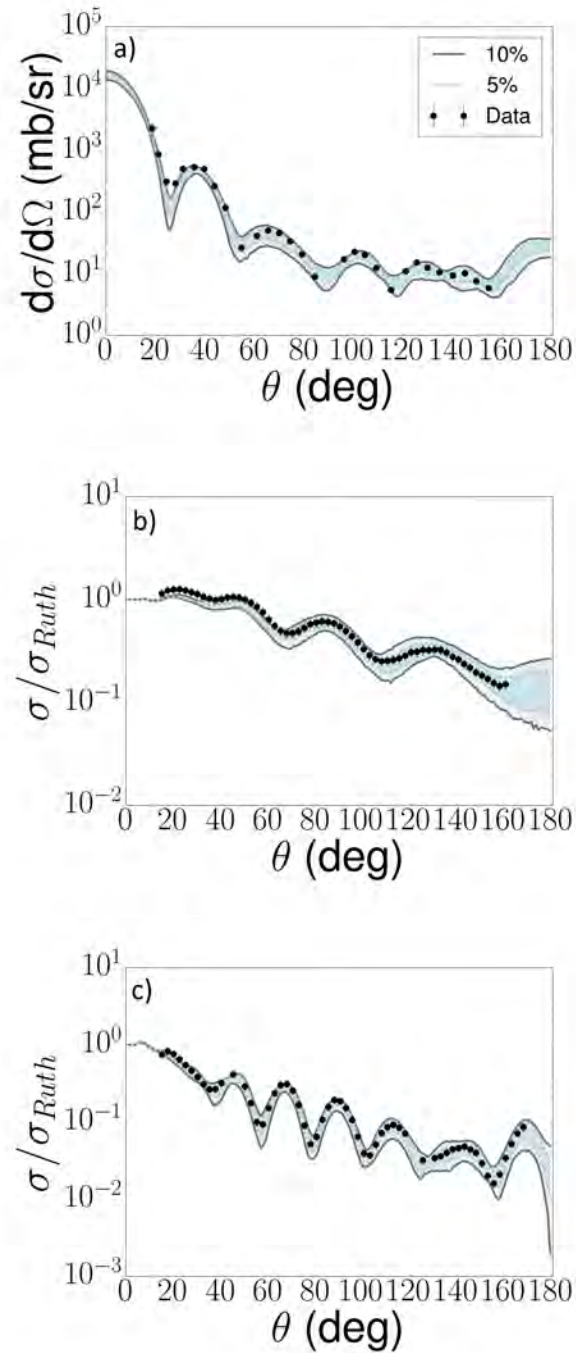
Figure C.14: 95% confidence interval for the (a) ^{208}Pb(n,n)^{208}Pb elastic scattering cross sections at 16.0 MeV, (b) ^{208}Pb(p,p)^{208}Pb at 16.9 MeV, and (c) ^{208}Pb(p,p)^{208}Pb at 35.0 MeV, from the posterior distributions of Figures C.13, C.15, and C.16, using 10% errors (gray) and 5% errors (blue).
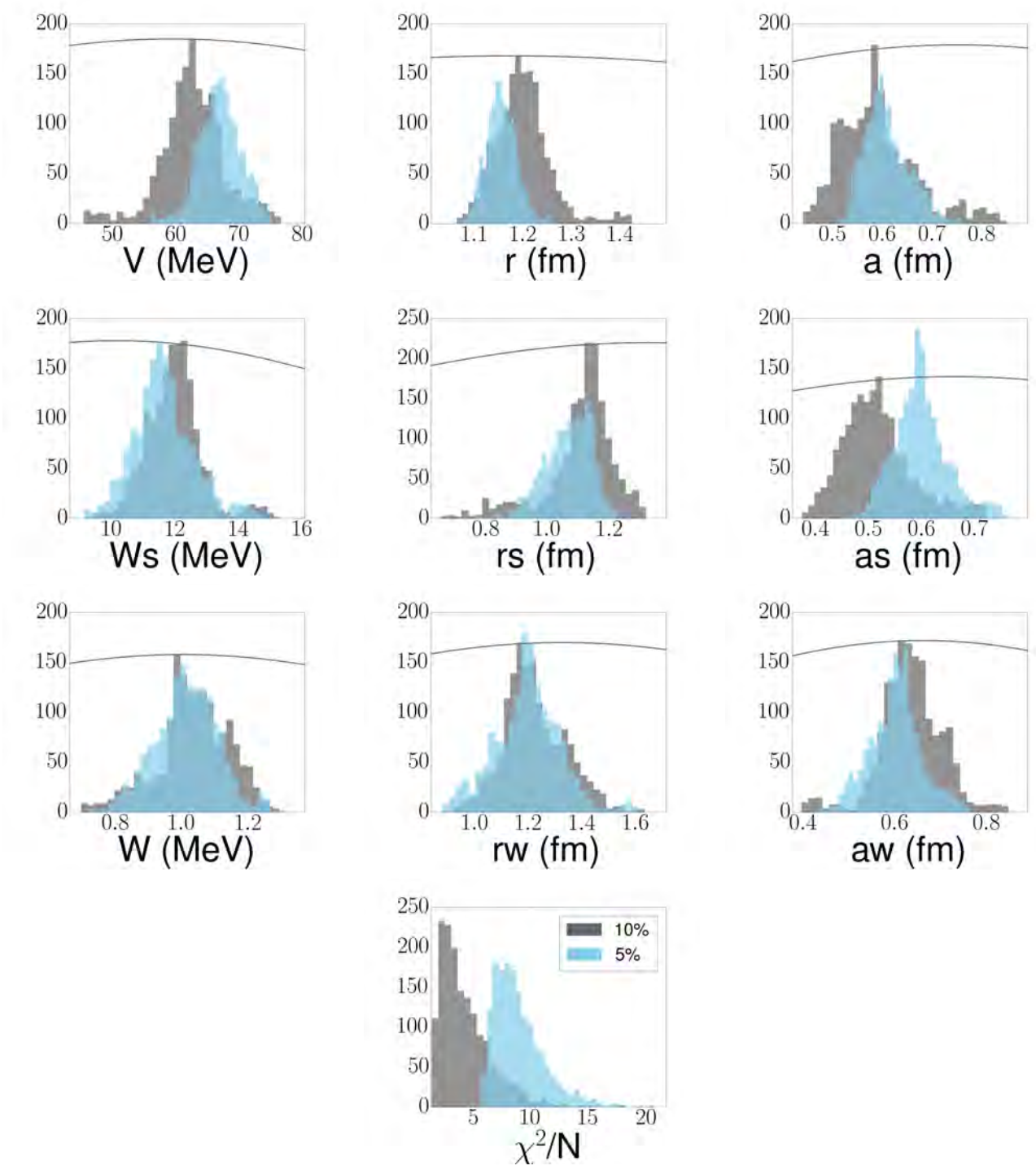
Figure C.15: Same as Figure C.13 for ^{208}Pb(p,p)^{208}Pb elastic scattering at 16.9 MeV.

The outgoing ^{209}Pb-p channel is constrained using ^{208}Pb(p,p)^{208}Pb elastic-scattering data at 35.0 MeV. The resulting posterior distributions, using 10% and 5% experimental errors to constrain the parameter distributions, are shown in Figure C.16 in gray and blue respectively. The resulting 95% confidence intervals for the elastic scattering cross sections are shown in Figure C.16 (c) as the gray and blue intervals, respectively. Again, for all three elastic scattering reactions, the parameters are well-constrained within physical limits (and have narrow widths). We do see, however, that the Coulomb radius for ^{116}Sn(p,p) elastic scattering at 16.9 MeV does not correctly describe the data at forward angles. There is also a slight down-turn in the ^{116}Sn(p,p) at 35.0 MeV that is not reproduced by the 95% confidence intervals.

Finally, we construct the ^{208}Pb(d,p)^{209}Pb(g.s.) transfer cross section with the posterior distributions displayed in Figures C.13, C.15, and C.16. These are shown in Figure C.17 (a), the 95% confidence intervals from the 10% and 5% experimental errors (gray and blue bands respectively). Panel (b) shows the percentage uncertainties for both of the calculations across the given angular range.

Deuteron Elastic Scattering

For the (d,p) and (d,n) transfer reactions on ^{90}Zr within the DWBA framework, we need to constrain the ^{90}Zr(d,d) elastic scattering optical potential parameters. This is done using data at 23.2 MeV. The posterior distributions are shown in Figure C.18 as gray (blue) histograms when 10% (5%) experimental errors were included on the data, compared to the prior distributions (gray solid). These posterior distributions are then used to create 95% confidence intervals for the ^{90}Zr(d,d)^{90}Zr elastic scattering cross sections shown in
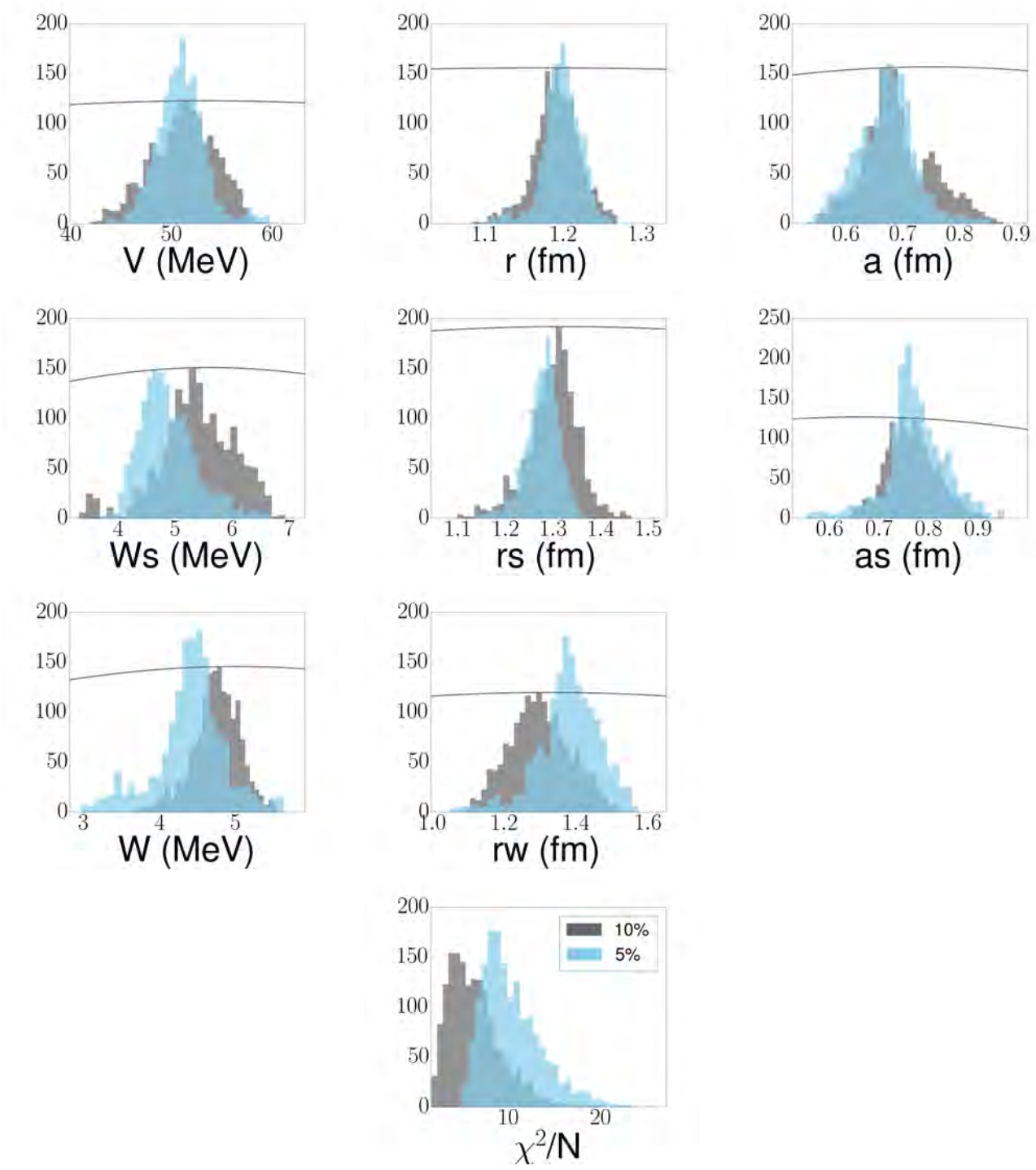
Figure C.16: Same as Figure C.13 for ^{208}Pb(p,p)^{208}Pb elastic scattering at 35.0 MeV.
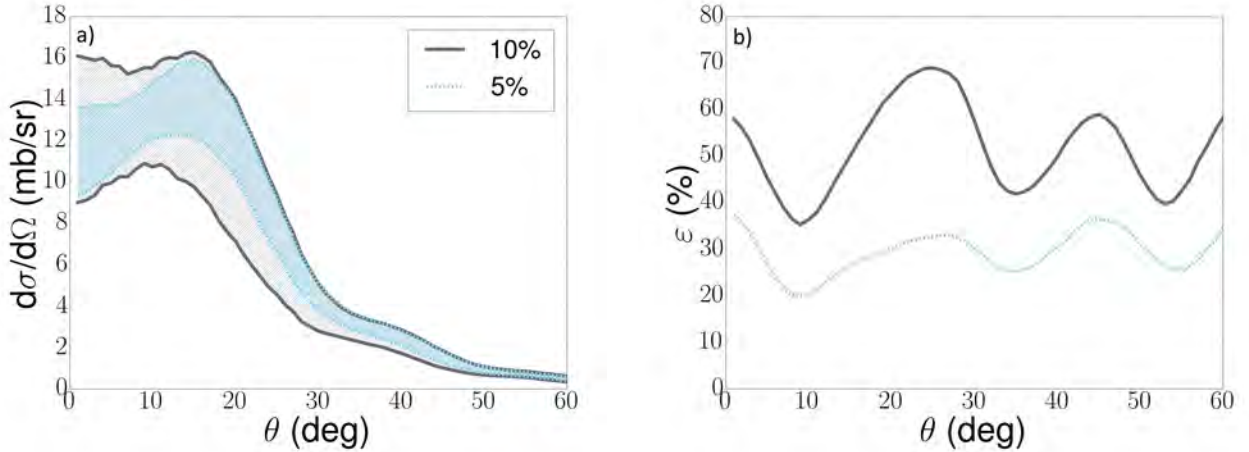
Figure C.17: Same as Figure C.6 for the ^{208}Pb(d,p)^{209}Pb(g.s.) transfer reaction at 32 MeV.

Figure C.19. Even though this reaction is at the same energy and over the same angular range as ^{48}Ca(d,d), there are more noticeable differences between the 10% and 5% cross section calculations than between the two for ^{48}Ca(d,d), especially at backwards angles. (The parameter posterior distributions, however, are not significantly different when using 5% errors compared to 10%.)

To calculate the transfer cross sections with DWBA, we use the posterior distributions from Figure C.18 for the incoming deuteron channel and the outgoing nucleon scattering from the previous section. First considering the ^{90}Zr(d,n)^{91}Nb(g.s.) calculation again at 20.0 MeV, the transfer cross sections using both 10% experimental errors and 5% experimental errors to constrain all of the elastic scattering potential parameters are given in Figure C.20 (a), gray and blue respectively, along with the corresponding percentage uncertainties in panel (b). We again see a reduction in the width of the confidence interval - as well as in the percentage uncertainty - but not to the same extent that the experimental error was reduced.

We can do the same calculation, exchanging the outgoing ^{90}Zr(n,n)^{90}Zr channel for the
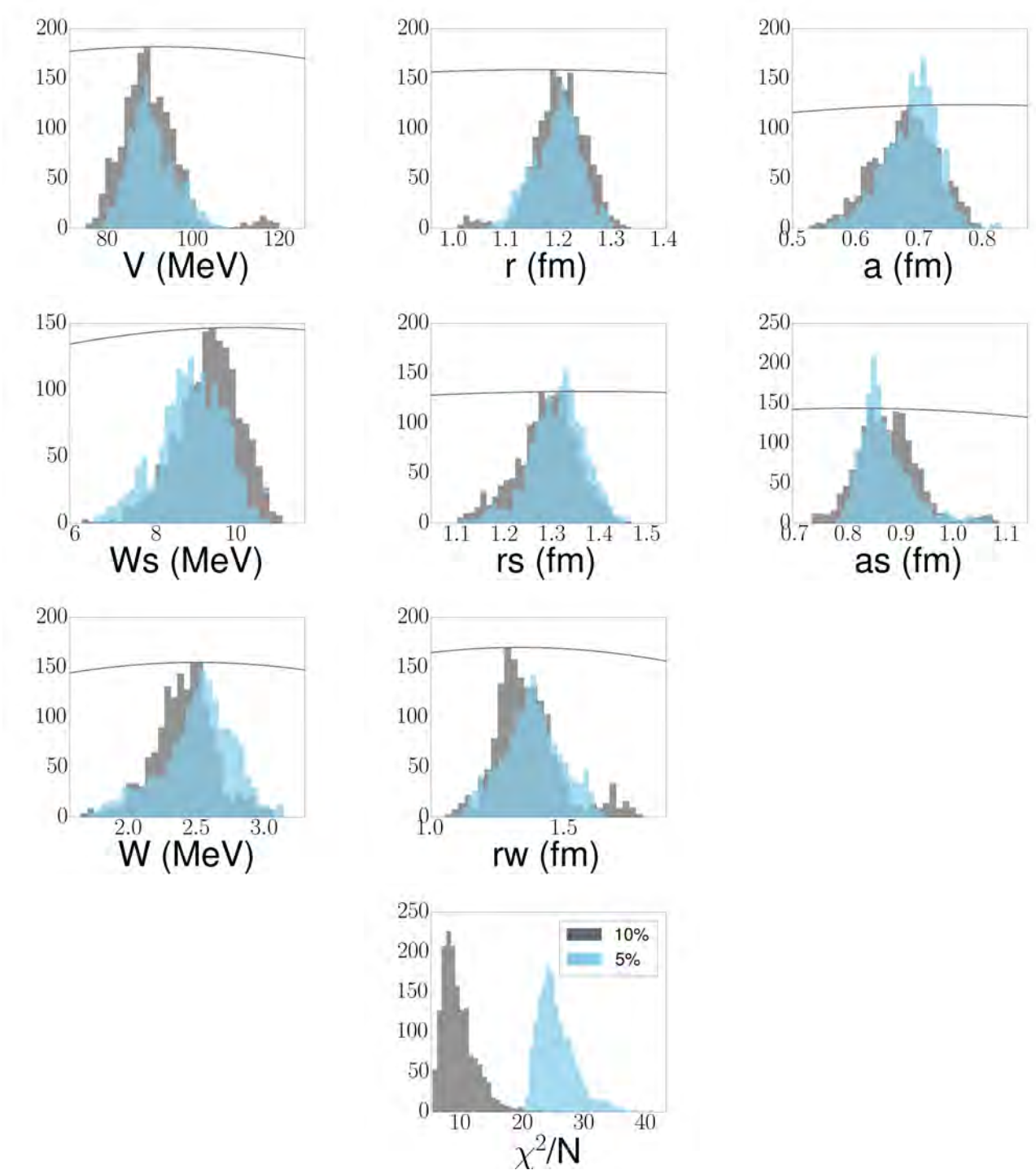
Figure C.18: Posterior distributions (histograms) constraining the optical potential parameters using ^{90}Zr(d,d)^{90}Zr elastic scattering data at 23.2 MeV, comparing 10% experimental errors (gray) and 5% experimental errors (blue). Original prior distributions are shown as gray solid lines.
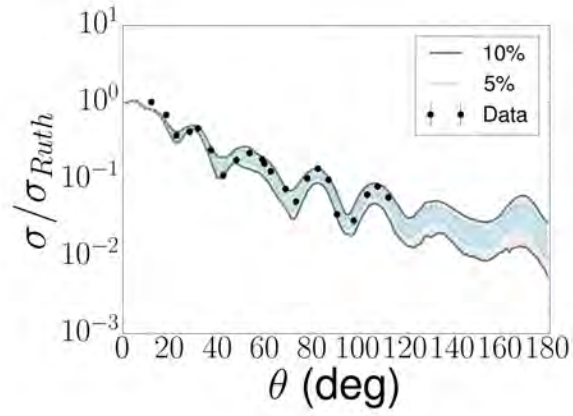
Figure C.19: 95% confidence interval for the ^{90}Zr(d,d)^{90}Zr elastic scattering cross sections at 23.2 MeV from the posterior distributions of Figure C.18 using 10% errors (gray) and 5% errors (blue).
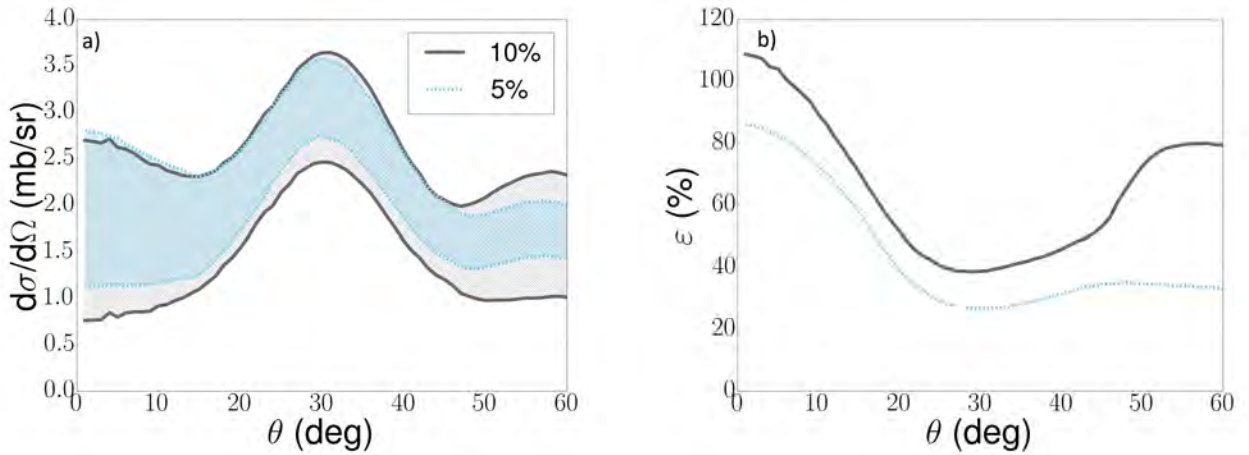
Figure C.20: Same as Figure C.6 for ^{90}Zr(d,n)^{91}Nb(g.s.) at 20.0 MeV using DWBA.
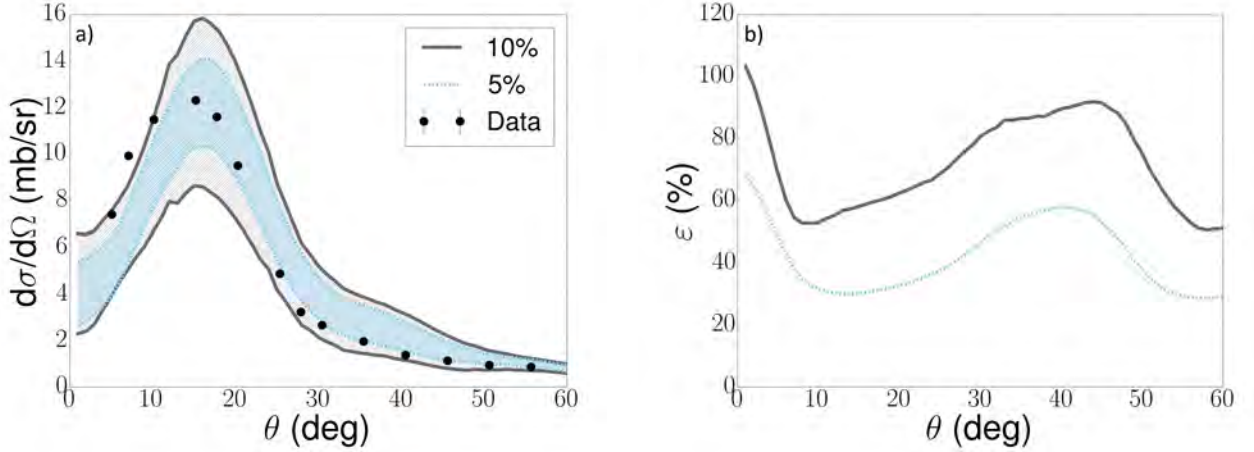
Figure C.21: Same as Figure C.6 for ^{90}Zr(d,p)^{91}Zr(g.s) at 22.0 MeV using DWBA.

outgoing ^{90}Zr(p,p)^{90}Zr to calculate the ^{90}Zr(d,p)^{91}Zr(g.s.) transfer cross section instead. (This includes replacing the relevant Q-value, single-particle bound state, and binding energy, as well.) The 95% confidence intervals for these cross sections using 10% (5%) experimental errors are shown in Figure C.21 (a) as the gray (blue) bands. There percentage uncertainties are shown in the corresponding colors in (b).

Although there is no deuteron elastic-scattering data for the ^{116}Sn target (and therefore, no DWBA calculation, as mentioned in a previous section), we can still consider the final case for ^{208}Pb(d,p)^{209}Pb(g.s) within this formalism using ^{208}Pb(d,d)^{208}Pb data at 28.8 MeV to constrain the parameters of the optical model. The comparison of the posterior distributions using both 10% and 5% experimental errors on the elastic-scattering data is shown in Figure C.22 as the gray and blue histograms, respectively. These distributions are compared to the prior distribution for each parameter, given as the solid gray lines. The posterior distributions are then used to compute the 95% confidence intervals for the elastic-scattering cross sections, as in Figure C.23. The gray (blue) region is produced from the posterior distributions of the 10% (5%) experimental error calculations. Here, there is more angular coverage than for

174

either the ^{48}Ca(d,d) or ^{90}Zr(d,d) data, but there is almost no noticeable difference between the 10% and 5% calculations. Over all, reducing the experimental errors appears to have less effect on the deuteron elastic-scattering calculations.

Finally, the transfer cross section, using DWBA, can be calculated for ^{208}Pb(d,p)^{209}Pb(g.s.). This calculation, again, uses the ^{208}Pb-d potential posterior distribution shown in Figure C.22 and the outgoing ^{208}Pb-p potential posterior distribution from the previous section, using both 10% and 5% experimental errors. The 95% confidence intervals are shown in Figure C.24 (a) for the 10% errors (gray) and 5% errors (blue). Panel (b) gives the percentage uncertainty as defined in Eq. (5.1).
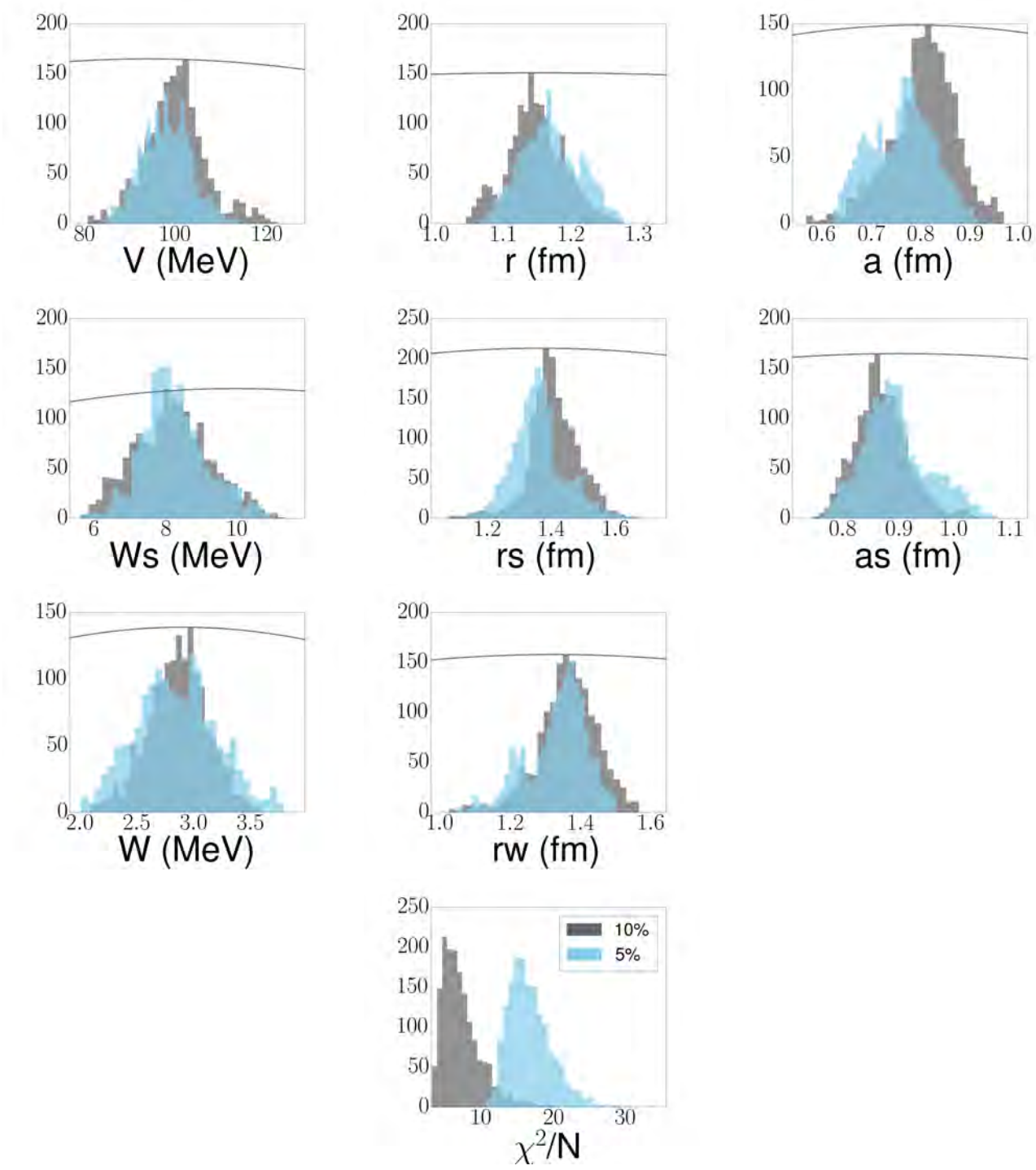
Figure C.22: Same as Figure C.18 for ^{208}Pb(d,d)^{208}Pb elastic scattering at 28.8 MeV.
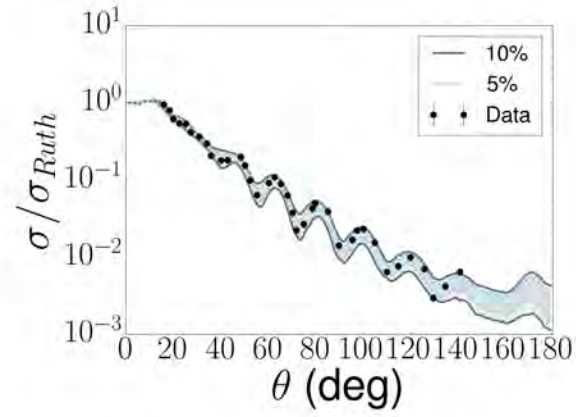
Figure C.23: 95% confidence interval for ^{208}Pb(d,d)^{208}Pb elastic scattering at 28.8 MeV from the posterior distributions of Figure C.22 using 10% errors (gray) and 5% errors (blue).
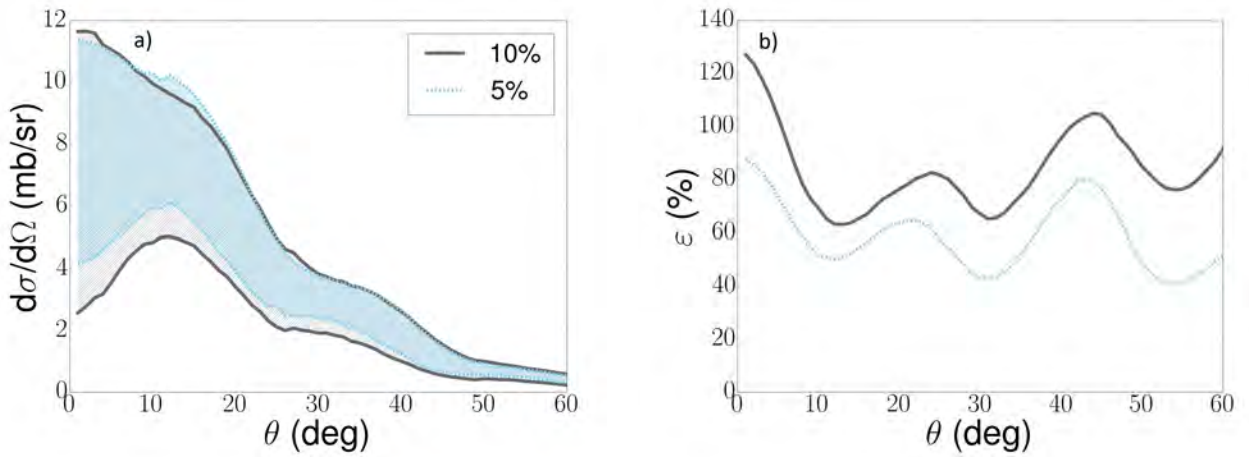
Figure C.24: Same as Figure C.6 for ^{208}Pb(d,p)^{209}Pb(g.s.) at 32.0 MeV using DWBA.

Appendix D

Energy Dependence in Non-local Optical Potentials

As has been discussed throughout this work, optical potentials are a useful tool to describe the interactions between projectile-target pairs. These effective interactions take into account the complexities that arise from simplifying the many-body to a two-body problem. Once the shape of the potential has been defined, the parameters within it are typically determined by fitting to elastic-scattering differential cross sections. These interactions are generally assumed to be local and strongly energy-dependent. This energy dependence is typically included to take into account the nonlocality. However, recent work has shown that including non-locality in reaction theory formulations such as the adiabatic distorted wave approximation (ADWA) is important [71]. Energy-dependent potentials are not enough to fully taken into account these effects.

This non-locality in the effective interactions arises intrinsically from many-body structure and it is also seen at the mean field level where the exchange term in Hartree-Fock introduces an explicit non-local potential [74]. In addition to non-locality originating from antisymmetrization, couplings from the elastic channel to all other channels not included in the model space can introduce non-locality [75, 149]. It had previously been assumed that the non-locality in these types of theories could be encapsulated in the energy de-

pendence of local potentials, but several studies over the past few years have shown that an explicit inclusion of non-locality in the calculation of reaction observables is important [150, 151, 71, 152, 153, 154, 155].

Although the potential is not an observable, it is well-known that non-locality is required in microscopic theories, and therefore, these theories should be able to provide insight into the form of the non-locality and energy dependence in phenomenological potentials. Effort has gone into deriving optical potentials from microscopic theories, in the dispersive optical model (DOM) [156, 157] which utilizes the link between the self-energy and the optical potential [158], and from *ab initio* theories, such as in [65]. The non-locality described by these studies is not a simple Gaussian and is larger than assumed in the original formulations of non-local potentials [151, 157, 65]. However, the non-local nucleon optical potentials derived from state-of-the-art *ab initio* theories, such as in [65] are still unable to provide a detailed description of the data.

While these microscopic potentials are still under development, global optical potentials should be improved upon. Such global potentials are important to the few-body community as effective interactions to model complex nuclear reactions such as transfer, breakup, and knock-out when few-body-like projectiles are involved. Having simple, easy-to-use parameterizations for complex reaction theory is still crucial for this field. Just as the phenomenological potential can be improved with insights from microscopic calculations, the behavior of microscopic potentials can be constrained by well-constructed phenomenological potentials. Towards that goal, here, we investigate whether the explicit introduction of an energy dependence in a non-local global optical potential improves the description of neutron scattering on spherical targets.

Non-local Potentials

Titus, *et. al.* [71] implemented non-locality into the adiabatic wave approximation (ADWA) [126] to understand its importance in the central nuclear potentials for (d,p) transfer reactions. As expected, they found that nonlocality causes a reduction in the bound-state wave function in the nuclear interior and a reduction of its asymptotic normalization. This typically causes an increase in the magnitude of the transfer cross sections relative to a completely local potential for peripheral reactions. This enhancement can be as large as 40%. Many of the same effects are seen in (d,n) transfer reactions as well [152]. Over the past few decades, there have been a few studies that aim to provide a completely non-local description of the optical potential, including works by Perey and Buck (PB) [159] and Tian, Pang, and Ma (TPM) [160]. The two parameterizations that were developed are briefly discussed below.

The Perey-Buck potential [159] is a phenomenological potential, assumed to be energy and mass independent, and was fit to two sets of data - neutrons on ^{208}Pb at 7.0 and 14.5 MeV. The range of the non-locality, β, was fixed at 0.85 fm, about the size of the nucleon. Even with the limited set of data that was fit, the PB potential does a reasonable job reproducing a variety of neutron elastic-scattering data, although mostly at energies less than 20 MeV.

Like the PB potential, the non-local potential of Tian, Pang, and Ma [160] was assumed to be energy and mass independent. It was fit to a larger variety of data sets than the PB potential, both in mass and energy, and a separate potential was developed for neutrons and protons. The range of the non-locality, β was taken as a free parameter in the TPM fit, however, the range of the non-locality is similar to that in the PB potential for both the

neutron and proton potentials. The TPM potential performs better than PB (has lower χ^2 values) for $20 \leq E \leq 30$ MeV, but the description of data for $E < 20$ MeV is similar.

Exploring Energy Dependence

In each of the previous non-local potentials, one assumed there was no mass or energy dependence. This stems from the assumption that most of the strong energy dependence present in local potentials arises from the non-locality of the interactions. The energy dependence of PB and TPM was investigated in the master's thesis of Bacq [2]. First, for the PB potential, the real volume depth and the imaginary surface depth were each independently fit to 24 sets of data, ^{40}Ca (E=9.9, 11.9, 13.9, 16.9, 21.7, 25.5, 30.1, 40.1 MeV), ^{90}Zr (E=5.9, 7.0, 8.0, 10.0, 11.0, 24.0 MeV), and ^{208}Pb (E=7.0, 9.0, 11.0, 14.6, 16.9, 20.0, 22.0, 26.0, 30.3, 40.0 MeV) [161, 162, 163, 164, 165, 166, 167, 168, 169, 170, 171, 172]. The same was done for the TPM potential, except additionally, the imaginary volume depth was also fit to these same 24 sets of data. For both cases, the real volume depth barely changed across the data sets, regardless of the mass or energy of the reaction.

Using each potential as a starting point, pairs of potential depths were fit simultaneously to each data set, and for the TPM potential, all three potential depths were fit simultaneously. Even in the cases where the real volume depth was varied simultaneously with either imaginary depth, the values of the this depth did not change significantly with energy. Furthermore, for the TPM potential, it was found that the energy dependence of both imaginary depths could not be determined by simultaneous fitting. Therefore, as a starting point, the depth of the imaginary surface term was fitted to each data set individually. For the three targets, the depth appeared to increase linearly with increasing energy.

System	a (PB)	b (PB)	a (TPM)	b (TPM)
^{40}Ca	0.24	11.73	0.48	9.26
^{90}Zr	0.19	11.97	0.24	12.53
^{208}Pb	0.41	10.43	0.25	15.87

Table D.1: Summary of the slope and intercept values for the W_s values from [2] using Eq. D.1 for the TPM and PB potentials.
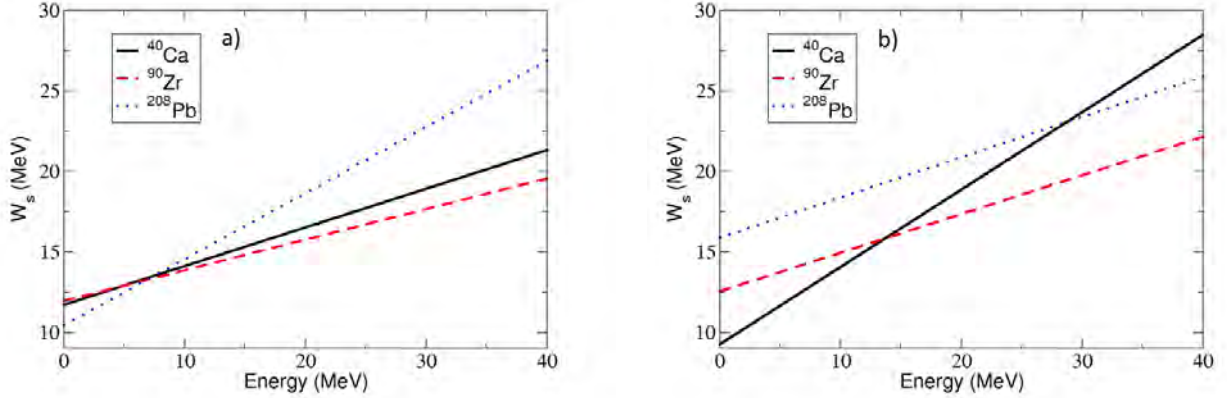
Figure D.1: Comparison of the linearizations of Table D.1 for the individually-fitted W_s values for the a) PB and b) TPM potentials.

In [2], the values for the imaginary surface depths, W_s, were fitted to

$$W_s = aE + b, \tag{D.1}$$

for each scattering pair. The resulting parameters are given in Table D.1. Plotting these linearizations (as shown in Figure D.1), it is difficult to tell whether the three fits are consistent with one another - even within error bands (which can be calculated using the method of Section 3.1.1).

However, the high energy W_s values had a significant impact on the linearization that was calculated in [2]. If we instead fit Eq. (D.1) using a consistent energy range for the three

System	a (PB)	b (PB)	a (TPM)	b (TPM)
^{40}Ca	0.531	6.807	0.726	4.436
^{90}Zr	0.193	11.885	0.239	12.505
^{208}Pb	0.376	11.536	0.042	19.052

Table D.2: Same as Table D.1 excluding fitted W_s values above $E = 26$ MeV.

systems - excluding the W_s values above 26 MeV, for ^{40}Ca and ^{208}Pb - we find the results shown in Table D.2. For the TPM potential, slopes (a) decrease with increasing mass of the target and the intercepts (b) increase with increasing mass, which indicates that the fits might be consistent with one another if a mass dependence is included. Mass dependences of A, $A^{1/2}$, and $A^{1/3}$ can be fit to the TPM slopes and intercepts, but the best description is found when an asymmetry dependence is included, in the form $(N - Z)/A$. Fitting the PB and TPM results separately, we find the following dependences for $W_s(E, (N - Z)/A)$:

$$W_s^{\text{PB}}\left(E, \frac{N-Z}{A}\right) = \left(0.206\frac{N-Z}{A} + 0.289\right)E + \left(12.033\frac{N-Z}{A} + 9.555\right), \qquad \text{(D.2)}$$

and

$$W_s^{\text{TPM}}\left(E, \frac{N-Z}{A}\right) = \left(-0.235\frac{N-Z}{A} + 0.341\right)E + \left(26.279\frac{N-Z}{A} + 9.264\right). \quad \text{(D.3)}$$

The first term in Eq. (D.3) and (D.2) which couples the asymmetry and energy is significantly smaller than the other three terms. Dropping this term, the remaining three energy and asymmetry dependences were fit directly to the W_s values found in [2]. The resulting equations for W_s are

$$W_s^{\text{PB}}\left(E, \frac{N-Z}{A}\right) = 0.304E + 15.036\frac{N-Z}{A} + 9.332, \qquad \text{(D.4)}$$

and

$$W_s^{\text{TPM}}\left(E, \frac{N-Z}{A}\right) = 0.330E + 21.655\frac{N-Z}{A} + 9.518. \tag{D.5}$$

The coefficients for each term are strikingly similar between the PB and TPM potentials, and this form for the energy and asymmetry dependences are reminiscent of those of Becchetti and Greenlees [1], which uses for its potential depths:

$$
\begin{aligned}
V &= 54 - 0.32E - 24\frac{N-Z}{A}, \\
W &= 0.22E - 1.6, \\
W_s &= 13 - 0.25E - 12\frac{N-Z}{A}.
\end{aligned}
\tag{D.6}
$$

Although we found no energy or asymmetry dependence in the real volume potential term (V), we do see a strong energy and asymmetry dependence in the imaginary surface term (W_s) which is about the same magnitude of Eq. (D.6) although opposite in signs for both parts. This leads us to directly fit the neutron scattering data for ^{48}Ca, ^{90}Zr, and ^{208}Pb to a form like Eq. (D.6) for the imaginary potential depths, through χ^2 minimization.

Energy and Asymmetry Dependences

Now, instead of fitting W_s for each reaction individually and then performing a join fit over the energy and asymmetry dependences, we instead fit all 24 data sets simultaneously, starting from both the PB and TPM parameterizations. Along with the form for W_s:

$$W_s\left(E, \frac{N-Z}{A}\right) = aE + b\frac{N-Z}{A} + c, \tag{D.7}$$

	PB-C	TPM-C	PB-C100	TPM-C100
a	0.141 ± 0.015	0.597 ± 0.018	-0.017 ± 0.015	0.200 ± 0.014
b	-1.737 ± 0.366	-3.145 ± 0.592	0.738 ± 0.458	4.477 ± 0.480
c	10.397 ± 0.327	5.019 ± 0.406	11.935 ± 0.377	12.154 ± 0.397
d	0.233 ± 0.011	-0.062 ± 0.011	0.335 ± 0.011	0.183 ± 0.009
e	-0.708 ± 0.234	5.507 ± 0.262	-2.003 ± 0.245	0.363 ± 0.255

Table D.3: Fitted parameters resulting from the simultaneous fit of all 24 data sets for the PB (TPM) potentials using data over the entire angular range (column two (three)) and only using data up to $100°$ (column four (five)).

we also parameterize the imaginary depth of the volume term, W (despite this term being zero in the PB parameterization). This depth is taken to only depend on energy and not asymmetry as in [1],

$$W(E) = dE + e. \tag{D.8}$$

The resulting parameters for a, b, c, d, and e are given in Table D.3 in columns two and three for the PB and TPM potentials, respectively, along with the associate error for each parameter. The errors are calculated as the square root of the diagonal of the parameter covariance matrix and give an indication as to whether or not the fitted parameters are consistent with zero. Although the comparison between the parameters of the PB and TPM fits are not nearly as close as when the double fit was performed (at an extreme, d and e switch signs between the two parameterizations), none of the parameters are consistent with zero. The χ^2 values resulting from these fits are shown in Table D.4 columns four and seven for the PB and TPM potentials respectively. The χ^2 values decrease, sometimes significantly, from the original values, especially, in the energy range where the potential was not originally fit.

The approximations that are used for elastic-scattering calculations with optical model potentials typically provide a more accurate description at forward angles than at backwards

angles. Therefore, in order to confirm that the backwards angles were not skewing the energy dependence, we performed the join fit excluding data at angles greater than $100°$. This fit is given in Table D.3, columns four (PB) and five (TPM). The χ^2 values compared to the original values and the values when the fit was performed over all angles are shown in Table D.4 for the PB (column five) and TPM (column eight) potentials, respectively. The energy dependence has now shifted to the imaginary volume term for PB and the imaginary surface potential for TPM. For the PB potential, a is consistent with zero, within errors, getting rid of the energy dependence in the imaginary surface term. The same is true of the TPM potential, only this time d is consistent with zero, removing the energy dependence in the imaginary volume term. Where as W_V is a constant in the TPM potential, W_s is a constant for the PB potential. The errors on the remaining parameters are at least an order of magnitude smaller than the parameter values themselves. (The exception to this is b - the asymmetry term - in PB.)

This shift in the energy dependence between the imaginary surface and volume terms is consistent with what was found in [2]: these two depths could not be constrained simultaneously. The differences in the asymmetry terms between the two potentials make it plausible that either this is not a robust form for the asymmetry-dependence, or the asymmetry in these data sets does not span a wide enough range to determine its dependence. Still the inclusion of an energy dependence term in the imaginary potential does significantly improve the description of these systems. The improvement is seen not only in the χ^2 values but also in the description of the experimental cross sections, as shown for select cases in Figure D.2.

Because the original PB parameterization does not contain an imaginary volume term, its geometry (radius and diffuseness) was arbitrary. In the fit outlined above, the geometry was the same as the geometry of the TPM potential. However, we could instead constrain

System	E (MeV)	χ^2_{PB}	χ^2_{PB-C}	$\chi^2_{PB-C100}$	χ^2_{TPM}	χ^2_{TPM-C}	$\chi^2_{TPM-C100}$
^{40}Ca	9.91	16.497	13.842	14.517	19.248	12.413	13.089
^{40}Ca	11.9	3.341	3.288	2.843	21.621	3.901	4.749
^{40}Ca	13.9	7.059	6.377	7.907	19.539	9.938	12.057
^{40}Ca	16.916	9.115	11.514	6.128	10.930	13.474	6.780
^{40}Ca	21.7	16.343	15.457	10.203	20.107	23.406	22.758
^{40}Ca	24.5	20.004	9.389	3.966	6.756	13.646	7.168
^{40}Ca	30.1	24.029	7.235	5.73	8.655	10.610	8.687
^{40}Ca	40.1	20.427	20.149	3.37	4.867	42.154	4.349
^{90}Zr	5.9	2.163	5.757	3.504	5.743	7.099	3.295
^{90}Zr	6.95	1.714	5.239	2.888	8.426	8.867	6.929
^{90}Zr	8.0	8.93	12.079	9.824	12.160	14.543	12.659
^{90}Zr	10.0	4.862	7.652	5.083	13.278	10.747	7.934
^{90}Zr	11.0	11.176	6.750	6.992	10.187	8.806	9.594
^{90}Zr	24.0	13.507	8.891	3.993	5.449	12.122	5.324
^{208}Pb	7.0	14.075	14.038	12.729	22.295	18.327	12.113
^{208}Pb	9.0	4.894	9.475	5.158	10.074	17.617	3.831
^{208}Pb	11.0	3.965	8.393	3.857	7.241	8.079	5.676
^{208}Pb	14.6	8.484	1.716	1.634	4.559	3.937	4.732
^{208}Pb	16.9	20.114	10.215	9.078	5.329	6.678	5.359
^{208}Pb	20.0	47.73	12.734	9.078	7.150	7.082	6.117
^{208}Pb	22.0	62.200	12.390	8.183	13.664	12.153	9.713
^{208}Pb	26.0	58.686	11.598	9.765	7.677	11.220	10.222
^{208}Pb	30.3	160.319	5.498	3.017	24.611	6.213	3.938
^{208}Pb	40.0	216.962	12.233	5.509	59.407	10.405	3.990

Table D.4: χ^2/N values comparing the various PB and TPM parameterizations. Column one lists the target and column two gives the energy of the neutron elastic scattering reaction. Column three (six) lists the χ^2 values for the original PB (TPM) parameterization, only including angles up to 100°. Column four (seven) lists the χ^2 values for the PB (TPM) parameterization using the full angular distribution of each data set - column two (three) of Table D.3. Column five (eight) lists the χ^2 values for the PB (TPM) parameterization including only angles up to 100° - using fitting parameters from column four (five) of Table D.3.
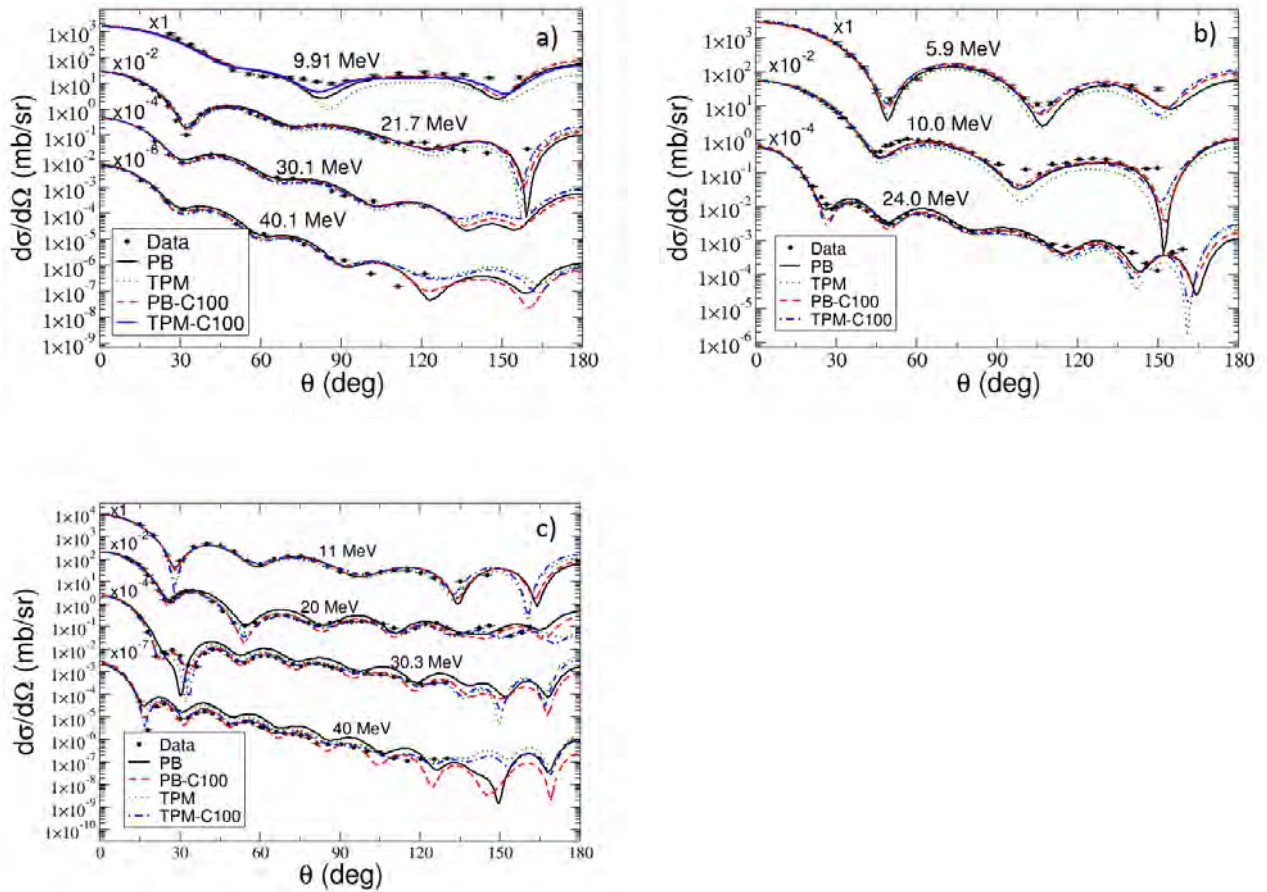
Figure D.2: Select cross section calculations comparing the original PB (black solid) and original TPM (green dotted) potentials to those calculated using the PB-C100 (red dashed) and TPM-C100 (blue dot dashed) parameterizations from Table D.3 for a) ^{40}Ca(n,n)^{40}Ca, b) ^{90}Zr(n,n)^{90}Zr, and c) ^{208}Pb(n,n)^{208}Pb (from [5]) elastic scattering at the listed energy. Cross sections are arbitrarily scaled for legibility.

	PB-G100a	PB-G100b
a	0.017 ± 0.0044	0.14 ± 0.0075
b	1.3 ± 0.59	0.066 ± 0.57
c	12.60 ± 0.097	9.3 ± 0.15
d	0.31 ± 0.0056	0.23 ± 0.065
e	-2.33 ± 0.068	$9.6 \times 10^{-5} \pm 5.4 \times 10^{-3}$

Table D.5: Fitted parameters resulting from the fit of all 24 data sets for the PB potentials using the same geometry between the two imaginary terms (column two) and further imposing $e \geq 0$ (column three), only fitting data with $\theta < 100°$.

the geometry to be the same as that of the imaginary surface term of PB (as is imposed by many local potentials). Fitting with this geometry instead, only including angles less than $100°$, we find the parameterization shown in column two of Table D.5. Comparing this to the fourth column of Table D.3, we now find a non-zero energy dependence in both imaginary terms as well as robust asymmetry dependences in both terms. However, e is significantly more negative in this new fit, giving a negative imaginary volume term for any energy less than 7.52 MeV (defined by $E < -e/d$). This is a larger cutoff than the previous parameterization ($-e/d = 3.04$ MeV).

We can instead impose $e \geq 0$ when performing the fit using this consistent PB geometry. The resulting parameters are shown in column three of Table D.5. Now, e is consistent with zero, indicating that this is not a true minimum but a result of the parameter hitting a boundary. However, this illustrates the differences that can arise when imposing various constraints on the fitting process. The energy dependence is still robust in both imaginary terms, but the asymmetry dependence now cannot be determined within its associated error. In each of the cases discussed above, there is a definite need for an energy-dependence, but the asymmetry dependence is not as well determined.
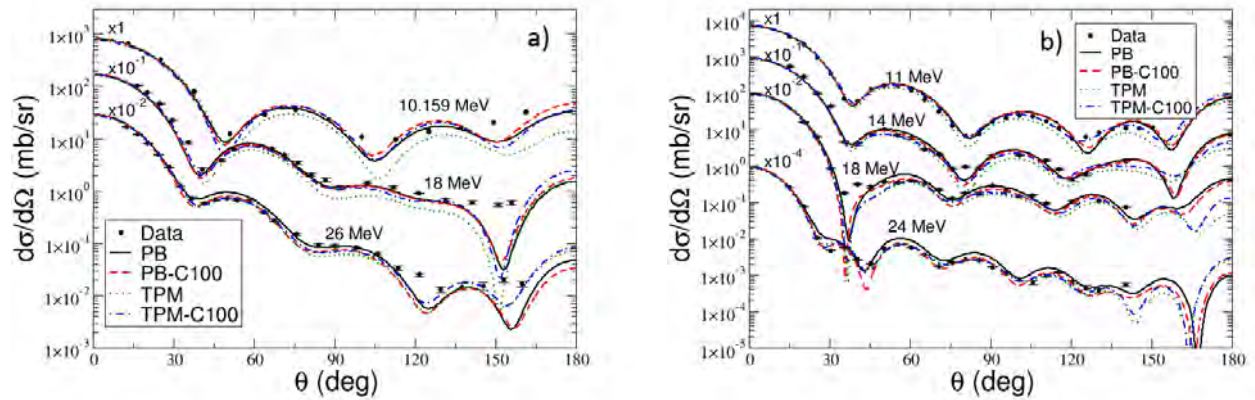
Figure D.3: Predicted angular distributions using PB-C100 (red dashed) and TPM-C100 (blue dot-dashed) for a) ^{27}Al(n,n)^{27}Al and b) ^{118}Sn(n,n)^{118}Sn elastic scattering compared to the original PB (black solid) and TPM (green dotted). Cross sections are scaled arbitrarily for legibility, and are calculated at the noted energies. Data from [6, 7, 8, 9]. Figures from [5].

Predictions

Using the PB-C100 and TPM-C100 fits from Table D.3, we can make predictions of the neutron scattering cross sections on various nuclei that were not included in the fit. For this, we used neutron scattering on ^{27}Al, ^{56}Fe, ^{60}Ni, and ^{118}Sn at several energies between 7 MeV and 26 MeV [6, 7, 8, 9, 173, 174, 175, 176]. The χ^2 values for the predicted cross sections are shown in Table D.6 compared to the values from the original parameterization (TPM, column three and PB, column five). In the case of ^{27}Al and ^{118}Sn, the χ^2 values are reduced when using the fitted parameterization. The visual comparison to the data also improves, as shown in Figure D.3.

However, for ^{56}Fe and ^{60}Ni, the description was worsened for nearly all energies regardless of whether the PB or TPM potential is used as a starting point. Most likely, this is because these two nuclei are not spherical nuclei, unlike the three nuclei used in the fit and ^{27}Al and ^{118}Sn. In general, we find that the fit we acquired is limited to the energy and mass range

190

System	Energy (MeV)	PB	PB-C100	TPM	TPM-C100
^{27}Al	10.159	9.086	9.043	23.278	14.551
^{27}Al	18.0	10.668	9.267	22.026	9.532
^{27}Al	26.0	10.251	7.027	8.190	4.794
^{56}Fe	7.96	32.380	75.533	11.190	4.794
^{56}Fe	11.0	11.362	18.588	20.896	73.294
^{56}Fe	20.0	21.369	14.701	4.069	32.689
^{56}Fe	26.0	24.677	16.465	8.906	29.540
^{60}Ni	7.904	35.881	89.927	12.612	120.228
^{60}Ni	9.958	49.979	81.225	9.508	87.922
^{60}Ni	11.952	21.124	27.778	17.674	44.157
^{60}Ni	13.941	13.923	23.801	12.745	43.495
^{60}Ni	24.0	19.163	7.531	4.570	10.581
^{118}Sn	11.0	9.058	8.365	7.753	16.799
^{118}Sn	14.0	6.680	5.811	16.041	15.051
^{118}Sn	18.0	12.121	11.355	16.871	8.151
^{118}Sn	24.0	20.935	5.526	9.243	8.533

Table D.6: χ^2 values for the systems that were predicted using the parameterizations from columns four and five of Table D.3. The first column lists the target, the second column lists the experimental energy at which the reaction had been performed. Column three (five) lists the χ^2 values calculated using the original PB (TPM) parameterization, and column four (six) lists the χ^2 values resulting from the fitted parameterization.

(specifically spherical nuclei) over which it was fit. A reasonable description is provided for interpolated masses but extrapolations are not trustworthy.

We also used the parameterization of Eq. (D.7) and (D.8) to fit this set of data for ^{27}Al, ^{56}Fe, ^{60}Ni, and ^{120}Sn to test the robustness of the values of Table D.3 (new fitted parameters given in Table D.7). The resulting fit was completely different from those given in Tables D.3 and D.5. Although the PB-O100 and TPM-O100 parameterizations are strikingly consistent with one another, the asymmetry term, in particular, is significantly larger than in the PB-C100 and TPM-C100 fits. This parameterization also did not provide as good a prediction for the previously fitted nuclei, ^{48}Ca, ^{90}Zr, and ^{208}Pb. This is once more indicative that the asymmetry dependence is not well-constrained, and that this theory is not correct to

	PB-O100	TPM-O100
a	0.411 ± 0.013	0.309 ± 0.011
b	-28.14 ± 2.42	-27.15 ± 2.94
c	5.64 ± 0.368	10.34 ± 0.25
d	-0.118 ± 0.013	-0.775 ± 0.065
e	7.96 ± 0.223	5.32 ± 0.12

Table D.7: Fitted parameters resulting from a fit to the data sets listed in Table D.6 (instead of to the data sets for ^{40}Ca, ^{90}Zr, and ^{208}Pb), only fitting data with $\theta < 100°$.

describe both spherical and non-spherical nuclei.

Summary

Using 24 sets of data in the energy range of $5 - 40$ MeV, we investigated the energy dependence of the imaginary depths of two non-local potentials that describe neutron elastic scattering from a target. Fitting the imaginary surface and volume depths of the PB and TPM potentials to three different targets at a variety of energies, we found that an energy-dependent interaction significantly improves the description of the elastic scattering cross sections for these targets in this energy range. Although the energy and asymmetry dependences were not robust among the different data sets that were fitted, in all cases, an energy dependence was necessary to improve the description of the angular distributions of the fitted and predicted systems. Even though non-locality is included explicitly in these calculations, this is not enough to completely remove the strong energy dependence that is found in local potentials.

This study calls for a new global non-local potential to be developed that includes an explicit energy dependence, is fit over a wider range of data than the PB and TPM potentials, and does not necessarily assume a Gaussian nonlocality. Informed decisions about the best span of data sets to consider when constructing and fitting this new non-local potential can

be approached using a principle component analysis. Recently, *ab initio* theories have been used in an attempt to derive a nucleon optical potential [65] which can guide assumptions about the shape and range of the non-locality in non-local potentials.

This same study can be performed using proton elastic scattering data across a variety of energies. In principle, one should be able to use the same form for the energy and asymmetry dependences as for neutrons; as in local interactions, the main differences between the proton and neutron interactions are in the depths of the potentials, due to the Coulomb interaction. However, preliminary studies [177] have shown that using the same form for the imaginary potential depths (and including a mass-dependent volume depth) does not provide the same level of improvement in the description of the data as the neutron study discussed in this Appendix. Further studies of a non-local global interaction for protons are underway.

Appendix E

Two-neutron Decay of ^{16}Be

Exotic nuclei, such as neutron and proton halo systems, are found across the nuclear chart, not only in the lightest mass nuclei but also in nuclei as heavy as neon [178]. These exotic systems are typically found near the neutron and proton driplines and can unsurprisingly lead to exotic decay modes, two-nucleon decay for example. Two-proton decay was first theorized in 1960 [179] but was not observed experimentally until almost 40 years later in ^{45}Fe [180, 181]. There are three possible mechanisms that allow two protons to decay from a parent nucleus, A. If there is a state in the $A-1$ nucleus that is below the ground state of A, the two protons can be emitted sequentially, stepping through the $A-1$ system. If there is no state in this region, the two protons can be emitted simultaneously, in a true three-body decay. However, if the two are correlated and the ground state of the $A-1$ system is energetically inaccessible to decay, the protons can be emitted in a diproton decay.

Although these decay mechanisms should also be present in neutron-rich systems, diproton decay was first observed in proton-rich systems, in two independent experiments at GANIL [180] and GSI [181]. Since then, several other nuclei have been observed to decay by diproton emission from the ground state [182, 183, 184], as well as from excited states [185]. These systems lend themselves naturally to three-body calculations because the degrees of freedom relevant in the decay are those related to the emission of the two protons from the parent nucleus. Varying the structural configuration of the parent nucleus causes differences

in the extracted values for the width, half-life, and energy shared between the three particles. Three-body models have been used in comparison with experimental data to gain insights into these exotic nuclei [186, 187]; the differentiation between a correlated decay and an uncorrelated three-body decay is based on model calculations such as these.

The diproton phenomenon is very hard to observe due to the Coulomb interaction which repels the two protons away from one another as soon as they exit the parent nucleus. This makes it difficult to observe the correlations between the two protons that were present in the parent nucleus. Nevertheless, diproton decay was observed before the equivalent process in neutron-rich material. Dineutron decay posses its own challenges. The neutron dripline generally extends farther from stability than the proton dripline, making it harder to reach. The statistics for neutron-rich decays in this region are also generally very low, as they rely on two-neutron coincidences.

In contrast to the large amount of literature on two-proton emitters, relatively few studies have been completed - theoretically or experimentally - for two-neutron emissions. Grigorenko performed one of the first theoretical studies of two-neutron emission [188], discussing the existence of one-, two-, and four-neutron emitters and compared their widths in a three-body frameworks. The first two-neutron decay from the ground state of a nucleus was observed in a 2012 experiment at the National Superconducting Cyclotron Laboratory through the decay of ^{16}Be to ^{14}Be plus two neutrons [72]. Since then, a few other cases have been observed [189, 190], mainly in the oxygen isotopes.

^{16}Be is an ideal case in which to investigate the possibility of dineutron decay. Before the observation of ^{16}Be, a lower limit of 1.54 MeV had been placed on the ground state of ^{15}Be [191]. In [72], the ground state of ^{16}Be was measured to be 1.35 MeV with a width of 0.8 MeV, which, depending on the width of this ground state of ^{15}Be, could make one-neutron

emission energetically inaccessible.

Comparisons of the ^{16}Be data in [72] to dineutron, sequential, and three-body decay models showed that the data was best described by the emission of a dineutron, this result caused some controversy due to the extreme models that were used to delineate between the dineutron and three-body decays [192, 193]. For the dineutron decay, the dineutron was modeled as a cluster and the decay as a two-body decay of ^{16}Be $\rightarrow^{14}$ Be $+ 2n$, in an s-wave relative motion. The three-body breakup was calculated only by the phase space factor. A full three-body calculation (modeling ^{14}Be $+ n + n$), as has been used to describe the continuum states of ^{26}O [194, 195], would be useful to help clarify this mode of decay.

Theoretical Framework

To model the relevant degrees of freedom within a three-body model, the form of ^{16}Be is taken to be core $+ n + n$, a formulation which should satisfy the three-body Schrödinger equation:

$$(T_r + T_s + V_{cn_1} + V_{cn_2} + V_{nn} + V_{3B})\Psi = E_{3B}\Psi, \tag{E.1}$$

where $\vec{r}$ and $\vec{s}$ are the standard Jacobi coordinates, as shown in Figure E.1. Here, r is the distance between two of the bodies, and s is the distance between the third body and the center of mass of the first two. (This formalism can be extended to higher dimension, as in [196].) For three bodies, three sets of Jacobi coordinates can be defined, X, Y, or T - (a), (b), and (c) in Figure E.1 respectively. With two identical neutrons, the X and Y coordinate systems are identical, and it is most convenient to work in the T-basis; this choice will be used throughout the rest of this appendix. V_{cn_i} and V_{nn} are the pairwise interactions between the core and one neutrons and between the two neutrons, respectively.

V_{3B} is the three-body interaction that accounts for the additional binding typically needed to reproduce the experimental binding energy caused by freezing the degrees of freedom in the core.
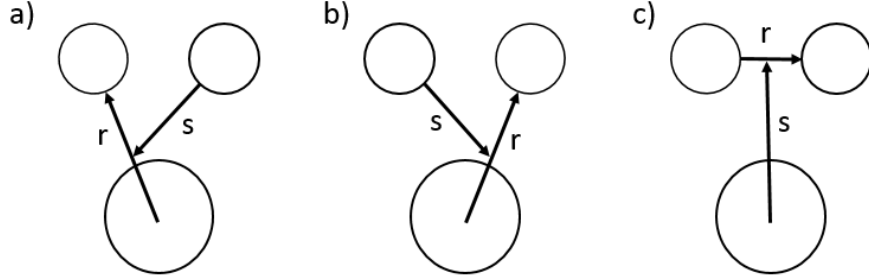
Figure E.1: Three sets of Jacobi coordinates, (a) Jacobi X system, (b) Jacobi Y system, and (c) Jacobi T system.

Equation (E.1) is a six-dimensional equation, where $\vec{r}$ and $\vec{s}$ do not separate as the pairwise interactions depend on both coordinates. Instead, a transformation can be made to hyperspherical coordinates where first, the scaled Jacobi coordinates, $\vec{x}$ and $\vec{y}$ are defined,

$$\vec{x} = \frac{\vec{r}}{\sqrt{2}},\tag{E.2}$$

and

$$\vec{y} = \sqrt{\frac{2A_3}{A_3 + 2}}\,\vec{s},\tag{E.3}$$

where A_3 is the mass number of the ^{14}Be core in the Jacobi T-basis. These are then used to define the hyperspherical coordinates

$$\rho^2 = x^2 + y^2,\tag{E.4}$$

and

$$\tan\theta = \frac{x}{y}, \tag{E.5}$$

where ρ is the hyperradius and θ is the hyperangle. Even though we are focusing on the T-basis, it is worthwhile to note that ρ is invariant among the three Jacobi bases while θ depends on the specific choice of basis.

A transformation of the kinetic energy operators T_r and T_s into hyperspherical coordinates gives

$$T = -\frac{\hbar^2}{2m}\left[\frac{1}{\rho^5}\frac{\partial}{\partial\rho}\left(\rho^5\frac{\partial}{\partial\rho}\right) + \frac{1}{\rho^2\sin^2 2\theta}\frac{\partial}{\partial\theta}\left(\sin^2 2\theta\frac{\partial}{\partial\theta}\right) - \frac{L_x^2}{\rho^2\sin^2\theta} - \frac{L_y^2}{\rho^2\cos^2\theta}\right], \tag{E.6}$$

where m is the unit mass ($m = 938.0$ MeV/c^2), and L_x and L_y are the angular momentum operators.

As discussed in Section 2.2, it is usual to perform a partial wave decomposition for the wave function, here giving

$$\Psi^{JM} = \sum_{l_x l_y l S j I} \psi_{l_x l_y}^{lSjIJ}(x,y)\left\{\left(\left[Y_{l_x}\otimes Y_{l_y}\right]_l\otimes\left[X_{\sigma_1}\otimes X_{\sigma_2}\right]_S\right)_j\otimes\phi_I\right\}_{JM}, \tag{E.7}$$

where l is the total orbital angular momentum, l_x is the relative orbital angular momentum of the $2n$ system, l_y is the relative orbital angular momentum of the core $+ 2n$ system, I is the spin of the core, S is the total spin of the two neutrons, j is the total angular momentum of the two neutrons relative to the core. Next, $\psi_{l_x l_y}^{lSjIJ}(x,y)$ is expressed using hyperspherical functions,

$$\psi_{l_x l_y}^{lSjIJ}(x,y) = \rho^{-5/2}\sum_{K=0}^{K_{\max}}\chi_{Kl_x l_y}^{lSIjJ}(\rho)\varphi_K^{l_x l_y}(\theta), \tag{E.8}$$

where $\varphi_K^{l_x l_y}(\theta)$ is defined to be an eigenfunction of the angular operator in Eq. (E.6), with the eigenvalue $K(K+4)$. This gives

$$\varphi_K^{l_x l_y}(\theta) = N_K^{l_x l_y}(\sin\theta)^{l_x}(\cos\theta)^{l_y}P_n^{l_x+1/2,l_y+1/2}(\cos 2\theta), \tag{E.9}$$

where $P_n^{l_x+1/2,l_y+1/2}(\cos 2\theta)$ are the Jacobi Polynomials, n is constrained through the relation $K = 2n + l_x + l_y$, and $N_K^{l_x l_y}$ is a normalization factor defined by

$$\int_0^{\pi/2} \varphi_K^{l_x l_y}(\theta)\varphi_{K'}^{l_x l_y}(\theta)\sin^2\theta\cos^2\theta d\theta = \delta_{KK'}. \tag{E.10}$$

For compactness, we introduce the hyperspherical harmonic functions,

$$\mathcal{Y}_\gamma^{JM}(\Omega_5,\sigma_1,\sigma_2,\boldsymbol{\xi}) = \varphi_K^{l_x l_y}(\theta)\left\{\left(\left[Y_{l_x}\otimes Y_{l_y}\right]_l \otimes \left[X_{\sigma_1}\otimes X_{\sigma_2}\right]_S\right)_j \otimes \phi_I\right\}_{JM}, \tag{E.11}$$

with γ containing the set $\{KlSIjl_x l_y\}$. Then, the total wave function can be written in the form

$$\Psi^{JM} = \rho^{-5/2}\sum_\gamma \chi_\gamma^J(\rho)\mathcal{Y}_\gamma^{JM}(\Omega_5,\sigma_1,\sigma_2,\boldsymbol{\xi}). \tag{E.12}$$

To solve for the hyperradial part of the wave function, Eq. (E.12) is substituted into Eq. (E.1), resulting in a set of coupled hyper-radial equations:

$$\left(-\frac{\hbar^2}{2m}\left[\frac{d^2}{d\rho^2} - \frac{(K+3/2)(K+5/2)}{\rho^2}\right] - E_{3B}\right) + \sum_{\gamma'}V_{\gamma\gamma'}(\rho)\chi_{\gamma'}^J(\rho) = 0, \tag{E.13}$$

where the coupling potentials are defined as

$$V_{\gamma\gamma'}(\rho) = \langle \mathcal{Y}_{\gamma'}^{JM}(\Omega_5, \sigma_1, \sigma_2, \boldsymbol{\xi})| \sum_{j>i=1}^{3} V_{ij}|\mathcal{Y}_{\gamma}^{JM}(\Omega_5, \sigma_1, \sigma_2, \boldsymbol{\xi})\rangle. \tag{E.14}$$

When the system is unbound, the hyperradial wave functions of Eq. (E.13), χ_γ^J, are regular at the origin and behave asymptotically as

$$\chi_{\gamma\gamma_i}^J \to \frac{i}{2}\left[\delta_{\gamma\gamma_i}H_{K+3/2}^-(\kappa\rho) - \mathbf{S}_{\gamma\gamma_i}^J H_{K+3/2}^+(\kappa\rho)\right], \tag{E.15}$$

as $\rho \to \infty$, where γ_i are plane wave components of the incoming channel. The final wave function is summed over γ_i since a specific incoming wave is not assumed for the ^{16}Be system. For this calculation, we also focus on the state $(J, M) = (0, 0)$, which corresponds to the ground state of ^{16}Be.

The hyperradial equation, Eq. (E.13), could in principle be solved using direct numerical integration for each set of quantum numbers, γ. However, at low scattering energies, the centrifugal barrier, $(K + 3/2)(K + 5/2)$, which is found in every channel including $K = 0$, would likely cause this method to develop numerical inaccuracies. Instead, we use the hyperspherical R-matrix method [83] (Chapter 6).

In this method, a basis w_γ^n is first created by solving the uncoupled equations from Eq. (E.13) in a box of size $\rho_{\max}$, setting all of the coupling potentials to zero except for the diagonal:

$$\left[T_\gamma(\rho) + V_{\gamma\gamma}(\rho) - \epsilon_{n\gamma}\right] w_\gamma^n(\rho) = 0. \tag{E.16}$$

At $\rho = \rho_{\max}$, the logarithmic derivatives,

$$\beta = \frac{d\ln(w_\gamma^n(\rho))}{d\rho} \tag{E.17}$$

are required to be equal, which causes the set of functions, w_γ^n, to form a complete, orthogonal basis with the box, $\rho < \rho_{\max}$. The scattering equation inside of the box can be solved by expanding in this R-matrix basis:

$$g_\gamma^p(\rho) = \sum_{n=1}^N c_\gamma^{pn} w_\gamma^n(\rho). \tag{E.18}$$

These functions, $g_\gamma^p(\rho)$, solve the corresponding coupled-channel equations,

$$\left[T_\gamma(\rho) + V_{\gamma\gamma}(\rho)\right] g_\gamma^p(\rho) + \sum_{\gamma' \neq \gamma} V_{\gamma\gamma'}(\rho) g_{\gamma'}^p(\rho) = e_p g_\gamma^p(\rho). \tag{E.19}$$

In order to find the coefficients c_γ^{np}, Eq. (E.18) is inserted into Eq. (E.19), multiplied by $w_{\gamma'}^{n'}$, and integrated over the size of the box. The resulting matrix equation

$$\varepsilon_{n\gamma} c_\gamma^{np} + \sum_{\gamma' \neq \gamma} \sum_{n'} \langle w_\gamma^n(\rho) | V_{\gamma\gamma'}(\rho) | w_{\gamma'}^{n'}(\rho) \rangle = e_p c_\gamma^{pn}, \tag{E.20}$$

provides the coefficients c_γ^{np}. The functions $g_\gamma^p(\rho)$ are only complete inside of the box and do not have the correct normalization or asymptotic behavior of the full scattering wave function. The full three-body wave function is then given by a superposition of these solutions

and matched to the correct asymptotic form of the wave function

$$\chi^{J}_{\gamma\gamma_i}(\rho) = \sum_{p=1}^{P} A^{p}_{\gamma_i} g^{p}_{\gamma}(\rho),$$ (E.21)

where the expansion parameter p tracks the number of poles considered in the R-matrix expansion. The asymptotic behavior of Eq. (E.15) is connected to the wave function inside of the box through the normalization coefficients, $A^{p}_{\gamma_i}$, which have the explicit form

$$A^{p}_{\gamma_i} = \frac{\hbar^2}{2m} \frac{1}{e_p - E} \sum_{\gamma'} g^{p}_{\gamma'}(\rho_{\max}) \left[\delta_{\gamma\gamma'} \left(H^{-'}_{K+3/2}(\kappa_{\gamma'}\rho_{\max}) - \beta H^{-}_{K+3/2}(\kappa_{\gamma'}\rho_{\max}) \right) \right.$$

$$\left. - \mathbf{S}_{\gamma'\gamma_i} \left(H^{+'}_{K+3/2}(\kappa_{\gamma'}\rho_{\max}) - \beta H^{+}_{K+3/2}(\kappa_{\gamma'}\rho_{\max}) \right) \right].$$

The S-matrix,

$$\mathbf{S} = \left[\mathbf{H}^{+} - \rho_{\max}\mathbf{R}(\mathbf{H}^{+'} - \beta\mathbf{H}^{+}) \right]^{-1} \left[\mathbf{H}^{-} - \rho_{\max}\mathbf{R}(\mathbf{H}^{-'} - \beta\mathbf{H}^{-}) \right],$$ (E.22)

can be directly computed from the R-matrix, which is determined by the values of $g^{p}_{\gamma}(\rho)$ at the edge of the box,

$$R_{\gamma\gamma'} = \frac{\hbar^2}{2m\rho_{\max}} \sum_{p=1}^{P} \frac{g^{p}_{\gamma}(\rho_{\max})g^{p}_{\gamma'}(\rho_{\max})}{e_p - E_{3B}}.$$ (E.23)

Each pole has a width, defined as

$$\Gamma = \frac{2\gamma^2 P(E)}{1 + \gamma^2 S'(E)},$$ (E.24)

where S and P are the shift function and penetrability at the pole energy $(E = e_p)$ with

$$S(E) = k\rho_{\max}\frac{\dot{F}F + \dot{G}G}{F^2 + G^2},$$ (E.25)

202

and

$$P(E) = \frac{k\rho_{\max}}{F^2 + G^2}. \tag{E.26}$$

Here, F and G are the regular and irregular Coulomb functions.

The phase shifts for each channel can be extracted from the diagonal elements of the S-matrix,

$$S_{\gamma\gamma} = e^{2i\delta_{\gamma\gamma}}. \tag{E.27}$$

However, the S-matrix does not have to be diagonal (it generally has strong off-diagonal components), and due to all of these off-diagonal terms, the diagonal does not have any special significance. Therefore, instead of using $S_{\gamma\gamma}$ directly to find the phase shifts, it is common to diagonalize the S-matrix and extract the eigenphases, δ^e [197]. The resonance energies and widths can then be extracted from the eigenphases.

If a Breit-Wigner shape is assumed for the resonances, resonant properties for a single-channel calculation can be directly extracted from a phase shift (or eigenphase) using

$$\tan\delta = \frac{\Gamma/2}{E_{3B} - E_{\text{res}}}, \tag{E.28}$$

where Γ is the width of the resonance and E_{res} is the resonance energy. In situations where this is valid, the width of the state at E_{res} can be computed as the full width at half maximum (FWHM) of the energy derivative of the phase shift

$$\Gamma = \frac{2}{\partial\delta/\partial E_{3B}}. \tag{E.29}$$

If there are multiple channels with weak couplings, the partial widths of the multiple channels

extracted this way can simply be added together to obtain the total width of the three-body resonance. For a strongly coupled problem, as is expected here, the pure Breit-Wigner approach is not expected to be valid, but we can still identify channels where this approach could be applied. Comparisons between the addition of the partial widths and the extraction of a width from the eigenphases can give some indication of how strongly coupled the system is.

The total three-body elastic cross section can also be defined [197],

$$\sigma_{3:3}^{J}(E_{3B}) \propto \frac{1}{4\kappa^5} \left[\sum_{\gamma} \left|1 - S_{\gamma\gamma}(E_{3B})\right|^2 + \sum_{\gamma\gamma'} \left|S_{\gamma\gamma'}(E_{3B})\right|^2 \right]. \tag{E.30}$$

Because this quantity automatically couples all of the channels within the model space, it should provide a consistent way to extract a resonance energy (seen as a peak in the cross section), verifying that the resonance energy extracted from the eigenphase is indeed associated with the resonance of the full three-body system.

Numerical Details

In three-body models, each two-body interaction is typically constrained by experimental data. However, since only one state in ^{15}Be is known [198], shell model calculations are used to supplement the available data. Shell model calculations for ^{15}Be were provided [10] using the WBP interaction [199]. The resulting levels are shown in Figure E.2, first column, compared with the measured experimental level, third column. Because the $1d_{5/2}$ level in the shell model calculation is 1.0 MeV higher than the experimental state, the levels used to constrain the ^{14}Be $- n$ states were the shell model levels lowered by 1.0 MeV, Figure E.2

middle column.
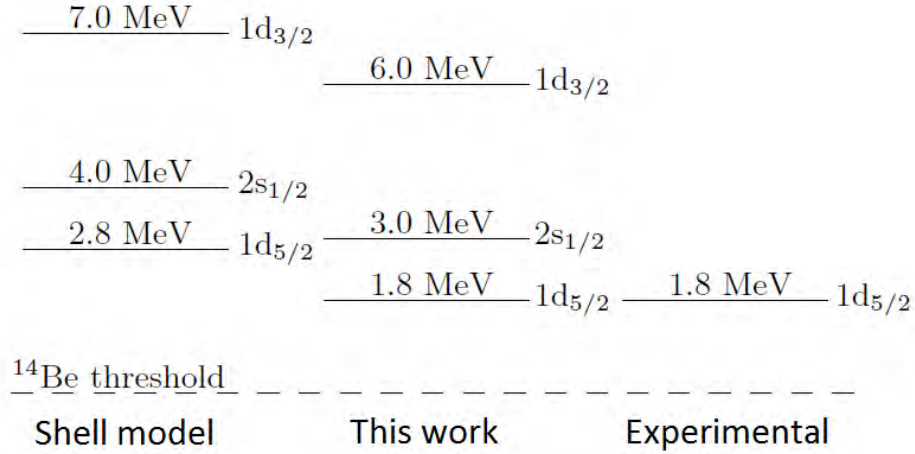
Figure E.2: Level scheme for ^{15}Be. First column: shell model provided by [10], second column: ^{15}Be levels used in this work (shell model levels lowered by 1.0 MeV so the $1d_{5/2}$ state reproduces the experimentally measured $l = 2$ state, shown in column three). Figure from [3].

The ^{14}Be-n interaction for each partial wave had a Woods-Saxon shape with $a = 0.65$ fm and $R = 1.2A^{1/3}$ fm, where A is the mass number of the ^{14}Be core. The depths of each potential are angular momentum dependent and are obtained by fitting the single particle resonances in ^{15}Be, Figure E.2, middle column. These depths were fitted using the code POLER [200] where a spin-orbit interaction could be included to reproduce the splitting between the $1d_{5/2}$ and $1d_{3/2}$ levels.

Core degrees of freedom are taken into account with the l-dependent potentials. A spin-orbit interaction was also included with the same geometry as the central nuclear force, where the depth was adjusted to reproduce the splitting of the $1d_{5/2}$ and $1d_{3/2}$ states. The definition of the spin-orbit strengths are the same as those of FaCE [201].

In this model for ^{14}Be, the lowest s- and p-orbitals are assumed to be full. To remove the effect of these occupied states in the ^{14}Be core, the $1s_{1/2}$, $1p_{3/2}$, and $1p_{1/2}$ states were projected out through a phase-equivalent supersymmetric transformation [201].

Parameter	D3B	D	DNN	S
V_s	–26.182	–26.182	–26.182	–41.182
V_p	–30.500	–30.500	–30.500	30.500
V_d	–42.730	–42.730	–42.730	–42.730
V_{so} (l$\neq$2)	–10.000	–10.000	–10.00	–10.000
V_{so} (l=2)	–33.770	–33.770	–33.770	–33.770
V_{3B}	–7.190	0.000	–7.190	0.000
α_{NN}	1.000	1.000	0.000	1.000

Table E.1: Interaction parameters for the various models considered. All depths are given in MeV. Table from [3].

Ultimately, four three-body models for ^{16}Be were considered. In **D3B**, the ground state of ^{15}Be is a $1d_{5/2}$ state and a three-body force is included to reproduce the experimental three-body ground state energy of ^{16}Be. A Woods-Saxon form is also taken for the three-body interaction, with a radius of 3.02 fm, and a diffuseness of 0.65 fm. In **D**, the ground state of ^{15}Be is still a $1d_{5/2}$ but there is no three-body force included. In **S**, the ground state of ^{15}Be is taken to be a $2s_{1/2}$ but no three-body force is included. The depths of the interactions producing these configurations are summarized in Table E.1.

All three of these models include the Gogny, Pires, and Tourreil (GPT) NN interaction [202], which has been used in previous three-body studies, as in [203, 204, 205, 206]. The GPT interaction reproduces NN observables up to 300 MeV, which is a suitable range for this calculation - even though the interaction itself is simpler than the AV18 [207] or Reid soft-core [208] interactions. We finally consider another model where the NN interaction is removed completely, model **DNN**. Table E.1 also includes the scaling α_{NN} which is the multiplicative factor for the GPT interaction in each calculation.

The energies for the $1d_{5/2}$ and $2s_{1/2}$ states in ^{15}Be for each model are given in Table E.2. Except for the s-wave states close to threshold, approximate values are given for the $2s_{1/2}$ state. Resonances in s-wave states are more difficult to calculate than $\ell \neq 0$ channels, since

there is no potential barrier to trap the particle. Instead of being able to define resonances as energies where the phase shift goes through $90°$ or a pole in $S(E)$, the pole is found on the imaginary k-axis at $k_p = i/a_0$, where a_0 is the scattering length. The position of the resonance can then be found by defining the phase shift as $\delta(k) = -\arctan(a_0 k)$, instead of using the Breit Wigner form in Eq. (E.28). As resonances go up in energy, they become broad, making them difficult to define exactly. However, each of the $2s_{1/2}$ states in the ^{15}Be models are near 3 MeV (except for **S**, which has the $2s_{1/2}$ state as its ground state). For each of these models, the $1d_{3/2}$ state was placed at 6.0 MeV.

	D3B	**D**	**DNN**	**S**
$^{15}Be(1d_{5/2})$	1.80	1.80	1.80	1.80
$^{15}Be(2s_{1/2})$	$\sim$3	$\sim$3	$\sim$3	0.48
$^{16}Be(g.s.)$	1.32	1.88	3.08	1.60*

Table E.2: Energy levels, in MeV, for ^{16}Be and ^{15}Be for the various models considered. Energies are measured with respect to the ^{14}Be threshold. Table from [3]. *This is an excited state.

Because these methods rely heavily on basis expansions to compute the wave function, the model space is determined by a number of numerical parameters - all of which must be tested for convergence. The subplots in Figure E.3 shows the convergence of several of these expansions parameters, including K, N_{Jac} (number of points in the hyperangular integrals of Eq. (E.14)), and the combination of ρ_{max} and N. In (a), the phase shift as a function of three-body energy is shown for increasing values of K_{max} where all other parameters are held constant. Convergence is reached for the shape of the phase shift around $K_{\text{max}} = 28$. The convergence of the phase shift with regards to number of Jacobi polynomials, N_{Jac} is shown in panel (b). The resonance energy and width of the resonance remain essentially consistent throughout the range of N_{Jac} shown here, but the low-energy behavior of the phase shift converges around $N_{\text{Jac}} = 65$. Panel (c) shows the convergence of the resonance energy as
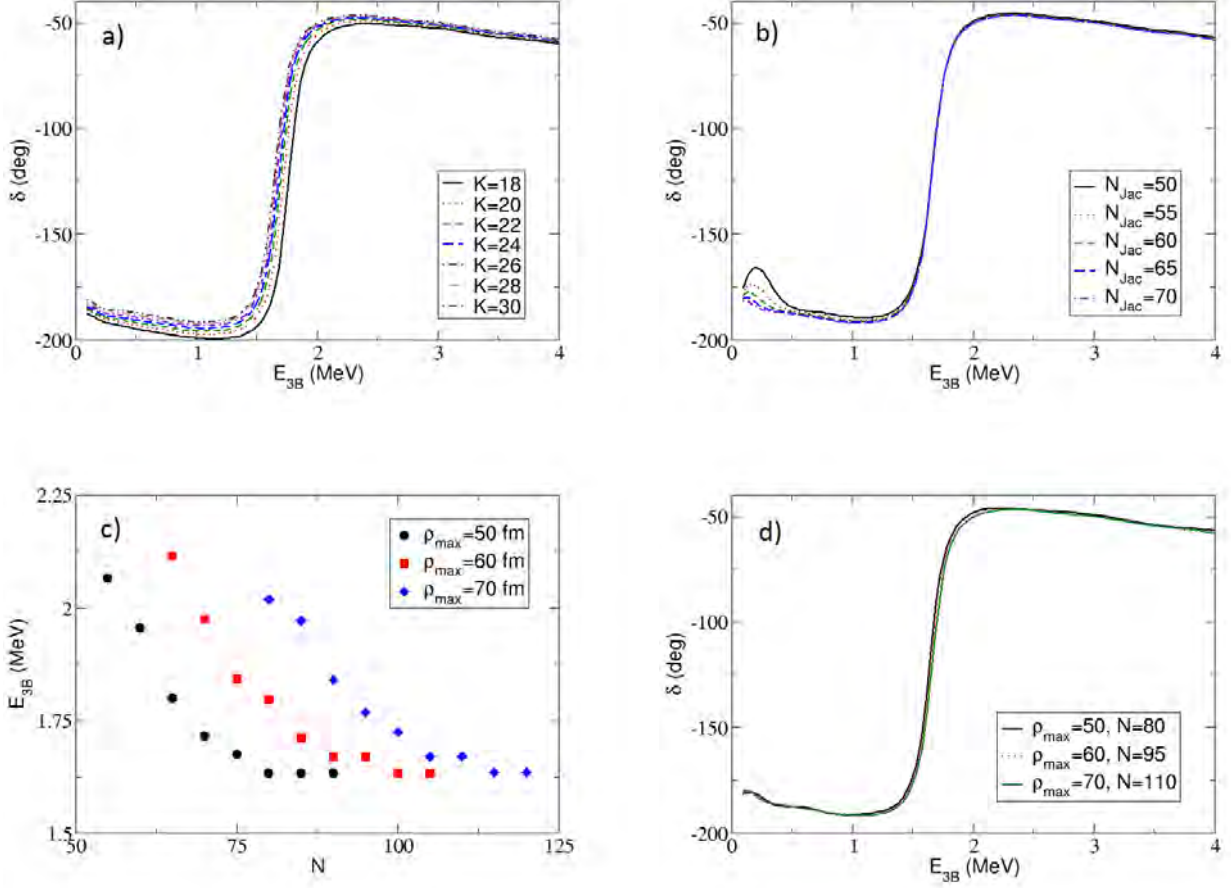
Figure E.3: Convergence of the various expansion parameters in the wave function, (a) convergence of K_{max}, (b) convergence of N_{Jac}, (c) convergence of the combination of $\rho_{\max}$ and N (both parameters must increase simultaneously to maintain a converged phase shift), and (d) convergence of N for several values of $\rho_{\max}$.

the number of R-matrix basis states, N, is increased for three values of $\rho_{\max}$. Clearly, as $\rho_{\max}$ is increased, the number of R-matrix basis states needed to reach convergence also increase. This is shown in (d), where the shape of the three-body phase shift is unchanged after $\rho_{\max} = 60$ fm, as long as N is large enough. The complete minimum requirements for convergence are given in Table E.3.

Parameter	Value
K_{max}	28
$l_x(\mathrm{max})$, $l_y(\mathrm{max})$	10
N_{Jac}	65
ρ_{max} (fm)	60
N	95

Table E.3: Minimum convergence values for the three-body wave function expansion. Table from [3].

Results and Discussion

Although convergence was studied using the phase shifts, the results that follow examine the eigenphases for each of the models described above. We first examine the eigenphases for model **D**, shown in Figure E.4 (a) (solid black). A clear resonance can be seen at 1.88 MeV, and as is expected for this type of three-body system, this is underbound with respect to the experimental resonance. Adding a three-body interaction, as in Table E.1 for model **D3B**, serves to further bind the ^{16}Be system, lowering the resonance energy extracted from the eigenphase in order to reproduce the experimental resonance energy. This is seen in panel (a) of Figure E.4 (dashed red). The shape of the resonance of **D3B** is nearly identical to that of **D**, although including the three-body interaction narrows the resonance somewhat. The width extracted from the FWHM of the derivative of the eigenphase is 0.17 MeV. This is consistent with the width of the R-matrix pole closest to the resonance energy, $\Gamma = 0.17$ MeV, as in Eq. (E.24).

We can also extract a width from the three-body cross section, shown in Figure E.4 (b). Ideally, one would like to remove any of the background contribution from the elastic cross section to be able to isolate the peak to extract the resonance. However, there is no clean way to do this. At first thought, one might attempt to calculate the cross section from Eq. (E.30) for the plane wave and then use that as a background measure, the plane wave
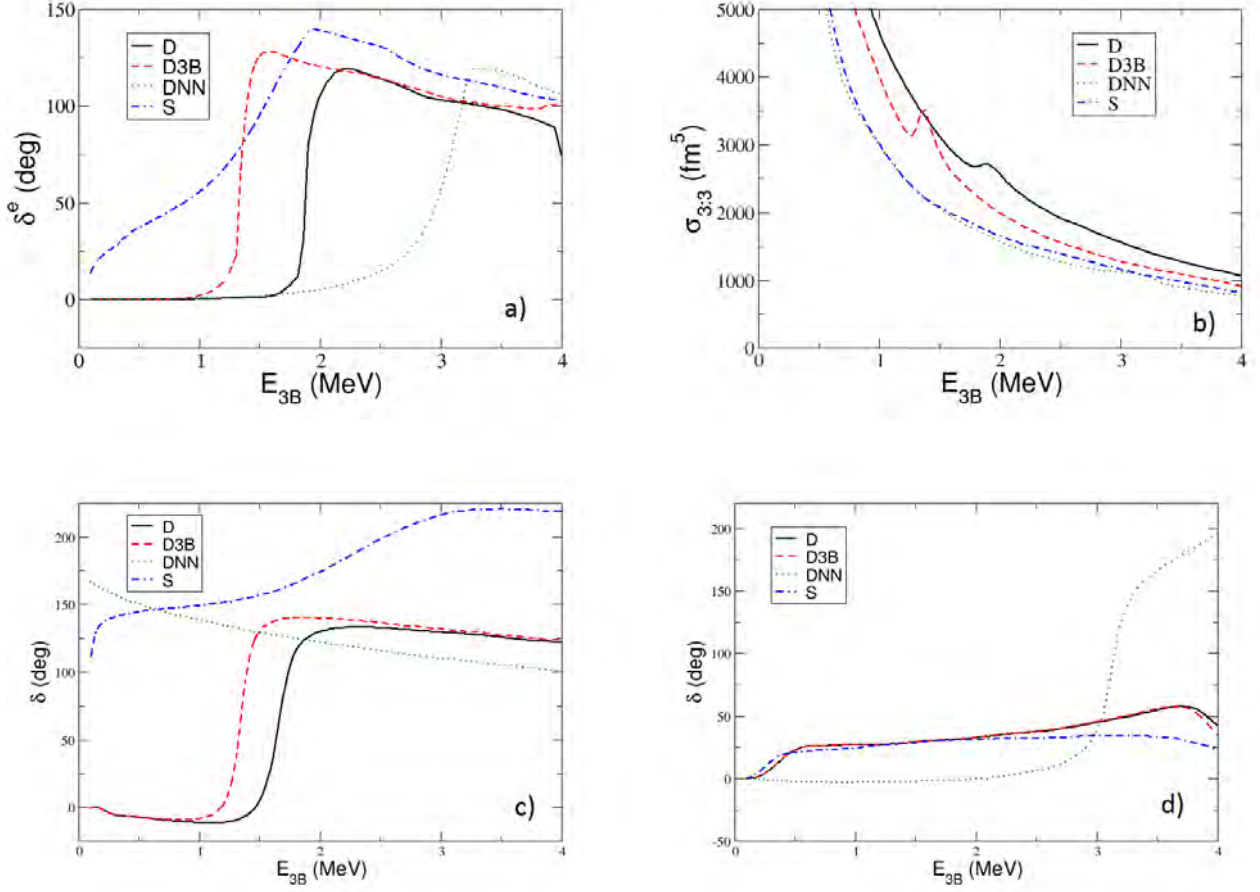
Figure E.4: As a function of three-body energy, (a) eigenphase shifts, (b) three-body cross section, and three-body phase shifts for the (c) $K = 0$ channel, (d) $K = 4$, $l_x = 0$, $l_y = 0$ channel for **D** (solid black), **D3B** (dashed red), **DNN** (dotted green), and **S** (double-dash dotted blue). Panels (a) and (b) from [3].

cross section does not follow a smooth, nearly exponential decay. Instead, we rely on finding the approximate width of the peak in the cross section. This gives a width of 0.16 MeV, consistent with the widths extracted from the eigenphase and the R-matrix pole.

Finally, it is worthwhile to note that out of all phase shifts (before diagonalization to the eigenphase shifts), one channel, the $K = 0$, $l_x = 0$, $l_y = 0$ channel, contained a nearly identical resonance to that extracted from the eigenphase. This is shown in Figure E.4 (c). The width extracted from the FWHM of this channel is 0.16 MeV, consistent with the other

extracted widths. However, each of these theoretical widths is nearly an order of magnitude lower than the experimental width of [72]. This is most likely due to experimental resolution and other effects that were not taken into account when extracting the width in this work.

In this project, we can also calculate the three-body spatial probability density of the two neutrons relative to the ^{14}Be core. This is done, using the wave function from Eq. (E.12) calculated at the resonance energy, through the following calculation,

$$P(x, y) = \int \left| \Psi^{JM}(\mathbf{x}, \mathbf{y}) \right|^2 d\Omega_x d\Omega_y.$$

(E.31)

This quantity contains information on all channels included in the wave function, not just the channel that contributes most strongly to the resonance. The regions of highest density show whether the internal configuration is mostly dineutron, helicopter, or three-body, as in Figure E.5 (a), (b), and (c) respectively.
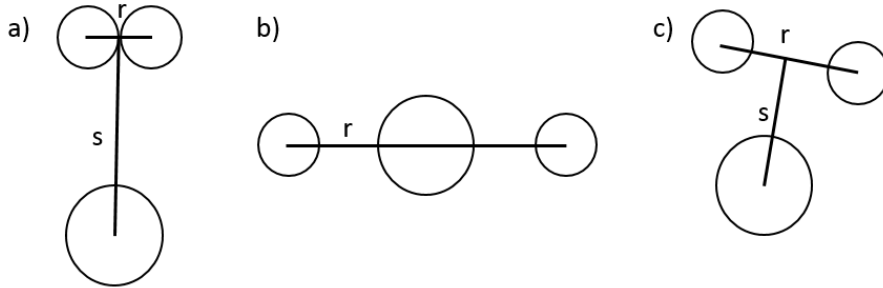
Figure E.5: Examples of three-body configurations, (a) dinucleon, (b) helicopter, and (c) three-body.

The density distribution for model **D3B** calculated at the extracted resonance energy of 1.32 MeV (Figure E.6 (a)), shows mainly a dineutron configuration, although a small helicopter component is also present. This is consistent with what was seen experimentally in [72]. Changing the three-body interaction does not change this picture. Even when the

211

three-body interaction is completely removed, the strength of the dineutron contribution relative to the helicopter contribution does not change.
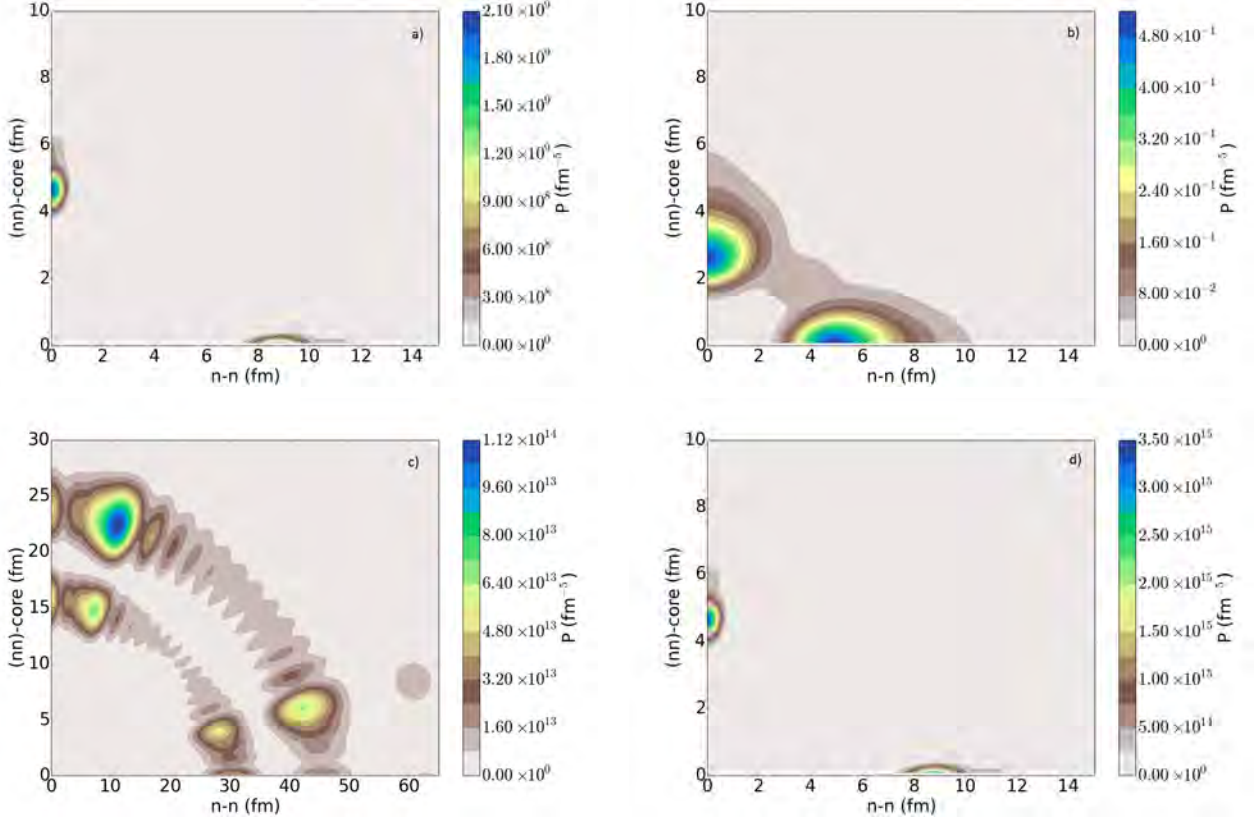
Figure E.6: Three-body density distributions for ^{16}Be as a function of the distance between the two neutrons (n-n) and the distance between the nn pair and the core for (a) **D3B**, (b) **DNN**, (c) no two- or three-body interactions (planewave), and (d) the model proposed by Kuchera, et. al. [11]. Panels (a), (b), and (c) from [3].

We can then investigate how robust the dineutron conclusion is under changes to the internal ^{15}Be structure or to weakening on the nn interaction. First, we can remove the nn interaction completely from model **3BD**, as in model **DNN**. The eigenphase, Figure E.4 (a) (green dotted), still shows a resonance, although pushed out to 3 MeV, compared to the 1.32 MeV resonance when the nn interaction was included. A small signature of this resonance is also seen in the three-body elastic-scattering cross section, Figure E.4 (b) (green dotted). Looking at the three-body density distribution in Figure E.6 (b), there are equal

contributions from the dineutron and helicopter configurations. This picture remains the same regardless of the magnitude of the three-body interaction that is included. Therefore, it is likely that the nn interaction is the cause of the strong dineutron seen. For comparison, panel (c) shows the density distribution when no two- or three-body interactions are included.

Next, we can explore how the internal configuration of ^{15}Be changes the previous results. Although the lowest experimentally measured state in ^{15}Be was measured to be a d-wave, low-lying, hard to measure, s-wave ground states have historically been important in nuclei such as ^{10}Li. A low-lying s-wave exists in ^{10}Li but was only experimentally observed after higher-lying resonances were discovered [209]. This is the motivation behind model **S** described in Table E.1. Using the same model space as in Table E.3, the $1d_{5/2}$ was kept at 1.8 MeV while the $2s_{1/2}$ was lowered to 0.48 MeV. The geometry of the potentials was kept the same, only the depth of the s-wave potential was changed to produce this lowered state. Even though the eigenphase in Figure E.4 panel (a) (blue double-dashed dotted) appears to have a signature of a resonance, the three-body elastic-scattering cross section in panel (b) of Figure E.4 (blue double-dashed dotted) does not show any signature of a resonance in the same region - not even a small one as for model **DNN**. The three-body ground state in this model is actually a bound state, meaning that a low-lying s-wave in ^{15}Be will not reproduce the experimentally observed ^{16}Be, and it is not needed in this model. (This case is not shown in Figure E.6.)

Finally, we consider the configuration suggested by Kuchera et. al. [11] where it was suggested, using two-neutron coincidences, that there could be a slight chance of finding the $1d_{3/2}$ state in ^{15}Be at 2.69 MeV, instead of the 6.0 MeV predicted by the shifted shell model calculation. With this state, keeping the $1d_{5/2}$ at 1.8 MeV, and using the s-wave interaction of models **D3B** and **D**, we found the ground state energy of ^{16}Be to be $E_{3B} = 1.05$ MeV,

without including a three-body interaction. In order for this configuration to reproduce the experimental ^{16}Be, any three-body interaction that would be included would have to be repulsive, which is atypical. Still the density distribution for this configuration, without a three-body interaction, (Figure E.6, panel (d)) is nearly identical to that of model **D** (Figure E.6 panel (a)). This change in configuration is not required to reproduce the experimentally observed ground state of ^{16}Be, and it is more likely that the $1d_{3/2}$ is above 2.69 MeV as an atypical, repulsive three-body interaction would be needed to reproduce the experimentally observed results.

Conclusion

In this work, a three-body model for ^{16}Be was developed to investigate the properties of this continuum system. Hyperspherical harmonics and the hyperspherical R-matrix were used to solve the three-body scattering problem. ^{14}Be-n interactions were constrained by experimental data for ^{15}Be and supplemented with shell model calculations. A three-body potential was included to reproduce the experimental ground state energy of ^{16}Be, as is typical for three-body models. As these systems rely on basis expansions for the wave functions, we obtained convergence for phase shifts, density distributions, and three-body elastic cross sections.

A strong dineutron component was found around the resonance energy of ^{16}Be, which is consistent with experimental observations, although the width extracted from our calculations is smaller than the experimental value (despite being consistent among several methods to extract it) [72]. The nn interaction is critical to produce the strong dineutron configuration in the ground state of ^{16}Be, and the structure of the resonance is completely different

when this component is switched off. The three-body interaction, however, plays almost no role in giving rise to the dineutron component. Several other configurations for ^{15}Be were explored, including a low-lying $2s_{1/2}$ (below the experimentally observed $1d_{5/2}$) and a slightly lower $1d_{3/2}$. However, neither of these configurations, regardless of the three-body interaction, produced the experimentally observed ground state of ^{16}Be at 1.35 MeV.

That data in [72] was presented in terms of several correlation observables, and it would be interesting to make predictions for these based on our three-body model. This involves introducing the predictions described here into a full experimental simulation code that includes the appropriate three-body assumptions as well as all of the information about the detector set-ups and efficiencies. Investigations along these lines have started.

BIBLIOGRAPHY

BIBLIOGRAPHY

[1] F. D. Becchetti and G. W. Greenlees. Nucleon-nucleus optical-model parameters, A > 40, E < 50 mev. *Phys. Rev.*, 182:1190–1209, Jun 1969.

[2] Pierre-Loïc Bacq. Analysis of the energy and mass dependence of nonlocal optical potentials used for the study of elastic scattering of neutrons. Master's thesis, Université libre de Bruxelles (ULB), 2016.

[3] A. E. Lovell, F. M. Nunes, and I. J. Thompson. Three-body model for the two-neutron emission of ^{16}Be. *Phys. Rev. C*, 95:034605, Mar 2017.

[4] A. E. Lovell, F. M. Nunes, J. Sarich, and S. M. Wild. Uncertainty quantification for optical model parameters. *Phys. Rev. C*, 95:024611, Feb 2017.

[5] A. E. Lovell, P.-L. Bacq, P. Capel, F. M. Nunes, and L. J. Titus. Energy dependence of nonlocal optical potentials. *Phys. Rev. C*, 96:051601, Nov 2017.

[6] G. Boerker, R. Boettger, H.J. Brede, H. Klein, W. Mannhart, and R.L. Siebert. Elastic and inelastic differential neutron scattering cross sections of oxygen between 6 and 15 mev. In S. Igarasi, editor, *Conference on Nuclera Data for Science and Technology*, page 193, Mito, Japan, May 30 - June 3 1988. Japan Atomic Energy Research Institute.

[7] J. S. Petler, M. S. Islam, R. W. Finlay, and F. S. Dietrich. Microscopic optical model analysis of nucleon scattering from light nuclei. *Phys. Rev. C*, 32:673–684, Sep 1985.

[8] J. Rapaport, Mohammed Mirzaa, H. Hadizadeh, D.E. Bainum, and R.W. Finlay. Neutron elastic scattering from ^{116,118,120,122,124}sn. *Nucl. Phys.*, A341(1):56 − 74, 1980.

[9] Satoshi Chiba, Yoshimaro Yamanouti, Masayoshi Sugimoto, Motoharu Mizumoto, Yutaka Furuta, Mikio Hyakutake, and Shin Iwasaki. Fast neutron scattering cross sections of sn-118 at 14.9 and 18.0 mev. *J. Nucl. Sci. Technol.*, 25(6):511–519, 1988.

[10] B.A. Brown. private communication. *private communication*, 2013.

[11] A. N. Kuchera, A. Spyrou, J. K. Smith, T. Baumann, G. Christian, P. A. DeYoung, J. E. Finck, N. Frank, M. D. Jones, Z. Kohley, S. Mosby, W. A. Peters, and M. Thoennessen. Search for unbound ^{15}Be states in the $3n +^{12}$ Be channel. *Phys. Rev. C*, 91:017304, Jan 2015.

[12] *Reaching for the Horizon Nuclear Physics Long Range Plan*, 2015.

[13] K. L. Jones, F. M. Nunes, A. S. Adekola, D. W. Bardayan, J. C. Blackmon, K. Y. Chae, K. A. Chipps, J. A. Cizewski, L. Erikson, C. Harlin, R. Hatarik, R. Kapler, R. L. Kozub, J. F. Liang, R. Livesay, Z. Ma, B. Moazen, C. D Nesaraja, S. D. Pain, N. P. Patterson, D. Shapira, J. F. Shriner, M. S. Smith, T. P. Swan, and J. S. Thomas. Direct reaction measurements with a ^{132}sn radioactive ion beam. *Phys. Rev. C*, 84:034601, Sep 2011.

[14] K. L. Jones, R. L. Kozub, C. Baktash, D. W. Bardayan, J. C. Blackmon, W. N. Catford, J. A. Cizewski, R. P. Fitzgerald, M. S. Johnson, R. J. Livesay, Z. Ma, C. D. Nesaraja, D. Shapira, M. S. Smith, J. S. Thomas, and D. W. Visser. Study of the ^{124}Sn(d, p) reaction in inverse kinematics close to the coulomb barrier. *Phys. Rev. C*, 70:067602, Dec 2004.

[15] J.S. Winfield, S. Fortier, W.N. Catford, S. Pita, N.A. Orr, J. Van de Wiele, Y. Blumenfeld, R. Chapman, S.P.G. Chappell, N.M. Clarke, N. Curtis, M. Freer, S. Gals, H. Langevin-Joliot, H. Laurent, I. Lhenry, J.M. Maison, P. Roussel-Chomaz, M. Shawcross, K. Spohr, T. Suomijrvi, and A. de Vismes. Single-neutron transfer from ^{11}Be(g.s.) via the (p,d) reaction with a radioactive beam. *Nuclear Physics A*, 683(1):48 – 78, 2001.

[16] M Labiche, C N Timis, R C Lemmon, W N Catford, R Chapman, N Amzal, N I Ashwood, T D Baldwin, M Burns, L Caballero, M Chartier, N Curtis, G de France, W Gelletly, X Liang, M Freer, N A Orr, S D Pain, V P E Pucknell, M Rejmund, B Rubio, H Savajols, O Sorlin, K Spohr, Ch Thiesen, and D D Warner. Study of transfer reactions in inverse kinematics with the tiara array. *Journal of Physics G: Nuclear and Particle Physics*, 31(10):S1691, 2005.

[17] G. Potel, F. M. Nunes, and I. J. Thompson. Establishing a theory for deuteron-induced surrogate reactions. *Phys. Rev. C*, 92:034611, Sep 2015.

[18] J.A. Cizewski, R. Hatarik, K.L. Jones, S.D. Pain, J.S. Thomas, M.S. Johnson, D.W. Bardayan, J.C. Blackmon, M.S. Smith, and R.L. Kozub. (d,p) reactions and the surrogate reaction technique. *Nuclear Instruments and Methods in Physics Research Section B: Beam Interactions with Materials and Atoms*, 261(1):938 – 940, 2007.

[19] Isao Tanihata. Neutron halo nuclei. *Journal of Physics G: Nuclear and Particle Physics*, 22(2):157, 1996.

[20] M.V. Zhukov, B.V. Danilin, D.V. Fedorov, J.M. Bang, I.J. Thompson, and J.S. Vaagen. Bound state properties of borromean halo nuclei: ^{6}he and ^{11}li. *Physics Reports*, 231(4):151 – 199, 1993.

[21] C.M. Shand, Zs. Podolyk, M. Grska, P. Doornenbal, A. Obertelli, F. Nowacki, T. Otsuka, K. Sieja, J.A. Tostevin, Y. Tsunoda, G. Authelet, H. Baba, D. Calvet, A. Chteau, S. Chen, A. Corsi, A. Delbart, J.M. Gheller, A. Giganon, A. Gillibert, T. Isobe,

V. Lapoux, M. Matsushita, S. Momiyama, T. Motobayashi, M. Niikura, H. Otsu, N. Paul, C. Pron, A. Peyaud, E.C. Pollacco, J.-Y. Rouss, H. Sakurai, C. Santamaria, M. Sasano, Y. Shiga, D. Steppenbeck, S. Takeuchi, R. Taniuchi, T. Uesaka, H. Wang, K. Yoneda, T. Ando, T. Arici, A. Blazhev, F. Browne, A.M. Bruce, R.J. Carroll, L.X. Chung, M.L. Corts, M. Dewald, B. Ding, Zs. Dombrdi, F. Flavigny, S. Franchoo, F. Giacoppo, A. Gottardo, K. Hadyska-Klk, A. Jungclaus, Z. Korkulu, S. Koyama, Y. Kubota, J. Lee, M. Lettmann, B.D. Linh, J. Liu, Z. Liu, C. Lizarazo, C. Louchart, R. Lozeva, K. Matsui, T. Miyazaki, K. Moschner, M. Nagamine, N. Nakatsuka, S. Nishimura, C.R. Nita, C.R. Nobs, L. Olivier, S. Ota, R. Orlandi, Z. Patel, P.H. Regan, M. Rudigier, E. ahin, T. Saito, P.-A. Sderstrm, I. Stefan, T. Sumikama, D. Suzuki, Zs. Vajta, V. Vaquero, V. Werner, K. Wimmer, J. Wu, and Z.Y. Xu. Shell evolution beyond z=28 and n=50: Spectroscopy of ^{81,82,83,84}zn. *Physics Letters B*, 773:492 – 497, 2017.

[22] C. M. Campbell, N. Aoi, D. Bazin, M. D. Bowen, B. A. Brown, J. M. Cook, D.-C. Dinca, A. Gade, T. Glasmacher, M. Horoi, S. Kanno, T. Motobayashi, W. F. Mueller, H. Sakurai, K. Starosta, H. Suzuki, S. Takeuchi, J. R. Terry, K. Yoneda, and H. Zwahlen. Measurement of excited states in ^{40}Si and evidence for weakening of the $n = 28$ shell gap. *Phys. Rev. Lett.*, 97:112501, Sep 2006.

[23] B. Bastin, S. Grévy, D. Sohler, O. Sorlin, Zs. Dombrádi, N. L. Achouri, J. C. Angélique, F. Azaiez, D. Baiborodin, R. Borcea, C. Bourgeois, A. Buta, A. Bürger, R. Chapman, J. C. Dalouzy, Z. Dlouhy, A. Drouard, Z. Elekes, S. Franchoo, S. Iacob, B. Laurent, M. Lazar, X. Liang, E. Liénard, J. Mrazek, L. Nalpas, F. Negoita, N. A. Orr, Y. Penionzhkevich, Zs. Podolyák, F. Pougheon, P. Roussel-Chomaz, M. G. Saint-Laurent, M. Stanoiu, I. Stefan, F. Nowacki, and A. Poves. Collapse of the $n = 28$ shell closure in ^{42}Si. *Phys. Rev. Lett.*, 99:022503, Jul 2007.

[24] R C Thompson. Precision measurement aspects of ion traps. *Measurement Science and Technology*, 1(2):93, 1990.

[25] S. Suchyta, S. N. Liddick, Y. Tsunoda, T. Otsuka, M. B. Bennett, A. Chemey, M. Honma, N. Larson, C. J. Prokop, S. J. Quinn, N. Shimizu, A. Simon, A. Spyrou, V. Tripathi, Y. Utsuno, and J. M. VonMoss. Shape coexistence in ^{68}Ni. *Phys. Rev. C*, 89:021301, Feb 2014.

[26] C. J. Prokop, B. P. Crider, S. N. Liddick, A. D. Ayangeakaa, M. P. Carpenter, J. J. Carroll, J. Chen, C. J. Chiara, H. M. David, A. C. Dombos, S. Go, J. Harker, R. V. F. Janssens, N. Larson, T. Lauritsen, R. Lewis, S. J. Quinn, F. Recchia, D. Seweryniak, A. Spyrou, S. Suchyta, W. B. Walters, and S. Zhu. New low-energy 0^+ state and shape coexistence in ^{70}Ni. *Phys. Rev. C*, 92:061302, Dec 2015.

[27] N. Mitchell and E. Salpietro. The use of deuterium-deuterium reactions to aid tritium breeding in tokamak fusion reactors. *Nuclear Fusion*, 26(9):1246, 1986.

[28] M. Yiğit, E. Tel, and A. Kara. Deuteron induced (d,p) and (d,2p) nuclear reactions up to 50 mev. *Journal of Fusion Energy*, 32(3):362–370, Jun 2013.

[29] Gregory Severin, Carsten H. Nielsen, Andreas Tue Ingemann Jensen, Jesper Fonslet, Andreas Kjr, and Fedor Zhuravlev. Bringing radiotracing to titanium-based antineo-plastics: Solid phase radiosynthesis, pet and ex vivo evaluation of antitumor agent [45ti](salan)ti(dipic). *Journal of Medicinal Chemistry*, 58(18):75917595, 2015.

[30] Stephen A. Graves, Reinier Hernandez, Jesper Fonslet, Christopher G. England, Hector F. Valdovinos, Paul A. Ellison, Todd E. Barnhart, Dennis R. Elema, Charles P. Theuer, Weibo Cai, Robert J. Nickles, and Gregory W. Severin. Novel preparation methods of ^{52}mn for immunopet imaging. *Bioconjugate Chemistry*, 26(10):2118–2124, 2015. PMID: 26317429.

[31] Marc C. Kennedy and Anthony O'Hagan. Bayesian calibration of computer models. *Journal of the Royal Statistical Society: Series B (Statistical Methodology)*, 63(3):425–464, 2001.

[32] Frederik Beaujean, Christoph Bobeth, and Danny van Dyk. Comprehensive bayesian analysis of rare (semi)leptonic and radiative $\boldsymbol{B}$ decays. *The European Physical Journal C*, 74(6):2897, Jun 2014.

[33] B. Aubert, M. Bona, D. Boutigny, Y. Karyotakis, J. P. Lees, V. Poireau, X. Prudent, V. Tisserand, A. Zghiche, J. Garra Tico, E. Grauges, L. Lopez, A. Palano, G. Eigen, B. Stugu, L. Sun, G. S. Abrams, M. Battaglia, D. N. Brown, J. Button-Shafer, R. N. Cahn, Y. Groysman, R. G. Jacobsen, J. A. Kadyk, L. T. Kerth, Yu. G. Kolomensky, G. Kukartsev, D. Lopes Pegna, G. Lynch, L. M. Mir, T. J. Orimoto, M. T. Ronan, K. Tackmann, W. A. Wenzel, P. del Amo Sanchez, C. M. Hawkes, A. T. Watson, T. Held, H. Koch, B. Lewandowski, M. Pelizaeus, T. Schroeder, M. Steinke, D. Walker, D. J. Asgeirsson, T. Cuhadar-Donszelmann, B. G. Fulsom, C. Hearty, T. S. Mattison, J. A. McKenna, A. Khan, M. Saleem, L. Teodorescu, V. E. Blinov, A. D. Bukin, V. P. Druzhinin, V. B. Golubev, A. P. Onuchin, S. I. Serednyakov, Yu. I. Skovpen, E. P. Solodov, K. Yu. Todyshev, M. Bondioli, S. Curry, I. Eschrich, D. Kirkby, A. J. Lankford, P. Lund, M. Mandelkern, E. C. Martin, D. P. Stoker, S. Abachi, C. Buchanan, S. D. Foulkes, J. W. Gary, F. Liu, O. Long, B. C. Shen, L. Zhang, H. P. Paar, S. Rahatlou, V. Sharma, J. W. Berryhill, C. Campagnari, A. Cunha, B. Dahmes, T. M. Hong, D. Kovalskyi, J. D. Richman, T. W. Beck, A. M. Eisner, C. J. Flacco, C. A. Heusch, J. Kroseberg, W. S. Lockman, T. Schalk, B. A. Schumm, A. Seiden, M. G. Wilson, L. O. Winstrom, E. Chen, C. H. Cheng, F. Fang, D. G. Hitlin, I. Narsky, T. Piatenko, F. C. Porter, R. Andreassen, G. Mancinelli, B. T. Meadows, K. Mishra, M. D. Sokoloff, F. Blanc, P. C. Bloom, S. Chen, W. T. Ford, J. F. Hirschauer, A. Kreisel, M. Nagel, U. Nauenberg, A. Olivas, J. G. Smith, K. A. Ulmer, S. R. Wagner, J. Zhang, A. M. Gabareen, A. Soffer, W. H. Toki, R. J. Wilson, F. Winklmeier, D. D. Altenburg, E. Feltresi, A. Hauke, H. Jasper, J. Merkel, A. Petzold, B. Spaan, K. Wacker, V. Klose, M. J. Kobel, H. M. Lacker, W. F. Mader, R. Nogowski, J. Schubert, K. R. Schubert,

R. Schwierz, J. E. Sundermann, A. Volk, D. Bernard, G. R. Bonneaud, E. Latour, V. Lombardo, Ch. Thiebaux, M. Verderi, P. J. Clark, W. Gradl, F. Muheim, S. Playfer, A. I. Robertson, Y. Xie, M. Andreotti, D. Bettoni, C. Bozzi, R. Calabrese, A. Cecchi, G. Cibinetto, P. Franchini, E. Luppi, M. Negrini, A. Petrella, L. Piemontese, E. Prencipe, V. Santoro, F. Anulli, R. Baldini-Ferroli, A. Calcaterra, R. de Sangro, G. Finocchiaro, S. Pacetti, P. Patteri, I. M. Peruzzi, M. Piccolo, M. Rama, A. Zallo, A. Buzzo, R. Contri, M. Lo Vetere, M. M. Macri, M. R. Monge, S. Passaggio, C. Patrignani, E. Robutti, A. Santroni, S. Tosi, K. S. Chaisanguanthum, M. Morii, J. Wu, R. S. Dubitzky, J. Marks, S. Schenk, U. Uwer, D. J. Bard, P. D. Dauncey, R. L. Flack, J. A. Nash, W. Panduro Vazquez, M. Tibbetts, P. K. Behera, X. Chai, M. J. Charles, U. Mallik, V. Ziegler, J. Cochran, H. B. Crawley, L. Dong, V. Eyges, W. T. Meyer, S. Prell, E. I. Rosenberg, A. E. Rubin, Y. Y. Gao, A. V. Gritsan, Z. J. Guo, C. K. Lae, A. G. Denig, M. Fritsch, G. Schott, N. Arnaud, J. Béquilleux, M. Davier, G. Grosdidier, A. Höcker, V. Lepeltier, F. Le Diberder, A. M. Lutz, S. Pruvot, S. Rodier, P. Roudeau, M. H. Schune, J. Serrano, V. Sordini, A. Stocchi, W. F. Wang, G. Wormser, D. J. Lange, D. M. Wright, I. Bingham, C. A. Chavez, I. J. Forster, J. R. Fry, E. Gabathuler, R. Gamet, D. E. Hutchcroft, D. J. Payne, K. C. Schofield, C. Touramanis, A. J. Bevan, K. A. George, F. Di Lodovico, W. Menges, R. Sacco, G. Cowan, H. U. Flaecher, D. A. Hopkins, S. Paramesvaran, F. Salvatore, A. C. Wren, D. N. Brown, C. L. Davis, J. Allison, N. R. Barlow, R. J. Barlow, Y. M. Chia, C. L. Edgar, G. D. Lafferty, T. J. West, J. I. Yi, J. Anderson, C. Chen, A. Jawahery, D. A. Roberts, G. Simi, J. M. Tuggle, G. Blaylock, C. Dallapiccola, S. S. Hertzbach, X. Li, T. B. Moore, E. Salvati, S. Saremi, R. Cowan, D. Dujmic, P. H. Fisher, K. Koeneke, G. Sciolla, S. J. Sekula, M. Spitznagel, F. Taylor, R. K. Yamamoto, M. Zhao, Y. Zheng, S. E. Mclachlin, P. M. Patel, S. H. Robertson, A. Lazzaro, F. Palombo, J. M. Bauer, L. Cremaldi, V. Eschenburg, R. Godang, R. Kroeger, D. A. Sanders, D. J. Summers, H. W. Zhao, S. Brunet, D. Côté, M. Simard, P. Taras, F. B. Viaud, H. Nicholson, G. De Nardo, F. Fabozzi, L. Lista, D. Monorchio, C. Sciacca, M. A. Baak, G. Raven, H. L. Snoek, C. P. Jessop, J. M. LoSecco, G. Benelli, L. A. Corwin, K. Honscheid, H. Kagan, R. Kass, J. P. Morris, A. M. Rahimi, J. J. Regensburger, Q. K. Wong, N. L. Blount, J. Brau, R. Frey, O. Igonkina, J. A. Kolb, M. Lu, R. Rahmat, N. B. Sinev, D. Strom, J. Strube, E. Torrence, N. Gagliardi, A. Gaz, M. Margoni, M. Morandin, A. Pompili, M. Posocco, M. Rotondo, F. Simonetto, R. Stroili, C. Voci, E. Ben-Haim, H. Briand, G. Calderini, J. Chauveau, P. David, L. Del Buono, Ch. de la Vaissière, O. Hamon, Ph. Leruste, J. Malclès, J. Ocariz, A. Perez, L. Gladney, M. Biasini, R. Covarelli, E. Manoni, C. Angelini, G. Batignani, S. Bettarini, M. Carpinelli, R. Cenci, A. Cervelli, F. Forti, M. A. Giorgi, A. Lusiani, G. Marchiori, M. A. Mazur, M. Morganti, N. Neri, E. Pa. Search for $b \to u$ transitions in $B^- \to [K^+\pi^-\pi^0]_D K^-$. *Phys. Rev. D*, 76:111101, Dec 2007.

[34] Feryal Özel and Dimitrios Psaltis. Statistics of measuring neutron star radii: Assessing a frequentist and a bayesian approach. *The Astrophysical Journal*, 810(2):135, 2015.

[35] Ian Vernon, Michael Goldstein, and Richard Bower. Galaxy formation: Bayesian history matching for the observable universe. *Statist. Sci.*, 29(1):81–90, 02 2014.

[36] Stefano Andreon and Brian Weaver. *Bayesian Methods for the Physical Sciences.* Springer, 2015.

[37] Luis Barboza, Bo Li, Martin P. Tingley, and Frederi G. Viens. Reconstructing past temperatures from natural proxies and estimated climate forcings using short- and long-memory models. *The Annals of Applied Statistics*, 8(4):1966–2001, 2014.

[38] Gowri Srinivasan, Daniel M. Tartakovsky, Bruce A. Robinson, and Alejandro B. Aceves. Quantification of uncertainty in geochemical reactions. *Water Resources Research*, 43(12):n/a–n/a, 2007. W12415.

[39] The Editors. Editorial: Uncertainty estimates. *Phys. Rev. A*, 83:040001, Apr 2011.

[40] B. D. Carlsson, A. Ekström, C. Forssén, D. Fahlin Strömberg, G. R. Jansen, O. Lilja, M. Lindby, B. A. Mattsson, and K. A. Wendt. Uncertainty analysis and order-by-order optimization of chiral nuclear interactions. *Phys. Rev. X*, 6:011019, Feb 2016.

[41] A Ekstrm, B D Carlsson, K A Wendt, C Forssn, M Hjorth Jensen, R Machleidt, and S M Wild. Statistical uncertainties of a chiral interaction at next-to-next-to leading order. *Journal of Physics G: Nuclear and Particle Physics*, 42(3):034003, 2015.

[42] S Wesolowski, N Klco, R J Furnstahl, D R Phillips, and A Thapaliya. Bayesian parameter estimation for effective field theories. *Journal of Physics G: Nuclear and Particle Physics*, 43(7):074001, 2016.

[43] R. J. Furnstahl, N. Klco, D. R. Phillips, and S. Wesolowski. Quantifying truncation errors in effective field theory. *Phys. Rev. C*, 92:024005, Aug 2015.

[44] J. A. Melendez, S. Wesolowski, and R. J. Furnstahl. Bayesian truncation errors in chiral effective field theory: Nucleon-nucleon observables. *Phys. Rev. C*, 96:024003, Aug 2017.

[45] Nicolas Schunck, Jordan D McDonnell, Jason Sarich, Stefan M Wild, and Dave Higdon. Error analysis in nuclear density functional theory. *Journal of Physics G: Nuclear and Particle Physics*, 42(3):034024, 2015.

[46] T Haverinen and M Kortelainen. Uncertainty propagation within the unedf models. *Journal of Physics G: Nuclear and Particle Physics*, 44(4):044008, 2017.

[47] J. D. McDonnell, N. Schunck, D. Higdon, J. Sarich, S. M. Wild, and W. Nazarewicz. Uncertainty quantification for nuclear density functional theory and information content of new measurements. *Phys. Rev. Lett.*, 114:122501, Mar 2015.

[48] J Dobaczewski, W Nazarewicz, and P-G Reinhard. Error estimates of theoretical models: a guide. *Journal of Physics G: Nuclear and Particle Physics*, 41(7):074001, 2014.

[49] Daniel Phillips. Building light nuclei from neutrons, protons, and pions. *Czechoslovak Journal of Physics*, 52(2):B49–B101, Feb 2002.

[50] Epelbaum, E., Krebs, H., and Meiner, U. -G. Improved chiral nucleon-nucleon potential up to next-to-next-to-next-to-leading order. *Eur. Phys. J. A*, 51(5):53, 2015.

[51] M.R. Schindler and D.R. Phillips. Bayesian methods for parameter estimation in effective field theories. *Annals of Physics*, 324(3):682 – 708, 2009.

[52] E. Epelbaum, H. Krebs, and U.-G. Meißner. Precision nucleon-nucleon potential at fifth order in the chiral expansion. *Phys. Rev. Lett.*, 115:122301, Sep 2015.

[53] Michael Bender, Paul-Henri Heenen, and Paul-Gerhard Reinhard. Self-consistent mean-field models for nuclear structure. *Rev. Mod. Phys.*, 75:121–180, Jan 2003.

[54] Markus Kortelainen. Propagation of uncertainties in the nuclear dft models. *Journal of Physics G: Nuclear and Particle Physics*, 42(3):034021, 2015.

[55] N. Schunck, J. D. McDonnell, D. Higdon, J. Sarich, and S. M. Wild. Uncertainty quantification and propagation in nuclear density functional theory. *The European Physical Journal A*, 51(12):169, Dec 2015.

[56] J. Novak, K. Novak, S. Pratt, J. Vredevoogd, C. E. Coleman-Smith, and R. L. Wolpert. Determining fundamental properties of matter created in ultrarelativistic heavy-ion collisions. *Phys. Rev. C*, 89:034917, Mar 2014.

[57] Evan Sangaline and Scott Pratt. Toward a deeper understanding of how experiments constrain the underlying physics of heavy-ion collisions. *Phys. Rev. C*, 93:024908, Feb 2016.

[58] A E Lovell and F M Nunes. Systematic uncertainties in direct reaction theories. *Journal of Physics G: Nuclear and Particle Physics*, 42(3):034014, 2015.

[59] J. L. Friar, B. F. Gibson, G. Berthold, W. Glöckle, Th. Cornelius, H. Witala, J. Haidenbauer, Y. Koike, G. L. Payne, J. A. Tjon, and W. M. Kloet. Benchmark solutions for a model three-nucleon scattering problem. *Phys. Rev. C*, 42:1838–1840, Nov 1990.

[60] A. Deltuva, A. C. Fonseca, A. Kievsky, S. Rosati, P. U. Sauer, and M. Viviani. Benchmark calculation for proton-deuteron elastic scattering observables including the coulomb interaction. *Phys. Rev. C*, 71:064003, Jun 2005.

[61] A. Deltuva. Deuteron stripping and pickup involving the halo nuclei ^{11}Be and ^{15}C. *Phys. Rev. C*, 79:054603, May 2009.

[62] N. C. Summers, F. M. Nunes, and I. J. Thompson. Extended continuum discretized coupled channels method: Core excitation in the breakup of exotic nuclei. *Phys. Rev. C*, 74:014606, Jul 2006.

[63] A. M. Moro and J. A. Lay. Interplay between valence and core excitation mechanisms in the breakup of halo nuclei. *Phys. Rev. Lett.*, 109:232502, Dec 2012.

[64] A. Deltuva. Faddeev-type calculation of three-body nuclear reactions including core excitation. *Phys. Rev. C*, 88:011601, Jul 2013.

[65] J. Rotureau, P. Danielewicz, G. Hagen, F. M. Nunes, and T. Papenbrock. Optical potential from first principles. *Phys. Rev. C*, 95:024315, Feb 2017.

[66] L. D. Faddeev. Scattering theory for a three-particle system. *Soviet Physics JETP*, 12(5):1014–1019, 1961.

[67] E.O. Alt, P. Grassberger, and W. Sandhas. Reduction of the three-particle collision problem to multi-channel two-particle lippmann-schwinger equations. *Nuclear Physics B*, 2(2):167 – 180, 1967.

[68] N. Austern, Y. Iseri, M. Kamimura, M. Kawai, G. Rawitscher, and M. Yahiro. Continuum-discretized coupled-channels calculations for three-body models of deuteron-nucleus reactions. *Physics Reports*, 154(3):125 – 204, 1987.

[69] R.C. Johnson and P.C. Tandy. An approximate three-body theory of deuteron stripping. *Nuclear Physics A*, 235(1):56 – 74, 1974.

[70] F. M. Nunes and A. Deltuva. Adiabatic approximation versus exact faddeev method for (d, p) and (p, d) reactions. *Phys. Rev. C*, 84:034607, Sep 2011.

[71] L. J. Titus, F. M. Nunes, and G. Potel. Explicit inclusion of nonlocality in (d, p) transfer reactions. *Phys. Rev. C*, 93:014604, Jan 2016.

[72] A. Spyrou, Z. Kohley, T. Baumann, D. Bazin, B. A. Brown, G. Christian, P. A. DeYoung, J. E. Finck, N. Frank, E. Lunderberg, S. Mosby, W. A. Peters, A. Schiller, J. K. Smith, J. Snyder, M. J. Strongman, M. Thoennessen, and A. Volya. First observation of ground state dineutron decay: ^{16}Be. *Phys. Rev. Lett.*, 108:102501, Mar 2012.

[73] D. R. Goosman and R. W. Kavanagh. ^{10}Be$(d, p)^{11}$Be. *Phys. Rev. C*, 1:1939–1945, Jun 1970.

[74] W.H. Dickhoff and D. Van Neck. *Many-Body Theory Exposed! 2nd ed.* World Scientific, New Jersey, 2008.

[75] Herman Feshbach. Unified theory of nuclear reactions. *Ann. Phys.*, 5(4):357 – 390, 1958.

[76] P. Fraser, K. Amos, S. Karataglidis, L. Canton, G. Pisent, and J.P. Svenne. Two causes of nonlocalities in nucleon-nucleus potentials and their effects in nucleon-nucleus scattering. *Euro. Phys. J. A*, 35(1):69–80, 2008.

[77] G. H. Rawitscher, D. Lukaszek, R. S. Mackintosh, and S. G. Cooper. Local representation of the exchange nonlocality in $n -{}^{16}$o scattering. *Phys. Rev. C*, 49:1621–1629, Mar 1994.

[78] J.M. Lohr and W. Haeberli. Elastic scattering of 913 mev vector polarized deuterons. *Nuclear Physics A*, 232(2):381 – 397, 1974.

[79] A.J. Koning and J.P. Delaroche. Local and global nucleon optical models from 1 kev to 200 mev. *Nuclear Physics A*, 713(3):231 – 310, 2003.

[80] W. W. Daehnick, J. D. Childs, and Z. Vrcelj. Global optical model potential for elastic deuteron scattering from 12 to 90 mev. *Phys. Rev. C*, 21:2253–2274, Jun 1980.

[81] R.L. Varner, W.J. Thompson, T.L. McAbee, E.J. Ludwig, and T.B. Clegg. A global nucleon optical model potential. *Physics Reports*, 201(2):57 – 119, 1991.

[82] C.M. Perey and F.G. Perey. Compilation of phenomenological optical-model parameters 19541975. *Atomic Data and Nuclear Data Tables*, 17(1):1 – 101, 1976.

[83] Ian J. Thompson and Filomena M. Nunes. *Nuclear Reactions for Astrophysics.* Cambridge University Press, 2009.

[84] M. Abramowitz and I. Stegun. *Handbook of Mathematical Functions.* Dover, 1970.

[85] B. Buck, A. P. Stamp, and P. E. Hodgson. The excitation of collective states by inelastic scattering the extended optical model. *Philosophical Magazine*, 8(95):1805–1826, 1963.

[86] L.D Tolsma and G.W Veltkamp. Measuring the accuracy of the solution subspace obtained by numerical integration of the schrdinger equation. *Computer Physics Communications*, 40(2):233 – 262, 1986.

[87] Mitsuji Kawai, Masayasu Kamimura, Yoshihide Mito, and Kazuo Takesako. A coupled channel variational method for multi-step direct nuclear reactions. i formalism and numerical test. *Progress of Theoretical Physics*, 59(2):674–676, 1978.

[88] Mitsuji Kawai, Masayasu Kamimura, Yoshihide Mito, and Kazuo Takesako. A coupled channel variational method for multi-step direct nuclear reactions. ii test on a (d, p) reaction. *Progress of Theoretical Physics*, 59(2):676–678, 1978.

[89] Masayasu Kamimura. Chapter v. a coupled channel variational method for microscopic study of reactions between complex nuclei. *Progress of Theoretical Physics Supplement*, 62:236–294, 1977.

[90] D Baye, M Hesse, J-M Sparenberg, and M Vincke. Analysis of the r -matrix method on lagrange meshes. *Journal of Physics B: Atomic, Molecular and Optical Physics*, 31(15):3439, 1998.

[91] M. Hesse, J.-M. Sparenberg, F. Van Raemdonck, and D. Baye. Coupled-channel r-matrix method on a lagrange mesh. *Nuclear Physics A*, 640(1):37 – 51, 1998.

[92] J.A. Christley and I.J. Thompson. Crcwfn: coupled real coulomb wavefunctions. *Computer Physics Communications*, 79(1):143 – 155, 1994.

[93] J. D. Harvey and R. C. Johnson. Influence of breakup channels on the analysis of deuteron stripping reactions. *Phys. Rev. C*, 3:636–645, Feb 1971.

[94] Steven Weinberg. Quasiparticles and the born series. *Phys. Rev.*, 131:440–460, Jul 1963.

[95] D. Y. Pang, N. K. Timofeyuk, R. C. Johnson, and J. A. Tostevin. Rapid convergence of the weinberg expansion of the deuteron stripping amplitude. *Phys. Rev. C*, 87:064613, Jun 2013.

[96] G. A. F. Seber and C. J. Wild. *Nonlinear Regression*. John Wiley & Sons, Inc., 2003.

[97] Roberto Trotta. Bayes in the sky: Bayesian inference and model selection in cosmology. *Contemporary Physics*, 49(2):71–104, 2008.

[98] Mr. Bayes and Mr. Price. An essay towards solving a problem in the doctrine of chances. by the late rev. mr. bayes, f. r. s. communicated by mr. price, in a letter to john canton, a. m. f. r. s. *Philosophical Transactions*, 53:370–418, 1763.

[99] D. S. Sivia. *Data Analysis: A Bayesian Tutorial*. Oxford Science Publications, 1996.

[100] Christian P. Rober and George Casella. *Monte Carlo Statistical Methods*. Springer Texts in Statistics, 2004.

[101] Dani Gamerman. *Markov Chain Monte Carlo*. Chapman & Hall, 1997.

[102] Nicholas Metropolis, Arianna W. Rosenbluth, Marshall N. Rosenbluth, Augusta H. Teller, and Edward Teller. Equation of state calculations by fast computing machines. *The Journal of Chemical Physics*, 21(6):1087–1092, 1953.

[103] W. K. Hastings. Monte carlo sampling methods using markov chains and their applications. *Biometrika*, 57(1):97–109, 1970.

[104] W. Fitz, R. Jahr, and R. Santo. Scattering and pick-up reactions with deuterons on be, b, c, n and o at 11.8 mev. *Nuclear Physics A*, 101(2):449 – 459, 1967.

[105] Yinlu Han, Yuyang Shi, and Qingbiao Shen. Deuteron global optical model potential for energies up to 200 mev. *Phys. Rev. C*, 74:044615, Oct 2006.

[106] J. P. Schiffer, G. C. Morrison, R. H. Siemssen, and B. Zeidman. Study of the (d, p) reaction in the $1p$ shell. *Phys. Rev.*, 164:1274–1284, Dec 1967.

[107] J. K. Dickens, F. G. Perey, and R. J. Silva. Elastic scattering of 12.0- and 14.0-mev deuterons from ^{90}zr and the reaction of ^{90}zr(d, p)^{91}zr: Tabulated differential cross sections. Technical Report ORNL-3850, Oak Ridge National Laboratory, 1965.

[108] R.D. Rathmell, P.J. Bjorkholm, and W. Haeberli. Vector analysing power and cross section for ^{90}zr(d, p)^{91}zr at 11 and 12 mev. *Nuclear Physics A*, 206(3):459 – 476, 1973.

[109] Z M Chen, K Baird, C R Howell, M L Roberts, W Tornow, and R L Walter. Neutron scattering from ^{12}c between 15.6 and 17.3 mev. *Journal of Physics G: Nuclear and Particle Physics*, 19(6):877, 1993.

[110] M B Chadwick, L J Cox, P G Young, and A S Meigooni. Calculation and evolution of cross sections and kerma factors for neutrons up to 100 mev on carbon. *Nucl. Sci. Eng.*, 123(1):17, 1996.

[111] Sally F. Hicks, S. E. Hicks, G. R. Shen, and M. T. McEllistrem. Collective doorway configurations in ^{49}Ca through neutron scattering on ^{48}Ca. *Phys. Rev. C*, 41:2560–2570, Jun 1990.

[112] D. Wilmore and P.E. Hodgson. The calculation of neutron cross-sections from optical potentials. *Nuclear Physics*, 55:673 – 694, 1964.

[113] R. S. Pedroni, C. R. Howell, G. M. Honoré, H. G. Pfutzner, R. C. Byrd, R. L. Walter, and J. P. Delaroche. Energy dependence of the deformed optical potential for neutron scattering from ^{54}, *56* fe and ^{58}, *60* ni up to 80 mev. *Phys. Rev. C*, 38:2052–2062, Nov 1988.

[114] J. Rapaport, T.S. Cheema, D.E. Bainum, R.W. Finlay, and J.D. Carlson. Neutron scattering from ^{208}pb. *Nuclear Physics A*, 296(1):95 – 108, 1978.

[115] D. E. Bainum, R. W. Finlay, J. Rapaport, J. D. Carlson, and W. G. Love. Excitation of low-lying collective states in ^{40}Ca and ^{208}Pb by inelastic neutron scattering. *Phys. Rev. C*, 16:1377–1388, Oct 1977.

[116] Roderick V Reid. Local phenomenological nucleon-nucleon potentials. *Annals of Physics*, 50(3):411 – 448, 1968.

[117] Alejandro Sonzogni. *http://www.nndc.bnl.gov/chart/chartNuc.jsp*, 2011.

[118] I.J. Thompson. *www.fresco.org.uk*, 2006.

[119] F. James. Minuit function minimization and error analysis: Reference manual version 94.1. *CERN Program Library Long Writeup D*, 506(CERN-D-506, CERN-D506), 1994.

[120] X. D. Liu, M. A. Famiano, W. G. Lynch, M. B. Tsang, and J. A. Tostevin. Systematic extraction of spectroscopic factors from ^{12}C$(d,p)^{13}$C and ^{13}C$(p,d)^{12}$C reactions. *Phys. Rev. C*, 69:064313, Jun 2004.

[121] F. Delaunay, F. M. Nunes, W. G. Lynch, and M. B. Tsang. Coupling and higher-order effects in the ^{12}C$(d,p)^{13}$C and ^{13}C$(p,d)^{12}$C reactions. *Phys. Rev. C*, 72:014610, Jul 2005.

[122] Y. Wang and J. Rapaport. Neutron scattering from ^{90,91,92,94}zr. *Nuclear Physics A*, 517(2):301 – 328, 1990.

[123] R. H. McCamis, T. N. Nasr, J. Birchall, N. E. Davison, W. T. H. van Oers, P. J. T. Verheijen, R. F. Carlson, A. J. Cox, B. C. Clark, E. D. Cooper, S. Hama, and R. L. Mercer. Elastic scattering of protons from ^{40,42,44,48}ca from 20 to 50 mev and nuclear matter radii. *Phys. Rev. C*, 33:1624–1633, May 1986.

[124] L. N. Blumberg, E. E. Gross, A. VAN DER Woude, A. Zucker, and R. H. Bassel. Polarizations and differential cross sections for the elastic scattering of 40-mev protons from ^{12}C, ^{40}Ca, ^{58}Ni, ^{90}Zr, and ^{208}Pb. *Phys. Rev.*, 147:812–825, Jul 1966.

[125] P. P. Guss, R. C. Byrd, C. R. Howell, R. S. Pedroni, G. Tungate, R. L. Walter, and J. P. Delaroche. Optical model description of the neutron interaction with ^{116}Sn and ^{120}Sn over a wide energy range. *Phys. Rev. C*, 39:405–414, Feb 1989.

[126] L.J. Titus, A. Ross, and F.M. Nunes. Transfer reaction code with nonlocal interactions. *Comput. Phys. Commun.*, 207:499 – 517, 2016.

[127] J.C. Lombardi, R.N. Boyd, R. Arking, and A.B. Robbins. Nuclear sizes in ^{40,44,48}ca. *Nuclear Physics A*, 188(1):103 – 114, 1972.

[128] J. M. Mueller, R. J. Charity, R. Shane, L. G. Sobotka, S. J. Waldecker, W. H. Dickhoff, A. S. Crowell, J. H. Esterline, B. Fallin, C. R. Howell, C. Westerfeldt, M. Youngs, B. J. Crowe, and R. S. Pedroni. Asymmetry dependence of nucleon correlations in spherical nuclei extracted from a dispersive-optical-model analysis. *Phys. Rev. C*, 83:064605, Jun 2011.

[129] R. H. McCamis, T. N. Nasr, J. Birchall, N. E. Davison, W. T. H. van Oers, P. J. T. Verheijen, R. F. Carlson, A. J. Cox, B. C. Clark, E. D. Cooper, S. Hama, and R. L. Mercer. Elastic scattering of protons from ^{40,42,44,48}ca from 20 to 50 mev and nuclear matter radii. *Phys. Rev. C*, 33:1624–1633, May 1986.

[130] M. Ermer, H. Clement, G. Holetzke, W. Kabitzke, G. Graw, R. Hertenberger, H. Kader, F. Merz, and P. Schiemenz. The deuteron optical potential at low energies. *Nuclear Physics A*, 533(1):71 – 94, 1991.

[131] J. K. Dickens, E. Eichler, and G. R. Satchler. ^{90,92,94}Zr(p, p'). *Phys. Rev.*, 168:1355–1372, Apr 1968.

[132] J. B. Ball, C. B. Fulmer, and R. H. Bassel. Scattering of 22.5-mev protons from zirconium and the symmetry term in the nuclear optical potential. *Phys. Rev.*, 135:B706–B710, Aug 1964.

[133] Clyde B. Fulmer. Elastic scattering of protons by single isotopes. *Phys. Rev.*, 125:631–638, Jan 1962.

[134] J. Rapaport, Mohammed Mirzaa, H. Hadizadeh, D.E. Bainum, and R.W. Finlay. Neutron elastic scattering from ^{116,118,120,122,124}sn. *Nuclear Physics A*, 341(1):56 – 74, 1980.

[135] G.S. Mani, D.T. Jones, and D. Jacques. Elastic scattering of 50 mev protons by nuclei in the range from ^{42}ca to ^{208}pb. *Nuclear Physics A*, 165(2):384 – 392, 1971.

[136] W. Makofske, G. W. Greenlees, H. S. Liers, and G. J. Pyle. Proton elastic scattering measurements at 16 mev with optical-model analysis. *Phys. Rev. C*, 5:780–791, Mar 1972.

[137] C. E. Floyd, Jr. *Scattering of polarized fast neutrons from beryllium-9, iron-54, copper-65, and lead-208: the determination of the nucleon-nucleus spin-orbit interaction.* PhD thesis, Duke University, 1981.

[138] W. T. H. van Oers, Huang Haw, N. E. Davison, A. Ingemarsson, B. Fagerström, and G. Tibell. Optical-model analysis of $p +^{208}$ Pb elastic scattering from 15 - 1000 mev. *Phys. Rev. C*, 10:307–319, Jul 1974.

[139] R. Rche, Nguyen Van Sen, G. Perrin, J.C. Gondrand, A. Fiore, and H. Mller. Evidence for the deuteron-nucleus tensor interaction. *Nuclear Physics A*, 220(2):381 – 390, 1974.

[140] A. M. Mukhamedzhanov, F. M. Nunes, and P. Mohr. Benchmark on neutron capture extracted from (d, p) reactions. *Phys. Rev. C*, 77:051601, May 2008.

[141] K. Hashimoto, Y. Aoki, Y. Tagishi, and K. Yagi. Mechanism of (d,) reaction: ^{208}pb(d,)^{206}tl and ^{90}zr(d,)^{88}y using vector- and tensor-polarized deuterons. *Nuclear Physics A*, 471(3):520 – 534, 1987.

[142] Haixia An and Chonghai Cai. Global deuteron optical model potential for the energy range up to 183 mev. *Phys. Rev. C*, 73:054605, May 2006.

[143] F.M. Nunes. private communication. *private communication*, 2017.

[144] M. H. Mahzoon, M. C. Atkinson, R. J. Charity, and W. H. Dickhoff. Neutron skin thickness of ^{48}Ca from a nonlocal dispersive optical-model analysis. *Phys. Rev. Lett.*, 119:222503, Nov 2017.

[145] J. Alster. Collective excitations in pb^{207}, pb^{208}, and bi^{209}. *Phys. Rev.*, 141:1138–1145, Jan 1966.

[146] V.R. Cupps, J.D. Brown, C.C. Foster, W.P. Jones, D.W. Miller, H. Nann, P. Schwandt, E.J. Stephenson, and J.A. Tostevin. The ^{116}si(d, p)^{117}sn l=0 reaction mechanism at intermediate energies. *Nuclear Physics A*, 469(3):445 – 466, 1987.

[147] E.J. Stephenson, V.R. Cupps, J.A. Tostevin, R.C. Johnson, J.D. Brown, C.C. Foster, W.P. Jones, D.W. Miller, H. Nann, and P. Schwandt. The effects of far-side dominance on the j-dependence of the medium energy ^{116}sn(d, p)^{117}sn reaction. *Nuclear Physics A*, 469(3):467 – 479, 1987.

[148] K. Hirota, Y. Aoki, N. Okumura, and Y. Tagishi. Deuteron elastic scattering and (d, p) reactions on ^{208}pb at e$_d$ = 22 mev and j-dependence of t$_{20}$ in (d,p) reaction. *Nuclear Physics A*, 628(4):547 – 579, 1998.

[149] Herman Feshbach. A unified theory of nuclear reactions. {II}. *Ann. Phys.*, 19(2):287 – 313, 1962.

[150] L. J. Titus and F. M. Nunes. Testing the perey effect. *Phys. Rev. C*, 89:034609, Mar 2014.

[151] A. Ross, L. J. Titus, F. M. Nunes, M. H. Mahzoon, W. H. Dickhoff, and R. J. Charity. Effects of nonlocal potentials on (p, d) transfer reactions. *Phys. Rev. C*, 92:044607, Oct 2015.

[152] A. Ross, L. J. Titus, and F. M. Nunes. Examining the effect of nonlocality in (d, n) transfer reactions. *Phys. Rev. C*, 94:014607, Jul 2016.

[153] N. K. Timofeyuk and R. C. Johnson. Nonlocality in the adiabatic model of $a(d, p)b$ reactions. *Phys. Rev. C*, 87:064610, Jun 2013.

[154] S. J. Waldecker and N. K. Timofeyuk. Implications for (d, p) reaction theory from nonlocal dispersive optical model analysis of ^{40}Ca$(d, p)^{41}$Ca. *Phys. Rev. C*, 94:034609, Sep 2016.

[155] G. W. Bailey, N. K. Timofeyuk, and J. A. Tostevin. Sensitivity of (d, p) reactions to high $n-p$ momenta and the consequences for nuclear spectroscopy studies. *Phys. Rev. Lett.*, 117:162502, Oct 2016.

[156] W. H. Dickhoff, D. Van Neck, S. J. Waldecker, R. J. Charity, and L. G. Sobotka. *Phys. Rev. C*, 82(5):054306, 2010.

[157] M. H. Mahzoon, R. J. Charity, W. H. Dickhoff, H. Dussan, and S. J. Waldecker. Forging the link between nuclear reactions and nuclear structure. *Phys. Rev. Lett.*, 112:162503, Apr 2014.

[158] C. Mahaux and R. Sartor. Single-particle motion in nuclei. In J.W. Negele and Erich Vogt, editors, *Advances in Nuclear Physics*, volume 20 of *Advances in Nuclear Physics*, pages 1–223. Springer US, 1991.

[159] F. Perey and B. Buck. A non-local potential model for the scattering of neutrons by nuclei. *Nucl. Phys.*, 32(0):353 – 380, 1962.

[160] Yuan Tian, Dan-Yang Pang, and Zhong-Yu Ma. Systematic nonlocal optical model potential for nucleons. *Int. J. Mod. Phys. E*, 24(01):1550006, 2015.

[161] J. M. Mueller, R. J. Charity, R. Shane, L. G. Sobotka, S. J. Waldecker, W. H. Dickhoff, A. S. Crowell, J. H. Esterline, B. Fallin, C. R. Howell, C. Westerfeldt, M. Youngs, B. J. Crowe, and R. S. Pedroni. Asymmetry dependence of nucleon correlations in spherical nuclei extracted from a dispersive-optical-model analysis. *Phys. Rev. C*, 83:064605, Jun 2011.

[162] W. Tornow, E. Woye, G. Mack, C.E. Floyd, K. Murphy, P.P. Guss, S.A. Wender, R.C. Byrd, R.L. Walter, T.B. Clegg, and H. Leeb. Analyzing power and differential cross section at 9.9, 11.9 and 13.9 mev for ca(n, n)ca. *Nucl. Phys.*, A385(3):373 – 406, 1982.

[163] G. M. Honoré, W. Tornow, C. R. Howell, R. S. Pedroni, R. C. Byrd, R. L. Walter, and J. P. Delaroche. Coupled-channel analysis of nucleon scattering from ^{40}ca up to 80 mev. *Phys. Rev. C*, 33:1129–1140, Apr 1986.

[164] R. Alarcon, J. Rapaport, and R.W. Finlay. Nucleon elastic scattering from ^{40}ca between 11 and 48 mev. *Nucl. Phys.*, A462(3):413 – 444, 1987.

[165] S. Tanaka and Y. Yamanouti. Fast neutron scattering from zr-90 and zr-92. In T. Fuketa, T. Taura, and S. Kikuchi, editors, *Progress Report (July 1976 to June 1977)*, page 11, Japan, 1977. Japan Atomic Energy Research Institute. NEANDC(J)-51/U.

[166] Y. Wang and J. Rapaport. Neutron scattering from ^{90,91,92,94}zr. *Nucl. Phys.*, A517(2):301 – 328, 1990.

[167] D.E. Bainum, R.W. Finlay, J. Rapaport, M.H. Hadizadeh, J.D. Carlson, and J.R. Comfort. Isospin effects in nucleon inelastic scattering from single-closed-shell nuclei. *Nucl. Phys.*, A311(3):492 – 506, 1978.

[168] J. Rapaport, T.S. Cheema, D.E. Bainum, R.W. Finlay, and J.D. Carlson. Neutron scattering from ^{208}pb. *Nucl. Phys.*, A296(1):95 – 108, 1978.

[169] L. F. Hansen, F. S. Dietrich, B. A. Pohl, C. H. Poppe, and C. Wong. Test of microscopic optical model potentials for neutron elastic scattering at 14.6 mev over a wide mass range. *Phys. Rev. C*, 31:111–119, Jan 1985.

[170] C. E. Floyd, Jr. *Scattering of polarized fast neutrons from beryllium-9, iron-54, copper-65, and lead-208: the determination of the nucleon-nucleus spin-orbit interaction.* PhD thesis, Duke University, 1981.

[171] R. W. Finlay, J. R. M. Annand, T. S. Cheema, J. Rapaport, and F. S. Dietrich. Energy dependence of neutron scattering from ^{208}Pb in the energy range 7⁻50 mev. *Phys. Rev. C*, 30:796–806, Sep 1984.

[172] R. P. DeVito, Dao T. Khoa, Sam M. Austin, U. E. P. Berg, and Bui Minh Loc. Neutron scattering from ^{208}pb at 30.4 and 40.0 mev and isospin dependence of the nucleon optical potential. *Phys. Rev. C*, 85:024619, Feb 2012.

[173] S.M. El-Kadi, C.E. Nelson, F.O. Purser, R.L. Walter, A. Beyerle, C.R. Gould, and L.W. Seagondollar. Elastic and inelastic scattering of neutrons from ^{54,56}fe and ^{63,65}cu: (i). measurements from 8 to 14 mev and a spherical optical model analysis. *Nuclear Physics A*, 390(3):509 – 540, 1982.

[174] S. Mellema, R. W. Finlay, F. S. Dietrich, and F. Petrovich. Microscopic and conventional optical model analysis of fast neutron scattering from ^{54,56}Fe. *Phys. Rev. C*, 28:2267–2277, Dec 1983.

[175] P.P. Guss, R.C. Byrd, C.E. Floyd, C.R. Howell, K. Murphy, G. Tungate, R.S. Pedroni, R.L. Walter, J.P. Delaroche, and T.B. Clegg. Cross sections and analyzing powers for

fast-neutron scattering to the ground and first excited states of ^{58}ni and ^{60}ni. *Nuclear Physics A*, 438(1):187 – 211, 1985.

[176] Y. Yamanouti, J. Rapaport, S.M. Grimes, V. Kulkarni, R.W. Finlay, D. Bainum, P. Grabmayr, and G. Randers-Pehrson. Elastic and inelastic scattering of 24 mev neutrons from even isotopes of ni. In *Brookhaven National Laboratory Reports*, volume 1, page 375, Knoxville, USA, 1979.

[177] Mahmoud Jaghoub. private communication. 2017.

[178] Isao Tanihata, Herve Savajols, and Rituparna Kanungo. Recent experimental progress in nuclear halo structure studies. *Progress in Particle and Nuclear Physics*, 68:215 – 313, 2013.

[179] V.I. Goldansky. On neutron-deficient isotopes of light nuclei and the phenomena of proton and two-proton radioactivity. *Nuclear Physics*, 19:482 – 495, 1960.

[180] J. Giovinazzo, B. Blank, M. Chartier, S. Czajkowski, A. Fleury, M. J. Lopez Jimenez, M. S. Pravikoff, J.-C. Thomas, F. de Oliveira Santos, M. Lewitowicz, V. Maslov, M. Stanoiu, R. Grzywacz, M. Pfützner, C. Borcea, and B. A. Brown. Two-proton radioactivity of ^{45}Fe. *Phys. Rev. Lett.*, 89:102501, Aug 2002.

[181] M. Pftzner, E. Badura, C. Bingham, B. Blank, M. Chartier, H. Geissel, J. Giovinazzo, L.V. Grigorenko, R. Grzywacz, M. Hellstrm, Z. Janas, J. Kurcewicz, A.S. Lalleman, C. Mazzocchi, I. Mukha, G. Mnzenberg, C. Plettner, E. Roeckl, K.P. Rykaczewski, K. Schmidt, R.S. Simon, M. Stanoiu, and J.-C. Thomas. First evidence for the two-proton decay of ^{45}Fe. *Eur. Phys. J. A*, 14(3):279–285, 2002.

[182] B. Blank, A. Bey, G. Canchel, C. Dossat, A. Fleury, J. Giovinazzo, I. Matea, N. Adimi, F. De Oliveira, I. Stefan, G. Georgiev, S. Grévy, J. C. Thomas, C. Borcea, D. Cortina, M. Caamano, M. Stanoiu, F. Aksouh, B. A. Brown, F. C. Barker, and W. A. Richter. First observation of ^{54}Zn and its decay by two-proton emission. *Phys. Rev. Lett.*, 94:232501, Jun 2005.

[183] C. Dossat, A. Bey, B. Blank, G. Canchel, A. Fleury, J. Giovinazzo, I. Matea, F. de Oliveira Santos, G. Georgiev, S. Grévy, I. Stefan, J. C. Thomas, N. Adimi, C. Borcea, D. Cortina Gil, M. Caamano, M. Stanoiu, F. Aksouh, B. A. Brown, and L. V. Grigorenko. Two-proton radioactivity studies with ^{45}Fe and ^{48}Ni. *Phys. Rev. C*, 72:054315, Nov 2005.

[184] I. Mukha, K. Sümmerer, L. Acosta, M. A. G. Alvarez, E. Casarejos, A. Chatillon, D. Cortina-Gil, J. Espino, A. Fomichev, J. E. García-Ramos, H. Geissel, J. Gómez-Camacho, L. Grigorenko, J. Hoffmann, O. Kiselev, A. Korsheninnikov, N. Kurz, Yu. Litvinov, I. Martel, C. Nociforo, W. Ott, M. Pfutzner, C. Rodríguez-Tajes, E. Roeckl,

M. Stanoiu, H. Weick, and P. J. Woods. Observation of two-proton radioactivity of ^{19}Mg by tracking the decay products. *Phys. Rev. Lett.*, 99:182501, Oct 2007.

[185] J. Gómez del Campo, A. Galindo-Uribarri, J. R. Beene, C. J. Gross, J. F. Liang, M. L. Halbert, D. W. Stracener, D. Shapira, R. L. Varner, E. Chavez-Lomeli, and M. E. Ortiz. Decay of a resonance in ^{18}Ne by the simultaneous emission of two protons. *Phys. Rev. Lett.*, 86:43–46, Jan 2001.

[186] L. V. Grigorenko, R. C. Johnson, I. G. Mukha, I. J. Thompson, and M. V. Zhukov. Two-proton radioactivity and three-body decay: General problems and theoretical approach. *Phys. Rev. C*, 64:054002, Oct 2001.

[187] L. V. Grigorenko and M. V. Zhukov. Two-proton radioactivity and three-body decay. ii. exploratory studies of lifetimes and correlations. *Phys. Rev. C*, 68:054005, Nov 2003.

[188] L. V. Grigorenko, I. G. Mukha, C. Scheidenberger, and M. V. Zhukov. Two-neutron radioactivity and four-nucleon emission from exotic nuclei. *Phys. Rev. C*, 84:021303, Aug 2011.

[189] Z. Kohley, T. Baumann, D. Bazin, G. Christian, P. A. DeYoung, J. E. Finck, N. Frank, M. Jones, E. Lunderberg, B. Luther, S. Mosby, T. Nagi, J. K. Smith, J. Snyder, A. Spyrou, and M. Thoennessen. Study of two-neutron radioactivity in the decay of ^{26}O. *Phys. Rev. Lett.*, 110:152501, Apr 2013.

[190] M. D. Jones, N. Frank, T. Baumann, J. Brett, J. Bullaro, P. A. DeYoung, J. E. Finck, K. Hammerton, J. Hinnefeld, Z. Kohley, A. N. Kuchera, J. Pereira, A. Rabeh, W. F. Rogers, J. K. Smith, A. Spyrou, S. L. Stephenson, K. Stiefel, M. Tuttle-Timm, R. G. T. Zegers, and M. Thoennessen. Two-neutron sequential decay of ^{24}O. *Phys. Rev. C*, 92:051306, Nov 2015.

[191] A. Spyrou, J. K. Smith, T. Baumann, B. A. Brown, J. Brown, G. Christian, P. A. DeYoung, N. Frank, S. Mosby, W. A. Peters, A. Schiller, M. J. Strongman, M. Thoennessen, and J. A. Tostevin. Search for the ^{15}be ground state. *Phys. Rev. C*, 84:044309, Oct 2011.

[192] F. M. Marqués, N. A. Orr, N. L. Achouri, F. Delaunay, and J. Gibelin. Comment on "first observation of ground state dineutron decay: ^{16}Be". *Phys. Rev. Lett.*, 109:239201, Dec 2012.

[193] A. Spyrou, Z. Kohley, T. Baumann, D. Bazin, B. A. Brown, G. Christian, P. A. DeYoung, J. E. Finck, N. Frank, E. Lunderberg, S. Mosby, W. A. Peters, A. Schiller, J. K. Smith, J. Snyder, M. J. Strongman, M. Thoennessen, and A. Volya. Spyrou *et al.* replies:. *Phys. Rev. Lett.*, 109:239202, Dec 2012.

[194] L. V. Grigorenko, I. G. Mukha, and M. V. Zhukov. Lifetime and fragment correlations for the two-neutron decay of ^{26}O ground state. *Phys. Rev. Lett.*, 111:042501, Jul 2013.

[195] K. Hagino and H. Sagawa. Correlated two-neutron emission in the decay of the unbound nucleus ^{26}O. *Phys. Rev. C*, 89:014331, Jan 2014.

[196] Rimantas Lazauskas and Jaume Carbonell. Testing nonlocal nucleon-nucleon interactions in four-nucleon systems. *Phys. Rev. C*, 70:044002, Oct 2004.

[197] B.V. Danilin, I.J. Thompson, J.S. Vaagen, and M.V. Zhukov. Three-body continuum structure and response functions of halo nuclei (i): ^{6}he. *Nuclear Physics A*, 632(3):383 – 416, 1998.

[198] J. Snyder, T. Baumann, G. Christian, R. A. Haring-Kaye, P. A. DeYoung, Z. Kohley, B. Luther, M. Mosby, S. Mosby, A. Simon, J. K. Smith, A. Spyrou, S. Stephenson, and M. Thoennessen. First observation of ^{15}be. *Phys. Rev. C*, 88:031303, Sep 2013.

[199] E. K. Warburton and B. A. Brown. Effective interactions for the 0 p 1 s 0 d nuclear shell-model space. *Phys. Rev. C*, 46:923–944, Sep 1992.

[200] Ian J. Thompson. private communication. 2013.

[201] I.J. Thompson, F.M. Nunes, and B.V. Danilin. Face: a tool for three body faddeev calculations with core excitation. *Computer Physics Communications*, 161(12):87 – 107, 2004.

[202] D. Gogny, P. Pires, and R. De Tourreil. A smooth realistic local nucleon-nucleon force suitable for nuclear hartree-fock calculations. *Physics Letters B*, 32(7):591 – 595, 1970.

[203] F.M. Nunes, J.A. Christley, I.J. Thompson, R.C. Johnson, and V.D. Efros. Core excitation in three-body systems: Application to ^{12}be. *Nuclear Physics A*, 609(1):43 – 73, 1996.

[204] N K Timofeyuk, I J Thompson, and J A Tostevin. Single-particle motion at large distances in 2n+core cluster systems near the drip line: a challenge for nuclear theory and experiment. *Journal of Physics: Conference Series*, 111(1):012034, 2008.

[205] I. Brida and F. M. Nunes. A microscopic hyper-spherical model: Application to ^{6}he. *International Journal of Modern Physics E*, 17(10):2374–2378, 2008.

[206] I. Brida, F.M. Nunes, and B.A. Brown. Effects of deformation in the three-body structure of ^{11}li. *Nuclear Physics A*, 775(12):23 – 34, 2006.

[207] R. B. Wiringa, V. G. J. Stoks, and R. Schiavilla. Accurate nucleon-nucleon potential with charge-independence breaking. *Phys. Rev. C*, 51:38–51, Jan 1995.

[208] Roderick V Reid Jr. Local phenomenological nucleon-nucleon potentials. *Annals of Physics*, 50(3):411 – 448, 1968.

[209] M. Thoennessen, S. Yokoyama, A. Azhari, T. Baumann, J. A. Brown, A. Galonsky, P. G. Hansen, J. H. Kelley, R. A. Kryger, E. Ramakrishnan, and P. Thirolf. Population of ^{10}Li by fragmentation. *Phys. Rev. C*, 59:111–117, Jan 1999.